Towards realisation of long-lived ensembles of circular Rydberg atoms

Guillaume Cœuret Cauquil

To cite this version:

Guillaume Cœuret Cauquil. Towards realisation of long-lived ensembles of circular Rydberg atoms. Quantum Physics [quant-ph]. Université Paris sciences et lettres, 2026. English. ⟨NNT : 2026UPSLE001⟩. ⟨tel-05603823⟩

HAL Id: tel-05603823
https://theses.hal.science/tel-05603823v1

Submitted on 27 Apr 2026

PSL
UNIVERSITÉ PARIS

THÈSE DE DOCTORAT
DE L'UNIVERSITÉ PSL

Préparée à l'École Normale Supérieure

Towards realisation of long-lived ensembles of circular Rydberg atoms

Soutenue par
Guillaume Cœuret Cauquil
Le 12 janvier 2026

École doctorale n°564
École Doctorale Physique en Île-de-France

Spécialité
Physique quantique

Composition du jury :

Frédéric CHEVY Professeur, Laboratoire de physique de l'Ecole normale supérieure	*Président du Jury*
Igor FERRIER-BARBUT Chargé de recherche, Laboratoire Charles Fabry	*Rapporteur*
Stefan KUHR Professor, University of Strathclyde	*Rapporteur*
Anaïs DRÉAU Chargée de recherche, Laboratoire Charles Coulomb	*Examinatrice*
Jérôme LODEWYCK Chargé de recherche, Laboratoire Temps Espace	*Examinateur*
Igor DOTSENKO Professeur, Laboratoire Collisions Agrégats Réactivité	*Directeur de thèse*
Michel BRUNE Directeur de recherche, Laboratoire Kastler Brossel	*Invité*

ENS | PSL

À ma famille,

Que dites-vous?. . . C'est inutile ? . . . Je le sais !
Mais on ne se bat pas dans l'espoir du succès !
Non ! non, c'est bien plus beau lorsque c'est inutile !

– Edmond Rostand, *Cyrano de Bergerac* (1897)

Acknowledgements

Tout d'abord, je remercie tous les membres du jury d'avoir accepté de relire et d'évaluer mon travail de thèse. Merci à Igor Ferrier-Barbut et Stefan Kuhr pour leur relecture attentive de mon manuscrit, ainsi qu'à Jérôme Lodewick et Anaïs Dréau pour leur présence à ma soutenance. Je remercie particulièrement Anaïs, qui a encadré mon premier stage de physique quantique expérimentale en L3, à qui je dois une bonne part de mes connaissances en optique et qui m'a beaucoup aidé depuis.

Ce travail de thèse n'aurait jamais pu être réalisé sans l'aide de nombreuses personnes, qui m'ont épaulé de près ou de loin au cours de ces dernières années.

Je remercie Igor de m'avoir accepté en thèse et encadré au cours des différents projets sur lesquels nous avons travaillé ensemble, de la thermodynamique quantique à l'inhibition de l'émission spontanée. Il y a eu au cours de ces recherches de nombreux rebondissements —le dernier en date étant un déménagement de la manip à l'autre bout du pays —mais je suis très heureux qu'on ait pu amener le projet aussi loin aujourd'hui, et j'espère qu'il ira aussi loin qu'on l'espère. Merci également à Michel de m'avoir accepté dans l'équipe, ainsi que pour son aide régulière pendant les premiers mois où Igor était à Toulouse. Je remercie aussi Jean-Michel, qui, bien qu'étant émérite, continue à venir régulièrement au laboratoire pour nous partager autant de précieux conseils que de bonne humeur et d'anecdotes toujours surprenantes les unes que les autres. Son aide m'a été particulièrement précieuse sur ces derniers mois, que ce soit pour la rédaction ou la préparation de la soutenance.

Merci aussi aux personnes qui ont travaillé avec moi sur ce projet. For this, I thank Ankul, with whom we built the experiment and shared both struggles and successes. Merci beaucoup à Gauthier, qui va reprendre la suite du projet après nous. Il a commencé dans l'équipe au moment où Igor partait sur Toulouse, un moment particulièrement difficile, et son arrivée a été comme un rayon de soleil, son enthousiasme et sa solidité amenant un renouveau au projet. Je n'ai aucun doute sur le fait qu'il saura faire briller la manip. Merci également à Julien qui a rejoint le navire sur Toulouse, avec ses questions toujours plus précises les unes que les autres, et qui, je suis sûr, sera d'une aide inestimable pour la suite de l'expérience. Merci aussi à Houssna qui a fait un stage avec nous au début du projet, avec qui il a toujours été un plaisir de travailler, surtout en écoutant de la bonne musique en salle manip ! Merci aussi à Diego et Charlotte avec qui nous avons travaillé sur Toulouse.

Je remercie aussi l'ensemble des membres de l'équipe Atomes de Rydberg de Paris. Je pense d'abord à Andrès, Baptiste et Benoît, qui ont tous les trois commencé leurs thèses en même temps que moi, et avec qui nous avons partagé de nombreux moments de la thèse, les hauts comme les bas, toujours en nous soutenant les uns les autres. Merci aussi à celleux présent·es à mon arrivée dans l'équipe, qui m'ont accueilli et beaucoup appris. Brice, toujours riche en conseils sur la thèse, Paul, Andrea, Maxime, Angelo, Léa, dont le soutien et les conseils ont été inestimables, Yohann, qui m'a énormément aidé pour la conception du système optique, toujours prêt à répondre à mes questions et enfin Haiteng, who started the inhibition project at room temperature, and who helped me a lot understanding the physics behind the inhibition and converted me to the use of emacs. Merci également à toustes les doctorant·es que nous avons accueilli·es au cours des dernières années, Mathis, Aurore, Gautier et Abderrahmane.

Je remercie aussi les personnes impliquées dans la création du jeu de société Qats, à savoir Gautier, Thiziri et particulièrement Kim, avec qui nous continuons le projet. Un énorme merci à Khamsa qui nous a accompagné·es pour Qats, et qui a dépensé une énergie considérable pour nous trouver des formations, du public pour la médiation et sans qui nous n'aurions jamais pu arriver aussi loin. Merci aussi à Frédéric qui continue à nous accompagner sur le projet.

Je souhaite aussi remercier le personnel des différents services du Collège de France pour son soutien constant. Mention spéciale à Pascal Travers et à l'équipe de l'atelier du Collège de France, avec qui nous avons travaillé en étroite collaboration pour la conception du cœur du montage expérimental et à qui nous devons la fabrication des pièces les plus cruciales.

Merci à tous les membres du LKB pour ces années riches en échanges, scientifiques ou non. Merci à Christelle, Audrey et Thierry qui m'ont beaucoup aidé pour mes missions et avec qui il a toujours été très agréable de discuter quand iels passaient nous voir au Collège. Merci aussi à Nancy et Nicolas dont l'accompagnement et les conseils ont été très précieux. Merci aussi aux personnes avec qui nous avons organisé les Ateliers du LKB, qui m'ont permis de garder un œil sur les fondements quantiques. Merci aussi aux membres du LCAR qui nous ont très chaleureusement accueillis lorsque nous avons déménagé sur Toulouse. Le déménagement et le changement de laboratoire ne se seraient pas aussi bien passés si nous n'avions pas eu la chance de trouver dans le sud un environnement aussi agréable.

Sur un plan plus personnel, j'aimerais aussi remercier mes ami-es, qui m'ont soutenu et aidé tout au long de ma thèse, supportant tant mes baisses de moral que mon enthousiasme débordant au gré des fluctuations de l'avancement de la manip.

Je remercie les ami-es que je me suis fait-es en étant sur Paris. Je pense notamment aux membres du groupe de musique Icy Seagull, nos répétitions hebdomadaires étant toujours un bon moment à partager (et l'occasion de se défouler quand la manip ne marchait pas !). Merci aussi aux personnes avec qui j'ai milité, en particulier Zeph et Kairos, avec qui j'ai partagé des moments inoubliables et avec qui j'ai adoré (et adore toujours) parler politique pendant des heures.

Merci à mes ami·es de lycée et collège, desquel·es je reste proche malgré les années, et le fait qu'on ne se voit pas toujours autant qu'on l'aimerait : Greg, Camille, Hugo, Théo, Antho, Yohann, Marie, Élise, Gus. Je remercie aussi ma prof d'histoire de première, Mme Larbi, qui m'a longtemps guidé dans mon orientation et sans qui je ne serai probablement pas là aujourd'hui. Merci également à Théo et Lucie, des ami·es de prépa que j'ai pu revoir plus régulièrement sur Paris et qui m'ont soutenu tout au long de ma thèse, et desquel·les je reste très proche. Je pense aussi à mes amis proches de l'ENS, Joa, Grode et Joël, avec qui on a pu partager nos différentes expériences de thèse.

Pour finir, j'aimerais remercier les membres de ma famille, sur lesquels je peux toujours compter et que j'espère rendre fiers aujourd'hui. Tout d'abord merci à mon chat Arkona, qui m'a soutenu à sa manière, en particulier en s'assurant à coups de miaulements que je prenne des pauses régulières pour jouer avec elle pendant la rédaction. Merci aussi à ma belle-famille qui a su m'accueillir, bien que je sois physicien et non chimiste. Merci à l'ensemble de la famille Cœuret: mes grands-parents, mes oncles et tantes, mes cousins et cousines, que j'aime toujours retrouver et qui me suivent pour la plupart depuis mes premiers pas. Merci aussi à mon frère et ma sœur, qui m'ont soutenu même si cela impliquait de m'entendre parler d'atomes et de lasers à tout va.

Je remercie du fond du cœur ma maman, qui m'a toujours soutenu et sans qui je ne serais jamais arrivé aussi loin. La vie n'a pas toujours été facile, mais dans les bons moments comme les plus durs j'ai toujours pu avoir son écoute, son soutien et son amour, et j'espère qu'elle est aujourd'hui fière de moi.

Enfin, je remercie Élise qui partage ma vie et à qui je dois beaucoup. Nous avons partagé ensemble tous les moments de la thèse, nous soutenant l'un l'autre malgré la distance, que ce soit pour les moments de joie, de tristesse, de réussite, d'échecs et tout ce qui va avec la recherche et la vie en général. Son soutien indéfectible et son écoute attentive m'ont aidé tout au long de la thèse, et m'ont permis d'arriver là où j'en suis aujourd'hui. Avancer dans la vie ensemble est toujours un bonheur, avec la fin de nos thèses se clôt un chapitre d'une très longue histoire.

Contents

List of Figures

Notations

Below are notations and abbreviation used in the manuscript, as well as the legend used for optical setups.

Fundamental constants

ϵ_0	Vacuum electric permittivity
e	Elementary charge
$\hbar$	Reduced Planck constant
a_0	Bohr radius
c	Speed of light
R_y	Rydberg energy
μ_B	Bohr magneton
α	Fine structure constant
k_B	Boltzmann constant

Abbreviation

BBR	Black-body radiation
CQED	Cavity quantum electrodynamics
MLE	Maximum likelihood estimation
TPM	Two-point measurement
KLU	Kullback-Leibler-Umegaki
CPTP	Completely positive trace-preserving
POVM	Positive operator-valued measurement
SLM	Spatial light modulator
RAM	Radiowave absorbent material
DT	Dipole trap
LG	Laguerre-Gauss
RF	Radiofrequency
AOM	Acousto-optics modulators
MOT	Magneto-optical trap
CCD	Charge-coupled device
DDS	Direct Digital synthesiser

Optical setup legend

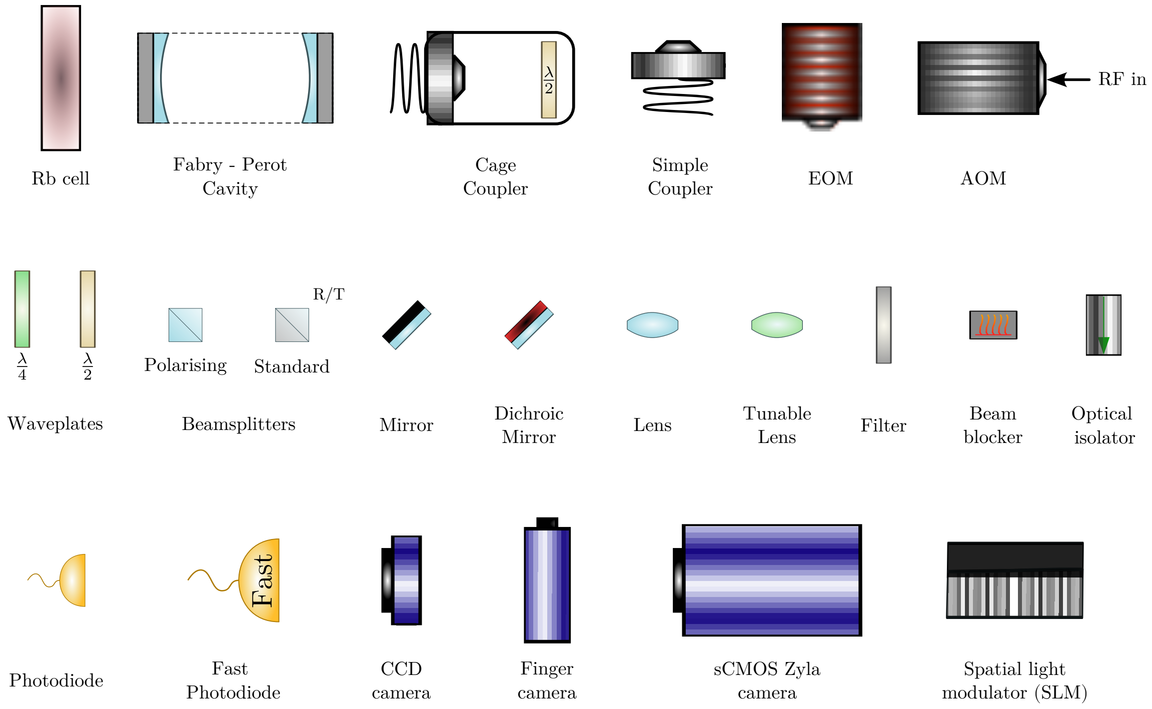

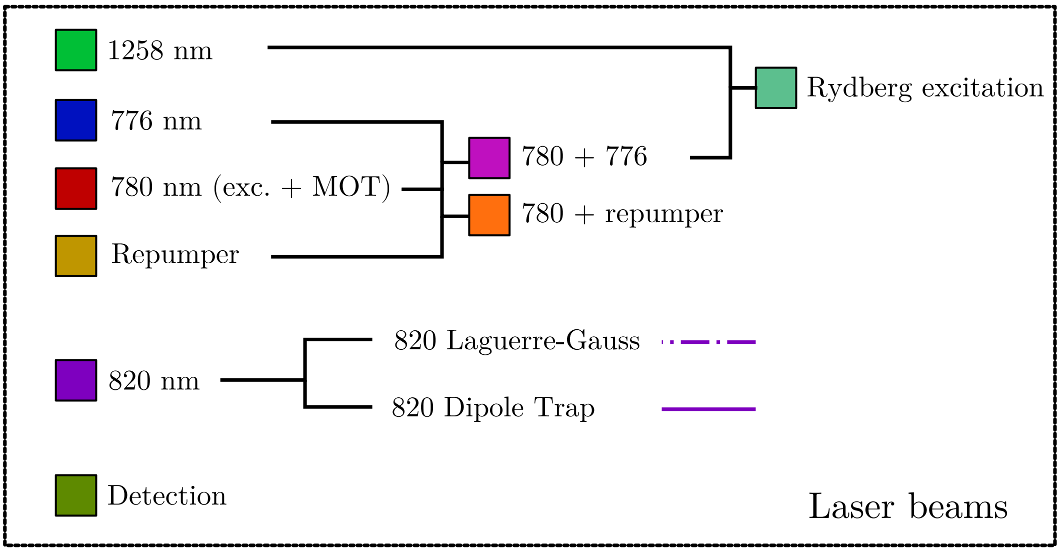

Introduction

> *La révolution sera la floraison de l'humanité comme l'amour est la floraison du cœur.*
>
> — Louise Michel, *La Commune, Histoire et souvenirs (1898)*

The quantum revolution(s)

The quantum theory emerged in the beginning of the XX$^{\text{th}}$ century. It arose from the observation of anomalies in the classical theory, such as the ultraviolet catastrophe. Quantum theory takes its name from one of its key observations, which is that energy states of matter are quantised [1]. This theory successfully allowed for a better understanding of matter behaviour at the atomic scale, and for example explained the hydrogen spectral lines [2]. This is often referred to as the first quantum revolution. In addition to explaining matter at a microscopic scale, quantum theory challenged fundamental physical concepts [3]. Key physical assumptions such as locality or determinism are undermined by the quantum formalism. One partial solution has been provided by the Copenhagen interpretation, but even today no single undisputed interpretation has emerged. Despite ontological issues, the modern formulation of the quantum theory emerged within a few years with a well-determined formalism.

Using this new description of matter, new technologies have been made possible. One example is the light amplification by stimulated emission of radiation, also known as laser, a technology widely used nowadays [4]. Applications of quantum mechanics remained dedicated to macroscopic systems for a long time, while manipulation of isolated quantum systems remained in the realm of thought experiments. This frontier was crossed at the end of the XX$^{\text{th}}$ century. Systems involving single atoms interacting with superconducting cavities allowed for an experimental realisation of the Schrödinger's cat experiment [5], and the manipulation of single photons refuted the existence of hidden variables in the theory [6]. The successful manipulation of individual quantum systems and its application to quantum information and sensing is often referred to as the second quantum revolution.

Taking Thomas Kuhn's description of progress in science, quantum theory is a scientific revolution [7]. Until now, the quantum paradigm remains uncontested, and we are in a period of “normal science”, with respect to the first quantum revolution. This requires an application of the paradigm to more and more systems until a new paradigm emerges.

Understanding the quantum

Looking for the limits of the paradigm can be done from different directions. One example is the path of quantum foundations, which directly studies the theory itself and aims at rationalising the basic axioms of the theory. Another direction is to extend the range of application of the theory until it fails to draw consistent conclusions.

The latter is done by studying various quantum systems, and often leads to technological progress in the meantime. Quantum systems are theoretically described by vector states in a Hilbert space, whose evolution is governed by Schrödinger's equation. In this equation, one key object is the system Hamiltonian. Consequently, similar behaviours are expected for systems that share the same Hamiltonian. The problem of this path then ultimately goes to the study of different Hamiltonian dynamics, together with a comparison with real systems.

Theoretical description and experimental manipulation of isolated systems already led to a finer understanding of key concepts of the theory, such as quantum superposition or decoherence [8, 9]. However, extension of these properties to many-body systems turned out to be more challenging. The discoveries of the first quantum revolution were based on macroscopic systems where the particles were independent. For other phenomena, such as quantum magnetism or phase transitions, a shared entanglement over a large ensemble of particles is essential. For some of these systems, there are no analytical solutions for the Hamiltonian dynamics. Some approximation methods exist, but their validity domain is limited. A way to circumvent this issue is to study such ensembles using simulation [10]. It is not so different from what is done classically by using computers to solve Navier-Stokes equations or scale models in a wind tunnel for studying the airflow around a plane.

Simulation can be done digitally. However, for describing large quantum systems, the use of classical computers quickly faces a complexity challenge coming from the Hilbert space size. For example, for a set of 100 qubits, the number of variables to store is $2^{100} \approx 10^{30}$ [11], and with a 32-bits encoding, total required memory is around 4×10^{19} Tb. This issue can be solved using digital quantum simulation or, in other words, a fully programmable quantum computer. A lot of work has been done towards this direction, and it is today one of the main pillars of quantum research. With its flexibility, the quantum computer would also provide a computational advantage for classical computation, one example being Shor's algorithm [12].

Alternatively, it is also possible to do analogue quantum simulation[1] [13]. By studying the evolution of a well-controlled system, one can indeed acquire knowledge about a target system, provided that their respective models are equivalent, *e.g.* if they have the same Hamiltonian dynamics. The practical advantage of such a quantum simulator is that it doesn't require the universality of a quantum computer, making its implementation less demanding. A quantum simulator is tailored for the resolution of a specific problem and thus allows one to draw conclusions about some specific systems, with fewer practical constraints [14].

Quantum simulation platforms

Analogue quantum simulation can be implemented on different experimental platforms, based on individually controlled systems [10, 15]. The following discussion will be restricted to a few illustrative examples, but numerous others exist.

A first example is the photonic platform [16, 17]. As its name suggests, the main elements are photons, which are already widely used in the context of quantum computing [18, 19, 20]. One of the main difficulties with such systems is engineering a deterministic two-photon gate, which requires mediating systems. Photonic simulators have for example been used for the realisation of the Bose-Hubbard model [21] or frustrated spin systems [22].

Another kind of simulator is based on trapped ions [23]. This textbook system involves rare-earth atoms with a missing electron, trapped in magnetic Paul traps. Using trapped ions, simulations of, for example, frustrated spin systems [24] have been performed. More recently, a 300-ion long-range Ising model was implemented [25].

Quantum simulation can also be implemented in various nuclear or electronic spin systems. Some examples are simulators based on nuclear magnetic resonance (NMR) of nuclear spins in molecules [26, 27, 28] or in solid-state matrices [29, 30], or based on electronic spins in semiconductor defects, such as NV centres [31, 32]. One asset of

---

[1] In this context, additional terminology also exists. If the target system studied is a physical system, it is called "analogue emulation". But if the target system is a formal model, it is called "analogue computation".

such systems is that most of them can be operated at room temperature and can exploit the long coherence time of nuclear spins.

Superconducting qubits are also promising systems for quantum simulation [33]. A typical example is the circuit quantum electrodynamics (cQED), where superconducting coplanar waveguides are used as resonators, with Josephson junctions to provide non-linearities and create effective two-level systems. Examples of simulations performed with such systems are studies of many-body localisation [34, 35].

Another possibility comes from the use of neutral atoms. One typical setup involves ultracold atoms in quantum gases trapped in optical lattices [36]. By changing the lattice, many parameters can be tuned to change, for example, the atoms tunnelling between sites or the on-site interaction, leading to a large variety of possible Hamiltonians. One simulation example is the observation of many body localisation of interacting fermions [37].

At last, the platform on which the focus will be put in the following is the use of individual atoms trapped in tightly focused laser beams, also known as optical tweezers. Large inter-atomic coupling can be obtained by exciting atoms to a Rydberg state, with the tweezers turned off. [38, 39]. One of the main advantages of such systems is the possible control and readout of each single atom used in the experiment. With it, simulations of 2D Ising models [40] and about topological spin liquids [41] have been performed.

Quantum simulation with neutral atoms in optical tweezers

Because of its control over every single atom of the simulator, experiments using single atoms trapped in optical tweezers are promising for quantum simulation. Different tools allow the creation of defect-free 2D arrays with arbitrary geometries, with a spacing of the order of a few micrometres [42]. Such spacing allows for single-site addressing by means of optical techniques.

This distance has a counterpart, which is that interaction between atoms in the ground state is too weak. To increase interaction strength, atoms can be excited to a Rydberg state, of large principal quantum number n. These states are well known for their large dipole moments, and hence for their strong coupling to external electric fields. They have been used in the cavity quantum electrodynamics (CQED) experiments [43], and more recently in Rydberg-based quantum simulators [44]. For a typical example of experiments involving Rydberg atoms, simulations are done by encoding the logical ground state $|0_L\rangle$ onto the atomic ground state and the logical excited state $|1_L\rangle$ onto the Rydberg state, for which the interaction takes place. Pairs of atoms in Rydberg states experience a dipole-dipole interaction, for which two typical regimes are usually considered [38].

For pairs in the same Rydberg state, the interaction doesn't have a first-order contribution in the perturbation theory. The obtained second-order contribution has a scaling in $\propto 1/R^6$, with R being the inter-atomic distance [45]. This contribution is often referred to as van der Waals interaction, and its strength Ω can reach tens of megahertz at a distance of several micrometres. This interaction is at the heart of the Rydberg blockade effect [46]. Considering a pair of atoms, excitation of one atom of the pair leads to an interaction that prevents the second one from being excited. This leads to the creation of a superposition state with one or the other atom excited. For a given laser excitation field, this blockade occurs if the inter-atomic distance is below a typical radius called the blockade radius.

For atoms in different Rydberg states, with $\Delta n = 1$, a first-order interaction appears. It is associated with an exchange energy, whose scaling is in $\propto 1/R^3$. Depending on the two states considered, the interaction strength can be dominant, negligible or of the order of the van der Waals interaction with micrometre inter-atomic distances [47]. Such systems have already demonstrated impressive results, both for quantum computing and quantum simulation [40, 41, 44, 48]

One of the main limitations of Rydberg atom-based simulators is the simulation time, relative to the interaction time Ω^{-1}. A first reason comes from the fact that Rydberg states are repelled by the dipole traps. The tweezers therefore have to be switched off during the simulation. Atoms are then free to move, and the array geometry is broken by the interaction-induced movements. A second, more fundamental limitation comes from the Rydberg state lifetime. For Rydberg states that are optically accessible, the intrinsic radiative lifetime is of the order of a few hundred microseconds. The global lifetime of an atomic ensemble decreases linearly with the number of particles. For a simulator with 100 atoms with a typical lifetime of $100\,\mu$s and an interaction strength of 10 MHz, a simulation with no decay is limited to around 10 interaction times.

Towards simulation of slow processes

Despite their limited simulation time, Rydberg atom-based simulators have already been intensively used to study spin systems. Such systems are indeed of particular importance, as they are closely related to the magnetic properties of matter. For a deeper understanding, the full phase diagram of a spin ensemble can be studied. This in-depth study includes the study of slow processes that can be involved when looking at phase transitions and so the necessity of having a longer simulation time.

Atomic lifetime can be increased by using Rydberg states with maximal angular momentum, also known as circular Rydberg states. To fully take advantage of these long-lived atoms, they can be trapped by means of the ponderomotive effect [49]. This ensures that atoms are not lost during the simulation. Recent work of our group demonstrated interaction and local addressing of circular states trapped in optical tweezers [50] [51]. These states have only one decay channel in the microwave range. As a consequence, their intrinsic lifetime is around 30 ms at 0 K, for $n \approx 50$. This property was already central for the CQED experiments.

More interestingly, their lifetime can be further increased. As suggested in the early 80's, spontaneous emission can be inhibited by changing the density of modes of vacuum electromagnetic fields around the atoms [52]. This has been experimentally demonstrated in an atomic beam setup [53]. More recently, an extended lifetime has been obtained for cold atoms in a room-temperature inhibition setup [54]. In the latter experiment, circular Rydberg states with a millisecond lifetime have been observed despite the black body radiation (BBR)-induced transfers. These transitions were the limiting factor of this setup and can be suppressed by going to temperatures below 1 K.

The combination of circular Rydberg atoms trapping with an inhibition setup was at the heart of the simulator proposed by our group a few years ago [47]. In this proposal, the inhibition of the spontaneous emission in an environment below 1 K suggested that a lifetime in the tens of seconds range should be achievable in a realistic experiment. In a simulator with 100 atoms with an interaction strength of 10 MHz, it would correspond to 1×10^6 interaction times. This would provide an advantage in the scaling of the simulator and in the study of effects with long timescales, *i.e.* slow processes.

More precisely, the proposed setup aims at simulating a chain of 1/2-spins with an XXZ model Hamiltonian. An artist view is given in Figure 1. To do so, circular Rydberg atoms are trapped using the ponderomotive effect in between two parallel plates, used to inhibit the spontaneous emission. A control of the electric and magnetic fields, combined with a microwave dressing allows one to tune the Hamiltonian parameters. In order to create a defect-free chain, two additional laser beams, also referred to as "plug beams", can be used. The two beams are moved closer to one another, compressing the chain and inducing atom jumps into empty sites, until no empty sites are available anymore [55].

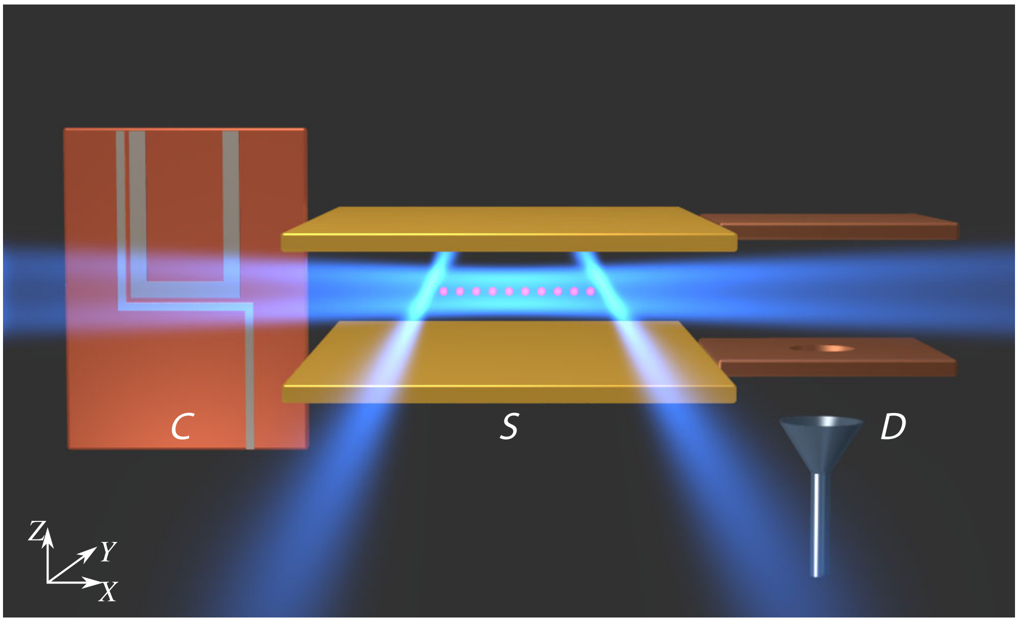

Figure 1. – Artist view of the proposed simulator. A cold atom sample is prepared in the atom chip C. Atoms are then transported and trapped in between the two inhibition plates in the science region S. Two plug-beams on both sides of the atoms chain are used to create a defect free chain. Once the simulation is complete, the detector D can be used to measure the atoms by ionisation.

This work

The main goal of my PhD was to design and build an experimental setup to observe the inhibition of the spontaneous emission in an environment with reduced BBR. In the long run, this setup is to be used to implement a simulator similar to the one proposed in [47]. This new setup conception is based on the previous achievements of the Rydberg atoms team of the LKB, combining the knowledge acquired with the room-temperature experiment [54] and the recent progress done in the trapping of circular Rydberg atoms [49, 56]. All these ideas are implemented in the cryostat historically used for the CQED experiments, providing the required BBR reduction.

Chapter 1 introduces the theoretical background used to describe atoms' properties. It especially focuses on the circular Rydberg atom states, describing their properties together with a theoretical description of the tools used to manipulate them. It finishes with a discussion of the lifetime of circular Rydberg states and the means to increase it.

Before presenting the new setup, chapter 2 discusses a quantum thermodynamics experiment that we performed using the CQED setup. The data treatment has been finalised during the first months of my PhD. In this experiment, the atom-cavity interaction is used to simulate different decorrelating environments. For each decorrelation process considered, the entropy production over a full thermodynamical cycle is measured and compared with the measured amount of information lost in the environment. This previous experiment provided me with a first experience of quantum simulation with Rydberg atoms, widely used for the new setup.

In chapter 3, the design and construction of the new experimental setup are discussed in detail, together with the adaptation of the previous setup. It begins with a presentation of the elements required to obtain circular Rydberg atoms with an extended lifetime. The preparation of these states and the deterministic delivery of ground states in the inhibition region, realised by two parallel conductive plates, is then discussed. It is followed by a presentation of the detection used to assess the successful realisation of each step. This chapter puts an emphasis on the trade-off between an efficient extension of the atoms' lifetime and keeping the means to manipulate the atoms.

The last chapters will present the first results obtained with this setup, which is the successful realisation of a deterministic source of cold ground-state atoms inside the inhibition region. Chapter 4 gives details about the atoms' cooling. It starts with a description of the atomic fountain. The realisation of a cold atom cloud, by means of a three-dimensional magneto-optical trap is then presented. Chapter 5 presents the trapping and transport of atoms in the inhibition region. It begins with the atom trapping inside a standing wave dipole trap. Results about the successful atom transport in between the inhibition plates are then presented. The first tests of Rydberg atom preparation and detection on the transported atoms are in progress, all required elements being already designed and assembled.

Chapter 1

Atomic physics and circular Rydberg states

Thrown into an endless circle
No end in sight, with nothing to lose
Left different choices, beneath the time
Beneath the leaves, Yearned and withered

— Dödsrit, *Endless circle*

The experiment presented in this PhD thesis aims at increasing the lifetime of circular Rydberg atoms. Before diving into the experimental details, it is beneficial to give a brief overview of the theory used to describe atom manipulation and Rydberg states.

This chapter begins with a general introduction about Rydberg atoms. It will start from the quantum description of the hydrogen atom and proceed all the way to the obtention of circular Rydberg states with alkali species. A second section will cover the coupling between atoms and external fields, in the static or time-variable regimes. Then another section will cover the specific case of atom-light interaction as a tool for atom and cavity manipulation. Finally, focus will be put on the lifetime of circular Rydberg states, with hints on how to increase it.

1.1. Rydberg atoms physics

The first step towards the description of atomic systems relies on the quantum description of isolated atoms. In the present work, it means describing atomic states where one electron is in a highly excited state: the Rydberg states. Such systems can be approximated by the model of a single electron interacting with a charged core; the simplest of them all being the hydrogen atom. This presentation doesn't intend to be exhaustive, and relies heavily on the already existing literature on the subject [57].

1.1.1. Hydrogen atom model

A hydrogen atom consists in a proton, of mass m_p and elementary charge $+e$, interacting with an electron, of mass m_e and charge $-e$, through an electrostatic potential V, which reads:

$$V(\mathbf{r}) = \frac{-e^2}{4\pi\epsilon_0}\frac{1}{r}\,. \tag{1.1}$$

Here $r = ||\mathbf{r}||$ is the distance between the two particles and ϵ_0 the vacuum electric permittivity. One can find that the Hamiltonian describing their relative motion reduces to:

$$\hat{H}(\mathbf{r},\mathbf{p}) = \frac{\hat{\mathbf{p}}^2}{2\mu} + \hat{V}(\hat{\mathbf{r}})\,, \tag{1.2}$$

where μ is the reduced mass of the system. The proton being approximately 1800 times heavier than the electron, the reduced mass can be approximated to the electron mass:

$$\mu = \frac{m_e m_p}{m_e + m_p} \approx m_e\,, \tag{1.3}$$

and the overall system reduces to the motion of an electron relatively to a static proton.

To get access to the energy states available for the electron, one has to solve the time-independent Schrödinger equation [58, 59]:

$$\hat{H}\,|\psi\rangle = E\,|\psi\rangle\ . \tag{1.4}$$

In the position basis $\{|\mathbf{r}\rangle\}$, this corresponds to the resolution of the eigenvalue equation:

$$\left[\frac{-\hbar^2}{2\mu}\Delta - \frac{2a_0R_y}{r}\right]\psi(\mathbf{r}) = E\psi(\mathbf{r})\,, \tag{1.5}$$

where $a_0 = 4\pi\epsilon_0\hbar^2/m_e e^2 \approx 0.53\,\text{Å}$ is the Bohr radius, $R_y = m_e e^4/8\epsilon_0^2 h^2$ is the Rydberg energy[1], $\hbar$ is the reduced Planck's constant, c is the speed of light and $\psi(\mathbf{r})$ is the wave-function in the position representation.

Spherical state basis

Since the potential has a spherical symmetry, radial and angular motions can be separated. The wave-function in spherical coordinates can thus be written as:

$$\psi_{nlm}(\mathbf{r}) = R_{nl}(r)\,Y_l^m(\theta,\varphi)\,, \tag{1.6}$$

where Y_l^m are the spherical harmonics and R_{nl} are the radial solutions to be found. The principal n, orbital l and magnetic m quantum numbers are integers with the conditions $n \neq 1$, $0 \leq l < n$ and $|m| \leq l$. These numbers allow one to completely determine an orbital state in spherical coordinates.

Note that l and m respectively relate to the electron angular momentum operator $\hat{\mathbf{L}}$ and its projection along the quantisation axis $\hat{L}_z$. The eigenvalues of operators $\hat{\mathbf{L}}^2$ and $\hat{L}_z$ associated to a state ψ_{nlm} are respectively $l(l+1)\hbar^2$ and $m\hbar$.

Combination of Equation 1.6 and Equation 1.5 allows one to compute the wavefunction of the bound states, for which $E < 0$. These states are associated to a discrete spectrum, for which energies are found to be:

$$E_n = \frac{-E_1}{n^2}\,, \qquad E_1 = \frac{m_e e^4}{32\pi^2\epsilon_0^2\hbar^2} = R_y\,, \tag{1.7}$$

where solutions are labeled by the principal quantum number n. $E_1 \approx 13.6\,\text{eV}$ is the ionisation energy.

---

[1] The Rydberg energy is the energy scale associated to the Rydberg constant R_∞ such that $R_y = hcR_\infty$.

The radial part can be analytically computed, and reads

$$R_{n,l}(r) = \frac{1}{a_0^{3/2}} \frac{2}{n^2} \sqrt{\frac{(n-l-1)!}{(n+l)!}} \mathrm{e}^{-r/na_0} \left(\frac{2r}{na_0}\right)^{l} L_{n-l-1}^{(2l+1)}\left(\frac{2r}{na_0}\right), \tag{1.8}$$

where $L_n^{(\alpha)}(x)$ are generalised Laguerre polynomials defined as

$$L_n^{(\alpha)}(x) = x^{-\alpha} \frac{\mathrm{e}^x}{n!} \frac{\mathrm{d}^n}{\mathrm{d}x^n} \left(\mathrm{e}^{-x} x^{n+\alpha}\right). \tag{1.9}$$

The spherical harmonic expressions are also well known and read

$$Y_l^m(\theta,\varphi) = (-1)^{\frac{|m|+m}{2}} \sqrt{\frac{2l+1}{4\pi} \frac{(l-|m|)!}{(l+|m|)!}}\, P_l^{|m|}(cos\theta)\, \mathrm{e}^{im\varphi}, \tag{1.10}$$

where P_l^m are Legendre polynomials.

In summary, bound state solutions are labeled by three quantum numbers (n, l, m), where only n defines the associated energy value. This leads to an energy degeneracy for a given n with associated constraints

$$\sum_{l=0}^{n-1} \sum_{-l}^{+l} 1 = n^2. \tag{1.11}$$

1.1.2. Circular Rydberg states

Atomic states with a large principle quantum number n, known as the Rydberg states, are particularely interesting. The electron orbit of such states extends far from the atomic core, which increases the atom polarisability. Among all Rydberg states, states with the largest possible angular momentum, known as circular states, are especially interesting for their stability.

Rydberg states

The name of "Rydberg state" finds its origin in the study of the spectral lines of chemical elements by the physicist Johannes Rydberg [60]. This led to the Rydberg formula which is a generalisation of the Balmer's formula to all hydrogen transitions, and describes the wavelength of electronic transitions. It especially describes an energy scaling of the atomic states in $\propto n^{-2}$, in agreement with Equation 1.7.

If this formula is verified for hydrogen atoms, it doesn't hold for other atomic species, because of the presence of core electrons. However, when the electron in an highly excited state, with $n \gg 1$, the effect of the core is weaker. For these states, a modified version of the Rydberg formula can be found which motivates the name of Rydberg states. [2] By extension, atoms in such states are called Rydberg atoms.

Using the result of Equation 1.8, it is possible to compute the two first moments of the position distribution [61]:

$$\langle r\rangle = \frac{a_0}{2}\left[3n^2 - l(l+1)\right], \tag{1.12}$$

$$\left\langle r^2\right\rangle = \frac{a_0^2}{2}n^2\left[5n^2+1-3l(l+1)\right]. \tag{1.13}$$

For Rydberg states, a first observation is that the electron is mostly located at a distance $r \sim n^2 a_0$. For experiments presented here, a typical n value is $n = 50$, which corresponds to an orbit size $2r \approx 260\,\mathrm{nm}$.

The electron is then localised at a distance much larger than for the ground state where it is localised at around a few a_0. From a classical point of view, increasing the distance between two opposite charges increases linearly the associated dipole moment, and this is the reason for the exceptional coupling of Rydberg states to external fields, as discussed later in this chapter.

From Equation 1.12 and Equation 1.13, the relative standard deviation can be computed, giving an idea of the orbital extension relatively to its distance to the nucleus, reading [51]

$$\frac{\Delta r}{\langle r\rangle} \approx \frac{1}{3}\sqrt{1-\left[\frac{l(l+1)}{n^2}\right]^2}, \tag{1.14}$$

with $\Delta r = \sqrt{\langle r^2\rangle - \langle r\rangle^2}$. Taking the extreme example of states for which $l = 0$, it is found that $\frac{\Delta r}{\langle r\rangle} \sim 1/3$. The electron then has a non negligible probability to get close to the ionic core, independently from its excitation level n. States with small l values are also called low-l states.

Circular Rydberg States

Among all the possible states with different angular momentum values, some especially interesting are ones with largest possible angular momentum $|m| = n-1$. Indeed, taking the extreme limit $l = n-1$ in Equation 1.14, one can find that the relative extension is $\frac{\Delta r}{\langle r\rangle} \sim \sqrt{2/9n}$, meaning that the larger the n the smaller the overlap with the ionic core. This results in a higher intrinsic stability of the state, as discussed in the following.

Such states are called circular states, and correspond to the classical limit of a circular orbit around the nucleus, from which the electron only sees a single point charge

---

[2] This formula is obtained by the quantum defect model, discussed in the next section.

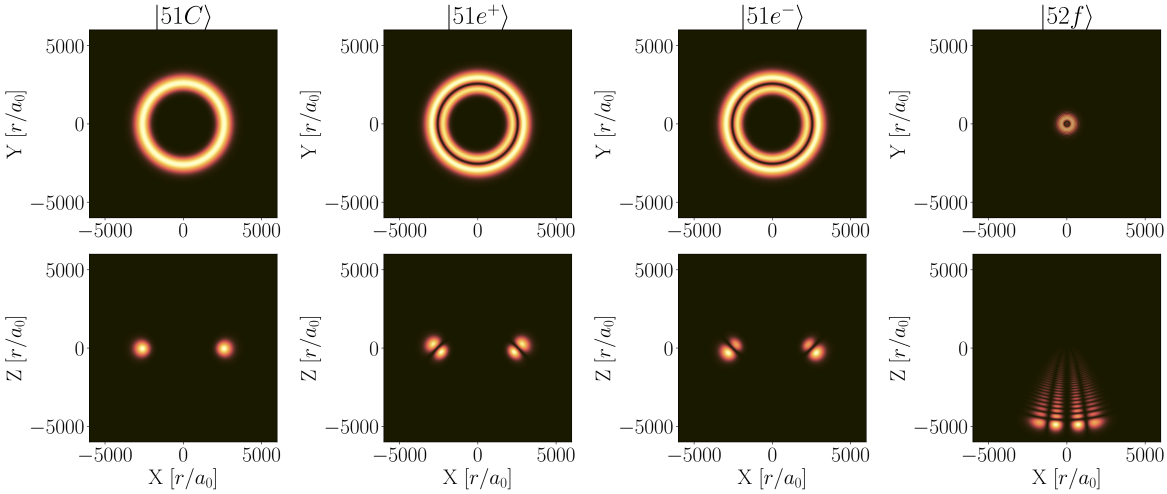

Figure 1.1. – **Density probability of different states:** $r^2|\psi|^2$ in phase space, computed using Equation 1.18 and Equation 1.19 in cartesian coordinates. State $|51C\rangle$ is a circular state, $|51e^{\pm}\rangle = |n=51, k=\pm1, m=50\rangle$ are elliptical states, and $|n=52, k=-47, m=2\rangle$ is an optically accessible state. Length are given in a_0 units.

potential.

The circular states wave function can be computed from Equation 1.6 and Equation 1.8:

$$\psi_{nC}(r,\theta,\varphi) = \frac{1}{\sqrt{\pi a_0^3}}\frac{1}{nn!}\left(\frac{-r}{na_0}e^{i\varphi}\sin\theta\right)^{n-1}\exp\left(\frac{-r}{na_0}\right), \tag{1.15}$$

where $\psi_{nC} = \psi_{n,n-1,n-1}$. Two-dimensional slices of the probability density in space of circular state are depicted in Figure 1.1. For the circular state $|51C\rangle$ the electron probability density is located far from the atomic core, whose size doesn't exceed a few a_0.

Parabolic states

When working with Rydberg states, two properties of the states are at the heart of the states description. The first one is the state angular momentum, which is maximised for circular states and is responsible for their stability. The second one is their response to an external electric field, more easily described in the parabolic basis.

Indeed, when the spherical symmetry is broken, the use of the parabolic basis can be preferred to the use of the spherical one. [3] The parabolic basis is described by three

---

[3] Main ideas and notations will be introduced here, but a much more complete discussion of involved symmetries and derivations in the context of Rydberg atoms can be found in Dr. Facon's thesis [62].

coordinates (ξ, η, φ), whose definitions in cartesian coordinates are:

$$\begin{cases} \xi & = r + z \,, \\ \eta & = r - z \,, \\ \varphi & = \tan^{-1}(y/x) \,, \end{cases} \tag{1.16}$$

where $r = \sqrt{x^2+y^2+z^2}$. In this basis, surfaces for which ξ and η are constant correspond to circular paraboloids of axis (Oz). The separation of coordinates leads to wave-functions such that

$$\psi(\xi,\eta,\varphi) = \Phi_1(\xi)\,\Phi_2(\eta)\,\mathrm{e}^{\mathrm{i}m\varphi} \,. \tag{1.17}$$

One typical example for which the parabolic basis is preferred is when an electric field along (Oz) is applied. In that case, the operator $\hat{\mathbf{L}}^2$ no longer commutes with the Hamiltonian, meaning that l is not longer an appropriate quantum number for state description. Alternative numbers are then to be found.

Quantum numbers n_1, n_2 — Using Equation 1.17, wave-functions can be analytically computed, and their normalised definition reads [63]:

$$\psi_{n_1,n_2,m}(\xi,\eta,\varphi) = \frac{\sqrt{2}}{n^2}\frac{\mathrm{e}^{\mathrm{i}m\varphi}}{\sqrt{2\pi}} f_{n_1,m}(\frac{\xi}{n})\, f_{n_2,m}(\frac{\eta}{n}) \,, \tag{1.18}$$

with:

$$f_{n_i,m}(x) = \sqrt{\frac{n_i!}{(n_i+|m|)!}}\, L_{n_i}^{|m|}(x)\mathrm{e}^{-x/2}x^{|m|/2} \,, \tag{1.19}$$

where n_1 and n_2 are two new quantum numbers.

The discrete energy spectrum associated to these states reads

$$E = \frac{-E_I}{(n_1+n_2+|m|+1)^2} \,. \tag{1.20}$$

By identification with the energies in spherical coordinates, they can be linked to the principal quantum number n such that

$$n = n_1 + n_2 + |m| + 1 \,. \tag{1.21}$$

The parabolic states ψ_{n_1,n_2} are found to be eigenstates of an operator $\hat{\mathbf{A}}$ defined as:

$$\hat{\mathbf{A}} = \frac{1}{2}(\hat{\mathbf{p}} \times \hat{\mathbf{L}} - \hat{\mathbf{L}} \times \hat{\mathbf{p}}) - \frac{\hbar^2}{a_0}\frac{\hat{\mathbf{r}}}{r} \,. \tag{1.22}$$

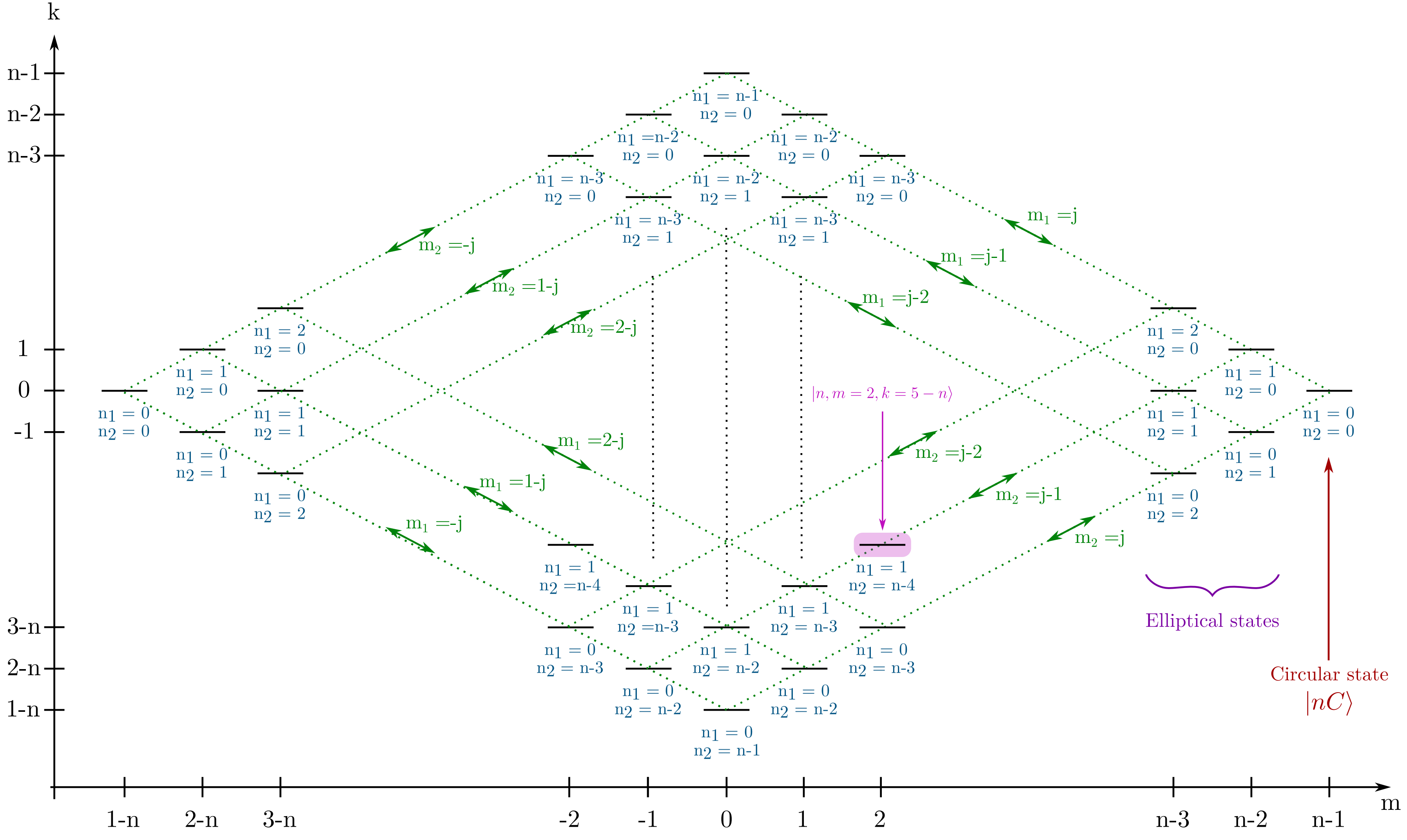

Figure 1.2. – **Level structure of a Rydberg manifold** for a given n and an hyrdogen-like atom. Different parabolic states labeling are used to show their relation. Some specific states are highlighted. Circular states are the largest angular momentum states $|nC\rangle = |n = n, m = n-1, k = 0\rangle$. Neighbouring states are $|ne^{+}\rangle = |n = n, m = n-2, k = 1\rangle$ and $|ne^{-}\rangle = |n = n, m = n-2, k = -1\rangle$. The starting point for circularisation of ^{85}Rb states for $n \approx 50$ is the state $|nf, m = 2\rangle = |n, m = 2, k = 5 - n\rangle$

Associated eigenvalues are $\hbar^2(n_2 - n_1)/(na_0)$. This operator commutes with the Hamiltonian and solution states can be properly parametrised using the quantum numbers (n, n_1, n_2). $\hat{\mathbf{A}}$ is the quantum analogue of the Laplace-Runge-Lenz vector used to study orbits of classical astronomical objects. For classical orbits, this vector is proportional to the eccentricity vector of an orbit. However, the operator $\hat{\mathbf{A}}$ doesn't commute with $\hat{\mathbf{L}}$ nor with $\hat{L}_z$. If the quantum numbers n_1 and n_2 are practical for computing the wavefunctions, they are not really convenient for angular momentum description. In fact, Equation 1.21 links n_1 and n_2 to the absolute value of m, leaving a sign ambiguity.

Quantum numbers m_1, m_2 — Using algebraic arguments [62], one can introduce two new operators

$$\hat{\mathbf{J}}_1 = \frac{1}{2}(\hat{\mathbf{L}} + \hat{\mathbf{A}}), \tag{1.23}$$

$$\hat{\mathbf{J}}_2 = \frac{1}{2}(\hat{\mathbf{L}} - \hat{\mathbf{A}}), \tag{1.24}$$

which commute with the Hamiltonian. The main reason for introducing these operators is that they correspond to two angular momenta with $j_i = (n-1)/2$. One can define their projection along the quantification axis $m_i = -j, -j+1, ..., j-1, j$.

Since $\hat{\mathbf{L}} = \hat{\mathbf{J}}_1 + \hat{\mathbf{J}}_2$, one directly gets $m = m_1 + m_2$. In addition, the operators difference gives $k = m_1 - m_2$. The number k corresponds to a static dipole moment, and is especially useful to describe the coupling with a static electric field.

As a result, atomic states in parabolic coordinates can be labelled using the quantum numbers (n, m, k). One parabolic state $|n, m, k\rangle$ corresponds to a superposition of spherical states of different l but with the same n and m. [4] The ensemble of parabolic states associated to a given n is often called a Rydberg manifold. The general structure is depicted in Figure 1.2, using the different parabolic states quantum numbers to illustrate their relations.

Among all parabolic states, some of them are especially important in the context of this work. First, there are the circular Rydberg states $|nC\rangle$, with a maximal angular momentum, for which $m = n-1$ and $k = 0$. The only possible value of l for $m = n-1$ is $l = n-1$. The parabolic circular state is therefore also a spherical state with

$$|nC\rangle = |n, l = n-1, m = n-1\rangle \ . \tag{1.25}$$

Their neighbouring states are labeled $|ne^{\pm}\rangle$, and are such that $m = n-2$ and $k = \pm 1$. These are especially important for discussing circular states decay. These states

---

[4] Parabolic states can be written as a sum of spherical states using Clebsh-Gordan coefficients and vice-versa.[62]

correspond to the symmetric and anti-symmetric superposition of elliptical states with $m = n-2$ with

$$\left|ne^{\pm}\right\rangle = \frac{|n, l = n-1, m = n-2\rangle \pm |n, l = n-2, m = n-2\rangle}{\sqrt{2}}. \tag{1.26}$$

Finally, the state $|n = 52, m = 2, k = -47\rangle$ is the starting point of the circularisation for ^{85}Rb. This state corresponds to a mix of different l states with $m = 2$. Probability of presence associated to these states are depicted in Figure 1.1.

1.1.3. Beyond the hydrogen atom: effect of the core

So far, the nucleus has been simplified to a single positive charge interacting with the electron, simplified to a negative charge. For the hydrogen atom, this representation can be completed by taking into account the internal properties of each particle, leading to the fine and hyperfine structures. For other elements, the presence of core electrons also affects the energy states. Corrections associated to the atomic core can be described by the quantum defect model. Both of these corrections are here shown for rubidium 85, the atomic species used in the experiment.

Fine and hyperfine structures

To match the experimentally measured hydrogen spectrum, several corrections have to be added. It is done by describing relativistic effects on the atom and the spin of the electron. The latter is associated to a quantum number $s = 1/2$ and its projection along the quantisation axis $m_s = \pm 1/2$. These corrections are described with the Dirac equation. Only the main conclusions of this equation will be discussed here, more details can be found in the literature [64].

Taking into account relativistic corrections, especially the spin-orbit coupling, it is convenient to describe the electron in terms of total angular momentum $\hat{\mathbf{J}} = \hat{\mathbf{L}} + \hat{\mathbf{S}}$. This operator is associated to a new quantum number and its projection (j, m_j), with $j = l \pm 1/2$. This lifts the degeneracy between states with the same principal quantum number n and leads to the atomic fine structure.

The Hamiltonian corresponding to the spin orbit coupling reads:

$$\hat{H}_{SO} = \frac{\Delta E_{SO}}{\hbar^2}(\hat{\mathbf{S}} \cdot \hat{\mathbf{L}}), \tag{1.27}$$

where $\Delta E_{SO} \sim \frac{\hbar^2 e^2}{4\pi\epsilon_0 m_e^2 c^2 a_0^3}$ is the spin-orbit energy shift.

> The spectroscopic notation of the fine structure, for a state (n, l, s, j, m_j) is:
>
> $$n^{2s+1} l_j \,,$$
>
> where l is associated to a letter such that $l = 0 \longleftrightarrow S$, $l = 1 \longleftrightarrow P$, etc.

For example in ^{85}Rb, the fine structure lifts the degeneracy between states $5^2S_{1/2}$, $5^2P_{1/2}$ and $5^2P_{3/2}$. In addition, state dependent radiative corrections called Lamb-shift are to be taken into account [65, 66].

Lastly, the atom nucleus also possesses an angular momentum, called the nuclear spin $\hat{\mathbf{I}}$. As for the spin, its coupling with other angular momenta can be taken into account, leading to a description in terms of total angular momentum $\hat{\mathbf{F}} = \hat{\mathbf{I}} + \hat{\mathbf{J}}$. This lifts the degeneracy inside the fine structure leading to the hyperfine structure, associated with a new quantum number and its projection (f, m_f).

If both of these structures are essential for the description of ground state atoms, their effect is relatively small for Rydberg states. The spin-orbit coupling asymptotic scaling is $\propto n^{-3} l^{-2}$, and equals a fraction of megahertz for $n = 50$ and low-l states.

Quantum defect

For non-hydrogen atoms, the core is not just a single proton and the presence of core electrons and a highly charged nucleus can have an effect even for highly excited states.

For circular states, the valence electron is localised far from the core. The electron thus behaves as if it was interacting with a point charge, and has an hydrogen-like behaviour.

However for states with low angular momentum, Equation 1.14 showed that the electron can get closer to the ionic core. By doing so, the valence electron is less screened by the core electrons. For such states, the hydrogen-like behaviour doesn't apply and some corrections can be applied [67].

Qualitatively, if the valence electron is less screened by core electrons, it feels a stronger bond to the nucleus and its energy is decreased. Polarisation of the core electrons cloud itself also induces a decrease of the energy. Quantitative accounting of these effects can be done by means of the quantum defect description.

In this framework, the Hydrogen like energy structure is corrected by a phenomenological term δ_{lj}, called quantum defect, such that state energy from Equation 1.7 becomes:

$$E_{n,l} = \frac{-Ry}{(n - \delta_{lj})^2} \,, \tag{1.28}$$

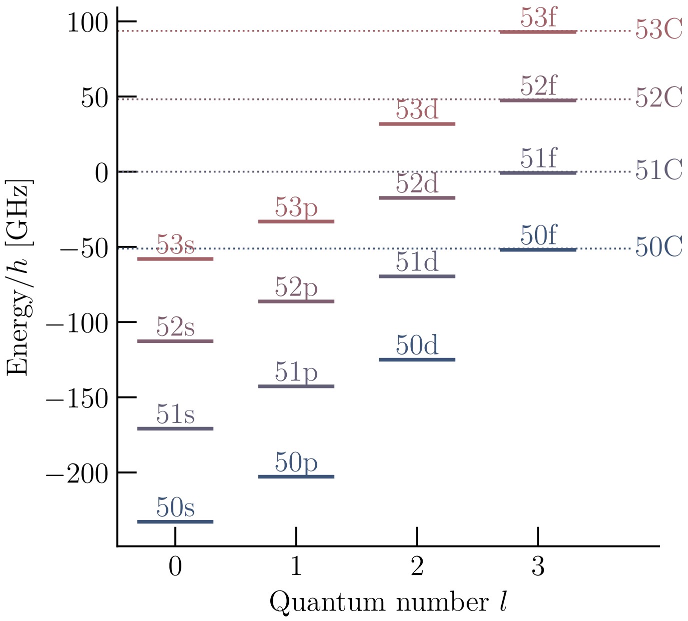

Figure 1.3. – Energy for low-l states taking into account the quantum defect correction, without external field. Dotted lines correspond to the associated circular state energy, which is the hydrogen-like limit. Energies are given relatively to the $|51C\rangle$ energy, and were computed using the *ARC* python package [68].

which now depends on the quantum numbers l and j. For large values of n, δ_{lj} is almost independent of n. For states that are affected by the quantum defect, it means that l remains a good quantum number. [5]

In addition, the larger the angular momentum l, the smaller is the overlap with the ionic core and the lower is the quantum defect value. For the typical n numbers involved in this experiment, the quantum defect is small enough for $l > 4$.

The energies of the low angular states of ^{85}Rb for n values close to $n = 51$ are depicted in Figure 1.3. For the lowest l values ($l < 3$), the quantum defect shifts the energy by hundred gigahertz from the circular state. For $l \geq 3$, energies are already close enough to the circular state energy to recover a relative degeneracy below 1 GHz. The hyperfine structure is not represented on the figure and is below 1 GHz for p and d states.

1.2. Coupling to external fields

Due to the electron-nucleus structure of atomic systems, electric and magnetic effects are useful tools to manipulate them. This section will first discuss the influence of static electric and magnetic fields on atoms, then give some details about the coupling with

---

[5] To emphasise that the lifted degeneracy is induced by the quantum defect and not the spin-orbit coupling, different l states are noted with lowercase instead of capital letters.

an oscillating field.

1.2.1. Static magnetic field

Magnetic coupling Hamiltonian

The first coupling considered is the coupling to a static magnetic field $\mathbf{B} = B_0\mathbf{e_z}$, where $\mathbf{e_z}$ is a unit vector. In the presence of this magnetic field, the different atomic magnetic moments couple to it. This changes the energy of states with different magnetic numbers. This is known as the Zeeman effect, and the corresponding interaction Hamiltonian reads [69]:

$$\hat{H}_B = \frac{\mu_B}{\hbar}\left(g_S\hat{\mathbf{S}} + g_L\hat{\mathbf{L}} + g_I\hat{\mathbf{I}}\right)\cdot\hat{\mathbf{B}}, \tag{1.29}$$

where g_S, g_L and g_I are the electron spin, orbital and nuclear g-factors. These factors describe the specificity associated to each moment. For the spin, g_s has been experimentally measured, and differs from the theoretical prediction $g_s^{Dirac} = 2$. This observation is known as anomalous magnetic moment. The orbital factor takes into account the finite nuclear mass and reads:

$$g_L = 1 - \frac{m_e}{m_{nuc}}, \tag{1.30}$$

in the first order of m_e/m_{nuc}, where m_{nuc} is the nucleus mass. At last, g_I represents the nucleus complex structure. Since the nucleus mass is much larger than the electron mass, the factor associated to the nuclear contribution g_I is much smaller than the two others, and the associated contribution to the Zeeman coupling will be neglected in the following.

In practice, this Hamiltonian can be approximated in different ways depending on the field intensity. Determination of the different regime depends on the relative strength between the spin-orbit coupling and the Zeeman interaction.

Weak regimes

If the Zeeman energy shift remains small enough, the hyperfine structure is conserved, and f remains a good quantum number. In this regime, the Zeeman Hamiltonian can be written as:

$$\hat{H}_B^{Zeeman,F} = \frac{\mu_B}{\hbar}\cdot g_F\cdot\hat{F}_Z\cdot\hat{B}_Z, \tag{1.31}$$

where g_F is the hyperfine Landé factor. For a state $|m_F\rangle$, the associated energy shift then reads:

$$\Delta E_F^{Zeeman} = \mu_B\, g_F\, m_F\, B_0. \tag{1.32}$$

It is called the Zeeman effect, and corresponds to the values used in the next chapters [69].

A similar reasoning can be applied if the magnetic field splitting is larger than the hyperfine splitting, but smaller than the fine structure splitting ($B_0\mu_B \ll \Delta E_{SO}/\hbar$). In this regime, j is a good quantum number, and the associated energy shift reads:

$$\Delta E_J^{Zeeman} = \mu_B g_J m_J B_0\,, \tag{1.33}$$

with g_j the Landé factor.

Strong regime

When the magnetic field is stronger, $B_0\mu_B \gg \Delta E_{SO}/\hbar$, it can overcome the fine and hyperfine structures. In this case, j is no longer a good quantum number, and the appropriate basis is the $|l, m_l, m_s\rangle$ basis. Qualitatively, it means that the coupling between the spin and orbital components becomes negligible. In that case the Hamiltonian can be approximated by the Paschen-Bach Hamiltonian, which reads:

$$\hat{H}_B^{PB} = \frac{\mu_B}{\hbar}\left(g_L\hat{\mathbf{L}} + g_s\hat{\mathbf{S}}\right)\cdot\hat{\mathbf{B}}\,. \tag{1.34}$$

The associated energy shift for a state $|l, m_l, m_s\rangle$ then reads:

$$\Delta E^{PB} = \mu_B(g_L m_l + g_s m_s)B_0\,. \tag{1.35}$$

This energy shift regime is also known as the Paschen-Bach effect. More details and values for ^{85}Rb can be found in the literature, also about the intermediate regime which is not discussed here [69].

1.2.2. Static electric field

Electric coupling Hamiltonian

The second situation is the coupling of an atomic system to a static electric field along the z axis, such that $\mathbf{F} = F_0\mathbf{e_z}$. The Stark Hamiltonian associated to the coupling to an electric field reads:

$$\hat{H}^{Stark} = -\hat{\mathbf{d}}\cdot\hat{\mathbf{F}}\,, \tag{1.36}$$

where $\hat{\mathbf{d}} = -e\hat{\mathbf{r}}$ is the dipole operator. This Hamiltonian couples the motional degrees of freedom of different states. This causes an energy shift of the states, which can be computed using the perturbation theory. Energy shifts especially depend on the dipole matrix elements $\langle n,l,m|\mathbf{r}|n',l',m'\rangle$. Due to the symmetry, these elements are non-zero when $l'=l\pm1$. This mixes states with different l, and the right basis to use for mixed states is the parabolic basis.

Linear Stark effect – degenerate scenario

Ignoring the fine and hyperfine structure, all states for a given n are degenerate in a zero field.[6] The perturbation theory then indicates that diagonalisation of the perturbation term should be performed in this degenerate subset. As previously discussed, the right basis to choose is the parabolic basis, in which the Stark Hamiltonian of Equation 1.36 is diagonal. In the $|n,k,m\rangle$ basis, the energy shift reads

$$\Delta E_{(1)}^{Stark} = \frac{3kn}{2} a_0 e F_0 \,. \tag{1.37}$$

The parabolic states for which $k \neq 0$ then experience a linear Stark shift. The underlying physical interpretation is that, since they are combinations of different spherical states with different angular momentum, the parabolic states can have a static dipole moment. They can then linearly couple to an electric field. On the contrary, states for which $k=0$, which is the case for circular states, don't have a static dipole moment and don't have an energy shift.

Quadratic Stark effect – non degenerate scenario

The linear Stark effect is observed for atoms for which there is degeneracy in zero-field. This is the case for Rydberg states of the hydrogen atom, for which spin-orbit coupling is small. However for other elements, the quantum defect can break the hydrogen-like energy structure. This lifts the degeneracy of low angular momentum states that are brought out of the manifold, even without an external field.

For this case, the perturbation theory in the non-degenerate case has to be performed. Since the spherical state doesn't possess a static dipole moment, the second order perturbation theory is required, and the associated energy shift reads [51]:

$$\Delta E_{(2)}^{Stark} = e^2 F_0^2 \sum_{n',\Delta l=\pm1} \frac{|\langle n,l,m_l|\hat{z}|n',l+\Delta l,m_l\rangle|^2}{E_{n,l,m_l} - E_{n',l+\Delta l,m_l}} \,. \tag{1.38}$$

Its variation is quadratic with the electric field. The associated physical interpretation is the following: since they are not part of the manifold, low-l states can't get mixed with other states into a parabolic state with a dipole moment. However, the electric

---

[6] This approximation corresponds especially to Rydberg states of large m, for which spin-orbit coupling and quantum defect are small.

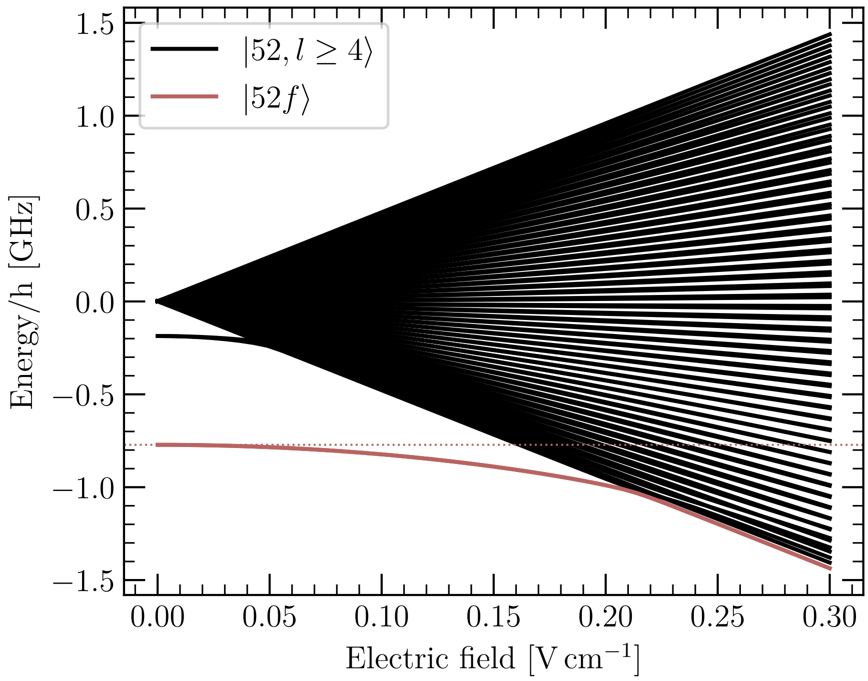

Figure 1.4. – **Stark map:** example for ^{85}Rb, with $m = 3$, for $|52f\rangle$ and states with $n = 52$ and $l \geq 4$.

field can still distort the wave-function, inducing a dipole moment. This dipole moment then couples back to the electric field, hence the quadratic dependency.

Rubidium atom in an increasing electric field

For non hydrogen atoms like ^{85}Rb, different regimes are reaching when increasing the applied static electric field. The states structure is represented in Figure 1.4.

For low fields, the quantum defect excludes low-l states from the multiplicity. One example on the figure is the state $|52f\rangle$. These low-l states are non-degenerate with other states with the same m, and can't get mixed into parabolic states. Their energy shifts is thus given by the quadratic Stark effects.

For states with large m (and therefore large l), there is a degeneracy in the zero-field. States with the same m and $\Delta l = \pm 1$ can thus be mixed into parabolic states, which experience a linear Stark shift.

At last, states with small m but large l are part of a multiplicity as well, but with some states missing (the ones that are affected by the quantum defect). Their shift is then not exactly linear.

When increasing the electric field, the linear Stark effect shifts the energy faster than the quadratic one. At some point, the states that were affected by the quantum defect reach the linearly shifted multiplicity. They can then be mixed with other states with the same m and enter the linear regime with the others. For the state $|52f\rangle$, this point is reached for fields around $0.2\,\mathrm{V\cdot cm^{-1}}$.

States that are more affected by the quantum defect, such as $|52s\rangle$, are too far from the multiplicity. A very high field would be required for them to join the multiplicity, so high that different n states mixing would have to be considered.

So far, only a same n multiplicity was considered, but the increase of the electric field eventually brings the states in a regime where different n states start to be mixed together. This is visible in Figure 1.3, where it is clear that the state $|52f\rangle$ is closer to the state $|51f\rangle$ than to the state $|52d\rangle$. A mixing between states with $n = 52$ and $n = 51$ will then occur before all states with $n = 52$ join the the multiplicity.

In the general case with different n, including different manifolds, a similar reasoning as the one applied for the non-degenerate case has to be applied, and the associated energy shift perturbative expansion can be written as:

$$\Delta E^{Stark}_{(full)} = \alpha_1 F^1 + \alpha_2 F^2 + \dots\,. \tag{1.39}$$

The first coefficients of this expansion depend on the parabolic quantum numbers n, m, k and reads[7] :

$$\alpha_1 = \frac{3ea_0}{2} kn\,, \tag{1.40}$$

$$\alpha_2 = \frac{-(ea_0)^2}{32R_y}(17n^2 - 9m^2 - 3k^2 + 19)\,. \tag{1.41}$$

For circular states, $k = 0$, which means that there is not linear Stark effect, and only the quadratic one.

1.2.3. Oscillating field

Coupling Hamiltonian

The description of the interaction with a time-dependent electromagnetic wave plane requires a different reasoning to take into account the time dependency. For the sake of simplicity, only the case of a monochromatic plane wave will be discussed here. This result can be extended to arbitrary electromagnetic fields, since the solutions of Maxwell's equation in vacuum can be written as a superposition of plane waves.

In vacuum, a classical electromagnetic plane wave is associated to a vector potential

---

[7] Expressions for higher order terms with a more detailed discussion can be found in the thesis of Dr. Wu [70].

$\mathbf{A}(\mathbf{r},t)$. Using the right gauge choice, it reads [59]:

$$\mathbf{A}(\mathbf{r},t) = \mathrm{Re}\left[A_0 \boldsymbol{\epsilon}_\sigma \mathrm{e}^{i(\mathbf{kr}-\omega t)}\right], \tag{1.42}$$

where $\mathbf{k}$ is along the wave propagation axis, ω is the wave angular frequency, ϵ_σ is the polarisation vector and A_0 is the wave amplitude.

The associated electric and magnetic fields can be recovered using the relations $\mathbf{F} = -\partial_t \mathbf{A}$ and $\mathbf{B} = \nabla \times \mathbf{A}$. The associated amplitudes are respectively given by $F_0 = \mathrm{Re}(i\omega A_0)$ and $B_0 = \mathrm{Re}(ikA_0)$.

For the quantum scenario, the interaction Hamiltonian between the electromagnetic wave and one of the atomic electrons, can be written as [71]

$$\hat{H}^{EM} = -\frac{q}{m_e}\hat{\mathbf{P}}\cdot\hat{\mathbf{A}}(\hat{\mathbf{R}},t) - \frac{q}{m_e}\hat{\mathbf{S}}\cdot\hat{\mathbf{B}}(\hat{\mathbf{R}},t) + \frac{q^2}{2m_e}[\hat{\mathbf{A}}(\hat{\mathbf{R}},t)]^2. \tag{1.43}$$

where $q = -e$ is the electron charge. For low field intensities, which is the case for the experiments discussed here, the last term in A_0^2 can be neglected. In addition, the first terms order of magnitude are given by $\hat{\mathbf{P}}\cdot\hat{\mathbf{A}} \sim q\hbar p A_0/m$ and the term $\hat{\mathbf{S}}\cdot\hat{\mathbf{B}} \sim q\hbar k A_0/m$. Their relative contribution is then governed by the ratio $\lambda p/\hbar$, where $\hbar/p$ is of the order of the atomic dimensions.

For the applications discussed here, the driving fields are optical or at higher wavelength. For ground state atoms, the atomic dimension is of the order of a_0 and the magnetic term can then safely be neglected since $a_0 \ll \lambda$ in the regimes considered here. Caution should be used when dealing with Rydberg states, whose dimension is of the order of $n^2 a_0$, but this case won't be discussed here.

Using further approximation, the Hamiltonian can finally be written as the dipole Hamiltonian, which reads:

$$\hat{H}^{Dip} = -\hat{\mathbf{d}}\cdot\hat{\mathbf{F}}, \tag{1.44}$$

where $\hat{\mathbf{d}}$ is the dipole operator.

This hamiltonian can only couple a limited number of states together. In fact, driving an electron with an electric field allows one to transfer population from one state $|\varphi_i\rangle$ to another state $\left|\varphi_f\right\rangle$ under the condition that the associated dipole matrix element $\left\langle\varphi_f\middle| H^{Dip} |\varphi_i\rangle \neq 0$ [71]. This essentially goes down to the computation of the overlap between associated spherical harmonics.

Considering two states with angular quantum numbers l_i, m_i and l_f, m_f, the matrix elements are non-zero if the following selection rules are fulfilled:

$$\Delta l = l_f - l_i = \pm 1\,, \tag{1.45}$$

$$\Delta m = m_f - m_i = -1, 0, +1\,. \tag{1.46}$$

Note that the condition on Δm depends on the polarisation of the electromagnetic field. Finally, in the presence of spin-orbit coupling, the conditions $\Delta j = 0, \pm 1$ and $\Delta j \neq 0$ if $j = 0$ have to be added.

Quantised field

For some problems, it is useful to describe the electromagnetic field as a quantised field. This second quantification formulation allows one to understand some effect in terms of photons, which are describing elementary excitations of a given electromagnetic field. Qualitatively, the electromagnetic field is now considered as another quantum system with which elementary excitations can be exchanged.

The quantised version of the electric field associated to the electromagnetic field previously introduced reads [59]:

$$\hat{\mathbf{F}}(\mathbf{r}, t) = \mathrm{i}\sqrt{\frac{\hbar\omega_{\mathbf{k}}}{2\epsilon_0\mathcal{V}}}\left(\boldsymbol{\epsilon}_\sigma \hat{a}_{k,\sigma}\mathrm{e}^{\mathrm{i}(\mathbf{kr}-\omega_{\mathbf{k}}t)} - \boldsymbol{\epsilon}^*_\sigma \hat{a}^\dagger_{k,\sigma}\mathrm{e}^{-\mathrm{i}(\mathbf{kr}-\omega_{\mathbf{k}}t)}\right), \tag{1.47}$$

where $\mathcal{V}$ is a the quantisation volume. $\hat{a}$ and $\hat{a}^\dagger$ are respectively the annihilation and creation operators associated to an electromagnetic field mode with a wave vector $|\mathbf{k}| = \omega/c$ and polarisation vector $\hat{e}_\sigma$.

The Hamiltonian associated to the corresponding single mode electromagnetic field reads:

$$\hat{H}_F = \hbar\omega_{\mathbf{k}}\hat{a}^\dagger_{k,\sigma}\hat{a}_{k,\sigma}\,. \tag{1.48}$$

Injecting this quantised field inside Equation 1.44 directly gives the coupling Hamiltonian of an electron with a single mode quantised field:

$$\hat{H}^{Dip}_{A,F} = \mathrm{i}\sqrt{\frac{e^2\hbar\omega}{2\epsilon_0\mathcal{V}}}\left[\hat{a}(\hat{\mathbf{r}}\cdot\boldsymbol{\epsilon}) - \hat{a}^\dagger(\hat{\mathbf{r}}\cdot\boldsymbol{\epsilon}^*)\right], \tag{1.49}$$

choosing the time and space origins such that the exponential terms drop, and using a lighter notation. Note that this Hamiltonian is a two system Hamiltonian, including the action of the coupling onto the electromagnetic field.

Dressed state formalism

Quantisation of the electromagnetic field allows for the introduction of the dressed state formalism [5]. The example taken here is the one of an atom coupled with a monochromatic electromagnetic mode. The atom-field Hamiltonian is written in the Hilbert state obtained by the tensor product of the atomic and field Hilbert spaces.

Consider a two level atomic system coupled to an electromagnetic field mode of pulsation ω. Their interaction is governed by the Hamiltonian given in Equation 1.49. The associated selection rules state that non-zero matrix elements are the ones coupling the ground state $|g\rangle$ and an excited state $|e\rangle$. Taking into account the number of photons N inside the mode, the creation and annihilation operators only couple states differing by a single photon.

Non-zero matrix elements associated to an excitation exchange between the atom and the field are:

$$\langle e,N|\,H_{AF}^{Dip}\,|g,N+1\rangle = \frac{\hbar\sqrt{N+1}}{2}\Omega_0\,, \tag{1.50}$$

where the single photon Rabi frequency reads:

$$\Omega_0 = \frac{-2}{\hbar}\sqrt{\frac{e^2\hbar\omega}{2\epsilon_0\mathcal{V}}}\,\langle e|\hat{\mathbf{r}}\cdot\boldsymbol{\epsilon}|g\rangle\ . \tag{1.51}$$

In the dressed state description, one has to compute the energies and states associated to the atom-field system. This comes down to the diagonalisation of the atom-field total Hamiltonian $H_{A,F} = H_A + H_F + \hat{H}_{A,F}^{Dip}$. In the $|e,N\rangle$, $|g,N+1\rangle$ subset, it reads:

$$\hat{H}_{A,F}^{(N)} = \hbar\omega(N+1/2)\mathbb{1} + \frac{\hbar}{2}\begin{pmatrix}\Delta & -\mathrm{i}\Omega_N\\ \mathrm{i}\Omega_n & -\Delta\end{pmatrix}\,, \tag{1.52}$$

where $\mathbb{1}$ is the identity matrix, the N photons Rabi frequency $\Omega_N = \sqrt{N+1}\Omega_1$ and where the detuning $\Delta = \omega_a - \omega$ between the atomic transition of frequency ω_a and the field has been introduced.

Finally, diagonalisation of this Hamiltonian is straightforward and gives the two eigenvectors:

$$|+,N\rangle = \cos\frac{\theta_N}{2}\,|e,N\rangle + \mathrm{i}\sin\frac{\theta_N}{2}\,|g,N+1\rangle\ , \tag{1.53}$$

$$|-,N\rangle = \sin\frac{\theta_N}{2}\,|e,N\rangle - \mathrm{i}\cos\frac{\theta_N}{2}\,|g,N+1\rangle\ , \tag{1.54}$$

where the mixing angle θ_N is defined by $\tan\theta_N = \Omega_N/\Delta$. Associated eigenenergies are:

$$E_N^{\pm} = (N+1/2)\hbar\omega \pm \frac{\hbar}{2}\sqrt{\Delta^2+\Omega_N^2}\,. \tag{1.55}$$

Without the coupling or in case of a very large detuning ($\theta_N \to 0$), the bare atom-field states are recovered. However, in the presence of a coupling, each bare state get mixed with the other state, leading to the so-called dressed states. The energy evolution with Δ is shown later, in Figure 1.5.

1.3. Atoms and fields: practical examples

In the experiment presented here, the system of interest is an atomic circular Rydberg state. In this context, electromagnetic fields are tools used to manipulate the atomic system. If the last section introduced the matter-light coupling from a general point of view, this section will take a more practical approach, and will focus on practical applications of this coupling with the description of specific examples.

1.3.1. Adiabatic passage

A first practical example for atom manipulation is the adiabatic passage. This technique allows one to efficiently transfer an excitation from the atom to the field, or vice-versa, by changing their relative detuning. The framework used is the dressed-state formalism.

The adiabatic passage technique relies on the observation that, for a large detuning, the dressed states coincide with the bare states, depending on the detuning sign. For a far positive detuning, atomic energy is larger than the field energy, the cost of putting the excitation in the field mode is smaller, so the system ground state is $|g,N+1\rangle$. For a far negative detuning, the ground state is $|e,N\rangle$ for similar reasons. The eigenstates energy as a function of the detuning is depicted on Figure 1.5.

This property can be exploited to efficiently transfer the state population from the bare ground state $|g,N+1\rangle$ to the bare excited state $|e,N\rangle$. The system is initially prepared in $|g,N+1\rangle = |-,N\rangle$, in the presence of a large positive detuning. Then, the detuning is changed from far positive to far negative values. The population remains on the system ground state $|-,N\rangle$ as long as the adiabaticity condition

$$\frac{\mathrm{d}\theta}{\mathrm{d}t} \ll \sqrt{\Omega_N^2+\Delta^2}\,, \tag{1.56}$$

is fulfilled. At the end of the protocol, the system ends up in the state $|e,N\rangle$ and the

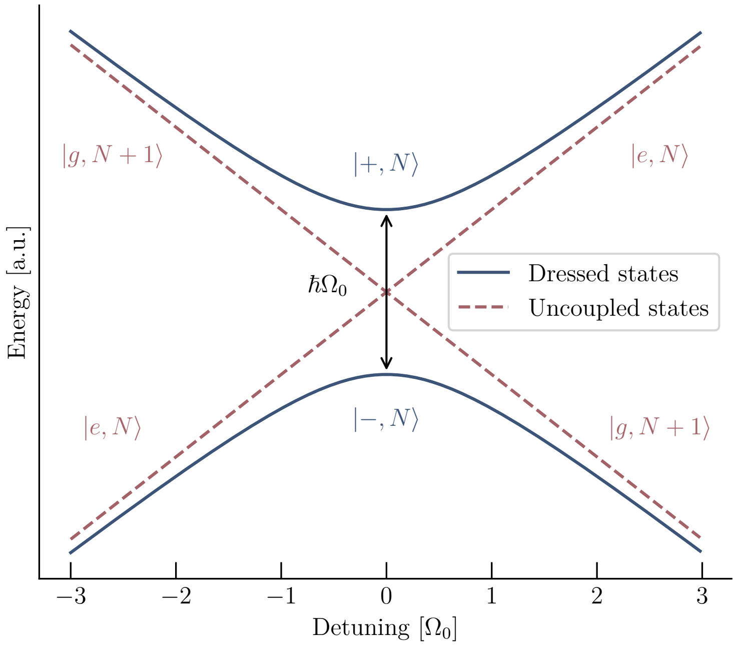

Figure 1.5. – **Dressed states energy** along the atom field detuning. For far positive and negative detuning, the eigenstates coincide with bare states. For intermediate detuning, the bare states are mixed into dressed states $|\pm,N\rangle$.

field can be turned off. In practice, it allows one to perform population transfer with almost certain efficiency. This technique has been widely used in the cavity quantum electrodynamics setup used for the quantum thermodynamics experiment.

1.3.2. Circular Rydberg state preparation

The preparation of a circular Rydberg state is done in several steps. A simplified scheme is depicted in Figure 1.6, focusing on the Rydberg state circularisation. This procedure is presented here for the state $|52C\rangle$ for ^{85}Rb.

The first step is to excite the atoms to a Rydberg state. This is done by means of a laser excitation.[8] The target state is the $|52f, m=2\rangle$ state, for two reasons.

First, since it is affected by the quantum defect, the state $|52f, m=2\rangle$ is isolated from the $n=52$ manifold, as depicted in the Stark map in Figure 1.4. It can therefore be selectively targeted by the Rydberg excitation.

Second, when a Stark field is switched on, the $|52f\rangle$ states reaches the multiplicity before a mixing between different n occurs. This can be used to bring the atomic

---

[8] For now, focus is on the circularisation part. Details about the Rydberg laser excitation will be given in the next chapter.

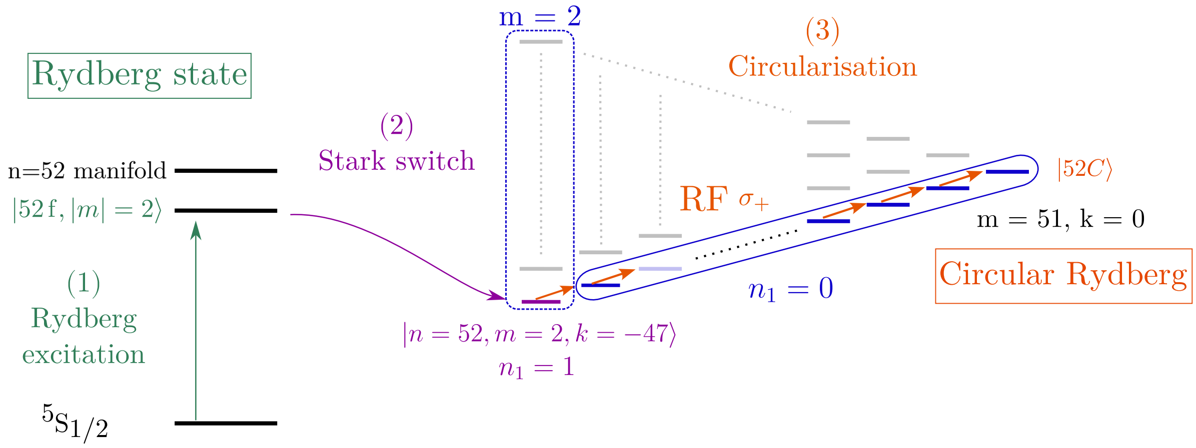

Figure 1.6. – Rydberg state circularisation. First, the atom is excited in the Rydberg state $|52f, |m| = 2\rangle$. The Stark switch allows one to branch the population to the state $|n = 52, m = 2, k = -47\rangle$. From there, a multiple photons adiabatic passage is used to go to the circular state $|52C\rangle$.

population into the Rydberg manifold. This corresponds to the so called Stark switch. For this step, the electric field is adiabatically switched on until the state $|52f, m = 2\rangle$ reached the multiplicity and mixes with other states to generate the parabolic state $|n = 52, m = 2, k = -47\rangle$. The adiabaticity criteria is required for the atomic population to be effectively branched into the state $|n = 52, m = 2, k = -47\rangle$. Otherwise, the population could spread over all other states with $m = 2$ but different k.

As previously discussed, the Stark shift in the linear regime given in Equation 1.40 is linear in k. For a hydrogen atom, the ladder associated to the lowest diagonal ($m_2 = j$ / $n_1 = 0$) is therefore harmonic in the linear Stark shift regime. For rubidium, the quantum defect induces an anharmonicity for the lowest m states. However, for $m \geq 3$, the lowest diagonal of the Rydberg manifold can be considered to be harmonic.

Interestingly, in the electric field regime where the state $|n = 52, m = 2, k = -47\rangle$ reaches the multiplicity, it joins the harmonic ladder of the lowest diagonal, as illustrated in Figure 1.6. In other words, the $|n = 52, m = 2, k = -47\rangle$ to $|n = 52, m = 3, k = -48\rangle$ transition is degenerate with the other transitions of the harmonic ladder $|n = 52, m, k\rangle$ to $|n = 52, m + 1, k + 1\rangle$.

From the state $|n = 52, m = 2, = k = -47\rangle$ the ladder can be climbed to the circular state by a succession of several adiabatic passages. This procedure has been introduced by Kleppner and Hulet in 1983 [73] and is called circularisation. The idea is similar to the adiabatic passage presented earlier, but in a larger subset. It is illustrated in Figure 1.7. First, a radiofrequency (RF) dressing at a constant frequency is switched on. This step fulfills the adiabaticity condition given in Equation 1.56 to avoid states mixing. In addition, the RF dressing is chosen to be σ_+ polarised. This ensures that

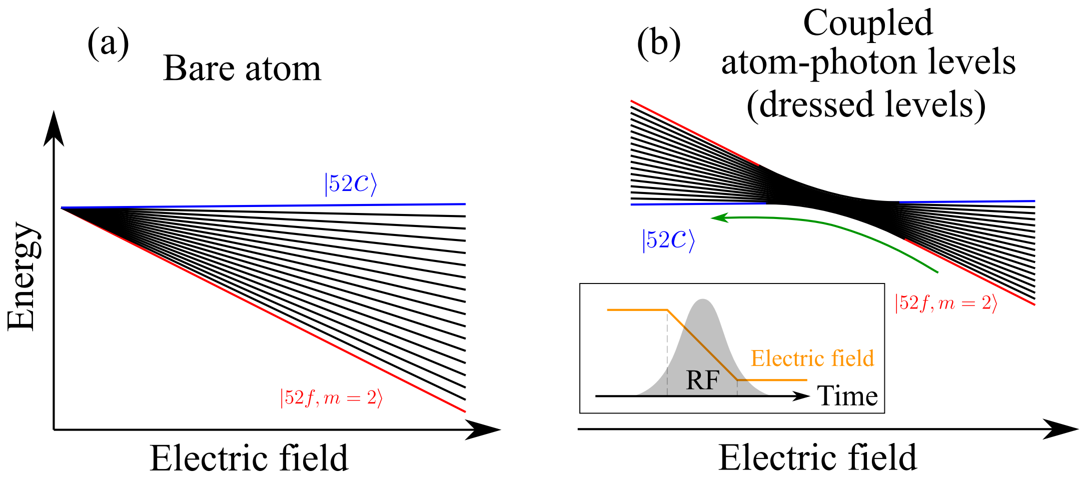

Figure 1.7. – Multi-photons adiabatic passage. For the bare atom (a), increasing the electric field lifts the degeneracy, quantum defect are not represented here. In the presence of RF dressing (b), the dressed state formalism applies. Reducing the electric field allows one to cross the resonance and adiabaticaly transfer the population from $|n=52, m=2, k=-47\rangle$ to $|52C\rangle$. Figure adapted from [72].

only transitions for which $\Delta m = +1$ will be driven and that the circular state prepared is $m = 51$ and not $m = -51$. A magnetic field can also be applied to lift the degeneracy between the transitions $m \to m+1$ and $m \to m-1$.

Then, the detuning is changed by ramping down the static electric field. The successive adiabatic passages are thus performed by crossing the resonance. In practice, the RF dressing amplitude can be modulated to optimise the circularisation efficiency and duration [74, 75].

1.3.3. Lightshift and atoms trapping

The dressed atom theory framework shows that even in the far from resonance regime, the energy of atomic states is affected by the coupling with an external field. By lowering the energy of a populated ground state, this reduces the atom total energy and can be used to trap neutral atoms [76]. In addition, this effect changes the frequency of atomic transitions, the energy shift being state dependent.

Second order perturbation theory

The energy shift induced by the coupling between an optical dressing and an atomic system is called lightshift. To efficiently describe it, the two-level approximation used above is too restrictive. In fact, the multilevel structure of atoms in the ground state has to be fully considered.

To do so, the second order perturbation theory can be applied to the atomic system, using the hamiltonian given in Equation 1.49 as the perturbative hamiltonian. Dressing is assumed to have a pulsation ω. When this pulsation is far from any atomic resonance, no perturbation is observed at the first order. In the dressed state formalism for a multi-level atom, the energy shift associated to the bare state $|i\rangle$ reads [71]:

$$\Delta E_i = \sum_{j\neq i} \frac{\left|\langle j|\hat{H}_{AF}^{Dip}|i\rangle\right|^2}{\mathscr{E}_i - \mathscr{E}_j}, \tag{1.57}$$

where $\mathscr{E}_i$ is the energy of $|i\rangle$. $|i\rangle$ can be written as the tensor product of the atom and field reduced states $|i\rangle = \left|\psi_i, N^{(i)}\right\rangle$ where $|\psi_i\rangle$ is an atomic state of energy E_i and $\left|N^{(i)}\right\rangle$ is a field state. The bare states energy is then $\mathscr{E}_i = E_i + \hbar\omega N^{(i)}$.

The matrix element can be explicitly written as:

$$\mathrm{i}\sqrt{\frac{e^2\hbar\omega}{2\epsilon_0\mathscr{V}}}\left[\left\langle N^{(j)}\middle|\hat{a}\middle|N^{(i)}\right\rangle\left\langle\psi_j\middle|\hat{\mathbf{r}}\cdot\boldsymbol{\epsilon}\middle|\psi_i\right\rangle - \left\langle N^{(j)}\middle|\hat{a}^\dagger\middle|N^{(i)}\right\rangle\left\langle\psi_j\middle|\hat{\mathbf{r}}\cdot\boldsymbol{\epsilon}^*\middle|\psi_i\right\rangle\right]. \tag{1.58}$$

The field ladder operators only couple field states which differ by one excitation. The sum over the different j states can be widely simplified to a sum over atomic states which reads:

$$\Delta E_i = \frac{e^2\hbar\omega}{2\epsilon_0\mathscr{V}} \sum_{\psi_j\neq\psi_i} \frac{N\left|\left\langle\psi_j\middle|\hat{\mathbf{r}}\cdot\boldsymbol{\epsilon}\middle|\psi_i\right\rangle\right|^2}{E_i - E_j + \hbar\omega} + \frac{(N+1)\left|\left\langle\psi_j\middle|\hat{\mathbf{r}}\cdot\boldsymbol{\epsilon}^*\middle|\psi_i\right\rangle\right|^2}{E_i - E_j - \hbar\omega}, \tag{1.59}$$

with $N^{(i)} = N$ for clarity. Estimation of the energy shift then essentially comes down to the computation of dipole matrix elements between the considered state and other atomic states, associated to transition energies $\hbar\omega_j = E_j - E_i$. In addition to the energy shift, the perturbation theory also predicts the corrections onto the eigenvectors, which will be explicitly written later.

Laser induced lightshift and dipole trapping

A relevant situation for our experiment context is the laser induced lightshift. Such driving field has a large number of photons $N \gg 1$. The associated laser intensity can be defined as $I = N\hbar\omega c/\mathscr{V}$.

All together, the induced lighshift reads:

$$\Delta E_i = \frac{-e^2 I}{2\epsilon_0\hbar c} \sum_{\psi_j\neq\psi_i} \frac{\left|\left\langle\psi_j\middle|\hat{\mathbf{r}}\cdot\boldsymbol{\epsilon}\middle|\psi_i\right\rangle\right|^2}{\omega_j - \omega} + \frac{\left|\left\langle\psi_j\middle|\hat{\mathbf{r}}\cdot\boldsymbol{\epsilon}^*\middle|\psi_i\right\rangle\right|^2}{\omega_j + \omega}. \tag{1.60}$$

Another result of the perturbation theory is the first order correction on the eigenvectors, for which the dressed state $\left|\tilde{\psi}_i\right\rangle$ associated to the bare state ψ_i reads:

$$\left|\tilde{\psi}_i\right\rangle = |\psi_i\rangle - \mathrm{i}\sqrt{\frac{e^2 I}{2\epsilon_0 \hbar^2 c}} \sum_{\psi_j \neq \psi_i} \left[\frac{\langle\psi_j|\hat{\mathbf{r}}\cdot\boldsymbol{\epsilon}|\psi_i\rangle}{\omega_j - \omega} - \frac{\langle\psi_j|\hat{\mathbf{r}}\cdot\boldsymbol{\epsilon}^*|\psi_i\rangle}{\omega_j + \omega} \right] |\psi_j\rangle \,, \tag{1.61}$$

omitting the field state change.

To better understand this expression, one can consider the contribution of a state of higher energy $\omega_j > 0$ to the lightshift. If the associated transition and driving field frequencies are not too far, then the denominator of the first term is close to zero and the second term in Equation 1.60 can be neglected. At last, if the driving is red-detuned from the transition, then $\omega_j - \omega > 0$ and the energy correction is overall negative and linear in the laser intensity.

This correction interpretation is similar to what was concluded in the adiabatic passage section. The presence of a driving field induces a contamination of the initial states into dressed states. The contamination from a more excited state can couple again to the field. By exchanging a photon with a less energetic field, this contamination overall reduces the atom energy. An opposite effect is observed for less excited states, or blue detuned driving.

Coming back to the general case, the sum in Equation 1.60 can be computed using the dipole elements expressions. Finally, the lighshift expression can be written as:

$$\Delta E_i = \alpha_i(\omega, \boldsymbol{\epsilon})\, I \,, \tag{1.62}$$

where α_i is the scalar polarisability of the atomic state $|\psi_i\rangle$, defined as:

$$\alpha_i(\omega, \boldsymbol{\epsilon}) = \frac{-e^2}{2\epsilon_0 \hbar c} \sum_{\psi_j \neq \psi_i} \frac{\left|\langle\psi_j|\hat{\mathbf{r}}\cdot\boldsymbol{\epsilon}|\psi_i\rangle\right|^2}{\omega_j - \omega} + \frac{\left|\langle\psi_j|\hat{\mathbf{r}}\cdot\boldsymbol{\epsilon}^*|\psi_i\rangle\right|^2}{\omega_j + \omega} \,. \tag{1.63}$$

In practice, this polarisability depends on the light polarisation through $\hat{\mathbf{r}}\cdot\boldsymbol{\epsilon}$ as well as the driving frequency. In the following, the polarisabilities are computed using the *ARC-Alkali Rydberg Calculator* python package [68]. The overall energy shift depends on the different contributions: for a red-detuned drive, contributions of more excited states lower the energy, when contributions of less excited states increase it.

A specific case arises for the ground state, that only has more excited states. All contributions are then negative for a red-detuned driving. This energy decrease can be seen as a negative potential, that can be used to trap ground state atoms. In addition, for ^{85}Rb, contributions of the first two excited states $\left|{}^5P_{1/2}\right\rangle$ and $\left|{}^5P_{3/2}\right\rangle$ (D_1 and D_2 lines) already gives a good estimation of the ground state lightshift.

Since the scalar polarisability is state dependent, the energy shift is different for all atomic states. It affects the spacing between states, meaning that the transition frequencies change linearly with the laser intensity. In other words, the transition between the bare states $|\psi_i\rangle \rightarrow |\psi_j\rangle$ will get a frequency shift which reads:

$$\Delta f_{(i,j)} = \frac{\alpha_j - \alpha_i}{h} I \,. \tag{1.64}$$

Scattering rate

On top of the energy shift, the contamination of the ground state by excited state has other consequences. In fact, if the excited states contamination can couple to the driving field, it can also couple to the environment field as well. As a consequence, the dressed ground state can scatter photons.

An excited state $|\psi_j\rangle$ can scatter a photon and decay back to the ground state with a decay rate Γ_j. From Equation 1.61, one can get the probability p_j to populate the excited state $|\psi_j\rangle$:

$$p_j = \frac{e^2 I}{2\epsilon_0 \hbar^2 c} \frac{\left|\langle\psi_j|\hat{\mathbf{r}}\cdot\boldsymbol{\epsilon}|\psi_i\rangle\right|^2}{(\omega_j - \omega)^2} \,. \tag{1.65}$$

Finally, the total scattering rate associated to the dressed ground state can be computed by taking the sum over all excited states contributions:

$$\Gamma_{sc} = \sum_j p_j \Gamma_j \,. \tag{1.66}$$

Similarly to the lightshift energy, the contributions of the two first excited states are usually enough to get a good estimation of the scattering rate for ^{85}Rb.

Ponderomotive trapping of circular Rydberg states

To complete the discussion, the trapping of circular Rydberg state is discussed. This trapping relies on the ponderomotive effect.

This effect is best described using Equation 1.43, before the dipole approximation. For the same reasons, the magnetic term can be neglected. However for Rydberg states, the term in $\hat{\mathbf{P}}\cdot\hat{\mathbf{A}}$ becomes small compared to the term in $\hat{\mathbf{A}}^2$, which is the ponderomotive term. This is due to the fact that $\hat{\mathbf{P}}$ amplitude decreases with n [61].

Consider a Rydberg atom placed inside a monochromatic electromagnetic field with an angular frequency ω_L and an amplitude F_0. In that case, the ponderomotive term leads to an effective potential for the electron reading

$$V(F_0) = \frac{e^2}{4m_e\omega_L^2}F_0^2\,, \tag{1.67}$$

after a time averaging over a period [77].

In practice, the field created by a laser can be shaped to be inhomogeneous in space. One can write the associated local intensity

$$I(\mathbf{r}) = \frac{F_0(\mathbf{r})^2 c\epsilon_0}{2}\,. \tag{1.68}$$

At last the space ponderomotive potential can be written as

$$V(\mathbf{r}) = \frac{e^2}{2m_e\epsilon_0 c\omega_L^2}I(\mathbf{r})\,. \tag{1.69}$$

Noticeably, this potential is always positive, regardless of the frequency. This means that the ponderomotive force is always repulsive for a Rydberg state. This makes circular Rydberg atoms low-field seekers. In practice, this effect is used to shape "ligth walls" inside which Rydberg atoms can be trapped. This method has been used to trap circular Rydberg atoms [49].

1.4. Atomic lifetime

Once atoms are in a circular Rydberg state, an important property to consider is the lifetime in the associated state. An atom placed in an excited state can decay to lower energy states by photon emission, or get excited to higher states by photon absorption. These transitions correspond to a coupling of the atom with an electromagnetic field.

For this discussion, the electromagnetic field considered will be the electromagnetic modes of the environment. Indeed, even in the absence of an intentional drive, the atom can still couple to the surrounding environment modes. The latter will be considered to be in a thermal equilibrium with a temperature T. This approach is similar to the one used by Einstein to introduce its eponymous coefficients [78]: the A coefficient associated to the spontaneous emission and the B coefficients associated to the absorption and stimulated emission of a photon.

Transition rates

One now needs to consider that electromagnetic modes of the environment are not at a single frequency compared, for example, to a laser drive. In other words, the transitions from an atomic state can be done through the absorption or emission of a photon in field modes that have different wavevector direction or polarisation.

To begin with, the coupling to a single mode will be considered. [9] The atom is assumed to be in a initial state ψ_i. The field mode considered has a polarisation vector $\boldsymbol{\epsilon}_\sigma$, a wavevector $\hat{k}$ and an angular frequency ω, and is initially in a state $N^{(i)}_{\hat{k},\sigma}$. Once again, their coupling is described by the Hamiltonian from Equation 1.49, written for the right mode.

After the transition, the atom ends up in a new state $\left|\psi_f\right\rangle$, and the field ends up in a state $\left|N^{(f)}_{\hat{k},\sigma}\right\rangle$. The probability for this transition to occur after a time Δt reads [59, 79]:

$$p_{i\to f}^{\hat{k},\sigma}(\Delta t) = \frac{2\pi}{\hbar^2}\left|\left\langle \psi_f, N^{(f)}_{\hat{k},\sigma}\right| H^{Dip}_{AF}\left|\psi_i, N^{(i)}_{\hat{k},\sigma}\right\rangle\right|^2 \Delta t\, \delta(\mathcal{E}_f - \mathcal{E}_i - \hbar\omega)\,, \tag{1.70}$$

using similar notation as in Equation 1.57, where the Dirac function δ ensures energy conservation. Similar arguments can be used here, and the ladder operators acting on the field part in the coupling Hamiltonian only couple the field states separated by one excitation[10], with the relations:

$$\left\langle N^{(j)}\right| a \left|N^{(i)}\right\rangle = \sqrt{N^{(i)}}\,\delta_{N^{(j)},N^{(i)}-1}\,, \tag{1.71}$$

$$\left\langle N^{(j)}\right| a^\dagger \left|N^{(i)}\right\rangle = \sqrt{N^{(i)}+1}\,\delta_{N^{(j)},N^{(i)}+1}\,, \tag{1.72}$$

where the field indexes have been dropped for clarity, and $\delta_{k,l}$ is the Kronecker symbol.

The first relation 1.71 corresponds to the absorption of a field photon. The associated probability is proportional to the number of photons in the field $N^{(i)}$, and is thus called “(stimulated) absorption". The second relation 1.72 corresponds to the emission of photons into the field mode. Noticeably, it is proportional to $N^{(i)}+1$, meaning that it occurs even if no photons are in the field. This emission can be splitted in two parts, one proportional to $N^{(i)}$ called “stimulated emission" and one independent of the photon number called “spontaneous emission”.

In the following, the example considered is the spontaneous emission, which corresponds to the limit $N^{(i)} = 0$. Other decay rates can be obtained in a similar way. The

---

[9] Note that with this approximation, the finite linewidth of atomic transitions are not described.

[10] This is true if the transitions considered are only single photon ones, which is the case here. In more general cases, multi-photons transitions should be included, with higher orders in the coupling Hamiltonian.

matrix element can then be explicitly computed and reads:

$$\left|\left\langle \psi_f, N_{\hat{k},\sigma}^{(f)} \middle| H_{AF}^{Dip} \middle| \psi_i, N_{\hat{k},\sigma}^{(i)} \right\rangle\right|^2 = \frac{\hbar e^2 \omega_{i,f}^2}{2\epsilon_0 \omega \mathcal{V}} \left|\left\langle \psi_j \middle| \hat{\mathbf{r}} \cdot \boldsymbol{\epsilon} \middle| \psi_i \right\rangle\right|^2 , \tag{1.73}$$

using once again the dipole approximation.

To get the full spontaneous emission decay rate associated to the $\psi_i \rightarrow \psi_f$ transition, this probability has to be divided by Δt and summed over all possible accessible field modes. It then reads:

$$\Gamma_{i,f}^{SpE} = \sum_{\epsilon} \int_{\omega,\beta} \frac{2\pi e^2 \omega_{i,f}^2}{2\hbar \epsilon_0 \omega \mathcal{V}} \left|\left\langle \psi_f \middle| \hat{\mathbf{r}} \cdot \boldsymbol{\epsilon} \middle| \psi_i \right\rangle\right|^2 \delta(\omega - \omega_{i,f}) \rho(\omega, \beta, \boldsymbol{\epsilon}) \, \mathrm{d}\omega \, \mathrm{d}\beta \ , \tag{1.74}$$

where $\omega_{i,f}$ is the transition angular frequency, and β contains information about the photon propagation direction. In this expression, the density of modes ρ at an angular frequency ω, direction β and polarisation ϵ has been introduced. This corresponds to the integrated form of the Fermi golden rule [79]. Physically speaking, this rule states that the transition rate is proportional to the oscillator strength and to the number of available field modes for this transition.

For an atom placed in free space, the density of modes is isotropic and only depends on ω. It reads[59]:

$$\rho(\omega) \, \mathrm{d}\omega \, \mathrm{d}\beta = \frac{\omega^2 \mathcal{V}}{c^3 (2\pi)^3} \mathrm{d}\omega \, \mathrm{d}\Omega \ , \tag{1.75}$$

where $\mathrm{d}\Omega$ is the infinitesimal solid angle, all directions being equivalent here.

The spontaneous emission decay rate in free space is then

$$\Gamma_{i,f}^{SpE} = \frac{\omega_{i,f}^3}{3\hbar \epsilon_0 c^3 \pi} D_{i,f}^2 \, , \tag{1.76}$$

where $D_{i,f} = \left|\left\langle \psi_f \middle| e\hat{r} \middle| \psi_i \right\rangle\right|$ is the dipole matrix element of the transition.

The same computation directly leads to a similar expression for the stimulated emission and absorption rates in free space:

$$\Gamma_{i,f}^{StE} = \Gamma_{f,i}^{StA} = \left\langle N(\omega_{i,f}) \right\rangle \Gamma_{i,f}^{SpE} = \frac{\omega_{i,f}^3}{3\hbar \epsilon_0 c^3 \pi} \left\langle N(\omega_{i,f}) \right\rangle D_{i,f}^2 \, , \tag{1.77}$$

where $\left\langle N(\omega_{i,f}) \right\rangle$ is the number of photons of the field at a frequency $\omega_{i,f}$.

Circular state lifetime

For a given state $|\psi_i\rangle$, the computation of the transition rate Γ_i for all possible transitions allows one to estimate its lifetime $\tau_i = \Gamma_i^{-1}$. To do so, one simply has to sum the transitions rates of all possible transitions starting from the state $|\psi_i\rangle$, leading to the global decay rate:

$$\Gamma_i = \sum_{g<i}\left(\Gamma_{i,g}^{StE} + \Gamma_{i,g}^{SpE}\right) + \sum_{e>i}\Gamma_{i,e}^{StA}, \tag{1.78}$$

where $g < i$ (respectively $e > i$) represents all the states that are less (more) excited than the state i.

For lifetime considerations, the environment is assumed to be in a thermal equilibrium at the temperature T. In that case, the number of photons in the environment mode follows a thermal distribution and reads:

$$N^{Th}(T,\omega) = \frac{1}{\exp[\hbar\omega/k_B T] - 1}, \tag{1.79}$$

for an environment temperature T. It is depicted in Figure 1.9 and shows that the number of thermal photons increases with T. For high temperatures, the photon number linearly increases with the temperature.

Using Equation 1.77, Equation 1.78 reads

$$\Gamma_i = \sum_{g<i}\Gamma_{i,g}^{SpE}(1 + N^{Th}(T,\omega_{i,g})) + \sum_{e>i}\Gamma_{e,i}^{SpE} N^{Th}(T,\omega_{i,e}). \tag{1.80}$$

Each contribution can then be explicitly computed using Equation 1.79 and Equation 1.74.

For this experiment, atoms used are circular Rydberg states. In the following, the state considered is the state $|51C\rangle$. Only transitions with the largest dipole matrix elements will contribute to the lifetime. A summary of the main single photon transitions involved for the circular state $|51C\rangle$ is depicted in Figure 1.8. [11]

It turns out that few states are involved into the state decay. First, there are the neighbouring circular states $|52C\rangle = |n = 52, m = 51, k = 0\rangle$ and $|50C\rangle$ circular states, with the largest dipole matrix elements. Other states are elliptical states in the $n = 52$ manifold: $|52e^{\pm}\rangle = |n = 52, m = 50, k = \pm 1\rangle$ and $\left|52ee^{\pm,0}\right\rangle = |n = 52, m = 49, k = \pm 1, 0\rangle$.

This coupling to only few states explains the intrinsic lifetime of circular states.[12] The

---

[11] Two-photons transitions are not represented here, but can become non-negligible in a room temperature setup with the inhibition plates, as discussed in [70].

[12] From a classical point of view, the circular states lifetime can be explained by the fact that an accelerated charge (here the electron) radiates. The circular orbit is the one for which the electron is the less accelerated, and therefore the most stable.

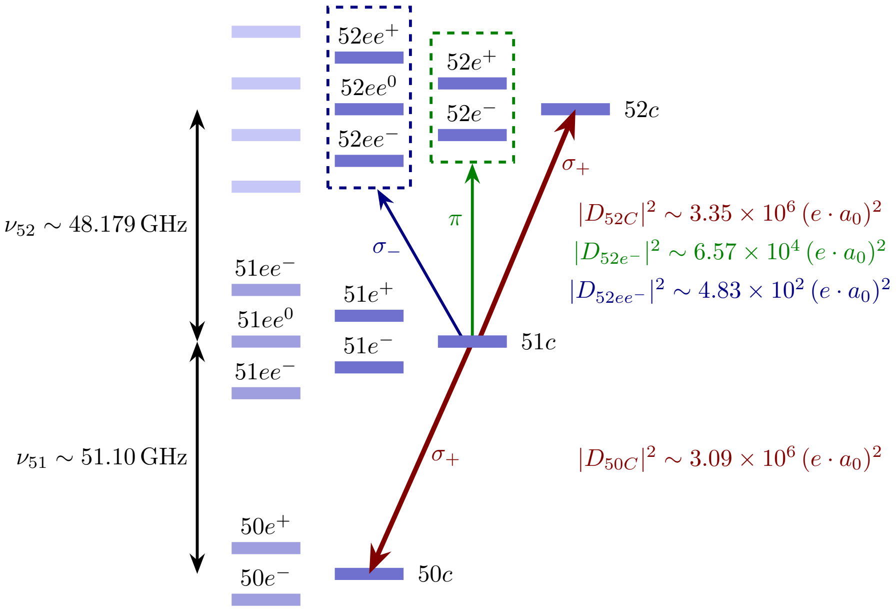

Figure 1.8. – **States involved in circular state decay** for the state $|51C\rangle$. Dipole element hierarchy shows that transitions between circular states are dominant, followed by transitions to first and second elliptical states $|52e^-\rangle$ and $|52ee^-\rangle$. Two-photon transitions and transitions with $|\Delta n| > 1$ are here neglected. Inspired from [80]

.

radiative lifetime τ_n^{SpE} of circular state $|nC\rangle$, associated to the spontaneous emission rate, is given by the decay rate into the lower circular state $|(n-1)C\rangle$. The associated decay rate is found to be [5]

$$\Gamma_n^{SpE} = \frac{4R_y\alpha^3}{3\hbar}n^{-5}, \tag{1.81}$$

where α is the fine structure constant, and R_y the Rydberg energy previously introduced. For $n = 51$, the radiative lifetime computation gives τ_{51}^{SpE} =36 ms at 0 K.

Comparison with low-l states can be done using Equation 1.76. This equation shows that transitions with higher frequencies have in general higher decay rates. The circular to circular transitions are in the tens of gigahertz frequency range. For low-l states, optical decay channels in the hundred of terahertz range exist. From Equation 1.76 and Equation 1.77, one sees that the decay rates for low-l states are roughly three order of magnitudes larger than for circular states, for comparable dipole matrix elements. The radiative lifetime scaling is $\propto n^3$ for low-l states.

Another observation relates to the environment temperature. The Equation 1.78 shows that the stimulated absorption and emission processes are directly proportional to the thermal photons population. For a finite temperature, the emission decay is then enhanced by a factor $1 + N^{Th}$, decreasing the lifetime.

In addition, the presence of environment photons allows for absorption processes,

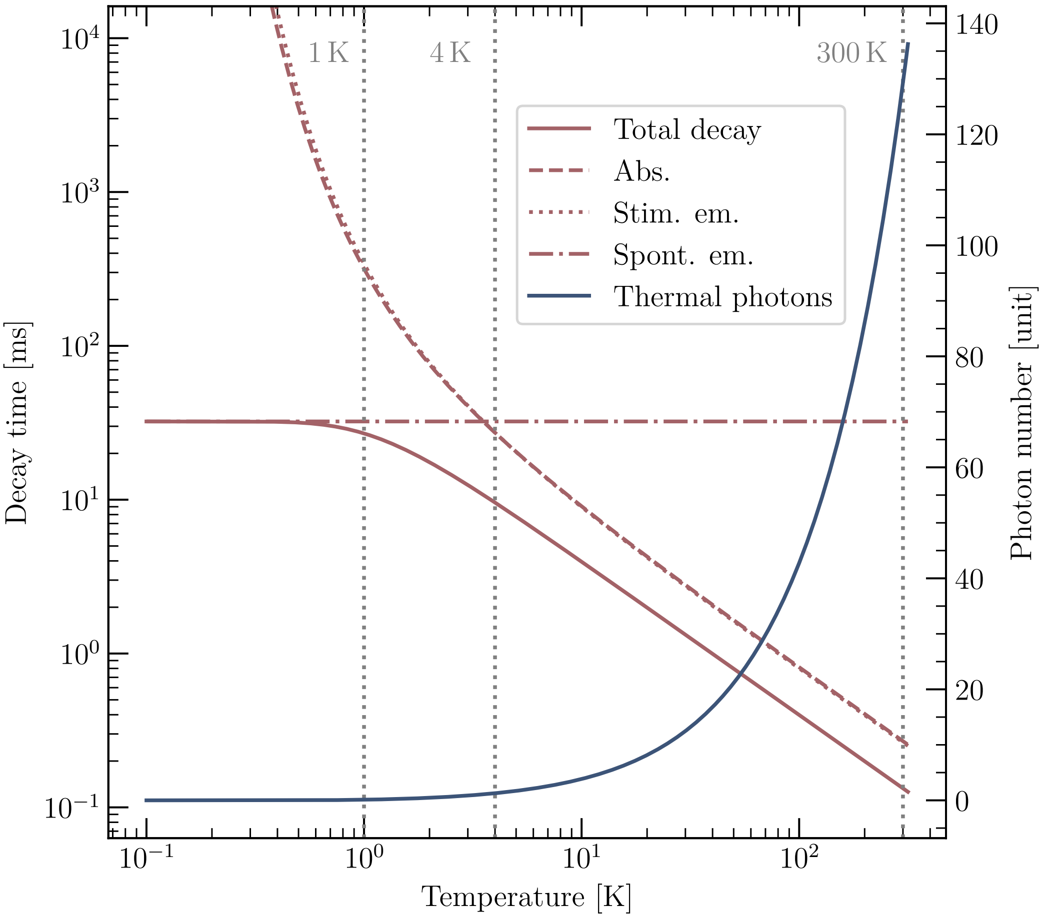

Figure 1.9. – Temperature effect on state decay: decay timescales and thermal photons number evolution with temperature, considering the transitions given in Figure 1.8. For high temperatures, the thermal photons number quickly increases, stimulated contributions are dominant and reduce the lifetime. For small temperatures, the spontaneous contribution dominates and the lifetime saturates in the tens of millisecond range.

and transitions to above states are to be considered. Evolution of the photon number and relative decay rates for different temperatures are depicted in Figure 1.9.

For high temperatures, the stimulated absorption and emission dominate the decay. At 300 K, $N^{Th} \approx 130$ the lifetime for $|50C\rangle$ is around 140 μs. In this regime, the lifetime linearly decreases with the temperature. Indeed, at 4 K, the lifetime is found to be around 10 ms. Note that for high temperatures, the scaling in n is found to be $\propto n^2$ for circular states.

For lower temperatures, the number of thermal photons is so small that the spontaneous contribution, constant with the temperature, becomes dominant. This induces a saturation of the lifetime in the tens of millisecond range. In the mean time, the stimulated decay rates decrease exponentially. In the absence of the spontaneous emission, an exponential increase of the lifetime with temperature decrease is then expected.

From this discussions, it turns out that the free space lifetime reaches a fundamental limit that cannot be overcome by temperature reduction. Fortunately, there is one last parameter to adjust, which is the density of available modes ρ that appears in Equation 1.74. By changing the geometry of the conducting surface around the atom, it is possible to control the modes density. One notable example is the Purcell effect [81], where an atom placed in a cavity with a resonance frequency close to an atomic transitions sees its emission factors enhanced.

Inhibition of circular state spontaneous emission

For circular states, the spontaneous decay channels are clearly identified. The main contribution comes from the decay to the first lower circular state by emission of a microwave circularly polarised photon. For the state $|51C\rangle$, this transition has a wavelength $\lambda_0 \sim 5.87$ mm. As suggested by Kleppner in the 80's [52], the density of modes corresponding to this transition can be largely reduced by putting two parallel plane conductive surfaces around the atom.

When an atom is placed between two infinite and perfectly conductive parallel plates, spaced by a distance $L \sim \lambda_0$, the boundary conditions quantify the number of allowed modes in the direction orthogonal to the plates, set as z here. Using Equation 1.74, this means that the plates also reduce the associated decay rates.

The decay rates given by the Fermi golden rule are the same as for a classical dipole (up to a factor). Using classical electrodynamics, the decay rates reduction can be explicitly computed for a dipole oscillation parallel (ρ) or orthogonal (π) to the plates.

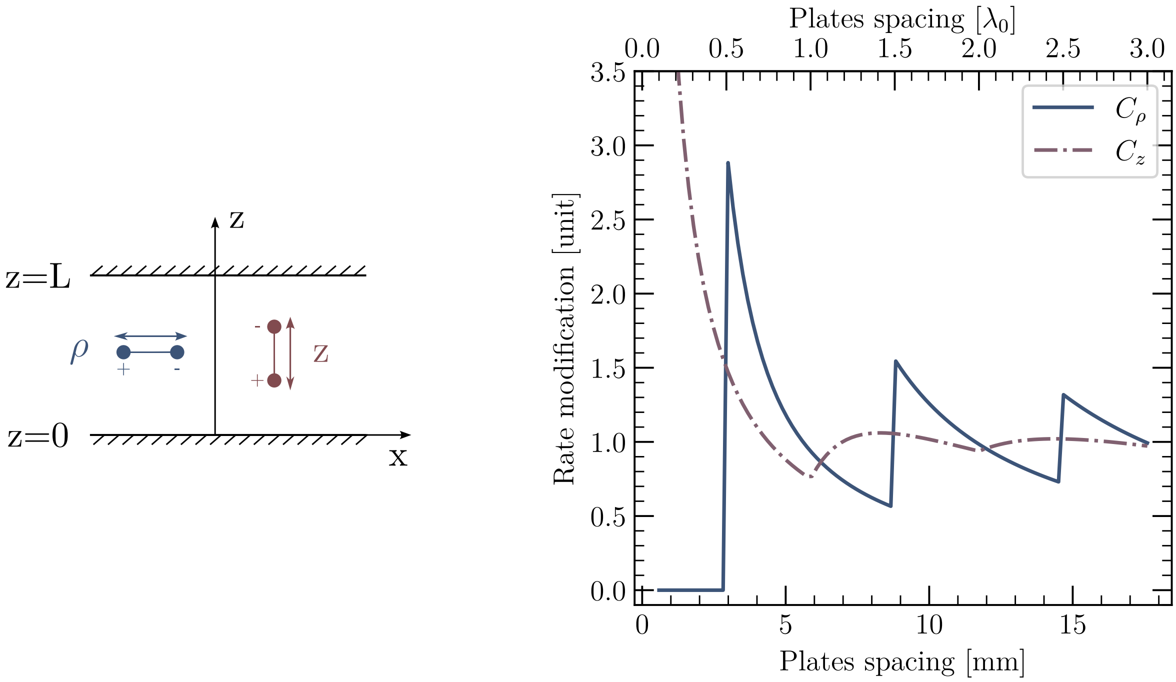

Figure 1.10. – **Rates modification factors** for different plates spacing, in mm and λ_0 units. The reference wavelength $\lambda_0 = 5.87\,\mathrm{mm}$ corresponds to the $|51C\rangle \rightarrow |50C\rangle$ transition. The diagram on the left shows the axis definition, as well as the dipole orientation corresponding to each curve.

The associated modification factors for a dipole placed at z are [82]:

$$C_\rho = \sum_{m=0}^{\lfloor 2L/\lambda \rfloor} \frac{3\lambda}{4L}\left[1+\left(\frac{m\lambda}{2L}\right)^2\right]\sin^2\left(\frac{m\pi z}{L}\right), \tag{1.82}$$

$$C_z = \frac{3\lambda}{4L} + \sum_{m=1}^{\lfloor 2L/\lambda \rfloor} \frac{3\lambda}{2L}\left[1-\left(\frac{m\lambda}{2L}\right)^2\right]\cos^2\left(\frac{m\pi z}{L}\right), \tag{1.83}$$

where λ is the wavelength of the considered transition. For a circular Rydberg atom with a quantisation axis along z, these coefficients correspond to different transitions polarisations. The coefficient C_ρ corresponds to circularly polarised photon transitions ($\sigma_\pm$) and the coefficient C_π to linearly polarised photon transitions (π).

These coefficients are given for different plates spacing in Figure 1.10, for an atom placed in the middle of the gap at $z = L/2$. Noticeably, there is a complete suppression of σ transitions when the spacing is smaller than half the wavelength. Moreover, when the spacing is equal to half of the wavelength, a resonance effect takes place and the decay rate is increased compared to the free space. It is similar to the Purcell effect. For π transitions, a similar resonance effect exists. When the spacing goes to zero the decay rate diverges.

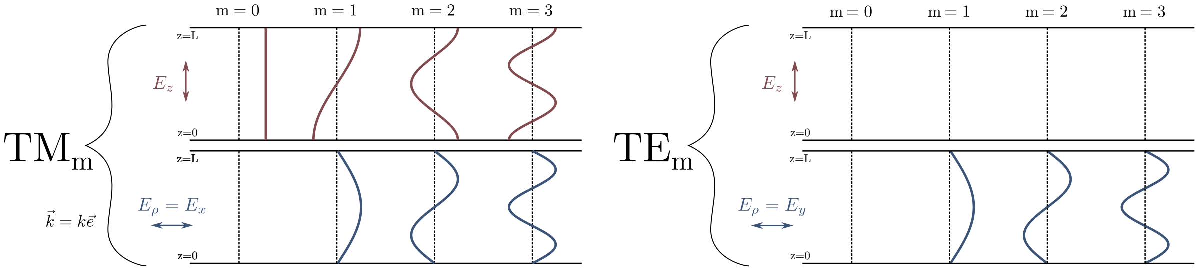

Figure 1.11. – Electric field amplitude of transverse modes for the first modes, assuming a wave propagating along the x direction. The parallel direction ρ is the sum of the y and x directions. For TE modes, $E_x = 0$ and $E_\rho = E_y$. For TM modes, the computation shows no contribution along y, and $E_\rho = E_x$. For $n = 0$, there is no TE mode, and the mode TM$_0$ corresponds to a TEM mode.

A first physical interpretation can be done in terms of modes propagation. From the waveguides physics, one can consider modes that have no electric field in the propagation direction which are transverse electric (TE) modes and modes with no magnetic field along the propagation direction are transver magnetic (TM) modes [83]. The electric field amplitude in the parallel (ρ) and orthogonal (z) directions of the first modes are depicted in Figure 1.11.

The TE modes have no electric field along z, and are associated with dipole oscillations orthogonal to z (σ transitions). The decay rates into these modes are modified by the factor C_ρ.

The TM modes can be populated by dipole oscillations along z (π transitions). Decay rates into these modes are modified by the second term of the C_z coefficient, which is the m-dependent term.

The first term of the C_z coefficient is m-independent and affects decay rates into TEM modes. These are modes for which both the electric and the magnetic fields are null in the propagation direction.

For a mode propagating in the x direction, the null-electric field boundary conditions on the plates quantify the possible values for the wavevector

$$k_z = \frac{m\pi}{L}, \tag{1.84}$$

where m is an integer. This quantisation comes from the fact that modes with $k_z \neq 0$, modes are made of waves reflected by the plates and require constructive interference conditions to exist.

If $k_z = 0$, propagating modes are not associated with waves reflections inside the waveguide. Boundary conditions imply that no TE mode exist for $m = 0$. This explains the complete suppression of modes in C_ρ when $L < \lambda_0/2$. However, a TM mode can exist. For this mode, both the electric and the magnetic fields are transverses. This is the TEM mode, that can propagate with no constraint on its wavelength. [13] Existence of this mode explains the divergence of C_z for small L.

Another interpretation can be done in terms of oscillating dipole and mirror images [84]. Indeed, in a semi-classical picture, an atomic transition can be seen as a dipole oscillation. For π transitions, the dipole oscillations are along the quantisation axis, which is set to be orthogonal to the plates. For σ transitions, the oscillations are parallel to the plates.

The perfectly conductive plates behave like mirrors. Using the image method for electric fields, it is possible to construct images of the dipole. These images create secondary images, creating also images, and in the end an infinite images chain is obtained, as depicted in Figure 1.12.

For a dipole parallel to the plates, the dipole images are in opposite directions. The field radiated by the dipole interferes with the one produced by its images. When $L \to 0$, the interference completely cancels the radiation. However when $L = \lambda(1/2+m)$, $m \in \mathbb{N}$, interference is constructive. The sharp cut-off comes from the infinite number of images in the chain. For realistic plates the transition is smooth [70].

For a dipole orthogonal to the plates, dipole images are aligned. In that case, the interference is constructive when $L \to 0$. The electric field produced by the dipole and its images add up, and the decay rate diverges.

This interpretation allows one to understand the effect of a finite conductivity for the plates. For a non-ideal plate, the surface reflection is not perfect, and each secondary image is weaker than the previous one. As a result, the inhibition effect is weaker. This effect highlights the necessity of good surface quality.

Coming back to the circular state lifetime, the ability to inhibit σ transitions is a key feature here. Indeed, as shown in Figure 1.9, most of the decay channels can be damped by reducing the temperature. The limiting channel at low temperature for circular states is the $|nC\rangle \to |(n-1)C\rangle$ spontaneous emission, which is σ polarised, and can therefore be inhibited by the plates.

As shown in Figure 1.10, this inhibition has a cost, which is the amplification of π transitions. Fortunately, it only affects the $|nC\rangle \to |(n+1)e^-\rangle$ transition, which has a dipole matrix elements two orders of magnitude below the circular-circular transition, and is affected by temperature reduction.

Another side effect arises from the possible amplification of circularly polarised transitions. This can amplify transitions that are usually neglected, such as two-photons transitions. For instance, the two-photons transition $|51C\rangle \to |53C\rangle$ has a wavelength $\lambda \sim 3.2\,\mathrm{mm}$. This effect is non negligible in the presence of inhibition plates at room

---

[13] The TEM mode corresponds to a mode TM_{10} in a rectangular waveguide, in the limit where the extension in the long direction (first index) is infinite.

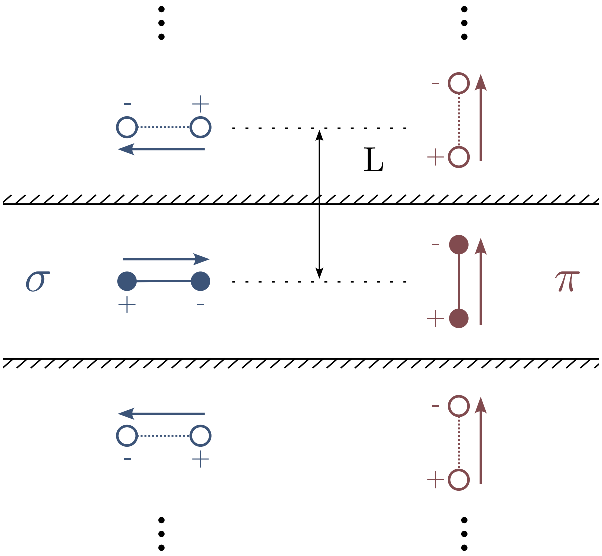

Figure 1.12. – Dipole images induced by the plates: the image method for conductive surfaces can be used to create image dipoles, shown with dashed lines and hollow circles. For a dipole parallel to the plates, the image dipole is in the opposite direction. For orthogonal dipole, images dipole are aligned.

temperature and discussed in details in the thesis of Dr. Wu [54, 70].

One final remark can be made about the inhibition efficiency evolution with the principal quantum number n. The Rydberg state energy scales in $E_n \propto n^{-2}$, as seen in Equation 1.28. The $|nC\rangle \rightarrow |(n-1)C\rangle$ transition wavelength then scales in $\propto n^3$. States of higher n then have spontaneous decay channels with larger wavelength, which are better inhibited for the same plates spacing L.

Conclusion

In this chapter, the basics of atomic physics have been introduced, starting from the hydrogen atom. It gives the tools used to describe Rydberg atoms, especially in high-angular momentum states, such as circular states. The quantum defect model has also been introduced to describe the deviation induced by the ionic core from the hydrogen model that appears for alkali atoms.

A second section described the coupling between atoms and external fields. The cases of static magnetic and electric fields have first been presented, as they are useful tools to control the atomic states energy and degeneracy. Since it is necessary to describe the interaction with electromagnetic waves, the case of oscillating fields was then introduced, and includes the quantised electromagnetic field description.

Lastly, the knowledge of coupling with fields has been applied to concrete examples used in our experiment. The interaction with radiofrequency fields, in the presence of a Stark field, allows one to prepare circular Rydberg atoms. In the non-resonant regime, the strong electromagnetic field produced by a laser beam can be used to shift the atomic states energy and trap the atoms. Moreover, the coupling with the environment field modes can be used to understand states decay. This knowledge provides clues to increase the circular Rydberg states lifetime.

Given all these information, one can guess the ideal setup to get circular states with an enhanced lifetime. Combining an inhibition setup, with two parallel plates, with a cryogenic temperature, below 1 K, should in principle be enough to get rid of most of the decays channels. The recent progress in circular Rydberg atoms trapping should give a means to hold the atoms in place for this extended duration [80]. This setup idea is not new, and was originally proposed few years ago by other members of the group [47]. Taking into account the different losses mechanisms, together with the plates finite size and conductivity, the expected lifetime for a single atom in this simulator is about a minute. The following chapters will give details about the design and realisation of an experimental setup implementing this idea.

Circular Rydberg atoms properties

For $|nC\rangle$, $n \geq 50$

- Size: $n^2 a_0$
- Energy[1]: $R_y n_*^{-2}$
- Trans. freq. $\omega_{nc\rightarrow(n-1)C}$:$\propto n^{-3}$
- Dipole: $D_{nC\rightarrow(n-1)C} = a_0 e n^2/\sqrt{2}$
- Radiative lifetime[2]: $\propto n^5$
- High T lifetime: $\propto n^2$

Values for $|51C\rangle$ in ^{85}Rb

- Size: 275 nm
- Trans. freq. $\omega_{51C\rightarrow 50C}$: 51 GHz
- Radiative lifetime[2]: 36 ms

[1]: $n_* = n$ for Hydrogen, and $n* = n - \delta_{lj}$ for other species (quantum defect).

[2]: in free space, at 0 K.

Chapter 2

A quantum thermodynamics experiment

> *"And some things that should not have been forgotten were lost. History became legend and legend became myth."*
>
> — Lady Galadriel, *The Fellowship of the Ring*

This chapter presents a quantum thermodynamics experiment we performed on the previous experimental setup, using two superconducting cavities interacting with flying circular Rydberg atoms. Finalisation of the data treatment has been realised during the first months of my PhD. This led to an article, which is soon to be published. The results and discussions of this chapter are directly taken from this article.

In this work, different information-erasing environments are simulated using atom-cavity interaction. The resonant coupling between a Rydberg atom and a superconducting cavity field is used to create a maximally entangled state. Different decorrelating processes are implemented before closing the thermodynamic cycle. The full access to both systems is used to perform a full tomography of the joint atom-cavity density matrix using a maximum likelihood estimation (MLE) algorithm. This allows for the measurement of the entropy production over the full cycle and its comparison with the amount of erased correlations.

This chapter starts with a brief introduction motivating this work in the framework of quantum thermodynamics. The underlying theory is then briefly introduced. After that, the experimental implementation is presented. At last, data treatment and results are discussed.

2.1. On entropy production

2.1.1. Quantifying irreversibility

The second law of thermodynamics plays a fundamental role in physics. It establishes the notion of irreversibility and provides constraints on the conversion of heat into work. For thermodynamically open systems, the second law is expressed as the positivity of the entropy production Σ, which quantifies irreversibility [85]. The irreversibility of a physical process can be understood as the inability to bring a system back to its initial state without investing more resources than used in this original process. For example, one can consider a forward process that extracts work W from the evolution of a system from state A to state B, while absorbing heat Q. The transformation will be said to be reversible if and only if there exists a backward process that brings the system from B to A with work $-W$ and ejecting heat $-Q$. In other words, the irreversibility is related to the cost of closing the forward-backward cycle.

In the last decades, considerable progress has been achieved to extend the concept of entropy production to microscopic nonequilibrium systems in both the classical [86, 87, 88] and quantum [89, 90, 91] realms. One particular approach is based on two-point measurement (TPM) schemes in stochastic quantum thermodynamics

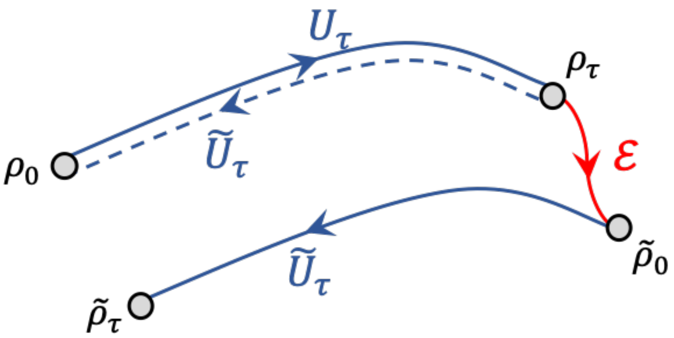

Figure 2.1. – **Forward-backward cycle** in the presence of an irreversible intermediate process $\mathscr{E}$. In the absence of $\mathscr{E}$, the cycle is completely reversed (dash backward evolution).

[92, 93]. In this approach, irreversibility is also associated with closing a forward-backward cycle. But this time, the cycle is modelled by three successive steps. The first and last steps are the forward and backward processes respectively associated to unitary evolution U_τ and $\tilde{U}_\tau$, and are hence reversible. The irreversibility comes from the second process $\mathscr{E}$. Such a cycle is depicted in Figure 2.1. The quantum trajectories are given by the measurement of the initial ρ_0 and final $\tilde{\rho}_\tau$ quantum states. These states are used to compute the entropy production of the intermediate irreversible process.

Mathematically speaking, the entropy production can be described by the Kullback-Leibler-Umegaki (KLU) divergence $D(\rho_1||\rho_2)$, a common information-theoretic quantifier of the relative distance between two states, ρ_1 and ρ_2 [94, 95]. The divergence, as the (von Neumann) entropy, is not associated with any observable. It is a nonlinear function of the states. The entropy production has been experimentally deduced not only for the typical thermodynamic process of thermalisation [96, 97, 98], but also for genuinely quantum processes such as quantum measurement [99, 100, 101].

2.1.2. Decorrelation processes

Quantum correlations, and especially entanglement, have been shown to be key resources for information processing tasks [102, 103]. However, it is very fragile and can be degraded by processes such as decoherence and relaxation of one of the constituting systems. In the following, three distinct decorrelating processes acting on a correlated bipartite system will be considered.

First the decoherence, which eliminates the coherence of either one or both subsystems in their eigenbasis. This process erases all quantum correlation but retains classical ones. A second process is the complete decorrelation, which erases both quantum and classical correlations while keeping reduced states unaffected. The last example considered is the local thermalisation, that brings one of the subsystems to a thermal state. This process erases all correlations as well.

For these irreversible processes, the entropy production has been shown to quantify the entropic cost of erasing the corresponding correlations [89]. For the local thermalisation process, the entropy production further accounts for the irreversibility of changing the reduced state to a thermal state.

In the following, entropy production is studied in a test bipartite system composed of a two-level atom (circular Rydberg atom) resonantly coupled to the electromagnetic field of a microwave cavity (high-quality superconducting) [104]. In order to assess the entropy production, quantum states are reconstructed at reference points of a realised cycle. A typical reconstruction method is based on the maximum likelihood estimation (MLE) of quantum states from measured data. Unfortunately, a state maximising the data likelihood may not have full support on the Hilbert space, a feature of the MLE that is usually innocuous and therefore ignored. However, a reference state of reduced support used for computing the divergence may lead to potential spurious nonphysical divergences, preventing us from adequately calculating entropy. To avoid this issue, the MLE protocol proposed in [102, 103] has been adapted to obtain more realistic full-rank density operators estimating quantum states in the cycle.

2.2. Theoretical description of decorrelating processes

2.2.1. Two-point measurement scheme

Employing TPM schemes [89, 105], a number of fluctuation relations [106, 107, 108] for thermodynamic stochastic variables have been derived for a variety of physical processes. A similar approach has been taken to derive expressions for entropy production for cycles similar to the one depicted in Figure 2.1.

After the forward process, the system evolves according to an uncontrollable dynamic represented by the completely positive trace-preserving (CPTP) map $\mathscr{E}$. It brings the state ρ_τ to a new state $\tilde{\rho}_0 = \mathscr{E}(\rho_\tau)$. The lack of control over this intermediate process means that applying the reverse evolution of the forward process would not bring the state back to its original state ρ_0. This inability is associated to the irreversibility of the intermediate process. Therefore, it is this intermediate process that is the source of entropy production. This step hence simulates the environment responsible for the decorrelation of the two systems.

After the irreversible intermediate stage, the backward process attempts to bring the system back to its initial state ρ_0. This backward evolution is realised by a unitary evolution $\tilde{U}_\tau$, which brings the state $\tilde{\rho}_0$ to $\tilde{\rho}_\tau = \tilde{U}_\tau \tilde{\rho}_0 \tilde{U}_\tau^\dagger$, such that $\tilde{U}_\tau = U_\tau^\dagger$ [109]. As for the forward process, this process is also reversible and carries no entropy production.

In the TPM scheme, a measurement is performed at the beginning and at the end of the forward and backward processes. Each pair of measurement outcomes defines a forward and a backward trajectory, respectively. The entropy production $\langle\Sigma\rangle$ of the intermediate process is obtained by appropriately averaging the ratio of forward and backward trajectory probabilities. The resulting entropy production ends up being given by

$$\langle\Sigma\rangle = D\left(\rho_\tau || \tilde{\rho}_0\right) = D\left(\rho_0 || \tilde{\rho}_\tau\right), \tag{2.1}$$

where the KLU divergence is defined as $D\left(\rho||\sigma\right) = -\mathrm{Tr}\left[\rho \ln \sigma\right] - S\left(\rho\right)$, with $S\left(\rho\right)$ being the von Neumann entropy of ρ. The first equality states that the entropy production of the irreversible process is given by the divergence between the states before and after application of the irreversible process. Since the forward and backward processes are reversible, *i.e.* have no entropy production, $\langle\Sigma\rangle$ also equals the divergence between the initial and final states of the whole protocol. The KLU divergence can be understood as the ability to distinguish two states [110]. If the two states are the same, the relative entropy is null. However, if it is not possible to mistake $\tilde{\rho}_0$ for $\tilde{\rho}_\tau$, the relative entropy is infinite. For example, if the two density matrices don't have the same support, a measurement of ρ_0 can give a result that is impossible to measure with $\tilde{\rho}_\tau$.

2.2.2. Entropy production and correlation erasure

From the TPM scheme, expressions of the entropy production can be derived for the different processes considered. In addition, these expressions allow one to highlight the relation between entropy production and the amount of correlations between the two subsystems erased by the irreversible process.

Mathematically speaking, these correlations are quantified by the mutual information between the two subsystems A and B. In fact, starting from a separable state of the systems A and B, the forward process will create correlations between them. The amount of created correlations is quantified by the mutual information which reads

$$I\left(\rho^{AB}\right) = D\left(\rho^{AB} || \rho^A \otimes \rho^B\right), \tag{2.2}$$

where ρ^{AB} is the bipartite system joint density matrix and ρ^A / ρ^B are the subsystems reduced density matrices.

Thermodynamical processes

A first situation considered is a fully reversible cycle. In that case, the intermediate process is given by the identity operation

$$\tilde{\rho}_0 = \mathscr{E}_{\mathrm{id}}\left(\rho_\tau\right) = \rho_\tau\,. \tag{2.3}$$

for which there is no entropy production

$$\langle \Sigma_{\mathrm{id}} \rangle = 0\,. \tag{2.4}$$

For the complete thermalisation process, the CPTP map is such that $\tilde{\rho}_0 = \mathscr{E}_{\mathrm{therm}}\left(\rho_\tau\right) = \zeta_\beta$, where ζ_β is the Gibbs state at inverse temperature β. When the intermediate process is a thermalisation, its entropy production becomes $\langle \Sigma_{\mathrm{therm}} \rangle = \Delta S_{\mathrm{therm}} - \beta Q_{\mathrm{therm}}$[89], where $\Delta S_{\mathrm{therm}}$ and Q_{therm} are the entropy change and energy change of the system during the thermalisation, respectively.

The identity and thermalisation processes are somewhat typical thermodynamic processes: the first one does nothing, in which case there is no irreversibility, while the second one lets the system thermalise with a heat reservoir.

Local dephasing on both subsystems

For the local dephasing, each subsystem is independently subject to a decoherence process in their eigenbasis. One can define $\left\{P_k^A\right\}$ and $\left\{\Pi_k^B\right\}$ which are the eigenoperators of the reduced states ρ^A and ρ^B, respectively. The CPTP map associated with the local dephasing of both subsystems then reads:

$$\mathscr{E}_{\mathrm{deph}}\left(\rho^{AB}\right) = \sum_{k,l} P_k^A \Pi_l^B \rho^{AB} P_k^A \Pi_l^B = \sum_{k,l} p\left(k,l\right) P_k^A \Pi_l^B\,, \tag{2.5}$$

with $p\left(k,l\right) = \mathrm{Tr}_{AB}\left[P_k^A \Pi_l^B \rho^{AB}\right]$. The resulting state is a classically-correlated quantum state [111], which means that the local-dephasing process erases all the quantum correlations present in the state ρ^{AB}.

Physically, local dephasing can be realised in two ways. First, each subsystem A and B is independently subject to a decoherence process in their eigenbasis. Second, an unread projective measurement in the eigenbasis of ρ^A and ρ^B is jointly realised, the state in Equation 2.5 being the resulting non-selective state. In the latter situation, $p\left(k,l\right)$ corresponds to the joint probabilities of obtaining the outcomes k and l for the joint measurement.

Considering the local-dephasing evolution $\mathscr{E}_{\mathrm{deph}}$ as the irreversible intermediate process, the TPM scheme gives the resulting entropy production:

$$\left\langle \Sigma_{\text{deph}} \right\rangle = D\left(\rho_\tau^{AB} || \mathscr{E}_{\text{deph}}\left(\rho_\tau^{AB}\right)\right) = S\left(\mathscr{E}_{\text{deph}}\left(\rho_\tau^{AB}\right)\right) - S\left(\rho_\tau^{AB}\right). \tag{2.6}$$

The last term corresponds to the relative entropy of coherence [111], which is a measure of the quantum correlations present in the state ρ_τ^{AB} [112].

Alternatively, the entropy production can be written as

$$\left\langle \Sigma_{\text{deph}} \right\rangle = I\left(\rho_\tau^{AB}\right) - I\left(\mathscr{E}_{\text{deph}}\left(\rho_\tau^{AB}\right)\right) \equiv \Delta I_{deph}, \tag{2.7}$$

which demonstrates that the effect of the local-dephasing is to erase only the quantum correlations. In fact, $I\left(\rho_\tau^{AB}\right)$ quantifies the total amount of correlations of ρ_τ^{AB}, classical and quantum, while $I\left(\mathscr{E}_{\text{deph}}\left(\rho_\tau^{AB}\right)\right)$ quantifies the total amount of correlations of $\mathscr{E}_{\text{deph}}\left(\rho_\tau^{AB}\right)$ which only contains classical correlations. Their difference quantifies the amount of correlations erased by the dephasing protocol ΔI_{deph}.

Local dephasing on a single subsystem

Local dephasing can performed only on the subsystem B. This in fact corresponds to the experimental implementation realised. In that case, only the system B is projected onto the eigenbasis of its reduced state. Associated CPTP map reads:

$$\mathscr{E}_{\text{deph2}}\left(\rho^{AB}\right) = \sum_l \Pi_l^B \rho^{AB} \Pi_l^B = \sum_l p(l)\,\rho_l^A \otimes \Pi_l^B, \tag{2.8}$$

where

$$\rho_l^A = \frac{\text{Tr}_B\left[\Pi_l^B \rho^{AB}\right]}{p(l)} = \sum_k p(k|l)\, P_{k|l}^A \tag{2.9}$$

and $P_{k|l}^A$ are the eigenprojectors of state ρ_l^A.

If all the states ρ_l^A are diagonalised by the same set of projectors $\left\{P_k^A\right\}$, then the resulting state of Equation 2.8 coincides with the resulting state of Equation 2.5, with $p(k,l) = p(k|l)\,p(l)$.

In this particular case, one can show that $\mathscr{E}_{\text{deph2}}\left(\rho^{AB}\right) = \mathscr{E}_{\text{deph}}\left(\rho^{AB}\right)$ meaning that all the quantum correlations of the state ρ^{AB} have been erased by applying the local dephasing only on the subsystem B. The local dephasing on one of the the subsystems erases as much correlations, hence creating as much entropy as a dephasing on both subsystems.

Complete decorrelation

For the complete decorrelation, both classical and quantum correlations are completely erased. For an arbitrary state ρ^{AB}, the associated map reads:

$$\mathcal{E}_{\text{decorr}}\left(\rho^{AB}\right) = \rho^{A} \otimes \rho^{B} \,. \tag{2.10}$$

This map is generally non-linear, since ρ^{AB} appears inside ρ^{A} and ρ^{B}, and therefore it does not correspond to a CPTP map [113] and cannot be physically realised. However, it can be simulated by using two copies of the same initial system and letting subsystems of the two copies interact. Details about this simulation implementation are given in the experimental part.

The resulting entropy production from the TPM scheme gives

$$\langle \Sigma_{\text{decorr}} \rangle = I\left(\rho_{\tau}^{AB}\right) \equiv \Delta I_{decorr}, \tag{2.11}$$

showing that the entropy production of the complete decorrelating process is exactly equal to the mutual information initially generated by the forward process. In other words, the entropy production is precisely given by the information-theoretic cost of erasing all the correlations and equals the amount of information ΔI_{decorr} erased by the decorrelation map.

2.3. Experiment implementation

2.3.1. Experimental system

Model system

One of the simplest experimental systems to study irreversibility and simulate different types of environment is a two-level atom (qubit) interacting with a resonant cavity (harmonic oscillator). This system provides some flexibility coming from the large Hilbert state while staying simple enough to maintain a good understanding of the correlations at each step. After preliminary studies, the chosen reversible interaction U_{τ} is the resonant interaction between atom and cavity. It corresponds to a coherent exchange of excitation between the two subsystems, allowing for correlation creation.

Indeed, starting from an atom in the excited state and a cavity in a vacuum state, the coherent exchange of half an excitation generates a maximally entangled state [114]. This is obtained by setting the interaction duration to a quarter of the Rabi oscillation period, to get a $\pi/2$ pulse. For this state, the mutual information between

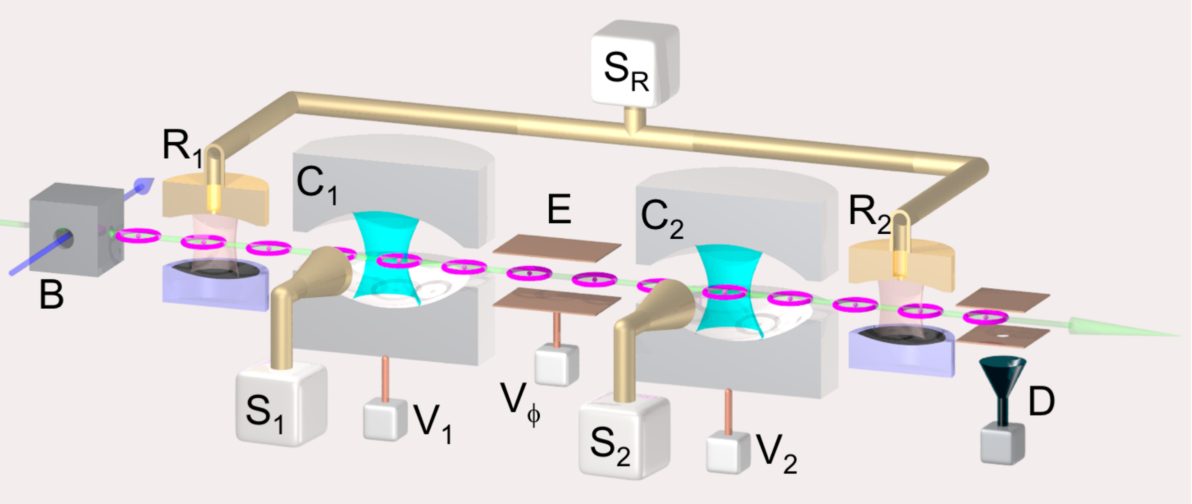

Figure 2.2. – CQED setup diagram. Flying circular Rydberg atoms (pink toroids), excited in box B, can sequentially interact with two high-quality microwave cavities, C_1 and C_2. The atom-cavity detuning is controlled by the electric field applied by the voltage potentials V_1 and V_2. The atomic state is prepared by a low-quality cavity R_1 and is measured by ionisation detector M. The cavity state is reconstructed by the Ramsey interferometer (zones R_1 and R_2 fed by source S_R) with a sequence of probe atoms and a homodyne microwave field injected by sources S_1 and S_2.

the two subsystems equals 2 bits. This is the maximal possible value for this system. This maximally correlating operation has been chosen because it generates a state that has a maximal contrast with respect to a decorrelated state.

Experimental platform

The experiment is performed in a cavity quantum electrodynamics (CQED) setup [98, 104], schematically represented in Figure 2.2. This setup has been used for previous quantum thermodynamics experiments, and more details can be found in the thesis of previous members of the group [115].

Qubits are encoded into circular Rydberg states with principal quantum numbers $n = 50$ and 51. The corresponding levels, denoted $|g\rangle$ and $|e\rangle$, are separated by 51 GHz. The resonator is a high-quality microwave superconducting cavity C. Its photon lifetime of 65 ms is much larger than the overall experiment duration.

The circular Rydberg states are obtained with a scheme similar to the one that will be used for the inhibition setup. This is realised with a three stages excitation into a Rydberg state, followed by a circularisation using the technique introduced in subsection 1.3.2 and purification steps.

For the CQED setup, the Rb^{85} atoms are ejected from an oven, with a velocity selected by Doppler effect ($250\pm1\,\mathrm{m}\cdot\mathrm{s}^{-1}$) and excited in box B to the circular Rydberg state $|e\rangle$ by a sequence involving laser, microwave, and radio-frequency pulses. The atomic states can be additionally manipulated by classical fields in two Ramsey zones R_1 and R_2 fed by the same source S_R.

The atom-cavity detuning is controlled by an electric field applied across the superconducting resonator's mirrors with potentials V_i, by means of the quadratic Stark effect. It provides a means to set the exact interaction time and realise the resonant $\pi/2$ interaction. Finally, atomic states are detected by ionisation in a channeltron detector D. The random atom number per atomic sample obeys Poisson statistics. In order to ensure a single-atom interaction, the mean atom number per sample is lowered down to about 0.2 atoms, and experimental results are post-selected on detection of exactly one atom in each sample.

The experimental setup consists of two similar cavities, C_1 and C_2, with independent control over atom-cavity interaction. For all experiments, the cavity considered for the atom-cavity joint system is the C_2. The cavity C_1 is used in addition to C_2 to simulate the complete decorrelation environment, as described later.

Quantum state reconstruction

The entropy production can be computed with quantities such as the mutual information, von Neumann entropy or KLU divergence. All these quantities are functions of the density matrix, here of the joint atom-cavity system. In order to be sure to grasp both classical and quantum correlations, a full quantum state tomography has to be performed [116]. In practice, it relies on a combination of different measurement procedures. A graphical representation of the probed density matrix elements in the energy basis is given in Figure 2.3.

First, the cavity field can be probed by quantum non-destructive (QND) measurement by means of a long sequence of atoms, interacting dispersively with the cavity field and detected one by one. These atoms are measured in the Ramsey interferometer configuration, using Ramsey cavities installed before and after C_2. This measurement provides information on the photon number distribution [117].

The atom is directly measured in the $\{|g\rangle, |e\rangle\}$ basis (z) by ionisation in D. Post-selection on each atomic state, combined with the photon distribution measurement, provides information about the diagonal terms of the joint density matrix, as depicted in Figure 2.3a.

To get access to off-diagonal density matrix elements, complementary measurements are required. The information on the cavity state coherence is extracted by additional homodyne injection of a reference microwave field from source S_2 into C_2, realis-

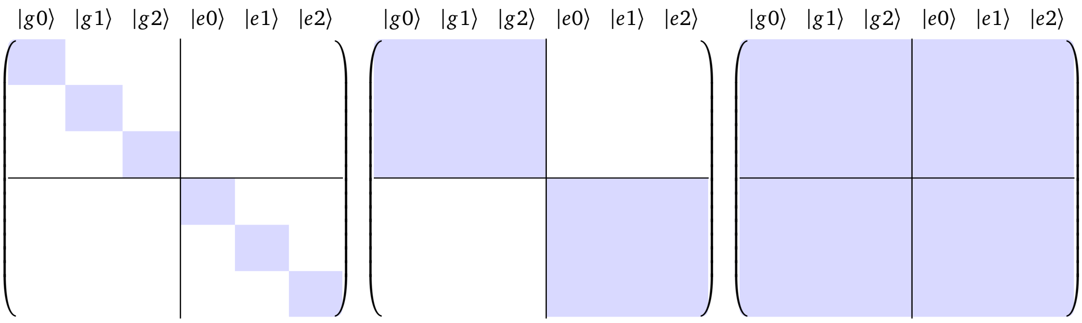

(a) **(b)** **(c)**

Figure 2.3. – **Different measurements sensitivity** schematically represented on the density matrix (blue squares), with the cavity Hilbert space limited to two-photons. For matrix 2.3a, a QND atom-based measurement gives acces to diagonal information. Adding the homodyne measurement provides information about the diagonal subblocks visible on the matrix 2.3b. At last, repeating this measurement with an atom measurement in the x basis completes the missing information and allows one to reconstruct the full density matrix visible in 2.3c.

ing a displacement operation, before performing a quantum nondemolition (QND) measurement [118].

To complete the tomography, the atomic coherence is probed by detecting the atom in the $\{|g\rangle + |e\rangle, |g\rangle - |e\rangle\}$ basis (x). Experimentally, it is done by applying a $\pi/2$ Rabi pulse in the last Ramsey zone before ionisation. The combination of all the above measurements allows one to get a sensitivity for all the coefficients of the joint density matrix, as depicted in Figure 2.3c.

In principle, the full tomography of a two-level system requires measurements in the (y) basis in addition to the energy (z) and (x) basis to have full access to the phase between the two levels. However here, the complete tomography of the cavity states already provides all the required information with measurements of the atom in the (z) and (x) basis.[1]

All different measurement settings and the corresponding measurement results from cavity probing and atomic detection are combined together in a single MLE algorithm [119], providing a reconstructed atom-cavity state of the composite system. The cavity Hilbert space is restricted to $n = 3$ photons for the reconstruction.

To reduce the number of required displacements, they have been strategically chosen to be sensitive to the states measured. An example is depicted in Figure 2.4, for the re-

---

[1] Off-diagonal coefficients depend on the relative phase between the atom and the cavity. A measurement in the (x) basis gives the real part of that phase, where the (y) basis gives the imaginary part. Up to a global phase, the relative phase can be chosen to be real, and a measurement in the y basis is not need. A redefinition of this phase would just result in a rotation of the displacement operations, which doesn't change the reconstruction protocol.

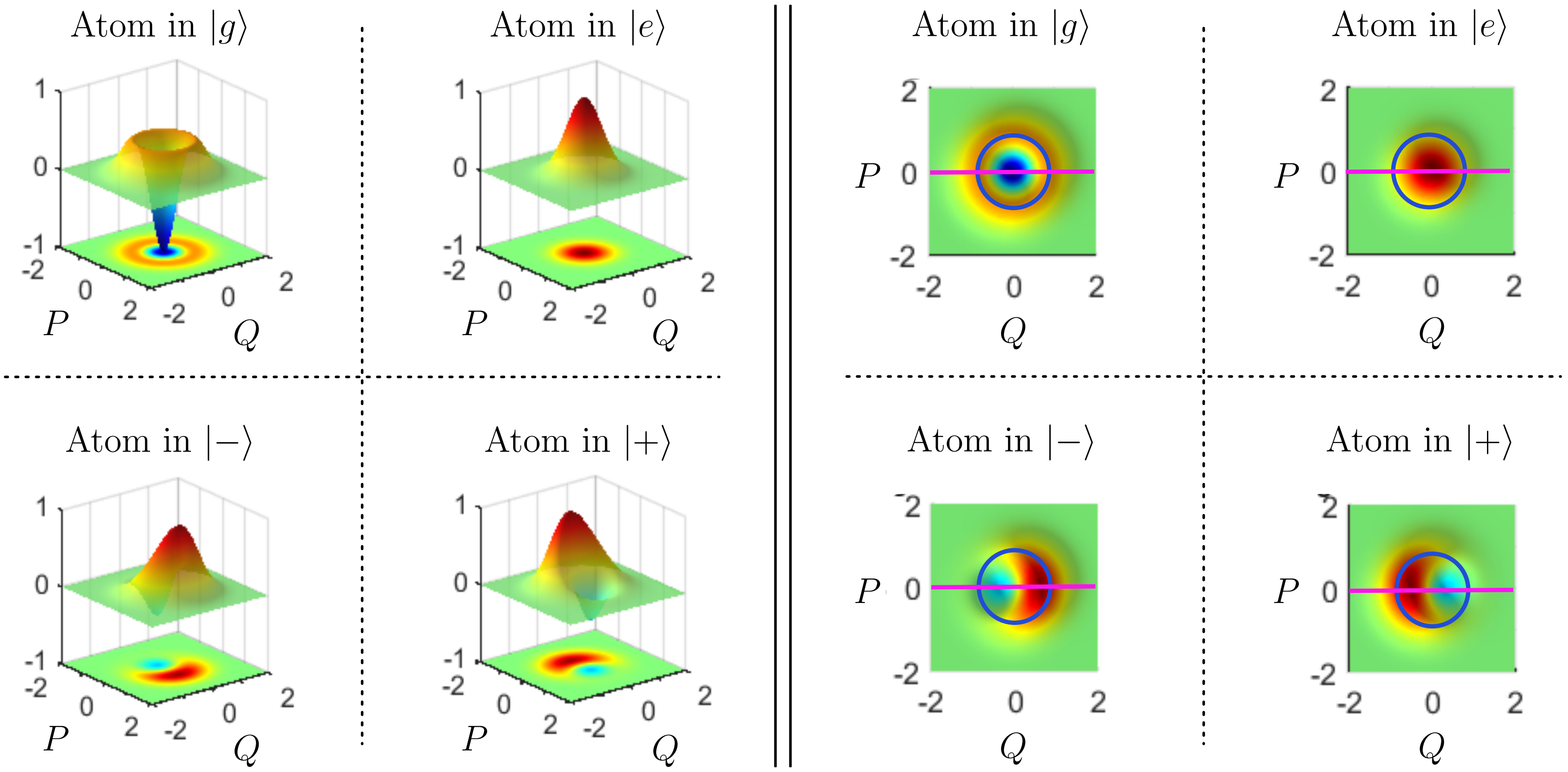

Figure 2.4. – **Displacement settings** for the reconstruction of the coherent superposition $(|g1\rangle + |e0\rangle)/\sqrt{2}$. The left panel shows the cavity state in phase space Q, P, associated with each post-selected atom state $g, e, +, -$. The right panel shows the view in the phase space from the top, with the "linear" (pink) or "circular" (blue) displacement scans used for the homodyne detection.

construction of the coherent superposition $(|g1\rangle + |e0\rangle)/\sqrt{2}$. The Wigner representation of the cavity state is given for a post selection of the atom in the energy basis (z) and the (x) basis. Two types of displacement scans have been chosen. The first ones are "linear" scans, more sensitive to the photon number, and the second ones are "circular" scans more sensitive to the cavity coherence [118].

2.3.2. Decorrelation protocols

Using this experimental setup and these measurement methods, the different decorrelation protocols have been experimentally simulated. In this section, the experimental implementation and associated reconstructed matrices are given.

Unitary processes

The first step of the cycle is the forward correlating process. The initial state is an atom in the excited state and an empty cavity (the cavity C_2). The initial density matrix thus reads

$$\rho_0 = |e0\rangle\langle e0| \,. \tag{2.12}$$

To generate the maximal amount of correlations between the two states, the forward process U_τ, which is a resonant $\pi/2$ interaction, is applied. This allows for the preparation of the maximally entangled state, whose joint density matrix reads

$$\rho_\tau = \frac{(|g1\rangle + |e0\rangle)(\langle g1| + \langle e0|)}{2} \,. \tag{2.13}$$

Experimentally, the voltage V_2 is tuned to set the atom resonant with the cavity for the required interaction time. The interaction strength (Rabi frequency) can slightly vary from one day to the other, and the effective Rabi frequency is calibrated every day to ensure that the proper interaction time is set.

The closure of the cycle requires the backward operation $\tilde{U}_\tau = U_\tau^\dagger$ to be performed, which corresponds to an effective $\pi/2$ pulse in the other direction. This can be realised by applying a $\hat{\sigma}_z$ operation to the atom followed by a $\pi/2$ resonant pulse. This sequence is similar to spin echo techniques.

Experimentally, the σ_z operation is realised by setting an atomic-cavity detuning of 1 MHz for 0.5 μs. The associated π pulse is calibrated using Ramsey interferometry [120].

An interesting feature of this implementation is that both the forward and backward operations can be realised with a single crossing of the cavity. Taking advantage of the spatial Gaussian mode of the cavity, the forward operation can be performed only using the first half of the spatial mode. The backward operation can then be realised on the second half of the mode. This flexibility also allows one to perform the decorrelation processes in between the forward and backward operations.

Identity process

The first environment ($\mathscr{E}$) realised is the identity operation introduced in Equation 2.3, which corresponds to no decorrelation at all. Ideally, it simply brings back the system in its initial state such that:

$$\tilde{\rho}_\tau^{id} = U_\tau^\dagger U_\tau \rho_0 U_\tau^\dagger U_\tau = \rho_0 \,. \tag{2.14}$$

Associated theoretical entropy production is null, *i.e.* $\langle \Sigma_{\mathrm{id}} \rangle = D\left(\tilde{\rho}_\tau^{id} || \rho_0\right) = 0$. Experimentally, technical imperfections mean that forward and backward processes are not exactly inverse of each other. Some entropy production consequently exists, leading to $\langle \Sigma_{\mathrm{id}}^{\mathrm{exp}} \rangle \neq 0$. It allows one to quantify the amount of entropy produced even in the absence of an intentional decorrelation process. Some examples of relevant imperfections are the finite atomic and photon lifetimes, the dispersion in atom-cavity coupling, the non-ideal σ_z flip or the non-negligible presence of a second non-detected atom in the flying atomic sample.

Most of these imperfections cannot be compensated for in this experimental setup but can be accurately estimated. It allows for the estimation of the realistic density matrix labelled “theoretical” in the following. They are to be compared with the matrices reconstructed from experimental data, labelled as “reconstructed”. The corresponding matrices for the identity process are depicted in Figure 2.5.

The reconstructed matrices are similar to the theoretical ones, meaning that the experimental imperfections are well understood. In addition, this experiment also validates the tomography protocol, demonstrating its ability to reconstruct quantum correlations as well.

The tomography method has been benchmarked on the theoretical matrices. The protocol used for tomography, with displacement, atom state rotation and measurements, was numerically simulated to the theoretical matrices using a Monte Carlo algorithm. The MLE algorithm is then applied on obtained simulated measurement results. Resulting density matrices are close to the reconstructed matrices depicted in Figure 2.5, strengthening the reconstruction protocol reliability.

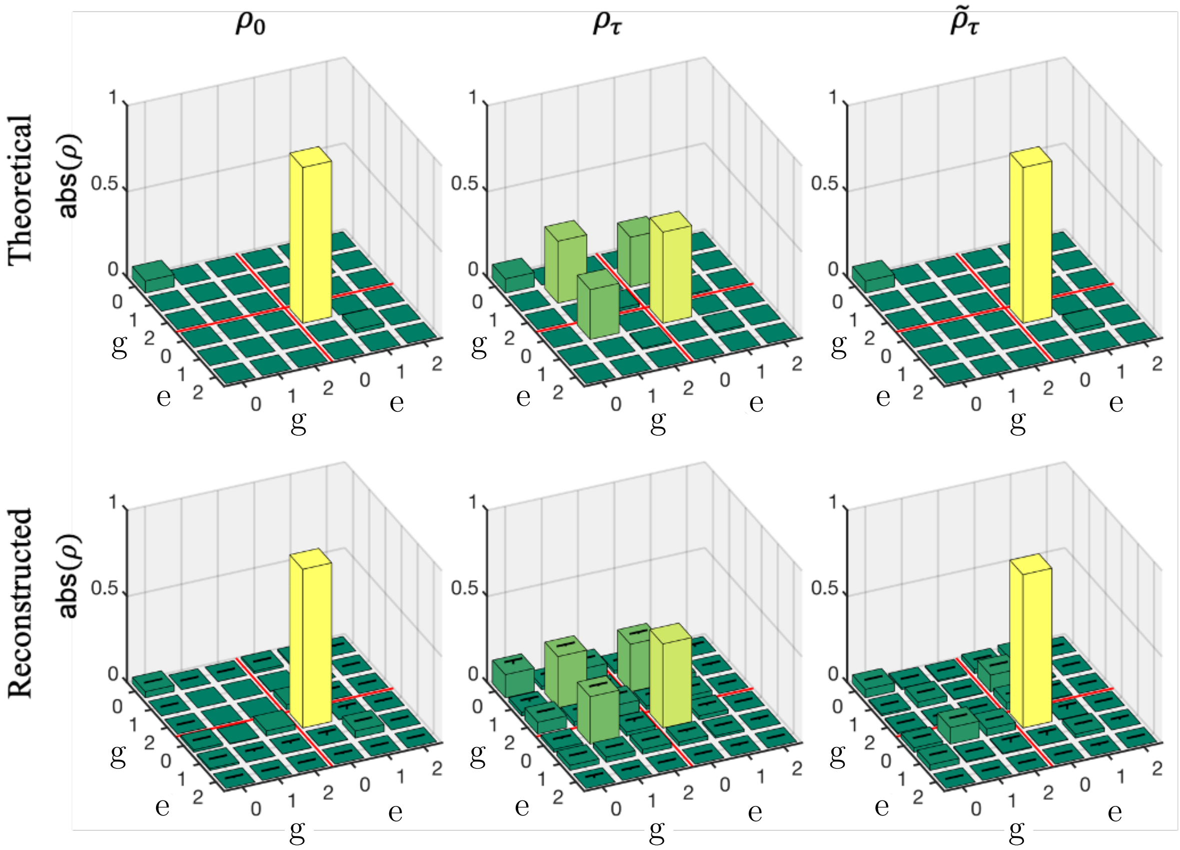

Figure 2.5. – Density matrices for the identity process with the initial state ρ_0, the state ρ_τ after the forward process and the state $\tilde{\rho}_\tau$ after the backward process. The upper row are theoretical matrices taking into account experimental imperfections. The lower row gives the ones reconstructed from experimental data. For the sake of clarity, the cavity Hilbert space shown is restricted to $n \leq 2$ (components with $n = 3$ being negligible).

Local dephasing

The first implemented decorrelation process is the local dephasing, associated with the erasure of quantum correlations. It is experimentally realised by applying a large detuning of several megahertz between the atom and the cavity for $0.8\,\mu$s. In practice, it means applying a large electric field across the cavity mirrors. Its large spatial inhomogeneity results in a random phase accumulated between the atom and the cavity, which provides an effective dephasing of the atom.

To make sure that this effect induces a large enough dephasing, a Ramsey interferometry sequence in the presence of this large detuning step has been tested. Indeed, this step completely suppresses the fringes contrast, demonstrating the effectiveness of the local dephasing.

The expected density matrix after local dephasing is:

$$\tilde{\rho}_0^{deph} = \frac{|e0\rangle\langle e0| + |g1\rangle\langle g1|}{2}. \tag{2.15}$$

The ideal backward unitary process leads to the same matrix. As for the identity, matrices taking into account theoretical imperfections and matrices reconstructed from experimental data have been obtained and are shown in Figure 2.6.

Complete decorrelation

Lastly, the complete decorrelation has been implemented. The ideal protocol would be the following. Atom and cavity start in a fully decorrelated state $\rho_0^{C,A} = \rho_0^C \otimes \rho_0^A$. The correlating operation U is then realised to obtain the correlated state $\rho_\tau^{C,A}$. The local states of each subsystem are $\rho_\tau^C = \mathrm{tr}_A(\rho_\tau^{C,A})$ and $\rho_\tau^A = \mathrm{tr}_C(\rho_\tau^{C,A})$. The complete decorrelation process is then applied, leading to the state $\tilde{\rho}_0 = \rho_\tau^C \otimes \rho_\tau^A$. Finally, the backward operation $U^\dagger$ is realised to get $\tilde{\rho}_\tau$.

No CPTP map exists for such process. However, it can be simulated using auxiliary systems. The implementation scheme in bloc diagram and an illustration of its physical implementation are depicted in Figure 2.7. An auxiliary atom is sent through the main cavity C_m, which is the second cavity C_2 in the setup. Their interaction prepares the fully correlated state $\rho_\tau^{C_m,A_a}$. Similarly, the main atom A_m is sent through the auxiliary cavity $C_a = C_1$, hence preparing the fully correlated state $\rho_\tau^{C_a,A_m}$. The two auxiliary systems are not measured. At this point, the joint state of the main atom - main cavity state is $\rho_\tau^{C_m} \otimes \rho_\tau^{A_m}$[2], which corresponds to the fully decorrelated state $\tilde{\rho}_0^{C_m,A_m}$, which reads

---

[2] Obtained after tracing out the auxiliary systems.

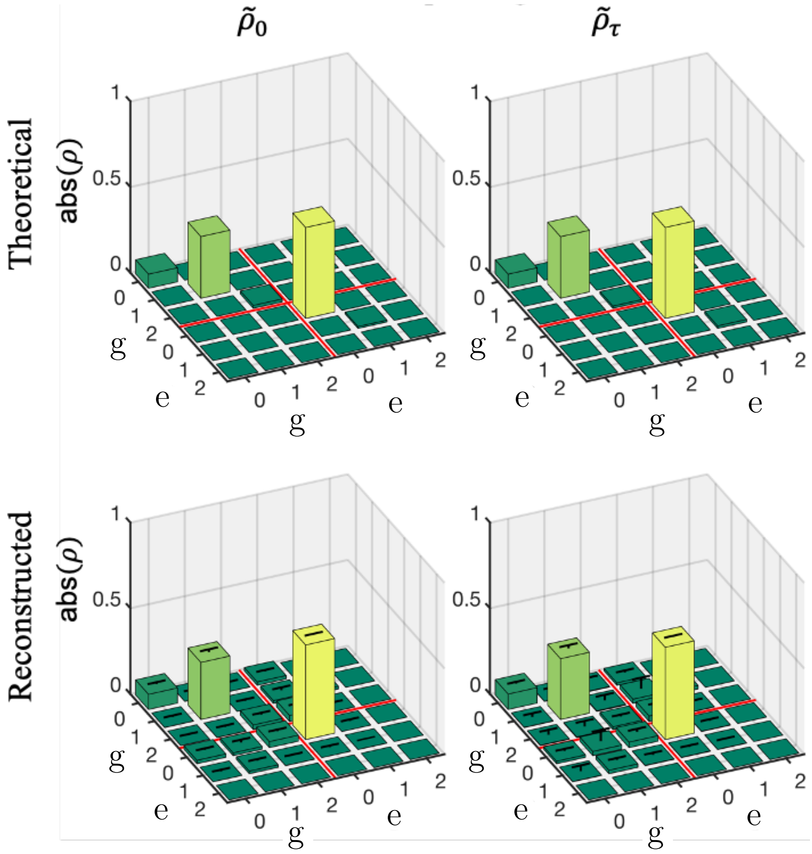

Figure 2.6. – Density matrices for the dephasing process after the dephasing process $\tilde{\rho}_0$ and after the backward process $\tilde{\rho}_\tau$.

$$\tilde{\rho}_0^{decorr} = \frac{(|e\rangle\langle e| + |g\rangle\langle g|) \otimes (|0\rangle\langle 0| + |1\rangle\langle 1|)}{2}. \tag{2.16}$$

From this state, the backward process between the main cavity and the main atom can be realised, leading to the state $\tilde{\rho}_\tau^{C_m,A_m}$. One assumption made here is that the two cavities are similar enough such that $U^\dagger$ in C_2 inverts the operation U in C_1. Associated theoretical and reconstructed density matrices are depicted in Figure 2.8. Once again, there is an agreement between theoretical and experimental matrices, meaning that the complete decorrelation is effectively simulated.

2.4. Data treatment and results

Once the different decorrelation cycles have been experimentally implemented and measured, their entropy production can be estimated. However, it turns out that directly using the MLE reconstructed matrices to compute the KLU divergence can lead to non-physical results. This section will first detail this issue before giving details on the solution used and the corresponding results obtained.

2.4.1. Entropy production from reconstructed matrices

MLE reconstruction

The MLE method works as follows. For each density matrix, measurements with the different settings are performed and repeated many times on different copies of the state. These experiments give N measurement results for each state to reconstruct, with typically $N \sim 10^4 - 10^5$.

An effect matrix E_i is associated to each measurement outcome i. They are positive semidefinite matrices, such that $\sum_i E_i = \mathbb{1}$, corresponding to a positive operator-valued measurement (POVM). The probability to obtain a measurement i associated with the matrix ρ is then given by $p(i|\rho) = \mathrm{Tr}(\rho E_i)$ [115].

One can define the sequence of all measurement outcomes $\mathscr{D} = (i_1, \ldots, i_N)$. Applying a Bayesian point of view, given a dataset $\mathscr{D}$, a likelihood L can be attributed to each possible density matrix, with

$$L(\rho|\mathscr{D}) \propto p(\mathscr{D}|\rho). \tag{2.17}$$

Mathematically speaking, the likelihood corresponds to the probability for a density matrix ρ to give the dataset $\mathscr{D}$.

Given this, the reconstruction algorithm consists of finding the matrix which max-

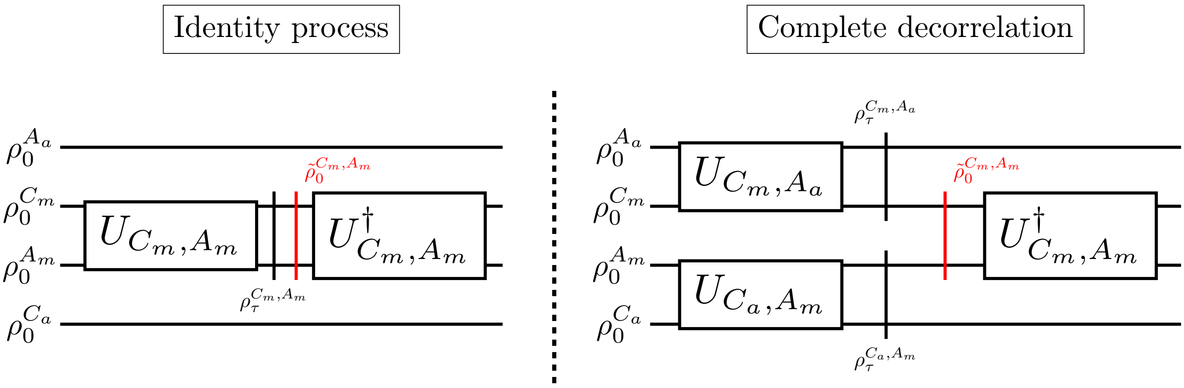

(a) Circuit diagram

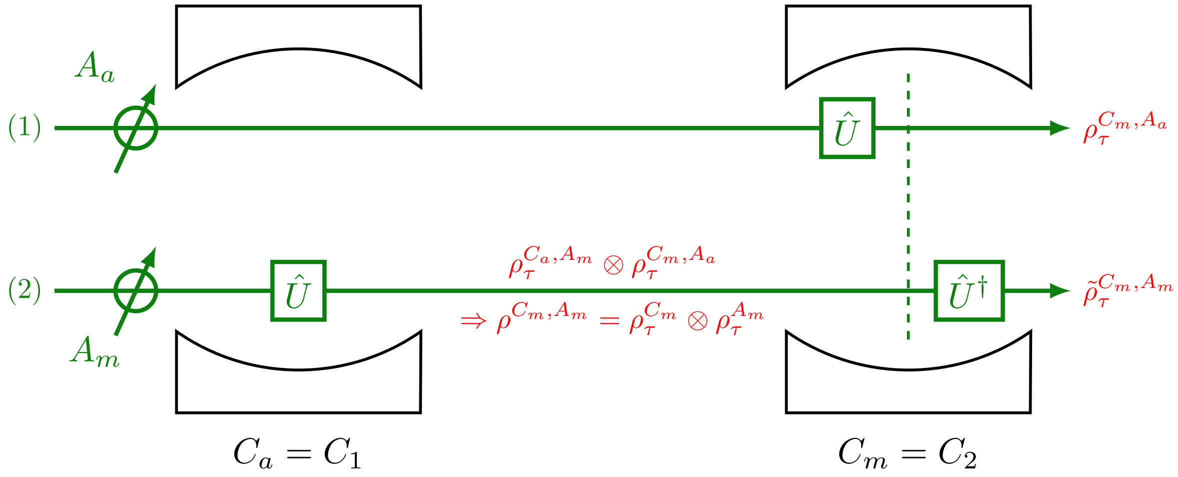

(b) Complete decorrelation physical implementation

Figure 2.7. – Complete decorrelation implementation. Figure 2.7a gives a circuit diagram representation of the identity process (left) for comparison and the complete decorrelation (right). The main cavity C_m realises the forward process with an auxiliary atom A_a. The same is done with the main atom A_m and an auxiliary cavity C_a. The backward process is then realised on the decorrelated state $\tilde{\rho}_0^{C_m A_m}$. Figure 2.7b illustrates the physical implementation. First, the auxiliary atom A_a is sent through the main cavity $C_m = C_2$ to interact with it. The main atom A_m is then sent to the auxiliary cavity $C_a = C_1$. The main atom- main cavity joint state is then $\rho_\tau^{C_m} \otimes \rho_\tau^{A_m} = \tilde{\rho}_0^{C_m A_m}$.

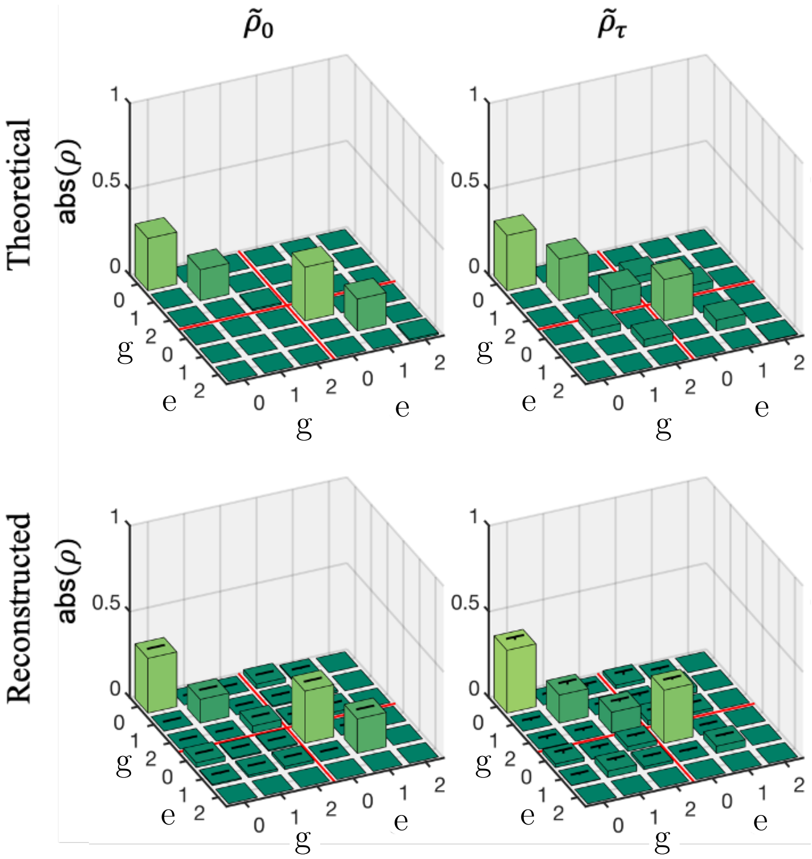

Figure 2.8. – Density matrices for the complete decorrelation process after the dephasing process $\tilde{\rho}_0$ and after the backward process $\tilde{\rho}_\tau$.

imises the likelihood. The reconstructed matrix is then defined as:

$$\rho^{ML} = \mathrm{argmax}_{\rho} \left[L(\rho|\mathscr{D}) \right] . \tag{2.18}$$

However, depending on the likelihood estimator and the algorithm used, this method can give matrices with some biased properties [115].

KLU divergence issues

Using the reconstructed matrix, any function f of the density matrix can be estimated using

$$f_{est}^{ML} = f(\rho^{ML}) . \tag{2.19}$$

This can be extended to functions of more than one density matrix.

However, the used reconstruction method tends to give matrices which don't have full support *i.e.* which have one or more null eigenvalues. For the KLU divergence computation, this leads to diverging values induced by mathematical artefacts. This can be understood by looking at the KLU divergence definition of two matrices ρ and σ:

$$D(\rho||\sigma) = -\mathrm{Tr}\left[\rho \ln \sigma\right] - S(\rho) = -\mathrm{Tr}\left[\rho \ln \sigma\right] + \mathrm{Tr}\left[\rho \ln \rho\right] . \tag{2.20}$$

The divergence is computed in a basis where ρ is diagonal, with associated ρ_l eigenvalues. For this illustrative example, σ is assumed to be diagonal in this basis as well, with eigenvalues σ_l.

If σ doesn't have full support, there exists a l value for which $\sigma_l = 0$. If the corresponding ρ_l is nonzero, then the associated contribution to Equation 2.20 ($-\mathrm{Tr}\left[\rho_l \ln \sigma_l / \rho_l\right]$) diverges. This is in fact an intended feature of the divergence, accounting for processes that would require an infinite amount of entropy production. For example, a rank-deficient thermal state corresponds to a state with $T = 0$, which, according to the 3^{rd} law of thermodynamics, requires an infinite amount of entropy to be prepared.

The decorrelating processes considered here are not associated with infinite entropy. Even with experimental imperfections taken into account, the KLU divergence computed on the theoretical matrices is non-diverging. However, the reconstruction method here leads to noise in the eigenvectors of the different matrices. Therefore, the support of the matrices is slightly different, and null eigenvalues of σ can encounter non-zero values for ρ because of this eigenbasis disagreement. As a consequence, computing the KLU divergence directly from the MLE matrices is not a good strategy.

2.4.2. Entropy production from the likelihood

To overcome the problem of diverging quantities when using Equation 2.18, one solution is to take a step back and compute the KLU divergence using the likelihood defined in Equation 2.17.

Likelihood of a function

The goal is to estimate a non-linear function of the density matrices, here the KLU divergence between two matrices. For a given function f of the density matrices ρ, a corresponding likelihood can be defined as

$$L_f(x|\mathscr{D}) = \int \mathrm{d}\rho \; L(\rho|\mathscr{D}) \; \delta(x - f(\rho)), \tag{2.21}$$

where the integral is over all density matrices (using Haar measure), and δ is the Dirac function.

From the L_f function, one can get an estimate for $f(\rho)$, given the dataset and the corresponding uncertainties. Here, the average of L_f has been used, such that

$$f_{est} = \int \mathrm{d}x \, x \, L_f(x|\mathscr{D}) = \int \mathrm{d}\rho \; f(\rho) \, L(\rho|\mathscr{D}). \tag{2.22}$$

It is to note that for this expression, any density matrix that is not excluded by experimental observations contributes to the estimation, with a weight given by its likelihood.

Similarly, the uncertainty on this estimate is evaluated as the standard deviation of the L_f distribution:

$$\delta f_{est} = \sqrt{\langle x^2 \rangle_{L_f} - \langle x \rangle_{L_f}^2}. \tag{2.23}$$

An emphasis has to be made on the fact that this procedure is not equivalent to the maximum-likelihood estimate done in Equation 2.19. While both approaches converge to the same estimate in the limit of infinitely many samples ($N \to \infty$), they lead to very different results when estimating non-linear functions, such as the KLU divergence, with a finite number of samples.

Furthermore, the approach implemented in this work is conceptually more satisfactory than the ML reconstruction, as it incorporates the complete statistical information contained in the likelihood function and is not plagued by the possibly very atypical properties of ρ^{ML}. Note that this approach is conceptually very similar to the mean Bayesian estimate proposed in [121], where one introduces the density matrix $\rho^{MBE} = \int d\rho \; \rho \; L(\rho|\mathscr{D})$, and then uses $f_{est}^{MBE} = f(\rho^{MBE})$. While this is equivalent when f is a linear function in ρ, the estimate used of Equation 2.22 is more generally suited

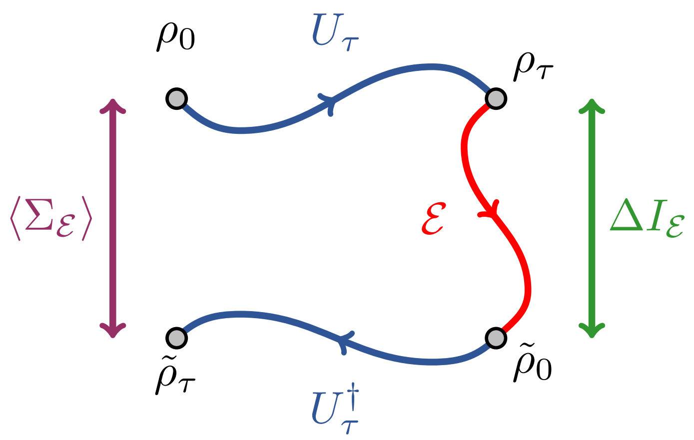

Figure 2.9. – Illustration of the quantities computation: represented on the thermodynamic cycle.

for estimating arbitrary functions of the density matrix.

Computation of the KLU divergence

Given that the density matrices are high-dimensional objects (in our case, they are 8×8 hermitian matrices), one cannot perform directly the integration as required by Equation 2.22 or Equation 2.23. To circumvent this issue, a numerical Monte-Carlo sampling over the density matrix space is realised.

In concrete terms, an ensemble of n density matrices $(\rho_1, \ldots, \rho_n)$ are sampled according to their likelihood, such that $(1/n)\sum_{k=1}^{n} f(\rho_k) = \int \mathrm{d}\rho\, f(\rho)\, L(\rho|\mathscr{D}) + O(1/\sqrt{n})$. Namely, averaging over the n sampled density matrices is equivalent to averaging over the L distribution, up to $1/\sqrt{n}$ corrections. This is achieved by using the Metropolis algorithm [122, 123].

2.4.3. Results and discussion

Following this method, entropy production and mutual information for the different decorrelations have been computed. For each decorrelation process, both the erased correlations ΔI during the process $\mathscr{E}$ and entropy production for the full cycle $\langle\Sigma\rangle$ are given. Using the notations introduced in Figure 2.1, their respective expressions for a simulated environment $\mathscr{E}$ are

$$\Delta I_\mathscr{E} = I(\rho_\tau) - I(\tilde{\rho}_0)\,, \tag{2.24}$$

$$\langle\Sigma_\mathscr{E}\rangle = D\,(\rho_0||\tilde{\rho}_\tau)\,. \tag{2.25}$$

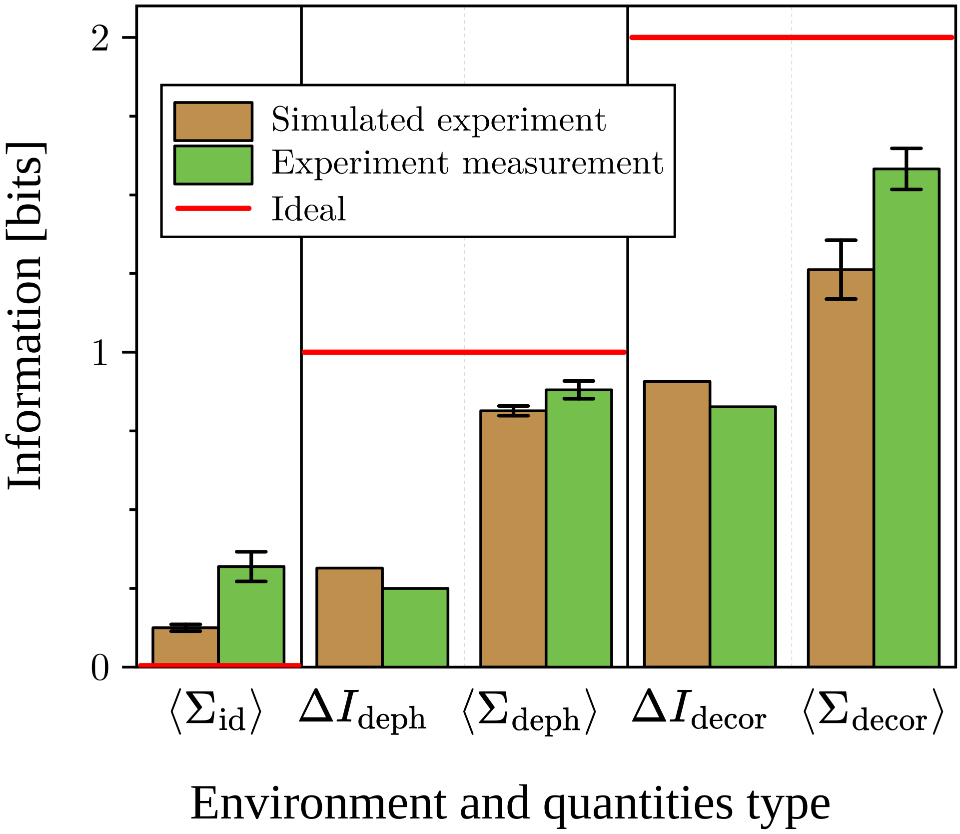

Figure 2.10. – Entropy production and mutual information results obtained for the different decorrelation protocols. Upper panel gives values for the simulated experiment (green) and from experimental data (brown). Red lines correspond to the ideal values. Lower panels shows the thermodynamic cycle together with the matrices used to compute each quantity.

The Figure 2.9 illustrates the different density matrices of the cycle used to compute each quantity.

Obtained results are depicted in Figure 2.10. For each quantity, values computed from experimental measurements are given in green. In addition, the tomography protocol has also been simulated on the theoretical matrices, and associated results are given in brown. Red lines indicate the ideal erasure processes, corresponding to the 1-bit limit for classical correlations erasure (dephasing) and 2-bits limit for all correlations erasure (complete decorrelation).

Identity process

The first measured quantity is the entropy production associated with the identity process. Since there is no intentional decorrelation process, ΔI_{id} is null by definition, and so is the entropy production for the cycle. However, for simulated and measured matrices, $\langle\Sigma_{id}\rangle$ is nonzero and corresponds to the entropy produced by experimental

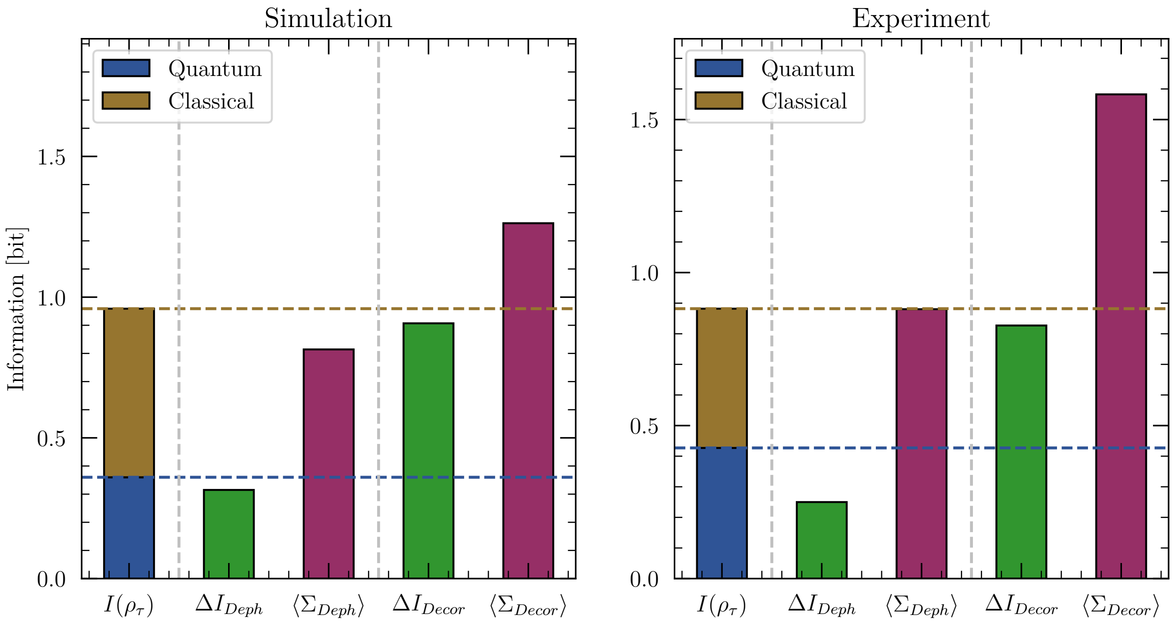

Figure 2.11. – **Amount of created correlations s** compared with the entropy production and mutual information obtained from the simulation (left panel) and experiment (right panel).

imperfections, such as atom and cavity decay. This allows one to estimate the systematic error on the entropy production coming from the imperfection of the forward and backward processes. At last, the associated entropy is higher for the experimental data than from the simulation. This can be due to an insufficient estimation of the experimental imperfections for the calculation of non-linear functions of the density matrices.

Local dephasing process

For the dephasing process, correlation erasure and entropy production are expected to equal the 1 bit of quantum information generated by the forward process. For the simulated and measured matrices, erased information ΔI_{deph} is below this limit. This difference has two possible origins.

First, since the forward process is imperfect, the amount of quantum correlations prepared is below 1 bit, and so is the amount of quantum information erased by the dephasing. The total amount of prepared correlations is given by $I(\rho_\tau)$. It is then possible to estimate the classical correlations by computing the mutual information, only taking the diagonal elements of ρ_τ into account. From this, the amount of effectively prepared quantum correlations can be computed. Second, if the dephasing is not perfect, some quantum correlations remain, $I(\tilde{\rho}_0)$ is larger, and ΔI_{deph} is smaller.

An estimation of the amount of effectively prepared correlations, compared with the mutual information difference and entropy produced is given in Figure 2.11. In both the simulation and the experiment, the amount of prepared correlations is way below the ideal values, with less than 0.5 bits of quantum correlations prepared in both cases, instead of the expected 1 bit, and is the main difference with the ideal case.

However, the amount of erased correlations ΔI_{deph} for the simulation is comparable to the amount of initially prepared quantum correlations, suggesting that the dephasing protocol is indeed efficient. For the experiment, the amount of erased correlations is smaller than the amount of quantum correlations prepared, with around 60 % of quantum correlations erased.

Regarding the entropy production for the full cycle, it is found to be higher than the amount of erased correlations in both simulation and experiment. This is likely due to the imperfection of the forward and backward processes, as estimated with the identity process. In fact, if the backward process is not exactly the inverse of the forward process, which is the case if they are not exactly unitary, then additional entropy can be produced.

For both the erased correlations and the entropy production, the experimentally measured values are close to the simulated one. This suggests that even if the measured values are far from the ideal values, the discrepancy is well understood.

Complete decorrelation process

Finally, the same quantities have been computed for the complete decorrelation. The discrepancy between experimental and ideal values can be understood in a similar way: the amount of effectively prepared correlations is likely to be smaller and the decorrelation process might be imperfect.

Since ΔI_{decor} is larger that ΔI_{deph}, it suggests that additional correlations are indeed erased. In fact, the values given in Figure 2.11 show that for both the simulation and the experiment, almost all correlations prepared are erased by the decorrelation protocol.

As for the dephasing, entropy of the full cycle $\langle \Sigma_{decor} \rangle$ is larger than erased correlations, meaning that the forward-backward processes also create entropy, and this for both experimental and simulation values.

For the mutual information difference, the simulation once again provides values close to the experiment ones, suggesting that the imperfections are once again well understood. However, for the entropy production the experiment gives a significantly higher value. This can be explained by the fact that the experiment involves two different cavities and two different atoms.

In fact, for the dephasing protocol, the forward and backward operations are realised inside the same cavity. Even if the atom doesn't exactly cross the cavity in the centre of the mode, resulting in an imperfection in the forward process, the same imperfect placement will affect the backward process. As a result, even if the forward and backward processes are imperfect, some of the imperfections can be compensated and ensure that the backward is indeed the inverse of the forward process.

However for the decorrelation process, the use of two cavities and two atoms prevents such compensation effect. For example, the auxiliary atom can be centred in the cavity mode, resulting in an efficient forward operation, but the main atom can be off, making the backward operation uncompleted. As a result, the backward operation is more likely not to be the inverse of the forward, which results in an additional entropy production.

Conclusion

In this chapter, an experiment simulating entropy production for different decorrelation processes has been presented. First, the theoretical framework using TPM schemes has been introduced. It allowed us to derive expressions for the entropy production of cycles involving different decorrelation processes. A first one is a local dephasing, erasing quantum correlations. A second one is complete decorrelation, which erases all correlations. In both cases, the entropy production for the whole cycle equals the amount of correlations erased at the decorrelation step.

Then, the highly controlled experimental platform used to study these cycles has been introduced. It involves two superconducting Fabry-Perrot cavities, interacting with flying Rydberg atoms. Protocols used to prepare and manipulate the different subsystem have been presented. This highly controlled system allowed us to simulate the different decorrelation processes and to perform the joint atom-cavity system tomography.

Finally, a computation method for the entropy production and mutual information for each process has been presented. The challenge here relied in the fact that the KLU divergence, involved in the entropy production definition, can take non-physical value when computed with matrices that don't have a full support. The solution proposed here was to compute these quantities using the likelihood of experimental measurements results.

Obtained entropy production and correlations erasure showed discrepancy between ideal and experimentally measured values. Simulations taking into account the experimental imperfections allowed us to partially explain these differences.

Several positive results of this experiment are to be highlighted. First, the reconstruction methods allowed us to fully reconstruct the target states, with relatively low errors. Second, a convincing method has been developed to allow for the estimation of non-linear functions of the density matrices, which proved to be challenging. Lastly, even if some of the differences remain unexplained, the relatively good agreement between simulation and experimental results reveals a good understanding of the experiment, even in such an unfavourable context.

From a broader perspective, this chapter gives a successful example of a simulation of thermodynamic systems, by using a Rydberg atom platform. In addition to all the previous studies performed with this experimental setup, all the knowledge acquired about Rydberg atoms gives a good basis for the design of the new experimental setup.

Chapter 3

Inhibition of spontaneous emission, a cryogenic implementation

- So – Plan B?

- No. Not Plan B. Plan 2. "Plan B" implies we only have 26.

— Mayor Sadie Sinclair and Cyclops, *Uncanny X-Men #541*

The first chapter introduced the theoretical ingredients required for the description of circular Rydberg atoms, from their preparation to their manipulation. The study of their interaction with environment electromagnetic modes showed the main causes of circular state relaxation. With this, a proposal to inhibit these decay channels emerged: [47]. In this paper, the simulation estimations suggest that the combination of an inhibition setup, with parallel plane plates, in a cryogenic environment would allow the circular Rydberg atoms to reach lifetimes in the minute range.

This chapter describes the experimental setup designed, fabricated and assembled during the last 4 years, towards obtaining circular Rydberg states with an extended lifetime. The circular states studied have $n \approx 50$ and are prepared with ^{85}Rb. This experiment can be seen as a combination of the techniques developed by the Rydberg atom team of the LKB. The group has been studying circular Rydberg atoms for decades, in experimental setups with reduced black-body radiation (BBR). More recently, inhibition of BBR transfers and spontaneous emission using inhibition plates have been studied in a room temperature experiment [54, 70]. In the mean time, other members of the group managed to trap circular Rydberg atoms into optical traps similar to the atomic tweezers used for ground state atoms [49, 61].

In this chapter, the main elements involved in the atomic lifetime extension will first be discussed. Inhibition of spontaneous emission is realised by parallel plates, and details about their design will be given. Then, the means to reduce the BBR around the atoms will be covered. Finally, the circular Rydberg atoms trapping setup will be discussed.

A second part will be dedicated to the circular Rydberg states preparation inside the inhibition region. Details about how to combine a good preparation and a good inhibition region will be discussed. This part starts with the atom excitation to the circular Rydberg states. Then, the details about how to deterministically deliver ground state atoms in between the plates will be provided.

The last part will discuss the means to measure the atoms at the different steps. It will begin with the optical detection of ground states atoms. Since they have optically accessible transitions, direct imaging with a camera is enough, and the associated setup will be discussed. For circular Rydberg atoms, there are no direct optical transitions that can be used to probe the excited state, and the ionisation signal measurement has been chosen. This allows for a state sensitive detection, and details about its experimental realisation will be discussed.

3.1. An isolated atom

The main goal of the experiment is to obtain circular Rydberg states with an extended lifetime. As seen in Equation 1.80, the state lifetime is governed by spontaneous and stimulated transfer rates. The stimulated processes are proportional to the number of thermal photons in the environment. Such processes are damped by reducing the amount of BBR around the atoms. This is done by lowering the temperature of the surfaces around the atoms and introducing microwave absorbing materials. The spontaneous processes are only affected by the density of electromagnetic modes to couple with, for a given transition. These can be damped by changing the geometry of the conductive surfaces around the atoms. This section covers the experimental setup designed to suppress the two kinds of decay channels mentioned above. To fully take advantage of this extended lifetime, circular Rydberg atoms have to be trapped and associated methods are discussed at the end of this part.

3.1.1. Isolation from vacuum fluctuations

In a 0 K environment, the only limitation of the atomic lifetime comes from spontaneous emission channels. The main spontaneous decay channel for circular state $|51C\rangle$ corresponds to the circularly polarised transition $|51C\rangle \rightarrow |50C\rangle$. As discussed in section 1.4, this transition can be inhibited by means of two plane parallel conductive plates with a sub-wavelength spacing.

Inhibition plates design

The inhibition effect depicted in Figure 1.10 is obtained for infinitely large plates with a perfect reflectivity. This ideal case can't be achieved in a real setup. In order to estimate the effect of a finite size and conductivity for the plates, numerical simulations of a dipole radiating in between realistic plates have been performed, using the software *CST Studio Suite*. The spontaneous decay rate with respect to the free space decay rate is depicted in Figure 3.1. The dipole frequency corresponds to the $|48C\rangle \rightarrow |47C\rangle$ transition. Since the inhibition increases with n, the inhibition is expected to be even better for $|51C\rangle$.

On top of the inhibition requirements, additional practical considerations are to be considered. A control of the electric field in between the plates is critical for the inhibition efficiency, as well as for the circular states preparation and detection. For the detection, ions collection requires a hole in one of the plates, hence constraining the possible materials. Finally, laser beams will be used to trap atoms in between the

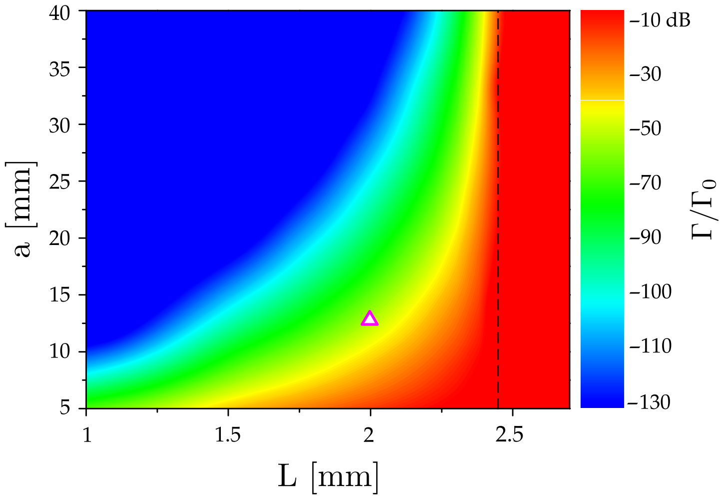

Figure 3.1. – **Decay rate between non-ideal plates** taking into account finite size and conductivity. The transition considered is $|48C\rangle \rightarrow |47C\rangle$. L is the spacing between the plates, and a the length of square plates. The rate Γ/Γ_0 gives the relative rate in between the plates Γ with respect to the free space rate Γ_0. The white triangle indicates dimensions of the initial proposal, leading to an inhibition around 50 dB. Figure from [47].

plates and electrodes will be used for the circularisation. Therefore, the plates spacing can't be infinitely small. The laser beams divergence also constrains the plates size, which can't be arbitrarily large. Combination of these constraints with the inhibition requirements led to the following plates design.

For the plates geometry, Figure 3.1 shows that a 50 dB inhibition is expected for plates with a size around 10 mm and a spacing of 2 mm. Such dimensions provide a good trade-off between the inhibition efficiency and a good access for lasers and electrodes.

Apart from their geometry, the plates surface needs to be as reflective as possible to optimise the inhibition. A high reflectivity can be provided with a high electric conductivity and a small roughness. To optimise these properties, the plate surface is polished to reduce its roughness and gilded to increase its conductivity. Gilding of the surfaces also prevents oxidation, and is done for all pieces of the setup placed inside the cryostat.

Last but not least, the bulk material of the plates is also important. The chosen solution is to make plates out of brass. This material is usually used in cryogenic experiments for several reasons. It has a relatively good thermal conductivity, which is essential for a good thermalisation. Second, its conductivity allows one to control its potential. This can be used to control the electric field in between the plates. It is also less sensitive to eddy currents compared to other metals, such as copper (which is another usually good candidate). Finally, it can be easily manufactured, leaving a lot of freedom for its geometry.[1]

Plates realisation

The dimensions chosen for the plates are 10 mm × 22 mm with a spacing of 2 mm. To ensure that the plates have the right spacing, they are both embedded in holding blocks, visible in Figure 3.2a. Once assembled, the two blocks ensure a correct spacing, as seen in Figure 3.2b.

The plates are glued to their holding blocks using an electrically conductive epoxy glue *330-GLUE3* from *allectra*. The conductivity is required to ensure good electric contact between the plates and the block, to allow for a good control of the plates potentials. Using glued plates instead of a bulk block also allows for the possibility to change them in future versions of the experiment. Details about the gluing procedure are given in Appendix A.

Once manufactured, the plates have been polished. The surface roughness has been measured using an atomic force microscope (AFM) to estimate the quality. A measured image can be found in Figure 3.3. The root mean square average of the profile height R_q was found to be 40 nm. Some defects with a size up to 500 nm were identified. They remain rare and small enough to not destroy the surface optical quality. Overall, the surface roughness is small enough to ensure a good reflectivity in the microwave domain, and with it an improved inhibition.

To gild them, plates have been covered with a 150 nm layer of gold. Gold coating is systematically applied on all surfaces of the experiment core to avoid surface oxidation and get a better electrical conductivity. Less critical pieces are electroplated by an external company. With this method, surfaces reflectivity is degraded. To avoid such issue for the plates, they have instead been gilded in the laboratory clean room, using evaporation deposition. With this method, the surface quality has been preserved. Details about the gilding procedure are given in Appendix A.

Electric field control

The electric field in the inhibition region needs to be controlled. Indeed the electric field is used to stabilise the circular state orbital to ensure an efficient inhibition. A tilt of the circular orbit would change the atomic dipole moment orientation, which needs to be orthogonal to the plates to get an efficient inhibition. For the proposed simulator, typical electric fields required are around $10\,\mathrm{V\cdot cm^{-1}}$ [47]. In addition, an electric field

---

[1] Another possibility could be the use of glass plates covered with Indium-Tin-Oxyde [70]. This configuration is optically transparent, which allows for an easier optical access, at a cost of a weaker inhibition and a lower flexibility in the plates manufacturing.

(a) Plates picture

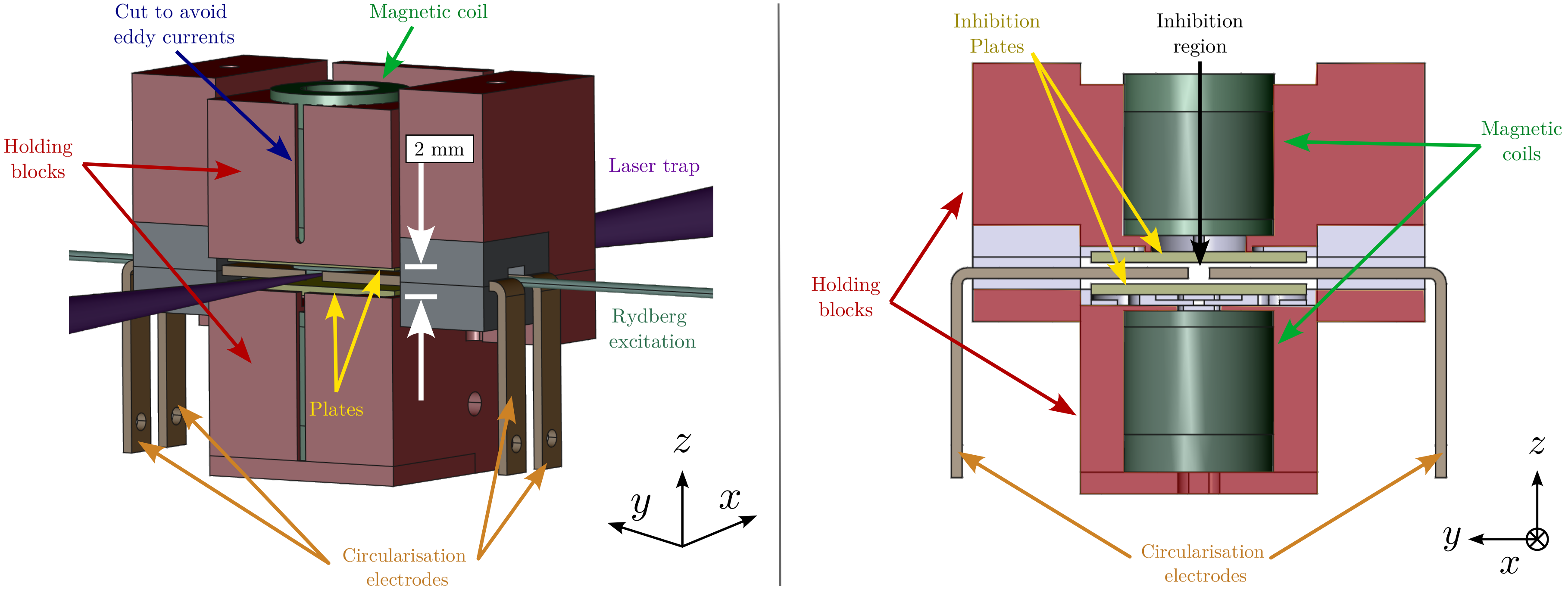

(b) Inhibition block

Figure 3.2. – **Inhibition plates** used in the experiment. Figure 3.2a shows the real plates embedded in their holding blocks. Figure 3.2b shows the inhibition block technical drawing once mounted side and cut views. The 2 mm spacing between the two plates (yellow) is visible. To illustrate the restricted optical access, Rydberg (teal) and trap (purple) laser beams are represented. Additional elements are represented: holding blocks (red), magnetic coils (green) and circularisation plates (orange).

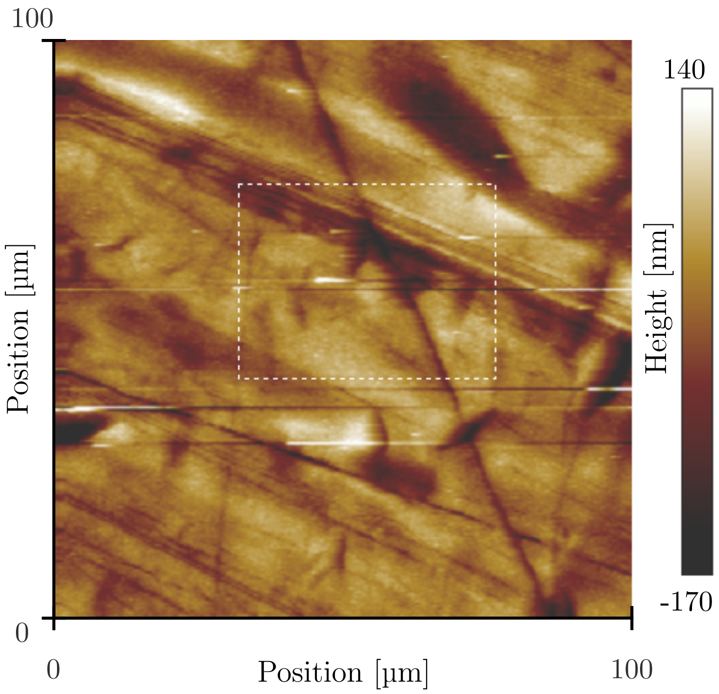

Figure 3.3. – Plates surface measurement obtained with an atomic force microscope. This device measured the height profile of the surface, over a $100\,\mu\text{m} \times 100\,\mu\text{m}$ square for this example. Some scratches are observed, with a depth below 500 nm. The average height profile root means squared was found to be around 40 nm. Image taken from the software used to control the AFM.

control is required for circular states preparation, to ionise the atoms for their detection and to tune the simulated Hamiltonian parameters.

Control of the electric field is realised by applying different potentials to the inhibition plates. By construction, it ensures that the atomic dipole moment is orthogonal to the plates. More precisely, the bottom plate is set to ground potential and the upper one to negative potentials. The plates spacing being 2 mm, setting the upper plate to around $-2\,\text{V}$ provides the electric field required for the orbit stabilisation.

Magnetic field control

The large magnetic quantum number m of circular states make them especially sensitive to magnetic field fluctuations. It is therefore important to control the magnetic environment of the atoms, and to protect them from external field fluctuations. For the simulator, control of the magnetic field in between the plates is also required to tune the simulated Hamiltonian and can be used to improve the circularisation efficiency. For the simulator, typical field values are around 10 G.

In order to screen external magnetic fields, a box covered with niobium sheets, whose picture is given in Figure 3.4, is put around the experiment core. The Niobium being

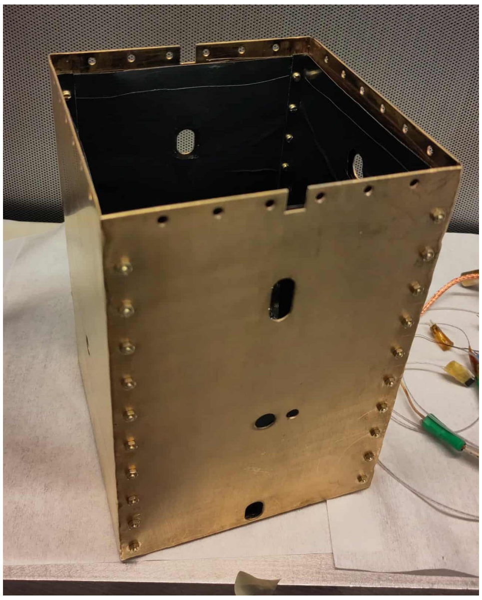

Figure 3.4. – **Niobium box:** a box covered with Niobium sheets protects the experiment at 4 K from external magnetic fields. Holes are cut for the laser beams.

superconducting at 4 K, it screens the experiment core from external magnetic fields variations. A drawback of such a superconducting screen is that if a bias field exists prior to the superconducting transition, this field will be maintained. To avoid this issue, a μ-metal screen is added. This nickel-iron alloy has a high magnetic permeability, which allows one to guide the magnetic field lines around the experiment, hence protecting it from bias at room-temperature.

To generate the required magnetic fields, superconducting coils are put in the inhibition block on both sides of the plates, as shown in Figure 3.2b. More details about the generated field are given in subsection 4.4.1. The necessity to change the magnetic field close to the experiment core brings another complication. Indeed, changing a magnetic field near a conductive surface can induce eddy current loops on its surface, creating a magnetic field response opposed to the initial change. For metals with non-zero resistivity, the loops eventually disappear, but this induces delays in the magnetic field stabilisation which can affect some steps' efficiency. In practice, magnetic field changes need to be stable after a few milliseconds. To reduce eddy currents, cuts are added on some pieces, as depicted in the Figure 3.2b. This also was a motivation for choosing brass instead of copper for experiment pieces, the latter being more sensitive to eddy currents due to its much higher electrical conductivity.

3.1.2. Isolation from black body radiation

On top of the inhibition structure, atoms need to be isolated from black-body radiation (BBR) to avoid stimulated transfers. To do so, the environment around the atoms is to be thermalised at the lowest possible temperature, below 1 K. In addition, BBR photons coming from hotter regions have to be screened.

In order to get a cold environment, the experiment core is placed inside a helium bath cryostat. This cryostat has been originally designed for CQED experiments. For this new experimental setup, several changes had to be realised. The original technical drawing of the cryostat is depicted in Figure 3.5, together with a picture of the current setup. In addition to this section, more details about the typical cooling procedure and cryostat properties are given in Appendix B.

The cryostat is divided into several regions, thermalised at different temperatures. The first cold region is thermalised by a nitrogen bath at 77 K and the second one by a helium bath at 4 K. The coldest region is the experiment core, connected to the science plate. This plate can be cooled to 1.6 K or 0.8 K [2] by means of ^{4}He and ^{3}He cryogenerators [124]. In the standard regime, losses of the helium part of the cryostat are around 450 mW. This corresponds to an autonomy of around 48 h for the helium reservoir.

The 77 K and 4 K regions are protected from the BBR of hotter regions by thermal shields, respectively called nitrogen (N) and helium (He) shields, which are shown in Figure 3.6. These shields had to be extended such that the new experimental setup could fit in. This increase in size also increases the amount of hotter BBR absorbed by the shields, which can increase the shields temperature. To reduce this absorption, each shield is wrapped with cryogenic thermal insulation *Coolcat 4K* from *beyond gravity*.

In addition, the niobium core is to be surrounded on both sides by a box of radiowave absorbent material (RAM) thermalised below 1 K. This material absorbs the microwaves, avoiding reflections and diffusion. The inner side of the RAM box ensures that the experiment core is properly thermalised at the lowest temperature. The outer side absorbs BBR photons that can come from outside. A drawing of the RAM box with elements of the inhibition block is depicted in Figure 3.7.

The new experimental setup requires more optical access than the previous one, and additional windows had to be cut in the thermal shields. To reduce the amount of BBR that can leak through, metallic screens are put on the windows, as shown in Figure 3.8. This reduces the effective opening, leaving just enough space for the laser beams to go through. These plates can easily be adjusted in later stages of the experiment, if it is

---

[2] Values given correspond to the last temperature measured in the previous experiments done in this cryostat [115].

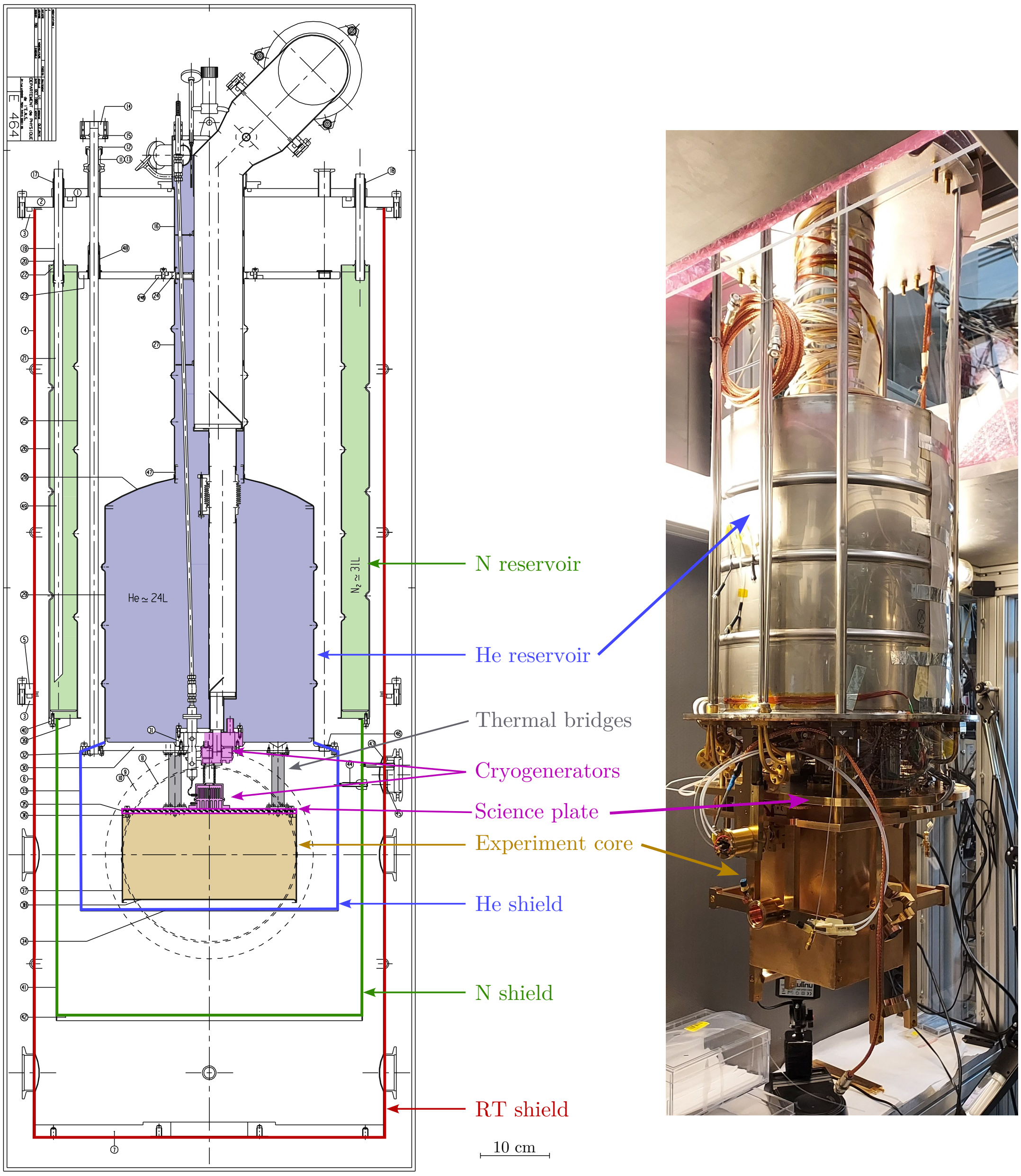

Figure 3.5. – Cryostat technical drawing and picture: the helium reservoir (blue region) is filled with liquid nitrogen to reach 4 K. A helium thermal shield (blue line) is connected to it. A second thermal protection at 77 K is done with a reservoir filled with liquid nitrogen (green region) connected to a N thermal shield (green line). At last, an external shield at room temperature (red line) delimits the vacuum chamber. To reach lower temperatures, the experiment region (yellow) is connected to the science plate. In this plate, ^{4}He and ^{3}He cryogenerators boxes can be used to go below 1 K. Thermal bridges connect the plate to the He reservoir. Note that the cryostat plan corresponds to the previous experiment. The new experiment core being taller, the shields had to be resized accordingly.

Figure 3.6. – Helium and nitrogen shields. Helium shield (blue) is wrapped with cryogenic thermal insulation and is mounted on the helium reservoir. On this picture, the nitrogen shield (green) is not yet covered with insulation and not mounted on the reservoir.

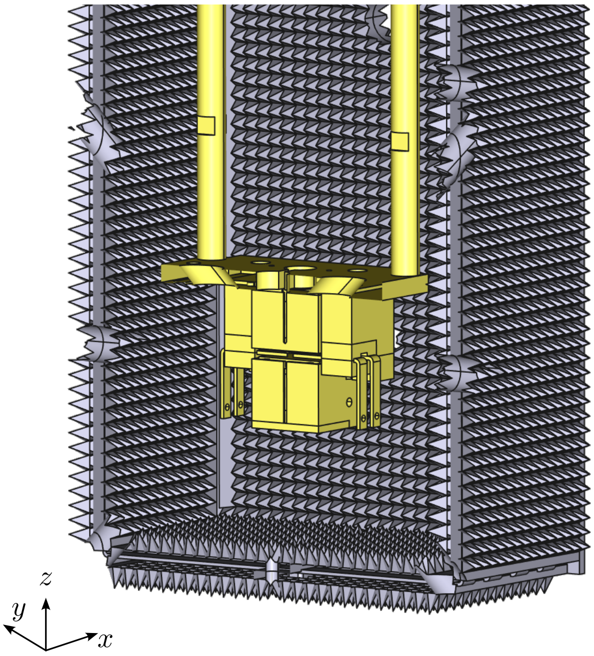

Figure 3.7. – **RAM box** 3D-drawing. A few elements of the inhibition block are represented in yellow for illustration purpose. The RAM box, made of pyramidal structure, ensures a proper microwave thermalisation of the experiment core, while absorbing photons that managed to cross the thermal shields.

required.

One final thing about the necessity of cryogenic cooling: a thermal environment below 1 K is crucial to reach very long atomic lifetimes, but not required for early stages of the experiment. Indeed, the ground state atoms manipulation can be realised with a cooling at 77 K. At this temperature, the coils resistance is low enough that several amperes can be applied without risk and atoms cooling can be performed. Therefore, most of the results presented in this manuscript have been obtained with only a cooling down to 77 K, putting liquid nitrogen in both the He and N reservoirs.

3.1.3. Isolation of the effect of atomic motion

To fully take advantage of their extended lifetimes, circular Rydberg atoms have to be trapped. This is done by means of laser traps using the ponderomotive force. In addition, a good vacuum is required to avoid collisions with background gases that could kick atoms out of the trap. Finally, a holding structure has been designed to ensure the relative stability of the optical system with respect to the experiment core.

Figure 3.8. – Thermal shield windows on the helium shield. Behind the window, a copper plate with holes can be seen, used to screen the external thermal field.

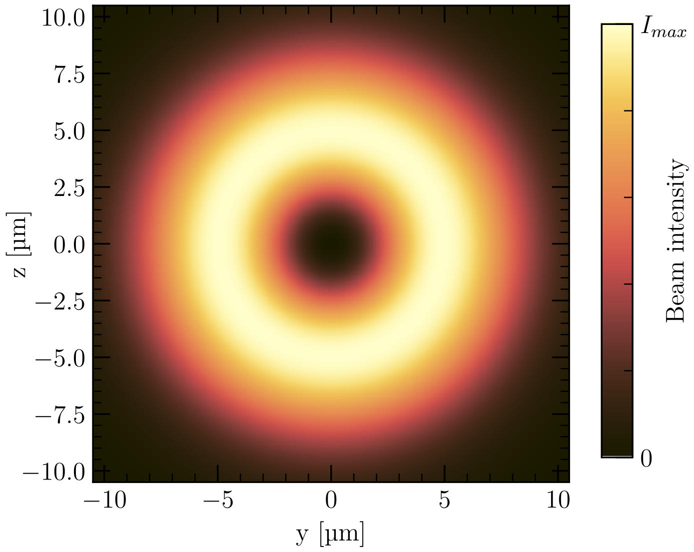

Figure 3.9. – Laguerre-Gauss intensity profile in the plane orthogonal to the propagation axis. Rydberg atoms being low field seekers, they are trapped in the center.

Circular states trapping

In the past decade, a lot of progress has been made in the field of Rydberg atoms trapping. Members of the group especially demonstrated trapping of circular Rydberg atoms a few years ago [80], using ponderomotive trapping.

In the first chapter, expression of the ponderomotive potential has been derived, giving

$$V(\mathbf{r}) = \frac{e^2}{2m_e\epsilon_0 c\omega_L^2} I(\mathbf{r}), \tag{3.1}$$

where ω_L is the laser angular frequency, and $I(\mathbf{r})$ its local intensity. The chosen laser has a 820 nm wavelength. A 1 mK deep trap then requires an intensity of around $14\,\mathrm{mW}\cdot\mu\mathrm{m}^{-2}$.

The ponderomotive trapping potential is always positive, and Rydberg atoms are trapped in the field minima. They are thus called “low field seekers”. The intensity profile thus has to be shaped to create "light walls" within which the atoms will be trapped. This shaping can be done by means of holographic techniques. For this experiment, this will be done with a Spatial Light Modulator (SLM). This device can locally modulate the phase of a wavefront reflected on it surface. This can also be used to correct aberrations, and many more details can be found in the thesis manuscript of Dr. Machu [51].

In another experiment of the group [51, 61, 125], atoms are trapped in bottle beam optical traps. An example of intensity profile for such traps is given in Figure 3.10a. These traps are useful to create arrays of trapped atoms, but their tight focus requires beams with a large divergence.

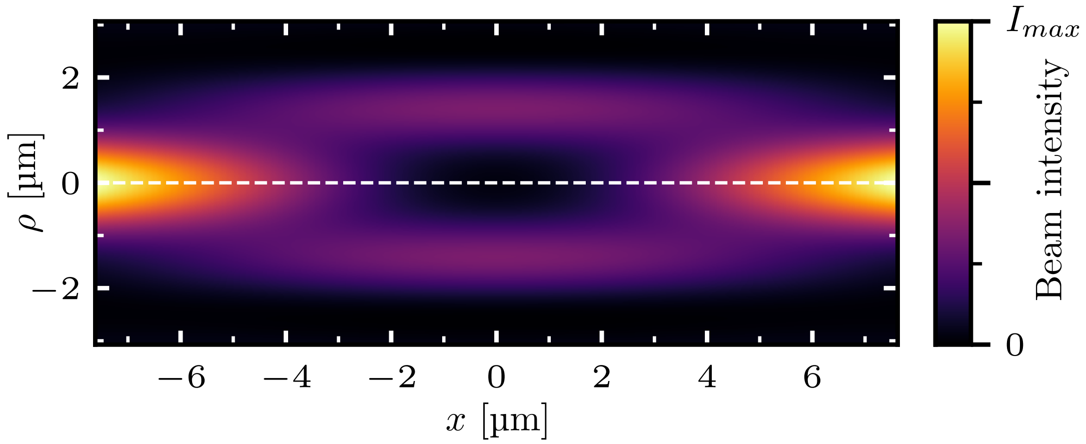

(a) Bottle beam

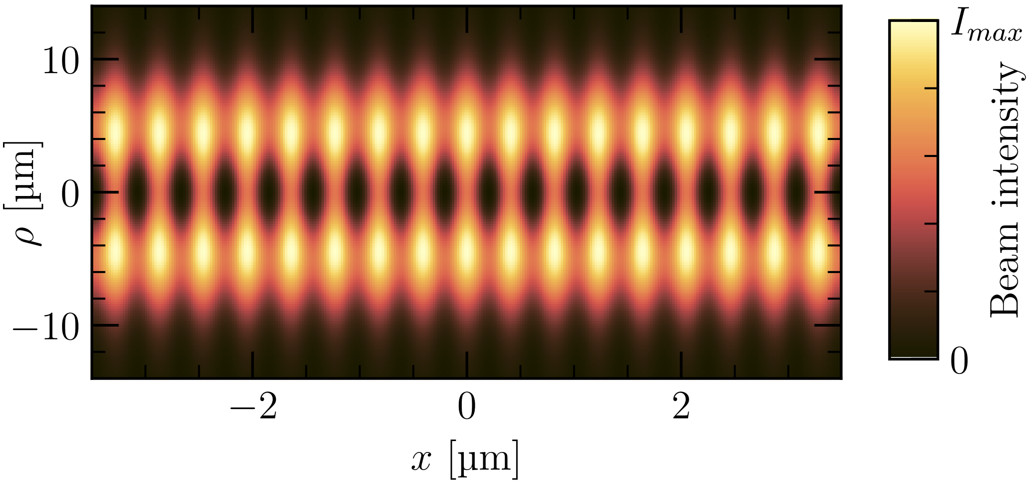

(b) Laguerre-Gauss and standing wave

Figure 3.10. – Rydberg traps intensity profiles for a bottle beam (Figure 3.10a) and Laguerre-Gauss + standing waves configuration (Figure 3.10b). Figure 3.10a is adapted from [125].

For the realisation of an atom chain, another solution has been chosen. Radial confinement of the Rydberg atoms will be provided by a Laguerre-Gauss (LG) intensity profile with a propagation along x given by

$$I_{LG} = P_L \frac{4\rho^2}{\pi w^4(x)} \exp\left\{-\frac{2\rho^2}{w^2(x)}\right\}, \tag{3.2}$$

with P_L the laser beam power, $w(x) = w_0\sqrt{1 + x/z_R}$ the waist profile, w_0 the waist size at focus point, z_R the Rayleigh length and ρ, x the cylindrical coordinates. The LG profile in a plane orthogonal to the propagation axis is depicted in Figure 3.9.

Axial confinement is provided by the addition of two counter-propagating beams, which interfere, hence creating a standing wave. The same trap is used for ground state atoms trapping and more details are given in chapter 5. The intensity profile provided by the overlap of the LG beam with the standing wave is given in Figure 3.10b. To avoid leaks between trapping sites, the waist of the LG beam has to be smaller than the waist of the standing wave beams. Respective designed values are 7 μm and 12 μm. Details about the optical setup used for both traps can be found in Appendix D.

The LG and standing wave traps are both generated with the same 820 nm laser. To avoid interference between the two traps, their polarisation are set to be orthogonal. Given the 7 μm waist for the LG beam, obtention of a 1 mK trap depth requires a laser power around 2.9 W. For the standing wave, such trap depth requires a total power 1.8 times smaller. [3] The standing wave is also used to trap the ground state atoms, which are trapped in the intensity maxima. Consequently, the intensity maxima and minima have to be inverted when going from ground state to Rydberg state atoms. This means that a π phase shift has to be applied to the standing wave.

High vacuum

The trapping time of atoms strongly depends on the vacuum inside the experiment core, since collisions with residual background gases can kick the atoms out of the traps. The required ultra-high vacuum inside the cryostat is obtained by a combination of a turbo-molecular pump with cryopumping. The vacuum is measured on the outer room-temperature shield and is found to be around 2×10^{-8} mbar. No vacuum gauge is present inside the experiment core, and the vacuum is therefore not directly measured.

The cryopumping efficiency is better for lower temperatures and is closely related to the evolution of vapour pressure with temperature [126]. It is represented in Figure 3.11 for usual gases present in the air. This evolution shows that for a nitrogen cooling at 77 K, cryopumping can bring the residual pressure below 1×10^{-8} mbar but only for part of the air components. However, helium cooling at 4 K will cryopump more species and will therefore be more efficient. As a result, a much better vacuum is expected within the N shield, and an even better one within the He shield.

For the results presented in this manuscript, the experiment was cooled down to 77 K. The resulting vacuum was probably one of the main limitation for the measured trapping times, which were however good enough for the studies performed. Once circular Rydberg atoms are obtained, the helium shield will be cooled down to 4 K. This will improve the cryopumping efficiency, and, with it, longer trapping times are expected.

---

[3] For the LG trap, the depth is given by the maximal intensity which reads $I_{LG}^{max} = 2P_L/e\pi w_0^2$ because of the trap geometry.

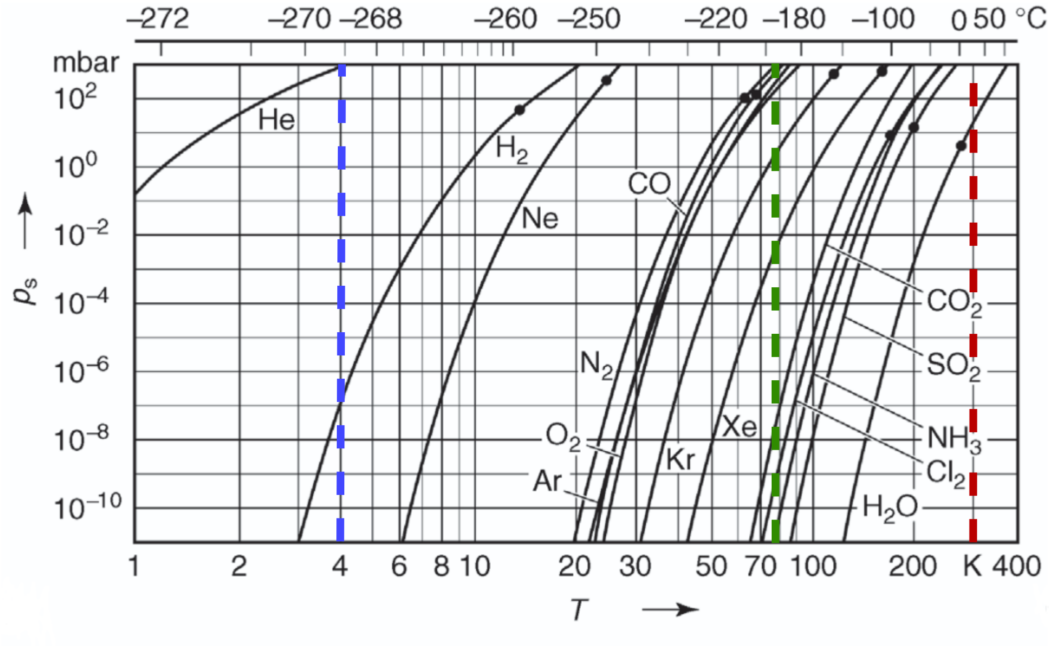

Figure 3.11. – **Vapour pressure of residual gases** for different temperatures. The different shield temperatures are highlighted, corresponding to room temperature (red), nitrogen temperature (green) and helium 4 temperature (blue). Figure adapted from [126].

Relative stability

Obtention of the standing wave with a maximal contrast requires a laser beams alignment with an interferometric precision. For the designed optical setup, some elements are directly mounted inside the cryostat. The relative stability between these elements and the ones mounted outside the cryostat, mounted on an optical table, need to be ensured. To do so, the structure holding the optical table needs to be connected to the structure holding the cryostat. In addition, it should be possible to disconnect-reconnect the optical table from the cryostat in case the latter needs to be opened for corrections. Ideally, this operation should not disturb the optical alignment.

With all this constraints in mind, a structure has been designed and is shown in Figure 3.12. It is made of two sub-structures, one for the cryostat and one for the optical tables. Locating pins ensure that the correct relative positioning of the sub-structures is recovered when they are re-attached together. The optical table is separated into two sub-tables. When the cryostat is to be opened, the small table can be taken out, which allows for the larger table to be removed from around the cryostat.

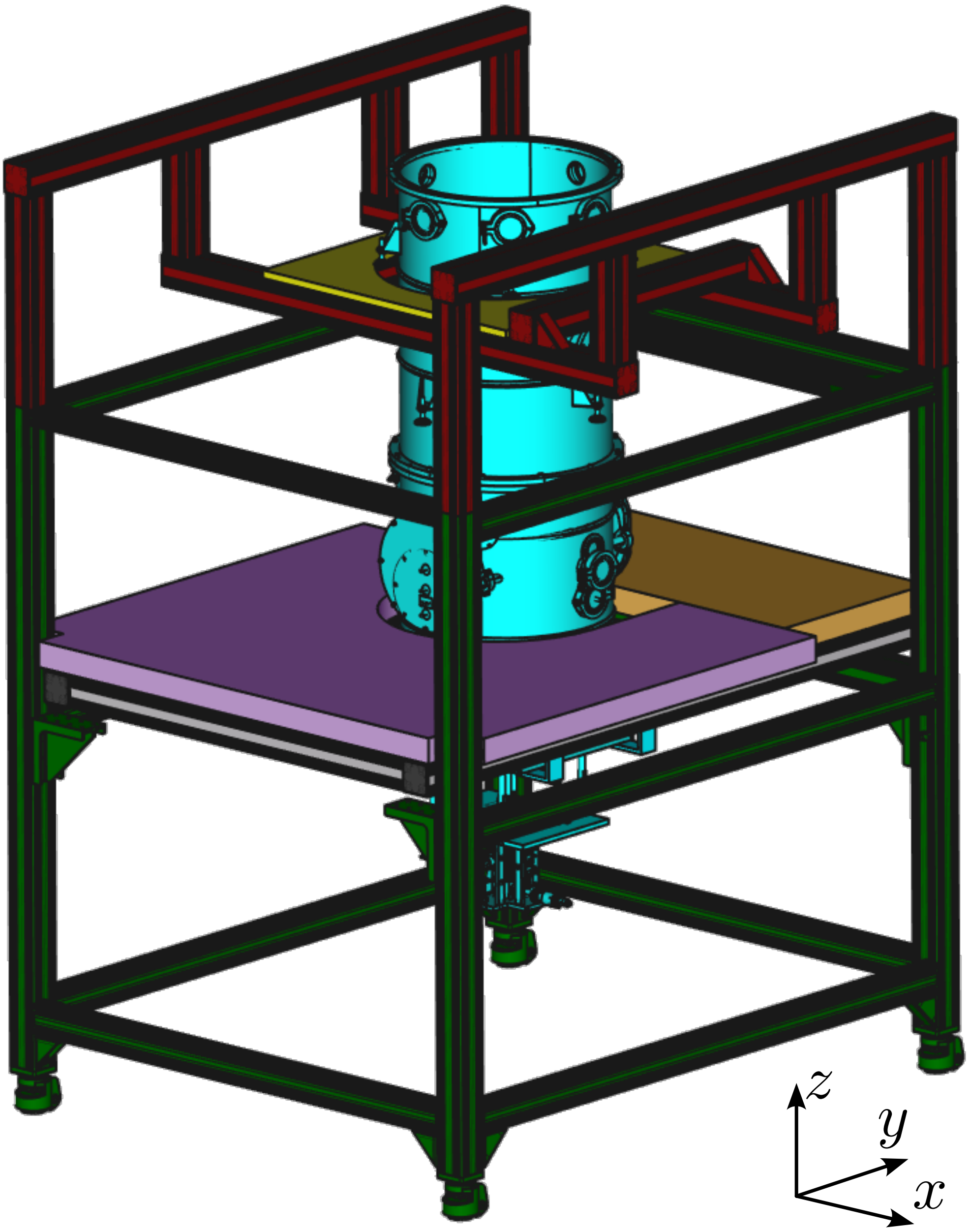

Figure 3.12. – Cryostat and optical support holding structure: the cryostat (light blue) is attached to an aluminium structure (red) through an aluminium plate (yellow). This structure sits on pneumatic isolators that are not depicted here. Optical tables (pink and orange) sit on a second aluminium structure (green). The two aluminium structures can be connected together, such that the red one lifts the green one, then disconnected from the floor. The orange optical table can be removed.

3.2. Circular Rydberg atoms preparation

In the previous section, experimental details about how to get the inhibition setup in a cryogenic environment and with a good control of trapped atoms position have been provided. However, observation of extended lifetimes of circular Rydberg states requires for these states to be efficiently prepared.

These states have been known and used in the group for several decades, providing considerable experience about their generation [5]. The challenge of this experiment relies on the obtention of an efficient preparation without affecting the isolation required in the inhibition region.

This section will be divided in two parts. The first one will detail the experimental setup used to prepare circular Rydberg states from ground state atoms in the inhibition region. The second will give an overview of the setup used to bring ground state atoms to the experiment core.

3.2.1. Circular Rydberg states excitation

Preparation of circular Rydberg state can be divided in four steps. An overview of the different steps is depicted in Figure 3.13. The first step is the Rydberg excitation. A succession of frequency locked laser excitations brings the atoms in the target Rydberg state $|52f,|m|=2\rangle$. Once the atom is excited in the Rydberg state, a static electric Stark field is applied to lift the degeneracy between the different states and adiabatically prepare $|n=52,m=2,k=-47\rangle$.

From this state, the circularisation to the state $|52C\rangle$ can take place, using the adiabatic passage technique discussed in subsection 1.3.2. Finally, microwaves can be used to transfer the population to a lower circular state $|51C\rangle$. A strong electric field can then be applied to ionise all states for which $n=52$, to purify the sample from all elliptical states contamination. This section will be dedicated to the experimental implementations designed to perform these steps.

Rydberg excitation

The first step towards circular Rydberg states preparation is the Rydberg excitation. A three-stage excitation of ^{85}Rb has been chosen. The first laser beam is resonant with the $\left|^5S_{1/2},F=3,m_f=3\right\rangle \rightarrow \left|^5P_{3/2},F=4,m_f=4\right\rangle$ transition, at 780 nm. The presence of a repumper beam is required to avoid depumping in the $\left|^5S_{1/2},F=2\right\rangle$ state. [4] The second

---

[4] The repumper beam is discussed in more details in chapter 4.

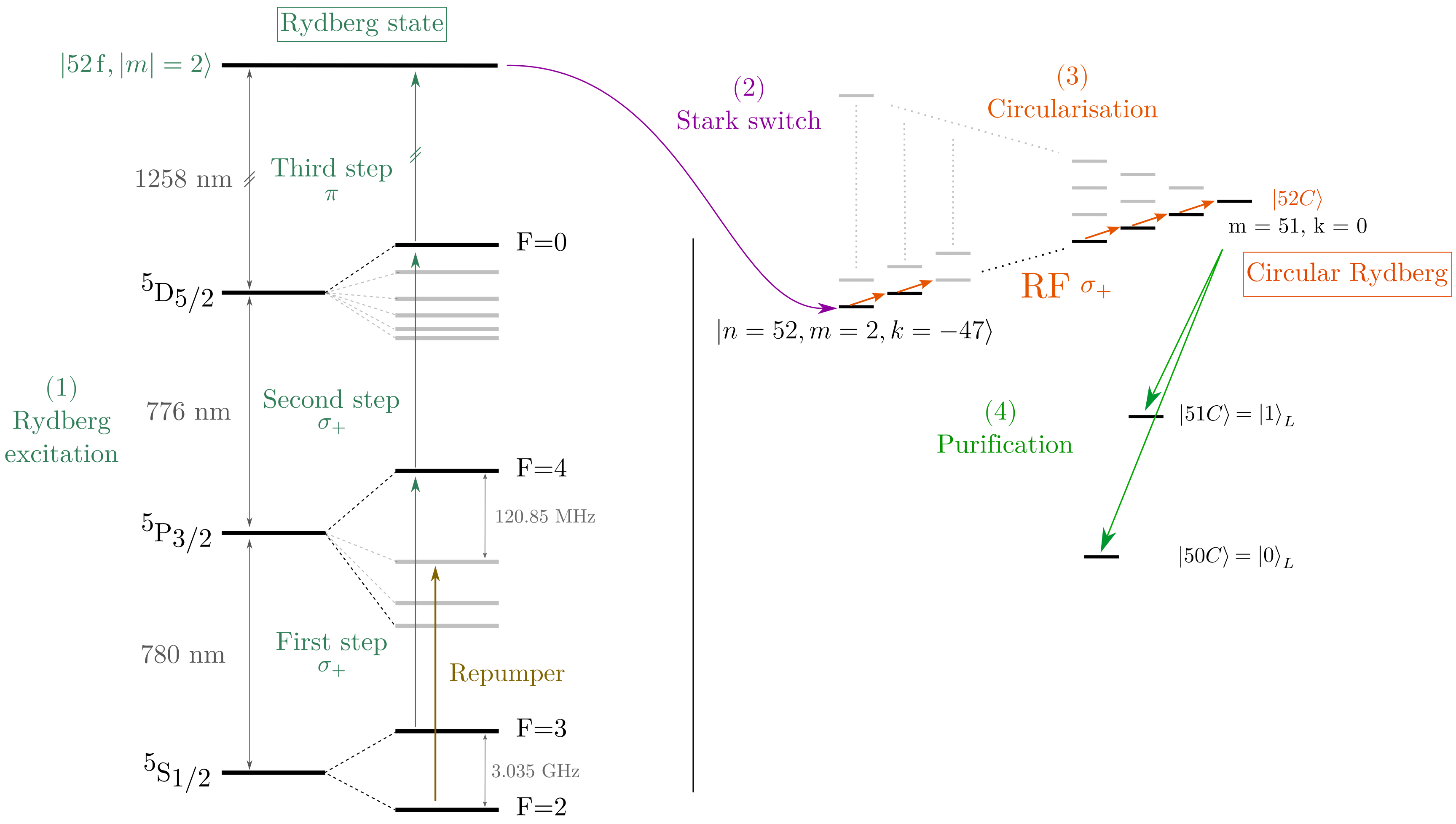

Figure 3.13. – **Circular Rydberg state preparation scheme:** the first step is the Rydberg excitation, by successive resonant excitations to the state $|52f, |m| = 2\rangle$. A Stark shift is applied to adiabatically transfer the population to the state $|n = 52, m = 2, k = -47\rangle$. Circularisation then takes place to the circular state $|52C\rangle$, using a circularly polarised radiofrequency. Population is then transferred to the state $|51C\rangle$ using microwaves. All states of higher energy can then be ionised to get rid of other states contamination. States $|50C\rangle$ and $|51C\rangle$ can be used as the logical qubit states $|0L\rangle$ and $|1L\rangle$ for quantum simulation.

excitation is resonant with the $\left|{}^5P_{3/2}, F=4, m_f=4\right\rangle \rightarrow \left|{}^5D_{5/2}, F=5, m_f=5\right\rangle$ transition, at 776 nm. The last step excites the $\left|{}^5D_{5/2}\right\rangle \rightarrow |52f, |m|=2\rangle$ transition, at 1258 nm.

In that scheme, the two first transitions are σ_+ polarised and the last one is π polarised. This ensures that the final state prepared has $m=2$, which is critical for the circularisation, as discussed in subsection 1.3.2. In practice, it means that the polarisation of each beam has to be properly set, by means of quarter and half waveplates. For practical reasons, the three excitation beams are overlapped prior to entering the cryostat. The corresponding optical setup is given in Appendix D. In addition, the frequency of each laser beam needs to be precisely locked to the associated transition. Details on the locking schemes can be found in Appendix C.

A hole in the inhibition block, visible in Figure 3.2, is used to address the atomic sample in between the two inhibition plates. Laser excitation is typically switched on for around $1\,\mu$s in order to excite atoms to the Rydberg states. A key aspect here is the number of excited atoms per trapping pocket. The target ground state atoms trapping region is around $10\,\mu$m in its largest direction. In this range, the dipole-dipole interaction between Rydberg atoms can prevent simultaneous excitation of two atoms which are close to one another. This effect is known as dipole blockade and is often used to control the number of excited atoms, as well as to perform logical gates [127]. This effect will have to be carefully considered to excite the right amount of atoms, especially since the atoms can move within the trap.

Circularisation

Once atoms are in the highly excited state $|52f, m=2\rangle$, the next step is to give the electron additional angular momentum until it reaches the circular state. This operation is called circularisation, and was theoretically introduced in section 1.2.3.

The first step of the circularisation is to adiabatically branch the spherical state $|52f, m=2\rangle$ to the parabolic state $|n=52, m=2, k=-47\rangle$ until it joins the lowest diagonal of the manifold. This is done with a Stark field, $F_{Dir} \approx 2.4\,\mathrm{V}\cdot\mathrm{cm}^{-1}$ [5], along the $+z$ direction [128]. This electric field is obtained by applying a potential of around -0.48 V on the upper inhibition plate while keeping the lower one grounded. By construction, this also sets the right orbit orientation for the inhibition.

The second ingredient required for circularisation is a mean to produce a circularly polarised σ_+ radiofrequency (RF) field. This can be realised using four electrodes around the atoms. Since the inhibition structure also suppresses RF fields, electrodes have to be put directly in between the plates. Their thickness is 1 mm. To limit the

---

[5] The Figure 1.4 shows that the state joins the multiplicity for a field of around $0.2\,\mathrm{V}\cdot\mathrm{cm}^{-1}$. Here the value is higher to tune the resonance frequency of the adiabatic passage.

electrodes effect onto the inhibition efficiency, their shape has been adjusted in a circular shape such that the atoms are equidistant from all electrodes surfaces, as shown in Figure 3.14. The electrodes are gilded, and made of bronze so that their end can be bent to facilitate their wiring. To ensure their right positioning, they are embedded in electrical insulator blocks. The latter are made out of ceramic material (macor). [6]

To generate the circularly polarised RF field, the method is the following. Using each diagonal pair of electrodes, it is possible to generate two orthogonal electric field F_1 and F_2 in the Oxy plane. Changing the potential of the electrodes with time allows one to make these fields oscillate, with a chosen frequency ω_{RF} such that $F_i(t) = F_{RF}\sin(\omega_{RF} t + \varphi_i)$.

Finally, choosing the dephasing between the two fields to be $\Delta\varphi = \varphi_2 - \varphi_1 = \pi/2$ allows one to generate the desired σ_+ polarised radio-frequency. In practice, the relative phase and field amplitudes have to be fine-tuned to compensate for the electrodes geometry if the produced fields are not exactly equal in amplitude or orthogonal.

For a Stark field of around $2.4\,\mathrm{V\cdot cm^{-1}}$, the energy splitting in the lower diagonal is slightly above $2\pi\times$ 230 MHz, which is the chosen RF dressing frequency. For the amplitude, a field of around F_{RF} $=1.5\,\mathrm{V\cdot m^{-1}}$ should provide a Rabi frequency of around $\Omega_{RF} = 2\pi\times$ 10 MHz[70]. The dressing has to be switched slowly enough to satisfy the adiabaticity condition given in Equation 1.56. The Stark field can then be decreased to $2\,\mathrm{V\cdot cm^{-1}}$, to cross the resonance frequency and perform the adiabatic passage, the crossing being around $2.36\,\mathrm{V\cdot cm^{-1}}$ for such dressing frequency [128].

In addition, a static magnetic field along the $+z$ direction can be applied to increase the circularisation efficiency. It adds a m dependent energy shift to the Stark shift, which allows one to reduce the effect of a possible σ_- Rf field contamination. A field of around 10 G would be enough [70]. Optimal control techniques can also be used as a shortcut to adiabaticity to speedup the circularisation sequence [129]. In practice, circularisation can be performed with efficiencies above 98%.

Microwave transfer between circular states

Transfer between circular states can be driven using microwave fields, with frequencies of around 50 GHz for $n \approx 50$. For the proposed simulator, this is used to engineer the target Hamiltonian. In the short run, this can be used to purify the atomic sample from elliptical state contamination.

The circularisation is efficient but not perfect, and it is usually preferable to only keep atoms that are prepared in a given circular state and to get rid of atoms wrongly

---

[6] Another insulator usually used is sapphire, which is harder to machine.

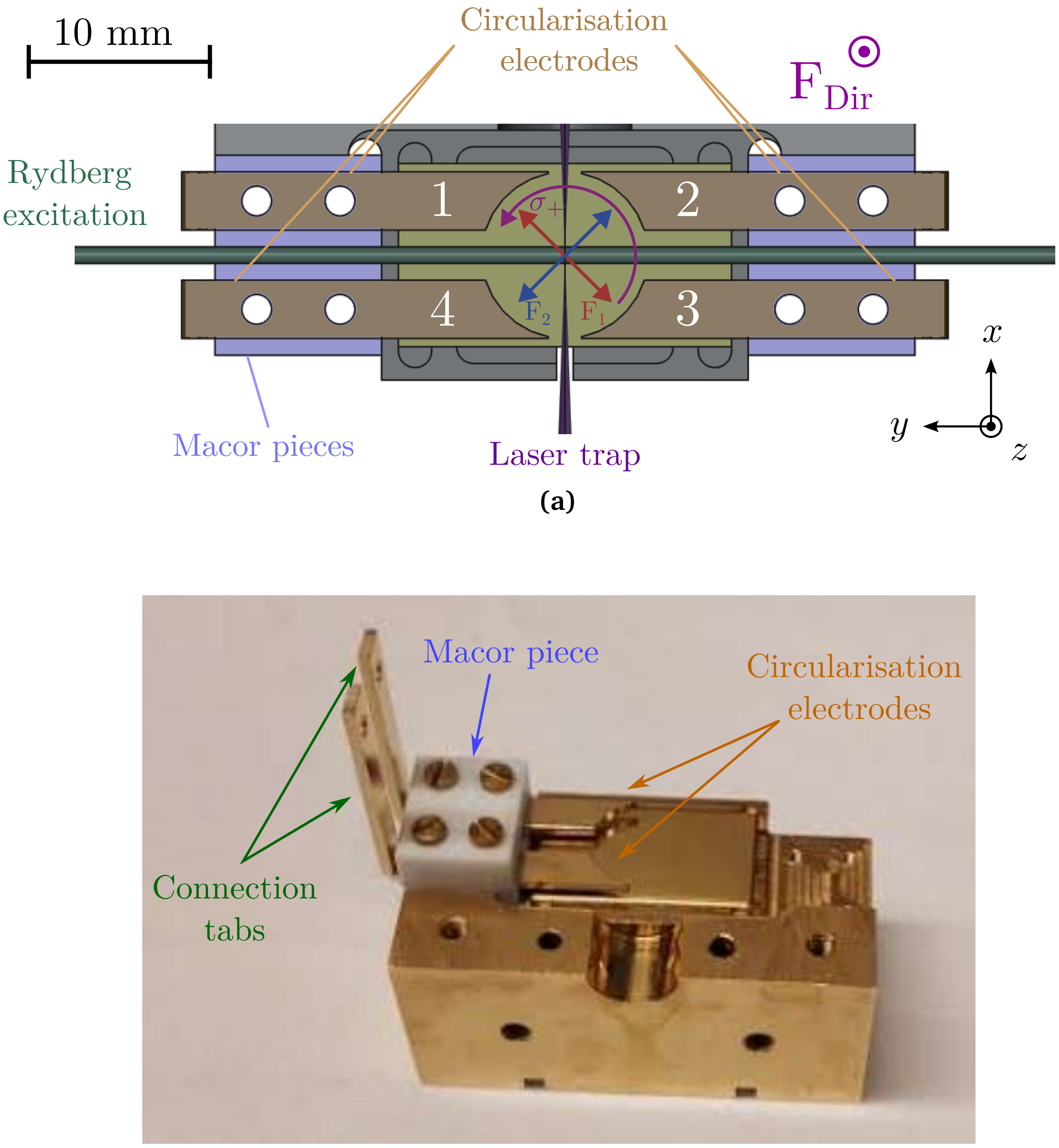

(a)

(b)

Figure 3.14. – Circularisation electrodes. Figure 3.14a shows a technical drawing, where the electrodes labelled from 1 to 4 and depicted in orange. Applying voltage on the odd and even pairs allows one to create two electric fields F_1 and F_2. Making these fields oscillate in quadrature phase creates the target σ_+ polarised field. The lower inhibition plate is visible in yellow, and the Rydberg excitation and trapping laser beams are in teal and purple, respectively. Electrodes are embedded in a holding block (grey) surrounded by macor pieces (lavender) for electric isolation. Directing field F_{Dir} direction is also indicated. Figure 3.14b shows a picture of the electrodes with only two electrodes mounted. Electrodes are embedded into macor pieces to ensure good positioning and electric isolation. The end of each electrode is elongated and bent to create a connection tab, in order to facilitate their wiring.

prepared in elliptical states. To do so, one technique is to transfer the circular state population to a lower circular state, and then to ionise all elliptical population remaining in the initial multiplicity. Starting from $|52C\rangle$, it means transferring the population to $|51C\rangle$ with a 51 GHz microwave drive and then ionising the $n = 52$ multiplicity. Ionisation of this multiplicity is realised by applying an electric field of around $-120\,\mathrm{V\cdot cm^{-1}}$ [62].

The issue for circular to circular transfer is that the inhibition plates suppress the microwave field corresponding to such transfers. Nevertheless, one way to circumvent this issue is to drive the atoms with evanescent fields. One first possibility is then to have a waveguide output in the experiment core, but still outside the inhibition region. With a powerful enough drive, an evanescent field can exist in between the plates and drive the atoms. A similar method has been used to drive the cavities in CQED experiments without reducing their quality factor [5]. The drawback of this method for atoms is that the control over the field polarisation is limited. This could possibly lead to an unwanted drive of π transitions.

A second possible solution is to use an evanescent field across a thin layer of conductive material. [7] For this configuration, illustrated in Figure 3.15a, the bottom inhibition brass plate is replaced by a gilded sapphire plate. In the center of the plate, the gold layer is made thinner and is around a few tens of nanometres. A waveguide is inserted in the inhibition block, such that its output touches the plates. When a microwave drive is sent inside the waveguide, it generates an electric field inside the plate. At the position where the gold layer is thinner, an evanescent field can go through and reach the atoms.

Numerical simulations have been performed to study the feasibility of this solution, using *CST studio suite*. The field required to drive the atoms should have components along the y and x directions to drive σ transitions, but not along z to avoid driving π transitions. Example of fields obtained along z and y in the plate are depicted in Figure 3.15b, for a driving at 51 GHz. In this example, the resulting field has no z component in front of the atoms position.

For this preliminary study, the resonant modes of the plates have been studied. Indeed, the presence of resonant modes in the sapphire plate can change the field spatial structure inside the plate. For resonance modes of the plates, the evanescent field at the atoms position can be considerably increased, reduced or along the wrong direction. This makes the atoms drive for different frequencies non-controllable near resonance modes of the plates.

Examples of modes spatial structure for different frequency drive are given in Fig-

---

[7] This solution has not yet been implemented, but preliminary studies have been performed and are discussed here.

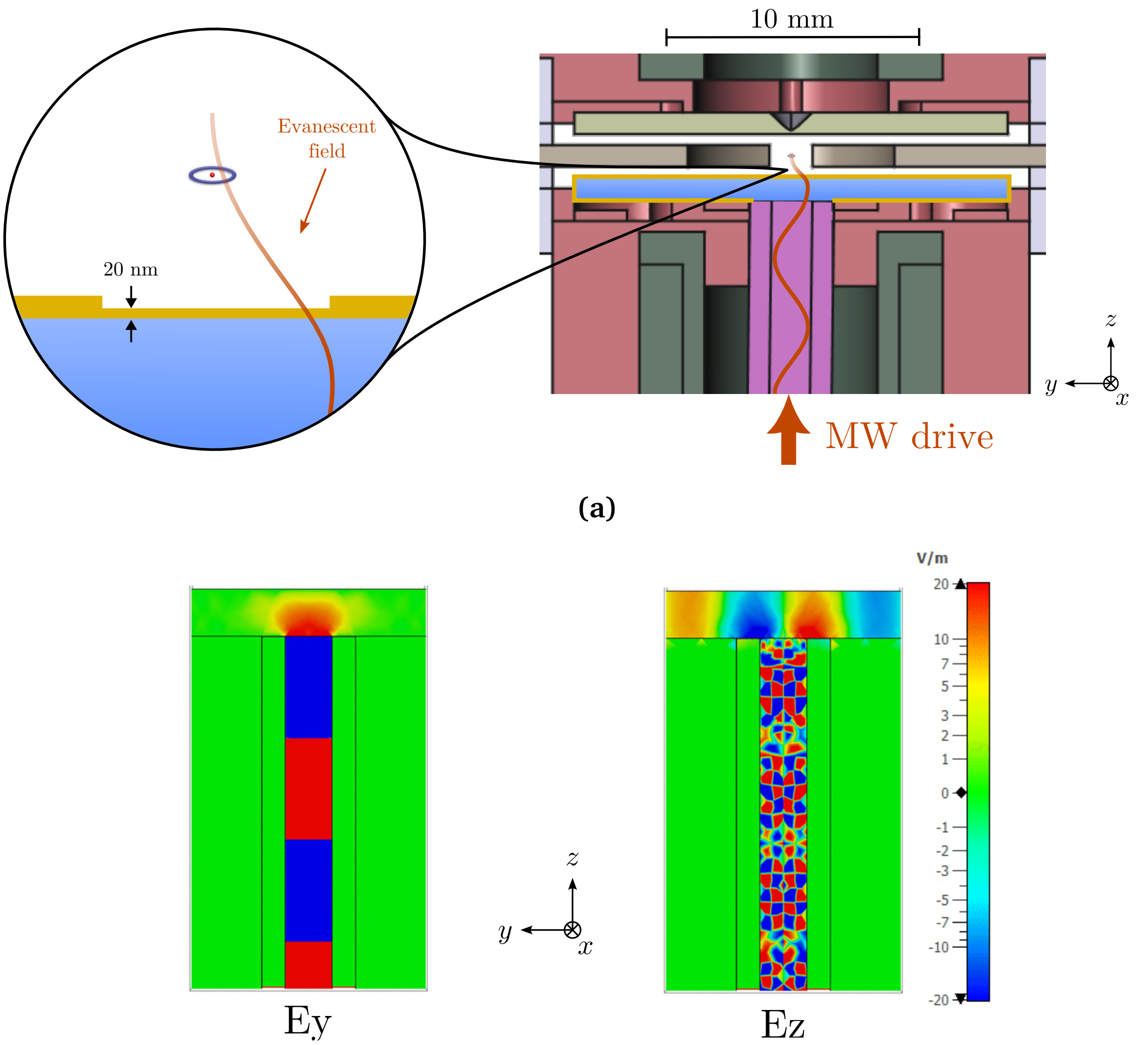

(a)

(b)

Figure 3.15. – Microwave driving through a plate made of sapphire and coated with gold. Figure 3.15a illustrates the general principle. The zoomed diagram is not at scale. A MW drive is sent through a waveguide and generates a field inside the plate. The plate gold coating is made thinner (∼20 nm) at the atoms position to allow the evanescent field to go through. Figure 3.15b shows simulation results examples for a drive at 51 GHz. In the center, in front of where atoms are supposed to be, some E_y component exists inside the plate, whereas no E_z component exists. The field in the plate then creates an evanescent field at the atoms position, where the gold layer is thinner.

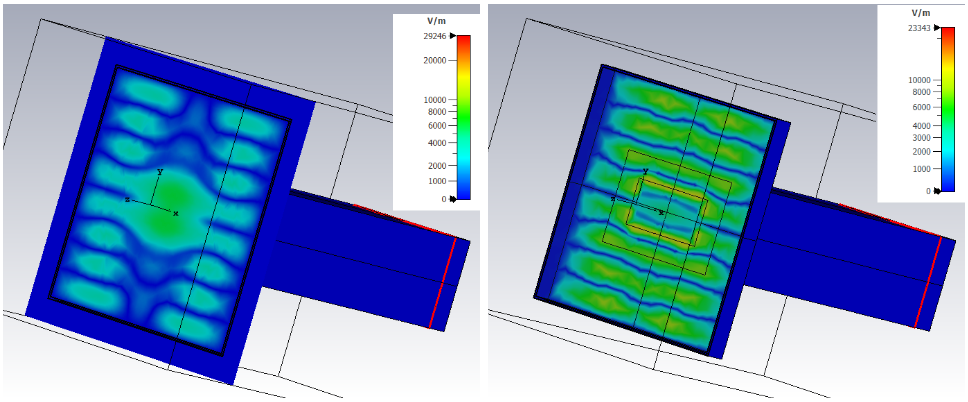

(a) 51 GHz **(b)** 50.23 GHz

Figure 3.16. – Spatial structure of the field in the plate. The field amplitude is given for two different driving frequencies. In Figure 3.16a, no resonant mode exists in the plate, and the field maximum is in the plate center, at the waveguide exit. However in Figure 3.16b, a resonant mode is driven, leading to a different spatial structure, where the field at the atoms position is weaker. Note that in this example, the plate has a square geometry, which is not the final geometry.

ure 3.16 for a square glass plate. [8] For a drive at 51 GHz no resonant mode of the plate is driven. The field maximum is at the waveguide output position, in front of the atoms, as shown in Figure 3.16a. The interference structure are visible but don't affect much the field in the center. For a drive at 50.23 GHz, a resonant mode of plate is driven. As a result, the field in front of the atoms is reduced. In this figure, only field amplitude is represented, but the resonance structure can also affect the field direction.

In order to avoid such resonant effect, preliminary optimisations have been realised on the plate geometry to have a mode-free range at around 51 GHz. A study of the plate response to a microwave driving is depicted in Figure 3.17, for a 20 mm × 10 mm × 1.4 mm glass plate. The frequency region between 50 GHz and 52 GHz is found to be free of resonant modes and is thus available for atoms manipulation.

3.2.2. Ground state atom manipulation

The experiment starts with the deterministic delivery of ground states atoms, ready to be excited to a circular Rydberg state, between the inhibition plates. The atomic species used is ^{85}Rb.

Different solutions are possible to have ground states atoms in a given region of the experiment. One example is the use of a dispenser which directly injects rubidium vapour in its surroundings. However, this can lead to uncontrolled deposition of rubidium atoms on the experiment surfaces, inducing an electric field in-homogeneity

---

[8] This doesn't correspond to the designed inhibition plates.

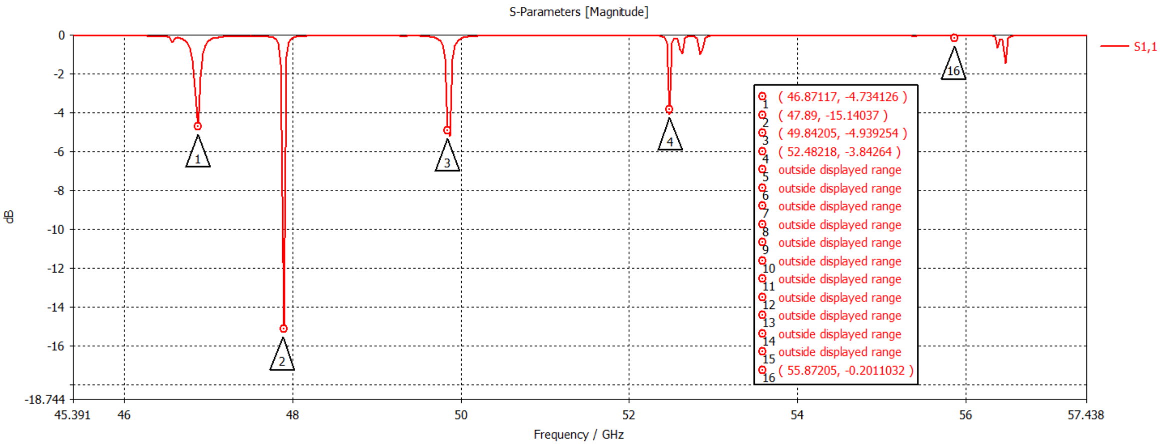

Figure 3.17. – **S-parameter for a glass plate** with dimensions 20 mm × 10 mm × 1.4 mm. For this simulation, a dip in the S parameter magnitude corresponds to a resonant mode. For this geometry, no mode is identified between 50 GHz and 52 GHz.

as observed in [70].

To avoid such issues, the solution chosen here was to use an atomic fountain to generate an atomic beam with a small divergence angle. Atoms from the beam are then cooled down further with a three dimensional magneto-optical trap (3D-MOT). The latter is placed outside the inhibition region to have a better optical access and avoid rubidium deposition on the inhibition plates. Atoms then need to be transported between the two plates. The chosen solution is a dipole trap in a conveyor belt configuration.

This section provides an overview of these different steps. An emphasis will be put on the constraints imposed by the inhibition setup, and the solutions chosen to circumvent them. The detailed study of their implementation and obtained results will be the subject of chapter 4 and chapter 5.

Atom source

The vertical atomic fountain is provided by a two-dimensional magneto optical trap (2D-MOT). A combination of red-detuned lasers with a well controlled magnetic field allows one to cool down the atoms in the two horizontal directions, leaving the third one unaffected. As a result, it creates an atomic beam in the vertical direction. Note that only atoms with a vertical velocity of around $20\,\mathrm{m\cdot s^{-1}}$ are efficiently slowed down in the horizontal directions, hence defining the velocity of the atoms of the beam.

In practice, a commercial device provided by the SYRTE laboratory from the Paris-PSL Observatory has been used, and is discussed in more details in section 4.3. In order to get the initial atomic vapour in the 2D-MOT chamber, a cell filled with rubidium is

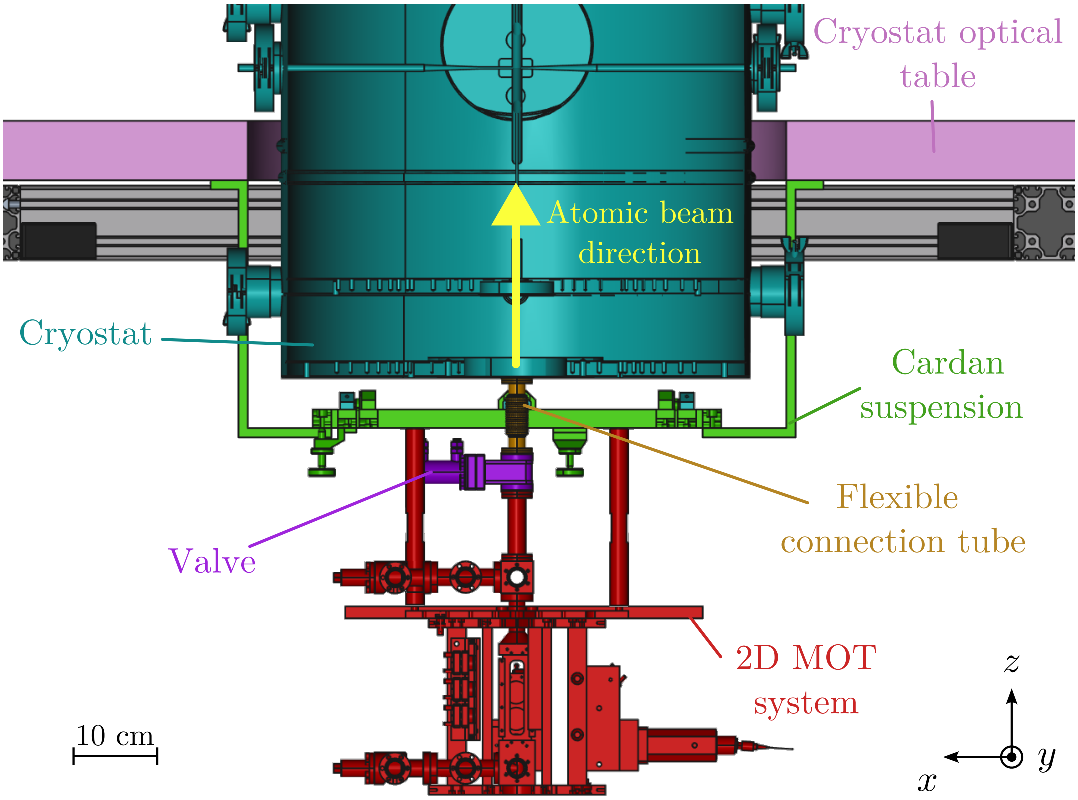

Figure 3.18. – 2D-MOT connection to the cryostat. The 2D-MOT (red) is connected to the cryostat (blue) through a flexible tube (orange). This connection can be closed by a valve (purple). To ensure a stable positioning, it is attached to the cryostat optical table (pink) by a holding structure with a gimbal (green). Together with the flexible tube, they allow for the control the 2D-MOT orientation to align the atomic beam with the 3D-MOT position.

heated up. A vacuum of around 6×10^{-9} mbar inside the 2D-MOT chamber is obtained with an ionic pump.

The 2D-MOT is connected to the bottom of the cryostat, such that the atomic beam enters the cryostat in the $+z$ direction, Figure 3.18. It is connected to the cryostat through a flexible tube, allowing for more freedom in the 2D-MOT alignment. A valve is used to disconnect the cryostat and 2D-MOT vacuum chambers without breaking the 2D-MOT chamber vacuum when the cryostat needs to be openned.

To ensure a reproducible positioning, the 2D-MOT is attached to the cryostat optical table. A cardan suspension is used to fine tune the atomic beam direction. In this configuration, only the flexible tube has to be disconnected and reconnected when the cryostat has be to opened, which ensures good reproducibility. Indeed, the atomic beam has to be aligned so that it is sent to the 3D-MOT position above the 2D-MOT output. The required precision of this alignment is defined by the beam divergence, and, in practice, is not critical.

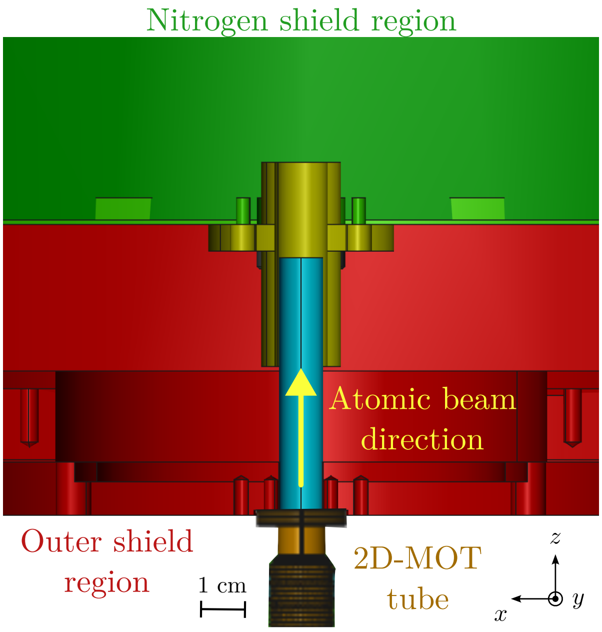

Figure 3.19. – Nested tubes for vacuum isolation between the nitrogen (green) and room temperature (red) regions. A first tube (blue) enters the 2D-MOT tube and the room temperature region. A second tube (yellow) is placed around the first one and goes out inside the nitrogen region. To go from the room temperature region to the nitrogen region, residual gas would need to go through the gap in between the two tubes instead of simply going through an open hole.

To reach the 3D-MOT, the atomic beam has to cross the three thermal shields, as seen in Figure 3.5. Holes had to be cut in the shields, and adjustments had to be made on the outer part of the cryostat. The vacuum is expected to be better within the helium shield and 2D-MOT region than in the other regions. To decouple the vacuum between the different regions, a combination of nested tubes has been designed, allowing for differential pumping. The associated design is depicted in Figure 3.19.

Atom cooling

The atomic jet is the first step to get trapped ground state atoms. Once atoms reach the experiment core, they are trapped and cooled down to around 10 μK with a 3D-MOT. [9] Such a trap requires an optical system combined with a well-controlled magnetic field. This section presents the design of the 3D-MOT setup, constrained by the inhibition setup. Experimental results associated to the successful cooling of atoms are detailed in section 4.4.

The required optical system is a set of three pairs of counter-propagating beams. To ensure a three-dimensional cooling, the pairs are along three orthogonal axes. The

---

[9] More precisely, atoms sub-Doppler cooling is realised by a combination of different 3D-MOT conditions and molasses cooling. The same optical (and imaging) system is used for all of these steps.

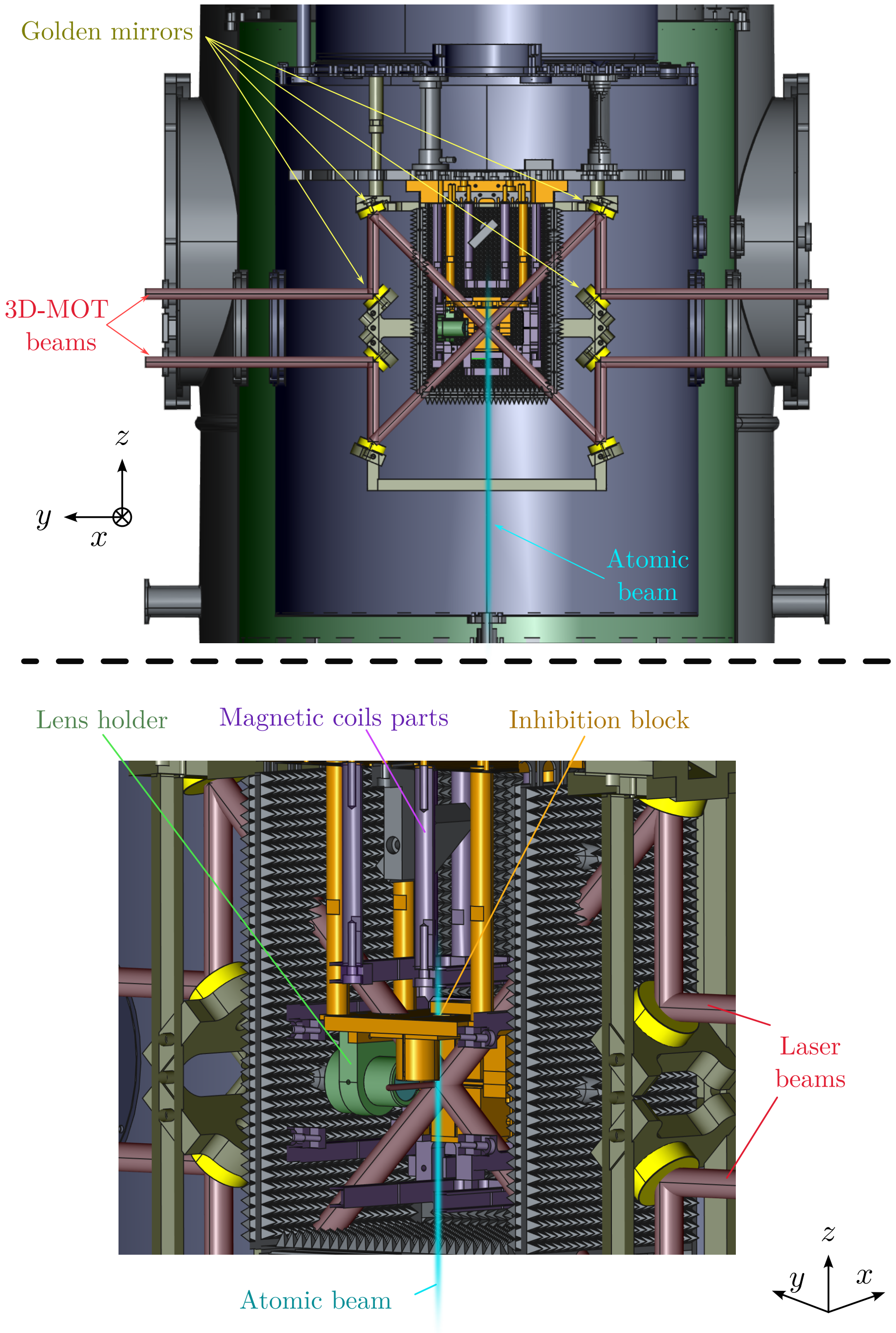

Figure 3.20. – 3D-MOT laser configuration: the top panel shows a cut in the Oyz plane, the bottom one shows a closer view from the side, with the same cut. On the top panel, laser beams are indicated in red, with a 1 cm diameter. A frame with gilded mirrors (yellow) has been designed to set the right geometry inside the cryostat. Inhibition block (orange) and atomic beam (cyan) are depicted as well. The bottom panel shows a closer view, to illustrate the geometrical constraints. The beams have to go through the magnetic coils structure (purple), in between coils of the inhibition block (orange) and the imaging lens holder (green). Holes had to be made in the RAM box, and the different thermal shields as well. These views includes many elements on purpose, and lighter views are to be found in chapter 4.

capture range of the trap, and with it the atom number, increases with the beam size. However, larger beams require larger openings in the thermal shields, which increases the amount of BBR leaking to the atoms. Finally, laser beams need to be circularly polarised.

The three directions chosen for the laser beam pairs are the x axis and two orthogonal directions in the Ozy plane at ±45°, as shown in Figure 3.20. Beams along the x axis are going through the inhibition region. Their beam size has then to be smaller than 2 mm to fit between the plates. In addition, these beams share optical elements with the 820 nm trapping beam. For the beams along ±45°, called transverse beams, optical access is larger and beam size is around 7 mm.

In order to keep a simple and compact optical system outside the cryostat, all beams enter the cryostat parallel to the optical table. The deflection of the transverse beams is then done directly inside the cryostat. To do so a frame with gilded mirrors has been designed to set the transverse beams geometry directly inside the experiment core, as depicted in Figure 3.20. Mirrors are made out of copper to get a better thermal conductivity and were gilded by evaporation, like for the inhibition plates (see Appendix A).

Finally, the different thermal shields and the RAM box have to be crossed by the laser beams. The number of beams being way larger than for the previous experiments, additional holes had to be cut. In order to avoid infiltration of BBR to the atoms, these openings were chosen to be as close as possible to the beam size. This constrained the optical access, and induced parasitic light which made the obtention of the first 3D-MOT signals particularly challenging.

The magnetic field required for the 3D-MOT is a gradient along each laser-pair direction, together with a zero field at the crossing of the laser beams. Such gradients configuration can be obtained with a quadrupole field. In practice, it can be realised by setting two coils in a anti-Helmoltz configuration along the x axis. Since the experiment core is isolated from the fields outside the cryostat, the coils have to be put inside the cryostat. To reduce the current required for the obtention of a given field, the coils are put as close as possible to the atoms, inside the RAM-box.

A first set of coils designed for this purpose is depicted in Figure 3.21, and referred to as the "large" coils. The coils size is chosen to generate a field as homogeneous as possible at the atoms position. Additional coils pairs are put along y and z directions to allow for bias field correction. For later stages of the experiment, magnetic field in between the plates will have to be controlled as well. A magnetic field along z is required in the proposed simulator and could be used to increase the circularisation efficiency. With the large coils, it is not possible to have both the quadrupole field

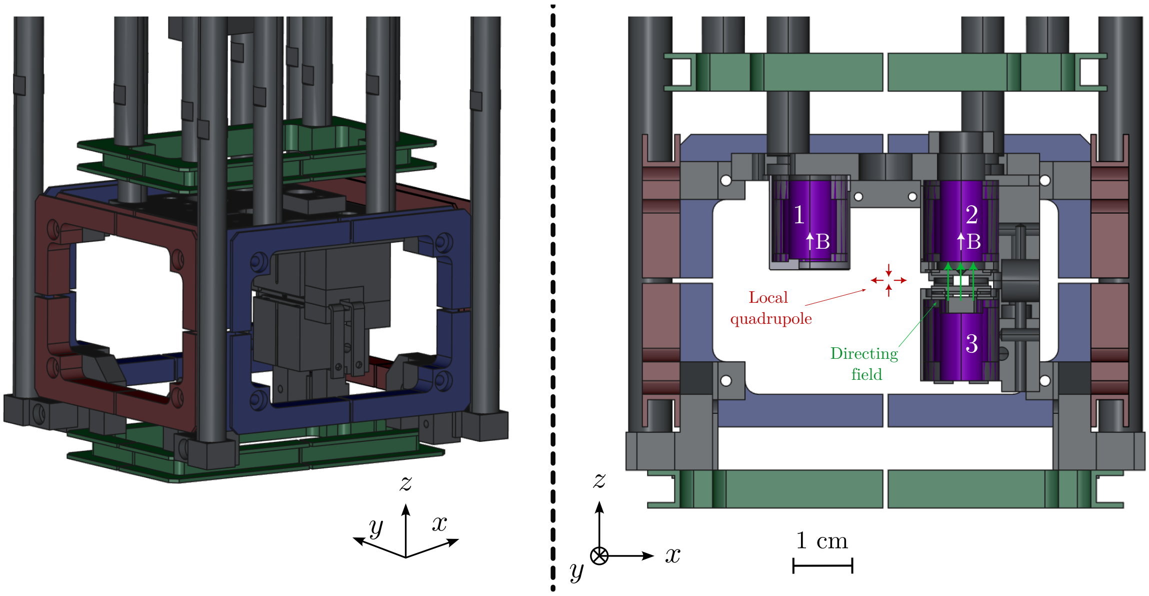

Figure 3.21. – Coils configuration used to control magnetic field in the experiment core. Left panel shows the large coils, along x direction in red, y direction in blue and z direction in green. On the right panel, the small coils are shown in purple. Using the coils 1 and 2, it is possible to generate a local quadrupole at the 3D-MOT position, as well a the directing field in between the inhibition plates. The third coil can be used to homogenise the field.

for the 3D-MOT and the field along z in the inhibition region at the same time. This means that the magnetic field produced by the coils will have to be switched off during an experimental sequence. The magnetic field change can be slowed down by eddy currents and coils images created by the superconducting niobium box.

To circumvent this issue, a second set of coils has been designed to realise both the 3D-MOT field gradients and the homogeneous field in between the plates. This configuration, denoted "compact", is depicted in Figure 3.21. The two coils "1" and "2" realise a kind of bent anti-Heltmoltz configuration, creating a local quadrupole at the MOT position. The third coil "3" can be used to tune the directing field inside the inhibition region. For that configuration, the large coils can be used to correct for bias fields or fine tune the local quadrupole position. More details about both configurations are given in subsection 4.4.1.

Atom delivery

The last step in the ground state atoms preparation is the deterministic delivery of ground state atoms inside the inhibition region. This is done with an optical dipole trap in a conveyor belt configuration. This technique relies on the lightshift effect presented in subsection 1.3.3, which requires a high intensity and far detuned laser beam.

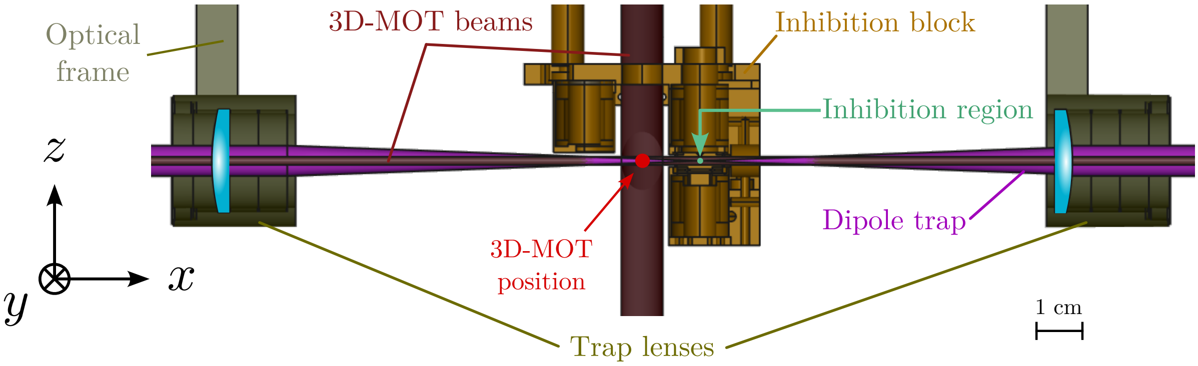

Figure 3.22. – **Dipole trap lenses** directly placed inside the cryostat. The same color code is used, with the inhibition block in orange, 3D-MOT beams in red and optical frame in yellow. Dipole trap beam is indicated in pink, and the lenses holder in yellow as well. Several elements have been hidden for sake of clarity. A light red dot indicates the theoretical 3D-MOT position.

The dipole trap is realised by the same 820 nm laser used for the Rydberg atom trapping. In order to get the required high intensity, this laser is tightly focused to a waist of around 12 μm. It is done with aspherical lenses with a focal length of 100 mm. The value of w_0 is a trade-off between the trapping depth and the beam divergence. Indeed, the smaller w_0, the deeper the trapping potential. In the mean time, the beam divergence is given by $w_0/z_R = \lambda_L/(\pi w_0) = 0.021$. A smaller w_0 thus creates a more diverging beam.

For a beam focused at the 3D-MOT position, the beam diameter ($2w_0$) between the inhibition plates 14 mm away is then around 0.6 mm. The beam being Gaussian, 99% of the power is contained in a $4w_0$ region. To have almost no heating of the plates, the effective size to consider is 1.2 mm. This size is already close to the plates spacing, and a smaller waist would have been even more difficult to align.

The trap lenses are put directly inside the cryostat, and mounted on the same optical frame used for the 3D-MOT beams, as visible in Figure 3.22. They are aligned such that they are symmetric with respect to the point in between the plates center and the MOT position. These are the two extreme positions between which atoms will need to be transported.

Atoms transport is done by means of a conveyor belt configuration [130]. Two counter-propagating beams create a standing wave. Ground state atoms are trapped in the intensity maxima. By changing the relative frequency of the two arms, one can scroll the interference fringes, and with them the atoms trapped inside them. This allows for a precise control of the atoms position along the propagation axis. More details on the implementation of this technique are to be found in chapter 5.

In order to carry atoms from the 3D-MOT to the inhibition region, the dipole trap axis goes through the 3D-MOT center and between the two inhibition plates, defining the two points on which the beams have to be aligned. By construction, the x axis MOT beams are co-linear with the dipole trap. Starting from a working 3D-MOT setup, the x beams can be used as a reference outside the cryostat to pre-align the dipole trap beams.

In addition, a pre-alignment of the trap can be done at room temperature while the cryostat is open. When the setup is cooled down, the capacitor block rises by approximately 2.84 mm because of thermal contractions. This can be compensated by shifting the optical table by the same distance relative to the cryostat. To maximise the transport efficiency, the two dipole trap beams have to be superposed with interferometric precision from the 3D-MOT to the inhibition region. Fine tuning of this alignment is done directly on the atomic signal.

3.3. Atoms detection

For the experiment realisation, it is essential to have themeans to assess the successful realisation of the different steps. This requires a characterisation of the atoms properties, for example their number, their temperature or their energy state. Two main situations are to be considered.

When atoms are in the ground state, optical transitions are accessible. Sending laser light resonant with these transitions make the atoms fluoresce. The fluorescence light can be collected and analysed to have access to different atom properties.

For atoms in a circular Rydberg state, optical transitions are no longer directly available. Taking advantage of their highly excited state, it is however possible to ionise them by mean of a static electric field. The energy state can be inferred from the ionisation field value. In this section, the experimental setup used to collect the atoms fluorescence light and ionisation signals will be detailed.

3.3.1. Ground state atom detection

Measurement of ground state atoms is done optically. Laser beams are used to drive the $\left|{}^5S_{1/2}, F=3\right\rangle \rightarrow \left|{}^5P_{3/2}, F=4\right\rangle$ transition, and the associated fluorescence is measured with a camera. There are two situations where ground state atoms are probed this way. First, during the cooling steps when the obtained cold atom clouds are characterised. Second, when atoms are trapped inside the dipole trap. In both cases, the signal to noise ratio suffers from parasitic light, coming from stray light from the lab or diffused laser light.

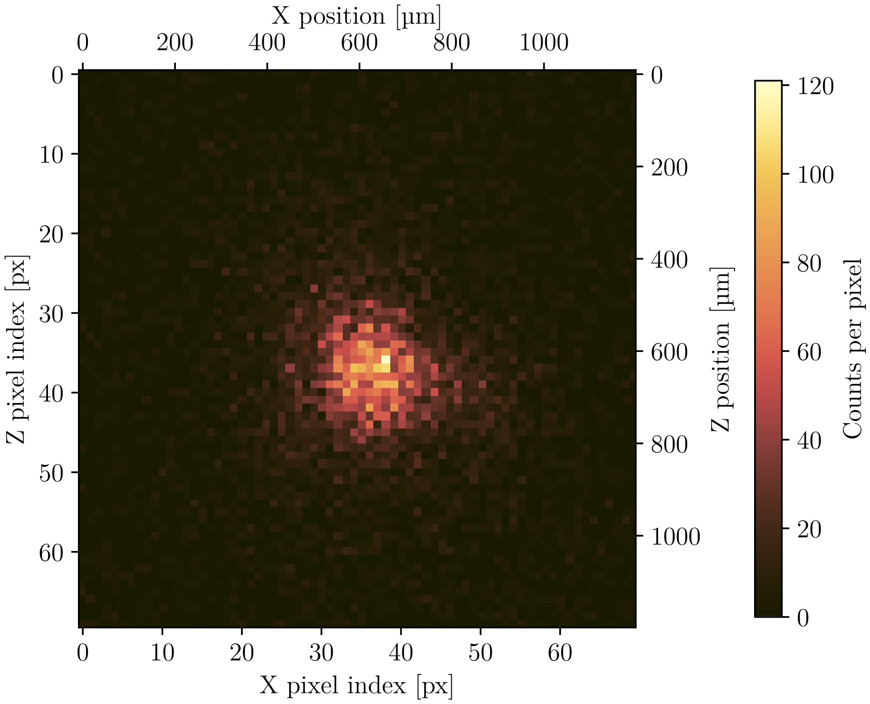

Figure 3.23. – Example image with the side camera of the 3D-MOT, zoomed on the 3D-MOT region.

For the design of the optical detection, the amount of collected light is an important parameter. This is especially critical for the dipole trap, for which the fluorescence signal is much weaker. Photons collection can be improved by increasing the numerical aperture (NA) of the lens which collects the light. However, such lenses usually have smaller focal length, meaning that they should be closer to the imaged source, therefore reducing the field of view.

This trade-off motivated the design of different imaging systems. First, an imaging system with a large field of view dedicated to the 3D-MOT imaging. It collects light from both directions to characterise the cloud in three directions, from the top (z axis) and from the side (y axis). A second setup involving a lens with a larger NA is used to collect the weak fluorescence of the dipole trap. It also involves a sCMOS Zyla camera, which has better performances. This second setup can be used to observe the MOT as well, but with a smaller field of view.

MOT imaging

The 3D-MOT can be directly characterised by analysing its fluorescence images. Indeed, the cooling itself relies on the absorption-emission cycles of near resonant light. Here, the $\left|{}^5S_{1/2}, F=3\right\rangle \rightarrow \left|{}^5P_{3/2}, F=4\right\rangle$ transition at 780 nm is used for atom cooling, and therefore to image them.

In terms of signal, conditions are also favourable. Typical MOTs with millimetre-sized beams can trap on the order of one million atoms. Inside the MOTs, each atom fluoresces with a rate of several tens of millions photons per second. This provides enough light for detection with standard charge-coupled device (CCD) cameras.

The optical setup used for 3D-MOT imaging is depicted on Figure 3.24 with the two paths from the top and from the side. A mirror above the 3D-MOT allows one to image the cloud from the top. Light is also collected from the side, along the $-y$ direction. For this axis, light is first collected with a 150 mm lens. It is then focused on the camera, *DMK 37BUX 273* from *Imaging source*, with a 25 mm lens.

Light being emitted in all directions, only a fraction is collected on the camera. This fraction reads:

$$f_{col} = \frac{\Omega}{4\pi} = \frac{r^2}{2d^2}, \tag{3.3}$$

where Ω is the solid angle, function of the aperture radius r and the distance between the object and the limiting aperture d. For the side lens, r =6 mm and d ≈30 cm. Collected fraction is then around 0.01%.

This only takes into account the geometrical fraction collected, not taking into accounts losses. In practice, light crosses three windows on its path. Each window induces losses of around 2% at 780 nm. These losses being small, they have not been taken into account for the data treatment.

When photons reach the camera, they create an electronic signal to which is associated a number of counts

$$N_{counts} = N_{col} \cdot Q_E \cdot G, \tag{3.4}$$

where N_{col} is the number of collected photons, Q_E (≈ 30%) is the camera quantum efficiency and G is the camera gain. The sensitivity $s = Q_E \cdot G$ depends on the wavelength and camera specifications. It has been measured, and a typical value is $s = 0.01$ counts per photon, for a gain settings G =5 dB at 780 nm. These values have been precisely characterised for the atom number measurement. For other experiments, higher gain was chosen to reduce the exposure time.

Knowing the lenses and distances, magnification for the side camera is around $M = 0.2$. The camera pixel size is 3.45 μm × 3.45 μm. The 3D-MOT total size is expected to be around one millimetre. Given the magnification, the signal is concentrated on a region of around 50 px × 50 px. This is only a fraction of the full camera chip.

Typical gain and exposure time used for the 3D-MOT are 35 dB for 0.2 ms. Values were chosen such that the pixels with the highest number of counts, around 130 counts, are just below camera saturation. These numbers have to be compared to the image background, to estimate the signal over noise ratio. Data treatment is only done on a

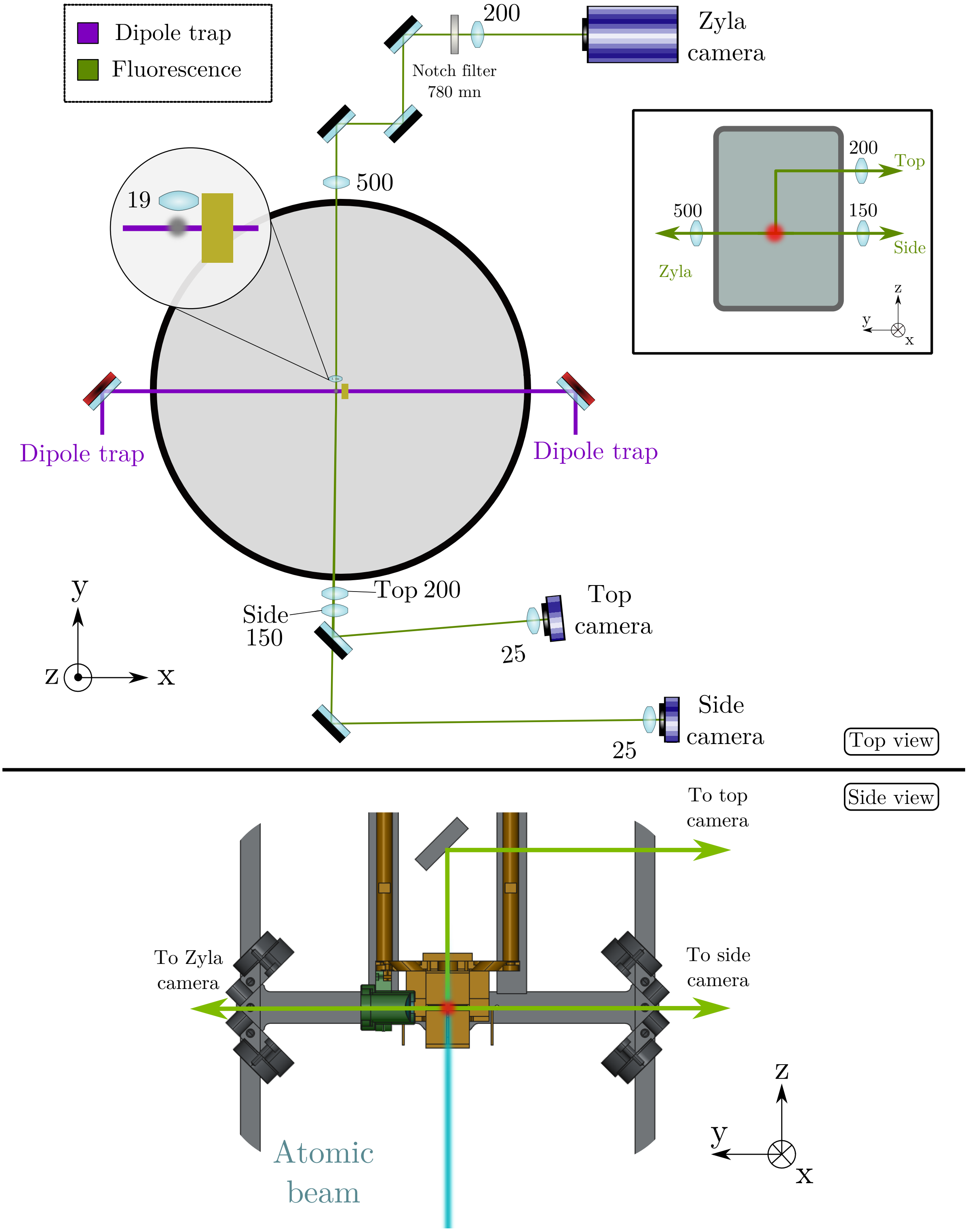

Figure 3.24. – **Cameras optical setup** for 3D-MOT and dipole trap imaging. Fluorescence light is collected by lenses and detected on CCD cameras. One collects light from the top (top camera) and the order one from the side (side camera). For the dipole trap, a lens with a large numerical aperture is required to collect enough fluorescence and a more performant camera (Zyla sCMOS) is used. Focal length are given in millimetres.

fraction of the camera chip, where the signal is. This region of interest (ROI) has the typical dimension of the 3D-MOT image, 50 px × 50 px. The average number of signal counts over this region is around 20 counts per pixel. Due to the restricted optical access, parasitic light has been especially deleterious in early stages of the experiment and challenging to get rid off. [10]

After reduction of the parasitic light, the average background light for the side camera was below one count per pixel, for 35 dB gain and 0.2 ms exposure time. For data treatment, the background signal is then removed from the main signal to increase the signal to noise ratio. A typical 3D-MOT image with the side camera after background corrections is given in Figure 3.23.

For the top camera however, background light was directly coming from the 2D-MOT fluorescence. The only way to remove it is to switch off the 2D-MOT during the imaging step, which was not directly possible without changing the optical setup. The side camera is hence used for most of the 3D-MOT characterisations. Its wide field of view is indeed required for some measurement based on the observation of the cloud expansion.

Unfortunately, this setup was not sensitive enough to measure the fluorescence from atoms in the dipole trap. As illustrated in Figure 3.25, the dipole trap signal is approximately one hundred times weaker than the 3D-MOT, even with a high NA lens. On the standard CCD cameras, this signal would be overcome by noise.

DT imaging

To be able to collect the weak fluorescence of the dipole trap, a third imaging path has been designed. For this path, a lens with a large numerical aperture $NA = 0.4$ is used to increase the collection efficiency. The latter can be computed using Equation 3.3 and is found to be around 4%, which is about fifty times higher than for the side camera optical setup. To avoid aberrations, an aspherical lens *49111* from *Edmund Optics* has been chosen. Using the software *Oslo* from *Lambda Research Corporation*, the effective focal length (EFL) has been computed at 780 nm. It is found to be around 19 mm. Due to the short effective focal length of the aspherical lens, the depth of focus is way shorter.

The number of atoms in the dipole trap is expected to be much smaller that for the 3D-MOT. A camera with better performances is then required. Indeed, for small number of photons per pixel, the readout noise of standard CCD cameras can overcome the signal [131]. An alternative solution is to use a complementary metal-oxide semiconductors

---

[10] In particular, some laser light was diffused by the windows and focused at the MOT position in the y direction. Adjustment on the metal screens solved this issue.

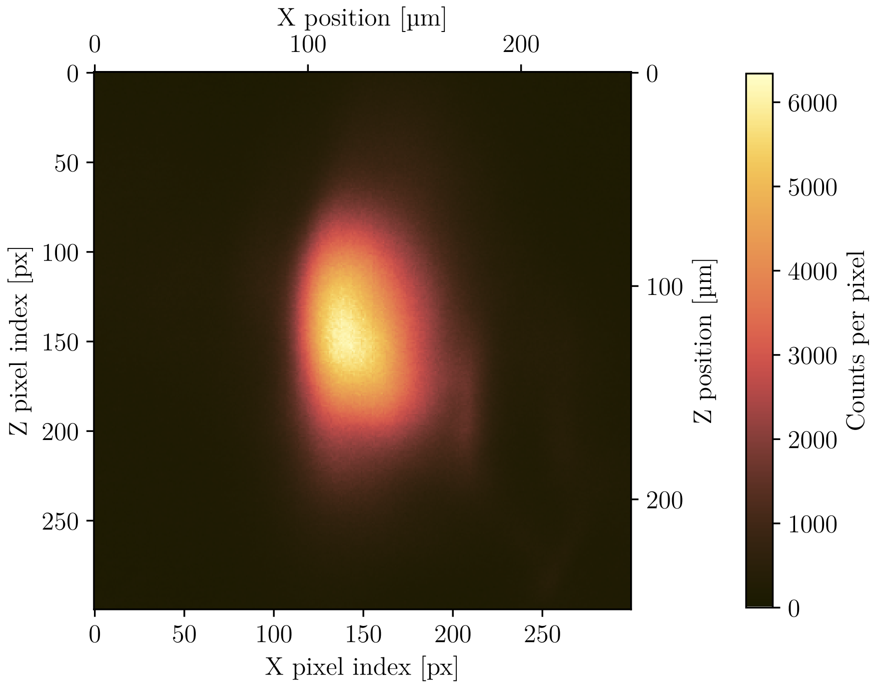

(a) 3D-MOT

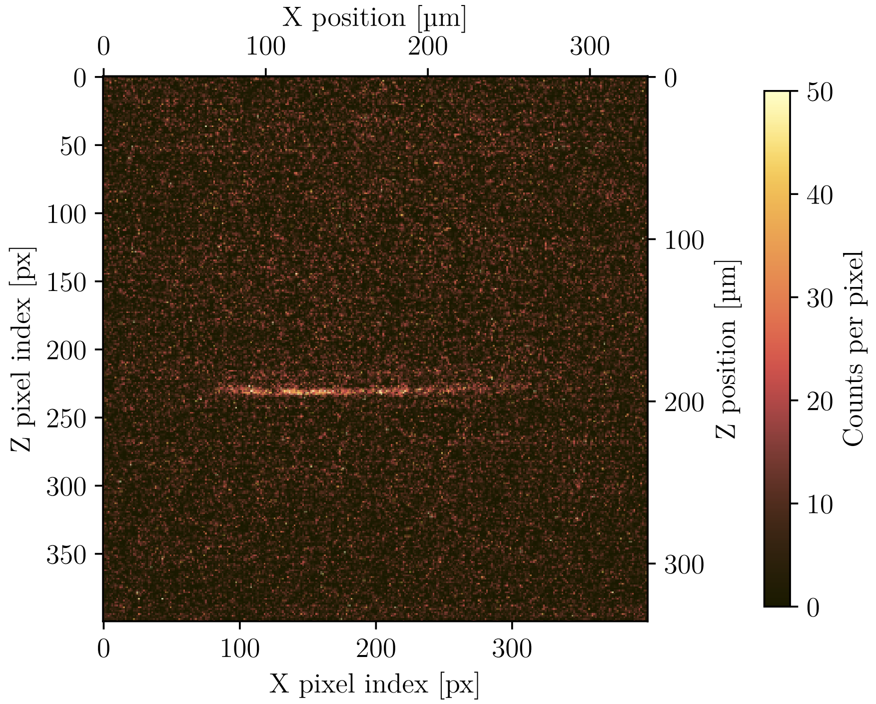

(b) Dipole trap

Figure 3.25. – Example images with the Zyla camera of the 3D-MOT and of the dipole trap.

(sCMOS) camera technology, which has a lower effective readout noise than standard CCD cameras. The camera chosen here is a *Zyla ZL41 Wave 5.5* from *Oxford Instruments*. Pixel size is $6.5\,\mu\text{m} \times 6.5\,\mu\text{m}$. The optical setup used to image atoms with this camera is depicted in Figure 3.24, and example images for the 3D-MOT and the dipole trap are given in Figure 3.25.

An additional 500 mm lens is put after the cryostat to increase the refocus of the light. Altogether, the optical system magnification can be computed, and is found to be $M = 7.8$. A pixel of the camera then corresponds to $0.83\,\mu\text{m}$ in the dipole trap plane. Dipole trap waist being around $12\,\mu\text{m}$, it thus covers around 14 px.

As for the 3D-MOT imaging, dealing with the parasitic light was challenging. One advantage was coming from the short depth of focus, making most of parasitic light out of focus, and therefore not collected on the camera. The detection being at 780 nm, some parasitic light is filtered by adding a notch filter *FBW5785-10* from *Thorlabs*. It especially filters the light of the dipole trap laser beams.

After careful optimisation of the optical system, the average counts for the dipole trap over the ROI was around 30 counts per pixel. Typical ROI is 100 px × 5 px. The maximal counts per pixel is around 50 counts per pixel. Finally, the typical background signal is around 10 counts per pixel. All these values are for a 20 ms exposure time.

3.3.2. Rydberg states detection

Atoms in the circular Rydberg state don't have accessible optical transitions, and fluorescence detection is not directly possible. [11] Yet, their highly excited state makes them easier to ionise. Moreover, the ionisation threshold depends on state energy, allowing for state measurement. This method has been historically used for the circular Rydberg state detection in CQED experiments [5].

It is worth mentioning that if optical direct detection doesn't exist, it is possible to use optical detection for an indirect measurement of a circular Rydberg state. For example, it is possible to selectively de-circularise the atoms, and infer the initial population from the detection of ground state atoms [61]. It is also possible to use a probe atom that can be optically detected and whose state depends on the circular Rydberg atom state [51].

---

[11] It is the case for alkali atoms. For other elements, such as alkaline earth metal, the presence of core electrons can be used to measure the Rydberg electron.

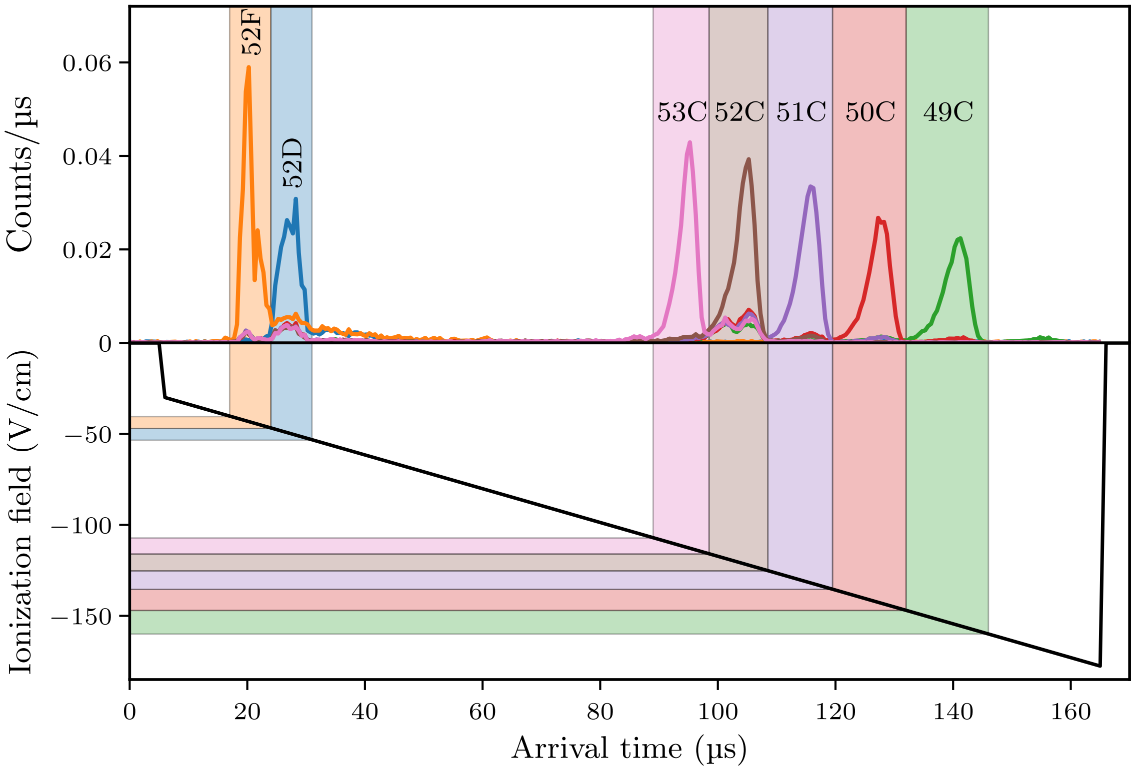

Figure 3.26. – **Example of an ionisation signal** by applying an electric field ramp and detecting ions. Ionisation field is linearly increased, leading to several ionisation peaks. Knowing the field and the detection system, each peak can be associated to a state. Figure taken from [61].

Rydberg states selective ionisation

Rydberg atom states are measured by ionisation. An electric field is applied using the inhibition plates. The ionisation threshold for the $|52C\rangle$ state is around $120\,\mathrm{V\cdot cm^{-1}}$. The gap between the plates being 2 mm, this can be done by applying a 24 V potential difference between the plates.

Different state have different ionisation thresholds. This can be exploited to measure the population in each state. To do so, an electric field ramp is applied. The different states are then successively ionised. The ionisation produces one electron and one ion, that can be detected to measure the number of ionised atoms. An example from another experiment of the group is shown in Figure 3.26.

Knowing the electric field ramp and the travel time of the detected particle, one can find the ionisation field associated to each peak and with it the corresponding energy state. The number of detected counts is directly proportional to the population in the state.

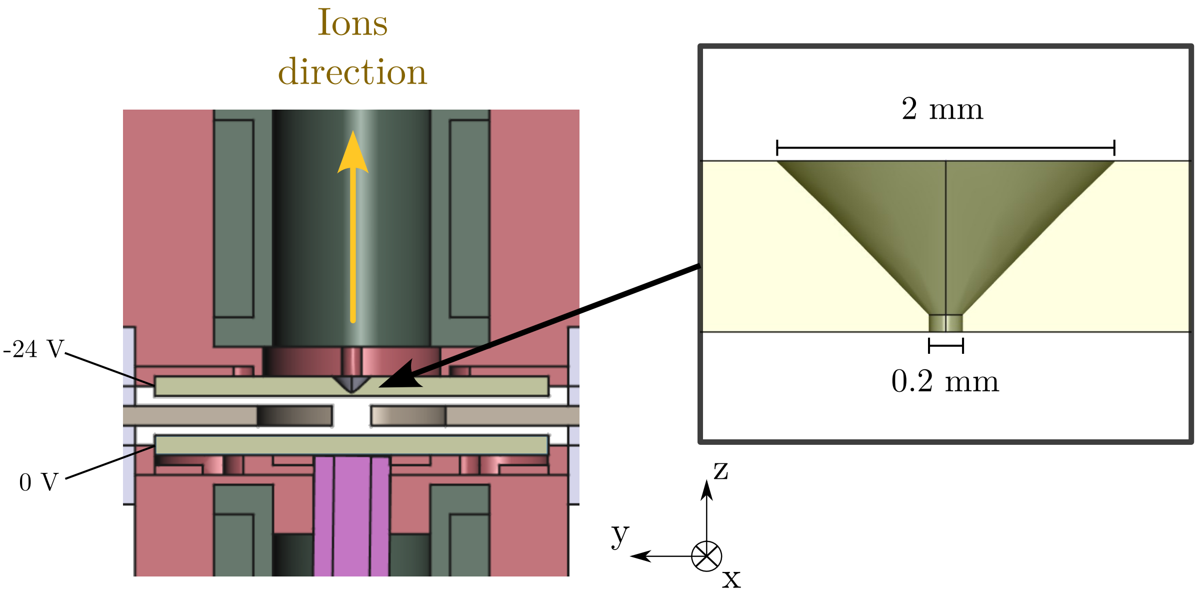

Figure 3.27. – Detection hole design for ions collection. The hole has a conic shape to increase ions collection without disturbing the inhibition properties.

Ions collection

In the experiment, the detected particles are ions. Since they are heavier than electrons, their trajectories are more robust to potentials fluctuations. To collect them, a hole is drilled on the upper inhibition plate to let the ions go through. This hole has to be much smaller than the transitions wavelength (λ_0 ~6 mm) to not disturb the inhibition property, and was designed to be around 0.2 mm. Due to machining constraints, the other side has a conic opening, as depicted in Figure 3.27.

Ions are detected with a channel electron multiplier *KBL 10RS-EDR* from *Dr. Sjuts Optotechnik GmbH*, also known as “Channeltron”. This device is used to amplify the signal of a single charged particle. The typical operation temperature of this channeltron inside a cryostat is around 40 K. To prevent the BRR it generates from reaching the atoms, the channeltron is placed away from the inhibition region and not directly facing towards the atoms.

A set of electrodes, depicted in Figure 3.28, has been designed in order to guide and accelerate the ions. Ions are created between the two inhibition plates (yellow), propagating in the $+z$ direction. The electric field is applied by setting the bottom plate to the ground, and the upper one to a voltage of around -30 V. Then, a first tube electrode (blue) is used to accelerate and guide the ions to keep a straight trajectory. Then, a set of four deflecting electrodes (green) are used to redirect the ions in the $+x$ direction. Their potential can be independently controlled to readjust the ion beam direction. A last electrode (purple) accelerates the ions to give them enough kinetic energy to generate the electronic signal. Ions then reach the channeltron (red), where

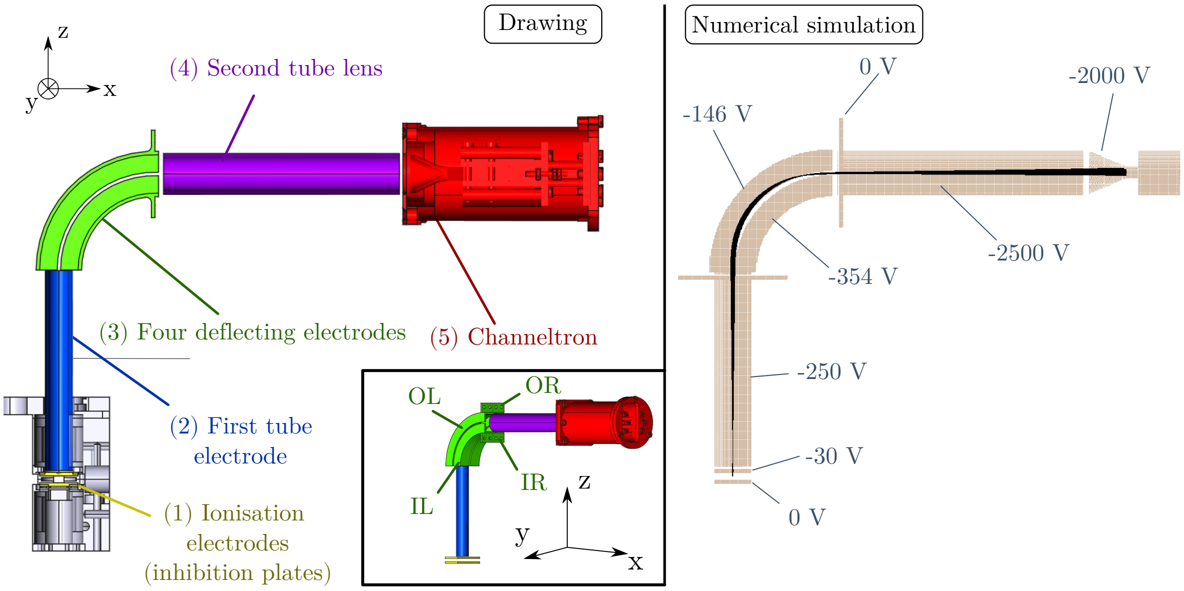

Figure 3.28. – **Ions detection path:** drawing and simulation results. On the drawing, ions are created in between the plates (yellow). Then a set of electrodes guide the ions to the channeltron where they are detected. A different point of view is depicted to better see the four deflecting electrodes (green), labelled here In-left (IL), In-right (IR), Out-left (OL) and Out-right (OR). The picture on the right shows the trajectories obtained with numerical simulations, using the indicated potentials.

the electronic signal will be generated and amplified.

This design has been numerically simulated using the simulation software *Simion*. The electrodes geometry and potentials have been optimised in order to maximise the number of ions reaching the channeltron. On the figure, typical voltages found with the simulations are given. Another important parameter given by the simulations is the ions travel time, found to be around $5.9\,\mu$s for the given potentials.

After the channeltron, the electronic signal is amplified, discriminated from noise and converted into TTL pulses. The latter are counted by the experiment control software and can be treated to estimate the population in each state. Altogether, this setup provides the means to detect the Rydberg state in a selective way, completing the set of required tools for the experiment.

Conclusion

This chapter provided all the details of the experiment designed to observe circular Rydberg states with extended lifetime. A schematic diagram in Figure 3.29 summarises the different elements. The first part showed how to obtain an environment isolated from black body radiation, residual gases and atomic motion, together with a decoupling from vacuum fluctuations.

Means to prepare circular Rydberg states, starting from a source of ground state ^{85}Rb atoms have also been presented. They involve the excitation scheme to excite atoms to a circular Rydberg state, as well as the means to cool and transport ground state atoms in the inhibition region.

Finally, the means to observe the different experiment stages have been introduced. Measurement of ground state atoms relies on optical detection of the atoms fluorescence, while Rydberg state detection is performed by measuring an ionisation signal.

So far, all the experiment elements have been manufactured and assembled inside the cryostat. The cooling and transport stages have been experimentally realised, showing promising results for the next steps. More details about associated results are given in the next chapters. Remaining steps are the excitation to the circular Rybderg state and the measurement of the state lifetime.

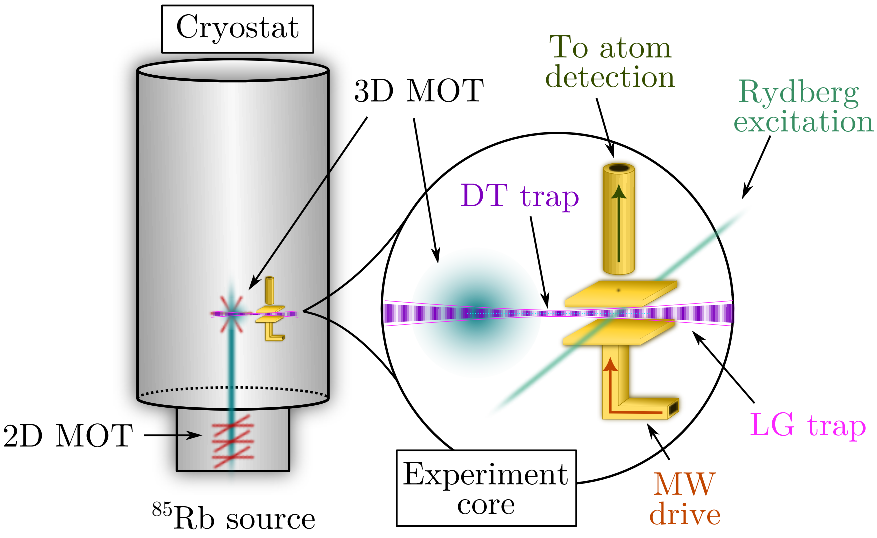

Figure 3.29. – Experiment scheme summary. Ground state atoms are cooled using a 3D-MOT, loaded from a 2D-MOT atomic fountain. A dipole trap in a conveyor belt configuration is then used to transport the atoms in between the inhibition plates. Once there, they are excited to the circular Rydberg state, using optical excitation and radiofrequency fields. Circular Rydberg atoms are trapped in a Laguerre-Gauss trap combined with a standing wave. Atom state detection is performed by ionisation, and a microwave drive can be used to manipulate the atoms.

Chapter 4

A cold atom source

Hold on! I'm about to say something really cool!
— Jinx, *League of legends*

In order to study the effect of a controlled environment on circular Rydberg states lifetime, one needs to start by bringing said atoms into this specific environment. In this setup, it means bringing and keeping atoms between the two inhibition plates. This requirement is made harder by the need for an isolated environment. It especially induces limitations on the optical access, both due to the cryostat structure and the need to prevent external thermal field from coming inside the experiment core.

Fortunately, the laser cooling and trapping techniques developed in the last decades allow for a precise control of the atoms position. One example is the use of dipole trapping to capture and move atoms [132]. Such traps are conservative and atoms need to be cooled down beforehand. This chapter will provide details about the experimental stages involved in the preparation of a cold atom sample.

First, a heated rubidium cell feeds a two-dimensional magneto-optical trap (2D-MOT), creating an atomic fountain. The created atomic beam then feeds a three-dimensional magneto-optical trap (3D-MOT) creating a cloud of cold atoms. From this cloud, one can get an optical molasses to bring the atoms to sub-Doppler temperatures.

This chapter begins with a short introduction about the basic elements of atom cooling by a magneto-optical trap (MOT). Details about the laser beams preparation will then be provided. Following this, the 2D-MOT setup and characterisation are presented. Finally, details about the 3D-MOT design and experimental implementation are given.

4.1. Magneto-optical traps

As previously mentioned, atoms cooling has been performed by means of magneto-optical trap (MOT) techniques. This section briefly introduces the theoretical framework used for both the 2D-MOT and the 3D-MOT, with references to the literature for more detailed analysis.

MOTs heavily relie on what is called Doppler cooling. Consider a moving atom, illuminated by a laser of angular frequency ω_L, close to an atomic transition of frequency ω_a. When it absorbs a laser photon, the atom gains momentum in the laser propagation direction. Spontaneous emission of the absorbed photon is isotropic, and in average doesn't change the atom momentum. All together, the atom feels in average a radiative pressure in the laser propagation direction.

An interesting scenario is when a pair of counter propagating red-detuned laser beams are used, with $\Delta = \omega_a - \omega_L > 0$. Thanks to the Doppler effect, the atom is closer to resonance with the beam propagating in a direction opposite to the atom movement, rather than the one propagating in the atom movement direction. As a result, the sum of both lasers radiative pressure in the lasers' axis is in average against the atom movement, resulting in an effective friction force.

Using this effect, it has been suggested in 1975 to use three pairs of counter-propagating beams to completely slow down, and so cool, an atomic sample [133]. Following this idea, the first optical molasses was obtained ten years later [134]. This method is called the Doppler cooling.

The laser beams also induce diffusion of the atoms in the momentum space. The balance between the friction and the diffusion effects leads to an equilibrium temperature T_D called the "Doppler temperature" which reads:

$$T_D = \frac{\hbar\Gamma}{2k_B}, \tag{4.1}$$

where $\hbar$ is the reduced Planck constant, k_B the Boltzmann constant and Γ the linewidth of the cooling transition used. This temperature is obtained in optimal friction conditions, when $\Delta = \Gamma/2$.

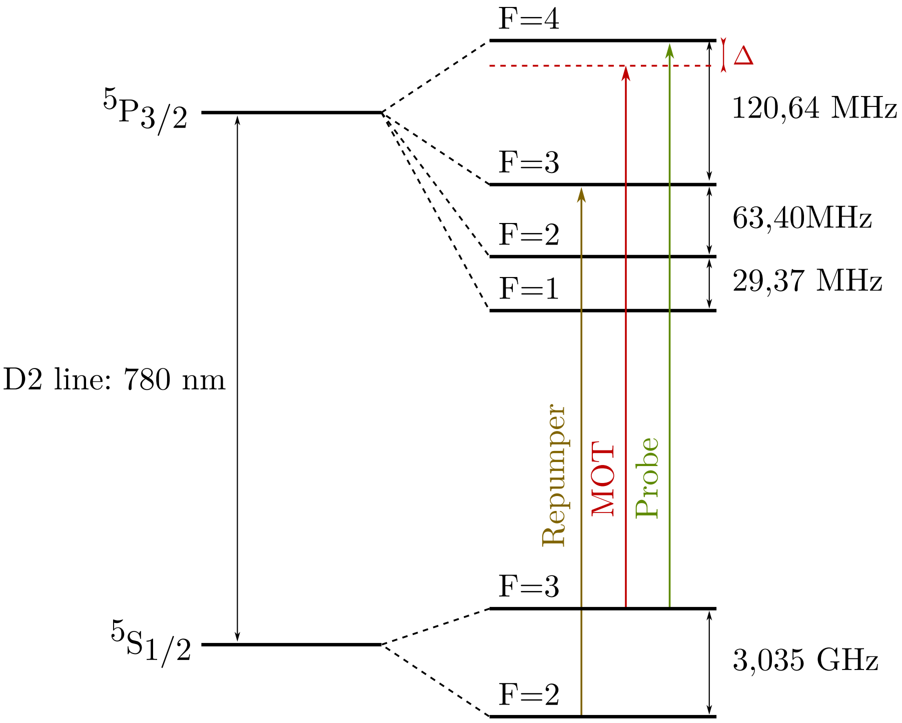

Figure 4.1. – Rubidium 85 D2 line hyperfine structure. The cooling transition used is $|5^2S_{1/2}, F=3\rangle \rightarrow |5^2P_{3/2}, F=4\rangle$, with a detuning Δ. The same transition is used for imaging. In both situations, a repumping light addressing the $|5^2S_{1/2}, F=2\rangle \rightarrow |5^2P_{3/2}, F=3\rangle$ transition is required.

In the experimental setup presented here, the Rubidium 85 D_2 line is used for cooling. Its hyperfine energy structure is given in Figure 4.1. More precisely, the chosen cooling transition is $|5^2S_{1/2}, F=3\rangle \rightarrow |5^2P_{3/2}, F=4\rangle$, whose natural linewidth is $\Gamma = 2\pi \cdot 6.06\,\mathrm{MHz}$ [69]. The corresponding Doppler temperature is $T_D = 146\,\mu\mathrm{K}$. However, due to sub-Doppler cooling effects, experimental values are usually much lower. For these effects, the lowest temperature are obtained for larger red-detuning, typically $2-3\Gamma$ [135].

Since there is a non zero probability for the cooling laser to excite the $\left|5^2S_{1/2}, F=3\right\rangle \rightarrow \left|5^2P_{3/2}, F=3\right\rangle$ transition, some atoms are pumped into the state $\left|5^2S_{1/2}, F=2\right\rangle$. To get these atoms back into the cooling cycle, a repumper beam is used to shine the transition $\left|5^2S_{1/2}, F=2\right\rangle \rightarrow \left|5^2P_{3/2}, F=3\right\rangle$.

If the molasses gives a mean to slow down the atoms, it doesn't spatially confines the atoms. In order to add spatial dependency, one can use a magnetic field gradient in order to break the local homogeneity that exists within the laser beams crossing region. It allows one to localise the atoms around the zero field point. In addition, the gradient allows for the trapping of atoms with much higher velocities, leading to a higher number of atoms. In the presence of a magnetic field gradient, the Zeeman effect lifts the degeneracy between different sub-levels, accordingly to their magnetic quantum number. A simplified one-dimensional example with a zero angular momentum ground state and an excited state with angular momentum $J_e = 1$ is depicted in Figure 4.2. In the positive magnetic field region, the state $m_f = -1$ sees its energy lowered, and the corresponding transition comes closer to resonance with laser beams with a red detuning Δ.

For laser beams with the same circular polarisation, the atoms will feel a polarisation σ_+ from one of the beam and σ_- from the second one, due to their opposite propagation directions. Due to selection rules, only one of this beams can then address the transition to $m_f = +1$. The other one addresses the transition to $m_f = -1$, which is far from resonance. By carefully choosing the circular polarisation that fits with the gradient sign, one can reach a configuration for which an atom placed at $z > 0$ will mainly feel the beam pushing it toward $z = 0$.[1]

Similar behaviour is then expected in the $z < 0$ region, and the atom is then confined around the zero magnetic field point. Applying this idea to all three directions allowed for the first 3D-MOT obtention in 1987 [136]. To get a magnetic field gradient in all three directions, a quadrupole field is generally used. Typical gradients used are around $10\,\mathrm{G} \cdot \mathrm{cm}^{-1}$.

---

[1] As illustrated in Figure 4.2, if the magnetic gradient is diverging along one direction (i.e. field pointing away from the zero field point), associated laser beam polarisation needs to be right-handed circular. If the gradient is converging, polarisation needs to be left-handed.

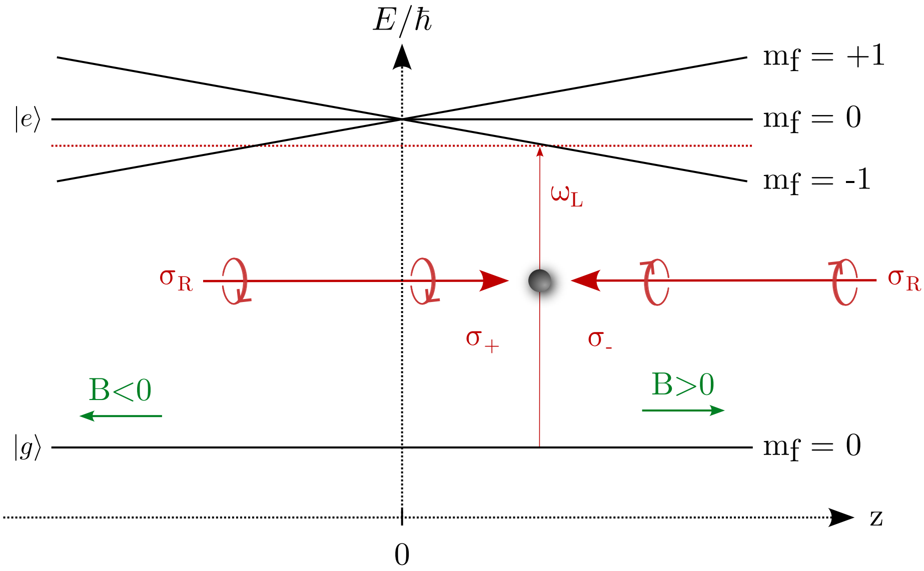

Figure 4.2. – Magneto-optical trap basic illustration. An atom placed in the positive z region experiences a positive magnetic field. It is illuminated by red-detuned right-handed circularly polarised light σ_R from the left and right directions, hence giving respectively σ_+ and σ_- polarisations. Due to the Zeeman effect, lasers are only resonant with the $m_f = 0 \rightarrow m_f = -1$ transition. Due to selection rules, this transition is only addressed by the σ_- laser from the right, which pushes the atom towards the center $z = 0$.

4.2. Laser beams preparation

In order to realise magneto-optical traps and image atoms in different conditions, it is necessary to have a control over the different laser beams parameters. Important ones are their power and frequency, precisely controlled in time. Control of these parameters is performed on a preparation optical table, whose detailed configuration can be found in Appendix D. Details about the lasers locking scheme can be found in Appendix C. A diagram summarising the frequency control scheme used is depicted in Figure 4.3.

First, a master oscillator power amplifier (MOPA) system *TA Pro* from *Toptica* is used to generate a near-resonance beam. Part of the seed beam is used to frequency-lock the beam -100.3 MHz from the cooling transition $\left|5^2S_{1/2}, F = 3\right\rangle \rightarrow \left|5^2P_{3/2}, F = 4\right\rangle$, by means of a saturated absorption spectroscopy onto a rubidium cell. This shift is mainly due to the presence of acousto-optics modulators (AOMs) later in the optical system.

The main part of the beam is amplified by a tapered amplifier, up to 1.5 W. The beam is then separated into several fractions, going into different couplers. On each path, one or two AOMs are used to fine tune the frequency, typically over few tens of megahertz. The powers of the different beams can also be controlled, with a microsecond time precision. It is done by adjusting the amplitude and the frequency of the radio-frequency generators driving the AOMs. The frequency range is such that most of the beams can

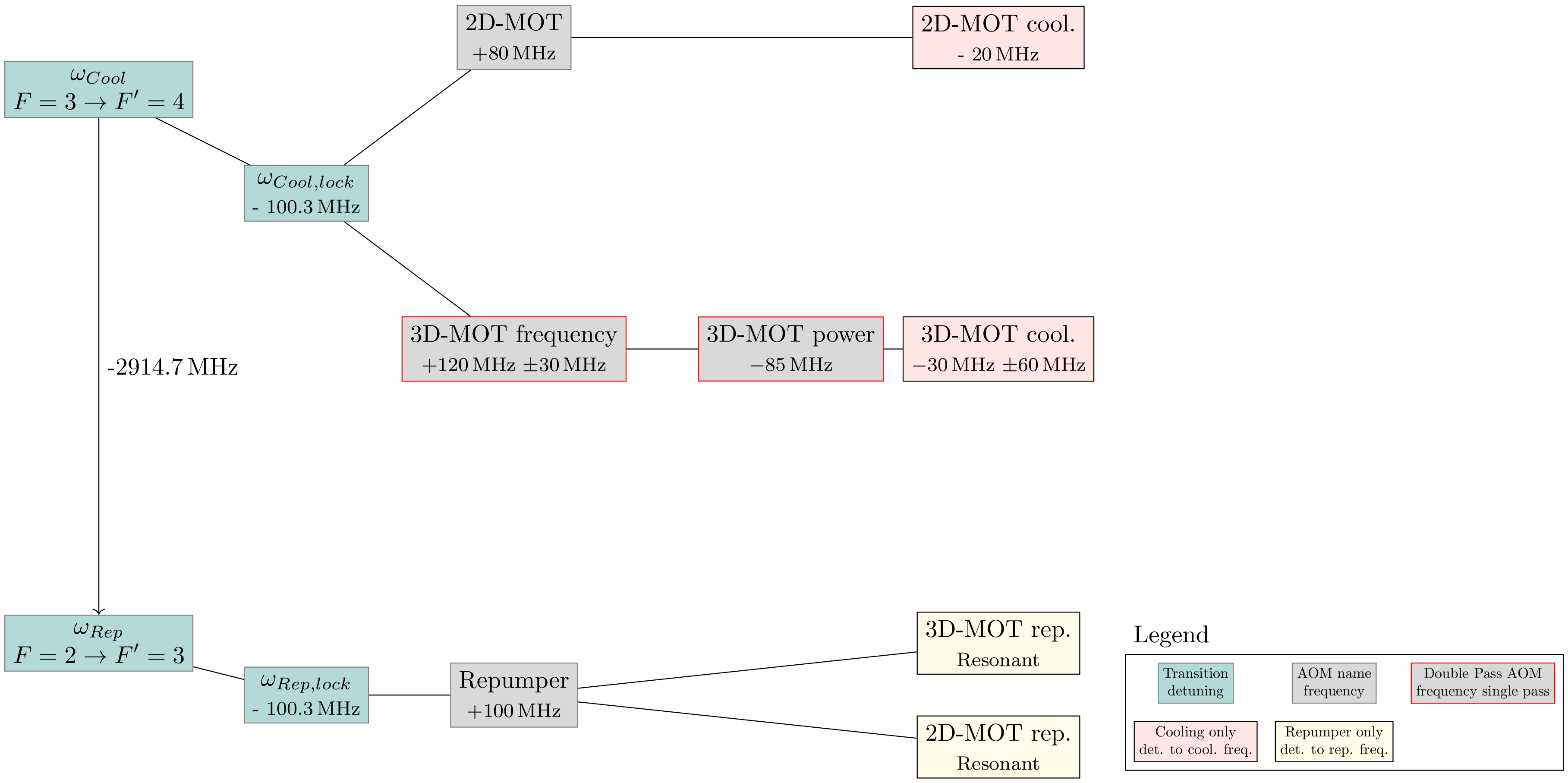

Figure 4.3. – **Summary of the beams frequency control** with lock frequencies and AOMs. Blue squares indicate the transitions and the frequency shift induced by the locking scheme. Grey squares indicate the AOMs, in single pass (black frame) or double pass (red frame). Frequencies correspond to one pass into the AOM. Red squares correspond to cooling light sent to the experiment, and yellow ones to repumper light, with the detuning with respect to the associated transitions.

be tuned around the atomic resonance, over a few tens of megahertz. This flexibility over different beams has been determinant in the early stages of the experiment, where accessing different configurations was useful to easily identify possible issues.

The repumper beam is generated by a tunable laser diode *DL pro* from *Toptica*. Part of the beam is used to lock its frequency 100 MHz below the repumping transition $\left|5^2S_{1/2}, F = 2\right\rangle \rightarrow \left|5^2P_{3/2}, F = 3\right\rangle$. To do so, the reference beam is overlapped with part of the MOPA seed beam to get a beating signal. The beating frequency is then set to 2914.7 MHz with a feedback loop, which corresponds to the frequency difference between the cooling and repumping transitions. The main beam is then splitted in different fractions, that are then controlled by different AOMs and sent to several fiber couplers in a similar configuration as for the MOPA beams.

Each beam is brought to the main optical table by means of single mode polarisation maintaining fibers. Beforehand, each of the main beams are separated and mixed together by two fiber port clusters from *Schäfter + Kirchhoff*, one for the 2D-MOT and one for the 3D-MOT. These clusters split the main cooling beam onto several pairs of outputs. More details can be found in Appendix D. It allows for a handy and precise independent control of the power balance of each counter-propagating pair of beams by means of half-wave plates. In addition, these clusters allow one to distribute the repumper power onto the different MOT beams, with a control independent from the cooling beams configuration.

4.3. 2D-MOT

4.3.1. Setup

In order to avoid rubidium depositions over the cryostat surfaces and so vacuum deterioration, it is convenient to canalise the atom source into an atomic beam. This can be performed by means of a 2D-MOT, which slows down two of the three velocity components, creating a narrow atomic jet along the third direction. In our experimental setup, a commercial device provided by the *SYRTE* laboratory from the *Paris-PSL Observatory* is used. A more detailed description of a similar model can be found in [128]. In the bottom of the 2D-MOT chamber, a rubidium cell is heated up to 60 °C. It creates a rubidium vapor that propagates into the main chamber. To prevent collisions with background gas, the chamber is pumped down to a pressure of 1×10^{-9} mbar with an ionic pump *3SMT TiTan* from *Gamma Vacuum*.

Inside the chamber, magneto-optical trapping is performed in the two horizontal directions x and y. It creates an atomic jet along the vertical direction z which remains

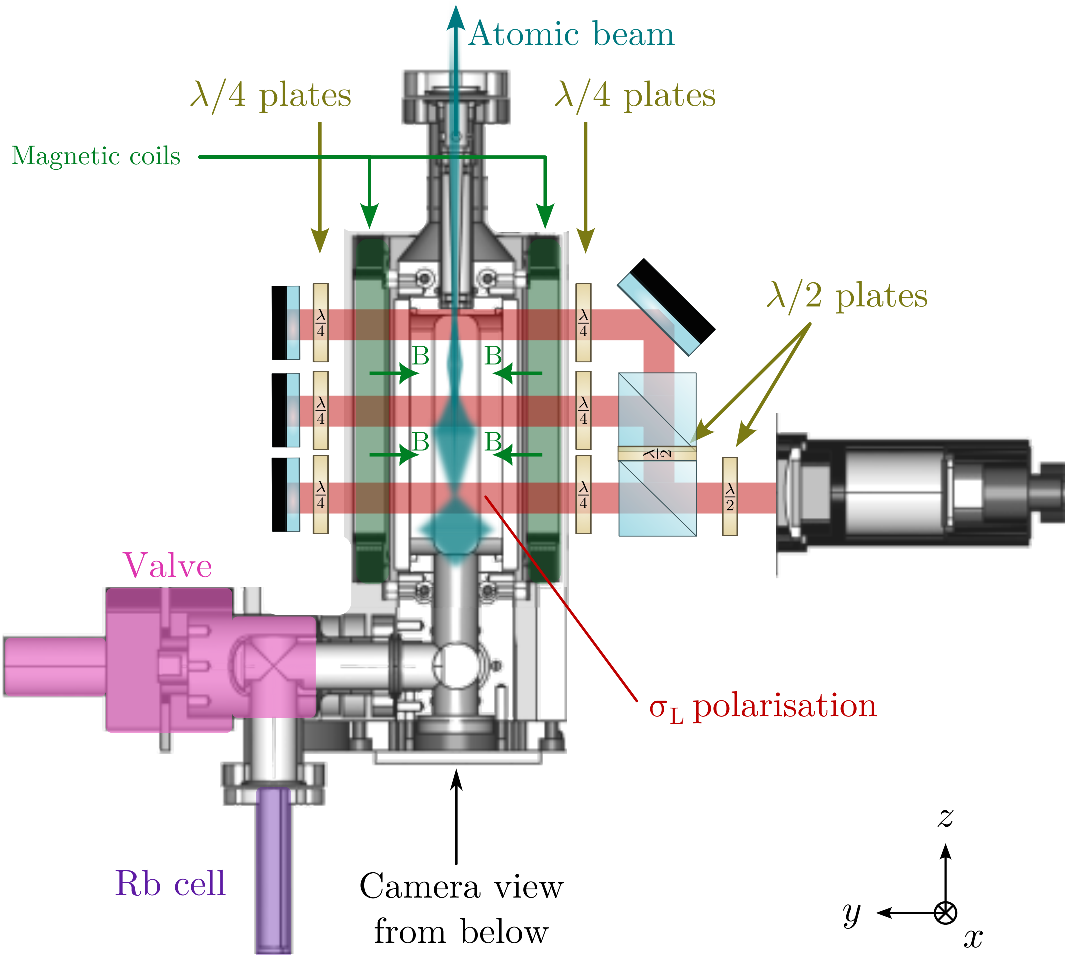

Figure 4.4. – **2D-MOT schematic view** in the Oyz plane. MOT beams (red) are splitted in three branches, balanced by means of halfwave plates. The required circular polarisation is set by quarterwave plates, in agreement with the magnetic field corresponding to the current direction (green). After the chamber, each beam is retroreflected, and a quarter waveplate compensates for the polarisation flip induced by the mirror. Rubidium comes from a heated rubidium cell (purple) that can be isolated from the vacuum chamber with a valve (pink). The rubidium vapor (cyan) is schematically represented all along the chamber, until the output of the 2D-MOT where the atomic beam is much less divergent. The system is symmetric and looks alike in the Ozx plane.

unaffected, as depicted in Figure 4.4. For each horizontal direction, a cooling laser beam with a 12 mm waist is split in three using half-wave plates and polarising beamsplitters. Each fraction goes through a quarter-wave plate to get the required left-handed circular polarisation. After the chamber, a second quarter-wave plate together with a mirror retro-reflects the beam to create a counter-propagating beam with the right polarisation.

For the 2D-MOT optimisation, several criteria were to be considered. First, the obtained fluorescence needs to be symmetric around the z axis. This ensures proper balance of the cooling around the two directions. An imbalance would result in an atomic beam deviation. This can be ensured by looking at the 2D-MOT from below. Second, the flux is maximised, to get an efficient feeding of the 3D-MOT.

In each direction a pair of coils are used to produce the required magnetic gradient. In each pair, current flows in opposite directions in an *anti-Helmoltz* configuration, in order to get the quadrupole field with the right gradient. One pair would be enough to obtain the right gradient, but using two pairs makes the system symmetric. This facilitates the obtention of a straight beam. The typical current applied in each pair is around 2.002 A for the x pair and 1.996 A for the y pair. This allows one to get a gradient of around $20\,\mathrm{G}\cdot\mathrm{cm}^{-1}$ in each direction.

In optimal conditions, the power was found to be around 30 mW for the x direction and 20 mW for the y direction. Optimal detuning was found to be around −20 MHz. In addition, some repumper light was added in the y direction beams, with a typical power of 1.4 mW.

The produced atomic jet then goes to the cryostat experiment core through a 1.5 mm hole. Having a small hole creates a differential pressure that protects the 2D-MOT chamber vacuum. One thing to notice is that the 2D-MOT is only efficient on atoms that are relatively slow along the z direction. Consequently, the atom velocity along the jet direction is in average between 10 and $20\,\mathrm{m}\cdot\mathrm{s}^{-1}$.

4.3.2. Characterisation

The produced atomic beam can be observed through a window directly after the main chamber exit, in the x direction. To see the atoms, a probe beam containing resonant light with the probing transition and some repumper is sent through the beam. A camera *DMK-37BUX252* from *Imaging source* is used to collect the fluorescence.

When the 2D-MOT is switched on, the 3D-MOT doesn't instantaneously start to load. It is possible to estimate the associated delay, found to be around 30 ms. It is mainly explained by the travel time between the 2D-MOT and the experiment core. The distance between the two is approximately 65 cm. It allows one to measure the atoms velocity, found to be around $22\,\mathrm{m}\cdot\mathrm{s}^{-1}$.

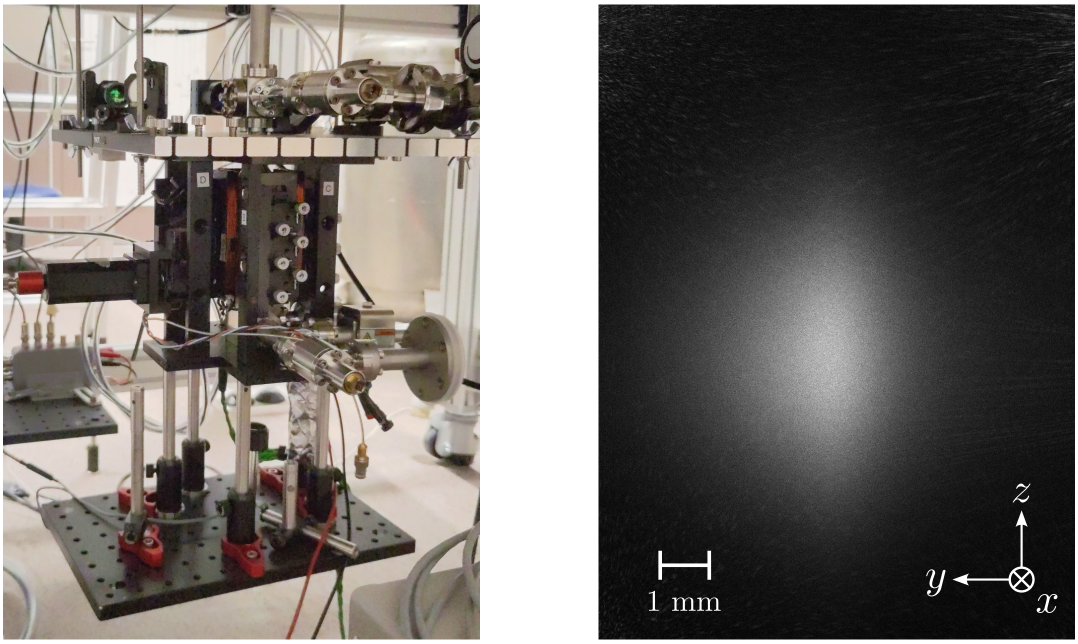

(a) (b)

Figure 4.5. – 2D-MOT pictures. 2D-MOT device 4.5a and a typical fluorescence image use for atom flux measurement 4.5b.

It is possible to measure the last atom presence in the 3D-MOT region after switching off the 2D-MOT. It gives the minimum waiting time required to be sure that atoms are no longer arriving. This delay is found to be around 30 ms as well.

Precisely knowing all these timescales allows for a more precise control of the experiment, in order to prevent possible disturbance between overlapping steps (for example, to prevent trapped atoms from being heated by atomic jet atoms collisions).

Knowing the mean atoms velocity $\langle v_z \rangle = 22\,\mathrm{m \cdot s^{-1}}$, it is possible to extract information about the atom flux from the fluorescence signal at the 2D-MOT exit. The resonant probe beam used has a waist w_p=3.6 mm and a power leading to a scattering rate R_{sc}. Once illuminated, atoms emit a fluorescence signal, as depicted in Figure 4.5b. This signal is collected on a camera with a solid angle Ω, leading to a collected fluorescence F_{col} in photons per second. This measurement allows one to extract the atom flux which reads:

$$\Phi = \frac{4\pi \cdot F_{col} \cdot \langle v_z \rangle}{\Omega \cdot 2w_p \cdot R_{sc}}. \tag{4.2}$$

In this experiment, the typical measured atom flux was around $3.4 \times 10^6\,\mathrm{atoms \cdot s^{-1}}$. This flux is smaller than the maximal value obtained in previous setup using the same device [72]. However, the 3D-MOT designed for this experiment is expected to trap around 1×10^6 atoms, which would lead to a loading time of few hundred milliseconds. This time being acceptable, no further optimisations have been performed.

4.4. 3D-MOT

Once they reach the experiment core, atoms are cooled down with a 3D-MOT in order to create a dense cloud of cold atoms. As for the 2D-MOT, it requires a magnetic field gradient in all of the cooling directions. It also requires a set of counter-propagating beams with proper polarisations. The limited optical access induced by the cryostat and other experimental constraints added to the challenge of this realisation, and the experimental setup is detailed below. Details about the experimental sequences, as well as characterisation results are then given to complete the study of this important step.

4.4.1. Magnetic field control

Compact coils configuration

The first key ingredient of a magneto-optical trap is indeed a well controlled magnetic field. It is possible to obtain this gradient by creating a single quadrupole magnetic field with only one pair of coils. However, the Rydberg excitation requires a static field in the z direction between the inhibition plates.

To comply with both of these constraints, a coil structure flexible enough to provide both configurations has been designed. Indeed, sudden changes to the magnetic field induce eddy currents. Avoiding the need to change the magnetic field to change the configuration would then be beneficial.

To adjust the geometry, numerical simulations using a software from the *CST studio suite* have been performed. In this configuration, represented in Figure 4.6a, two upper coils create a quadrupole field at the MOT position, acting as a kind of folded *anti-Helmoltz* configuration. To allow for the creation of a uniform field along the z direction in the inhibition region, a third coil is placed on the opposite side of the plates.

If the obtained magnetic field produced is not exactly a quadrupole field, it locally creates the required gradients along the three lasers directions. Another requirement is a null magnetic field at the 3D-MOT position. This condition is also fulfilled. For an imperfect experiment realisation, this can be adjusted by using compensation fields to cancel the magnetic field at this position.

Using only the two upper coils, with 40 turns and a current of 0.5 A, the expected gradients are around $2.1\,\mathrm{G\cdot cm^{-1}}$ for x axis, $-0.9\,\mathrm{G\cdot cm^{-1}}$ for y axis and $-1.2\,\mathrm{G\cdot cm^{-1}}$ for z axis. Typical gradient required are around $10\,\mathrm{G\cdot cm^{-1}}$. The magnetic field produced is linear in the coils current. The right gradient can then be achieved with 5 A. In practice, superconducting wires are used to avoid heat dissipation due to such high current values.

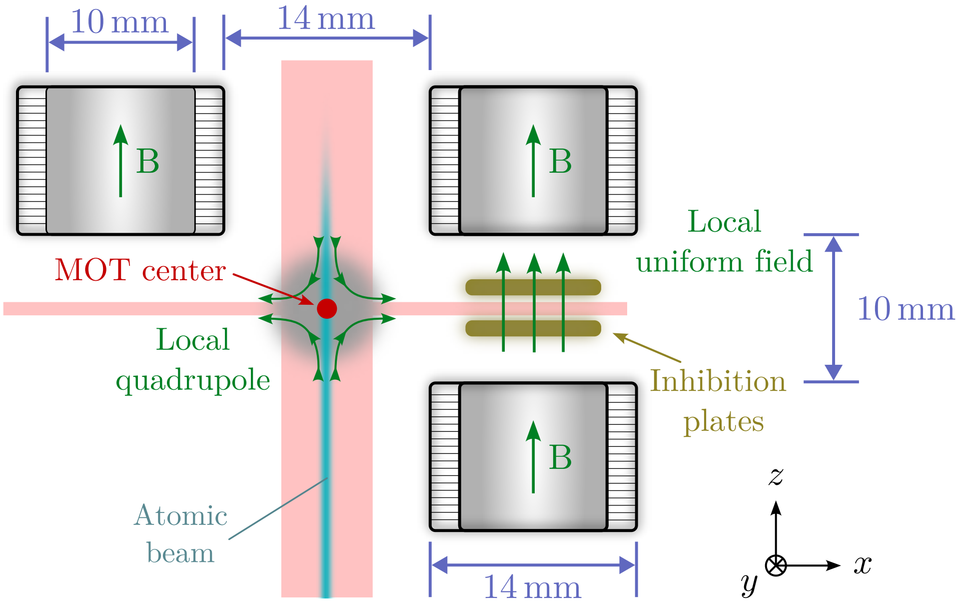

(a) Coils configuration diagram.

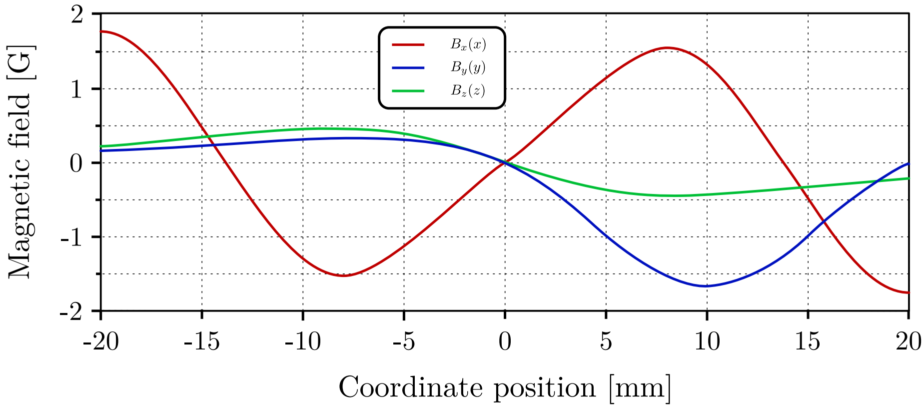

(b) Magnetic field at MOT position.

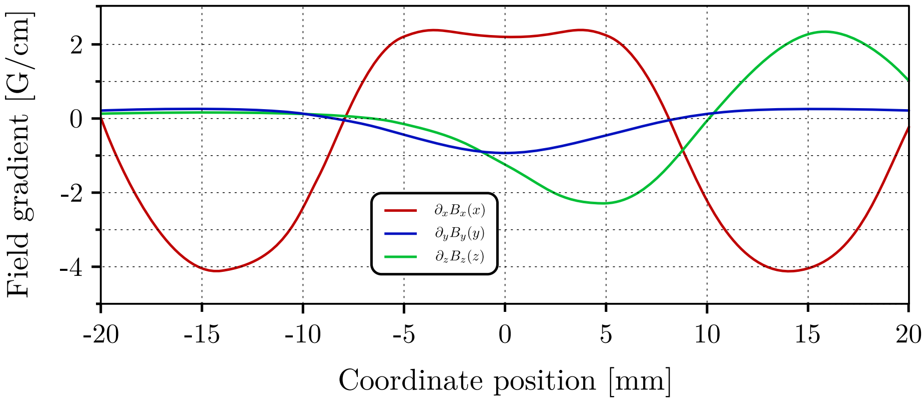

(c) Magnetic field gradients at MOT position.

Figure 4.6. – 3D-MOT compact coils configuration. Compact coils geometry 4.6a, with the three coils and the direction of the magnetic field they create (green). Other experimental constraints are also represented; MOT beams (red) propagate through the inhibition plates (yellow) and in between the coils to create an atom cloud (grey) in the center. Expected MOT centre is indicated by a red dot. Numerical simulations respectively give the magnetic field 4.6b and magnetic field gradients 4.6c at MOT position, using the two upper coils only.

Due to the Gauss law for magnetism, it is usual to have a gradient twice as large with opposite sign in one direction (here x), referred to as main quadrupole axis from now on. In this configuration, there is a small imbalance between z and y that can induce an angle, estimated to be around 20°, between the atom quantisation axis and the laser beam propagation axis. This would lead to parasitic polarisation components that only have a small effect onto the MOT efficiency.

For the Rydberg steps, a magnetic field of around 10 G is required. With the two coils above and below the capacitor in *Helmholtz* configuration [2] , simulations have shown an homogeneous magnetic field around this value for a current of around 1 A, which is an acceptable value.

With this configuration, the magnetic field can be properly set and adjusted to realise both configurations. If it is handy, it is also more complex to optimise. For preliminary stages of the experiment where Rydberg excitation is not required, a configuration with larger coils has been used. Larger coils indeed allow for a more homogeneous field, easier to use for coarse optimisation of the setup.

Large coils

In order to create an homogeneous field, three pairs of larger coils have been installed inside the niobium box, one pair along each direction, as depicted in Figure 4.7. Coils for x and y axis have a rectangular shape of 66 mm × 44 mm and are placed at a distance of 38 mm from the MOT center. Due to geometrical constraints, the z axis coils have different dimensions (72 mm × 42 mm and 78 mm × 42 mm for the top and bottom respectively) and are a bit closer (35 mm from the MOT center).

Each coil is wired with superconducting wire *SC T48B-G-0.3mm* from *Supercon-wire*, glued to the holder using *Stycast 1266* to ensure both solidity and a good thermal conductivity. The number of turns is 210 turns for z axis coils and 200 turns for the two other axes. By applying a current of 0.1 A in one of the pairs, the expected magnetic field at the MOT position is around 0.6 G.

The x coils have also been used to produce the quadrupole field required for the 3D-MOT. By applying 1.5 A to the x axis coils in *anti-helmoltz* configuration, the quadrupole field gradient along its main axis is expected to be around $10.5\,\mathrm{G\cdot cm^{-1}}$. In addition, their size allows one to create an homogeneous field in the experiment core region. This can be used to produce compensation fields, that could be useful even when using the compact coils configuration.

---

[2] Strictly speaking, the Helmholtz configuration corresponds to a pair of symmetric circular coils spaced by half their diameter, with a current flow creating a magnetic field in the same direction. For the sake of clarity, the same name is used here in the situation where the magnetic field produced by the pair of coils is in the same direction, with no regard for the exact spacing.

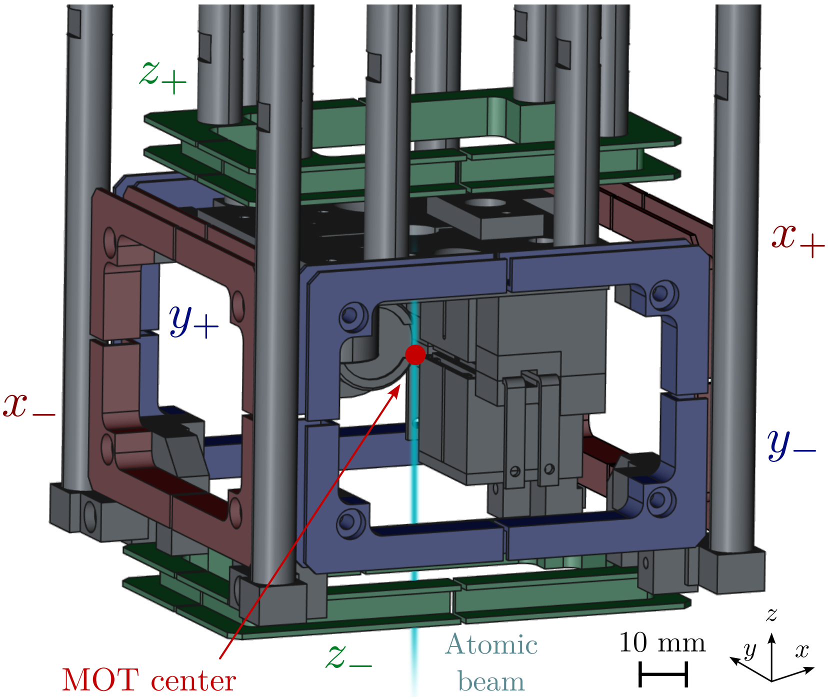

Figure 4.7. – Large coils drawing of the three pairs of used to create homogeneous bias field along x axis (red), y axis (blue) and z axis (green).

Magnetic field characterisation

The real magnetic field can differ from numerical simulations. In order to check that the right field is produced, it has been measured using atomic spectroscopy. Key parameters are the magnetic field produced by each coil, as well as the gradient produced by the x pair in *anti-helmoltz* configuration.

By means of one MOT beam x_- (cooling + repumper) along the x axis in the positive direction, one can indeed see the fluorescence of atoms coming from the 2D-MOT at the 3D-MOT position, as visible in Figure 4.8b. Due to the Zeeman effect, a hyperfine magnetic sublevel $\left|F, m_f\right\rangle$ in the presence of a small enough magnetic field B along its quantisation axis experiences a linear energy shift:

$$\Delta E = \mu_B g_F m_F B\,, \tag{4.3}$$

where μ_B is the Bohr magneton and g_F is the hyperfine Landé g-factor.

The atomic transitions probed in this situation are $\left|5^2S_{1/2}, F=3, m_f\right\rangle \rightarrow \left|5^2P_{3/2}, F=4, m_{f'}\right\rangle$, which consequently experience frequency shifts given by:

$$\Delta f = \mu_B(m_{f'} \cdot g_{F=4} - m_f \cdot g_{F=3})B/h\,, \tag{4.4}$$

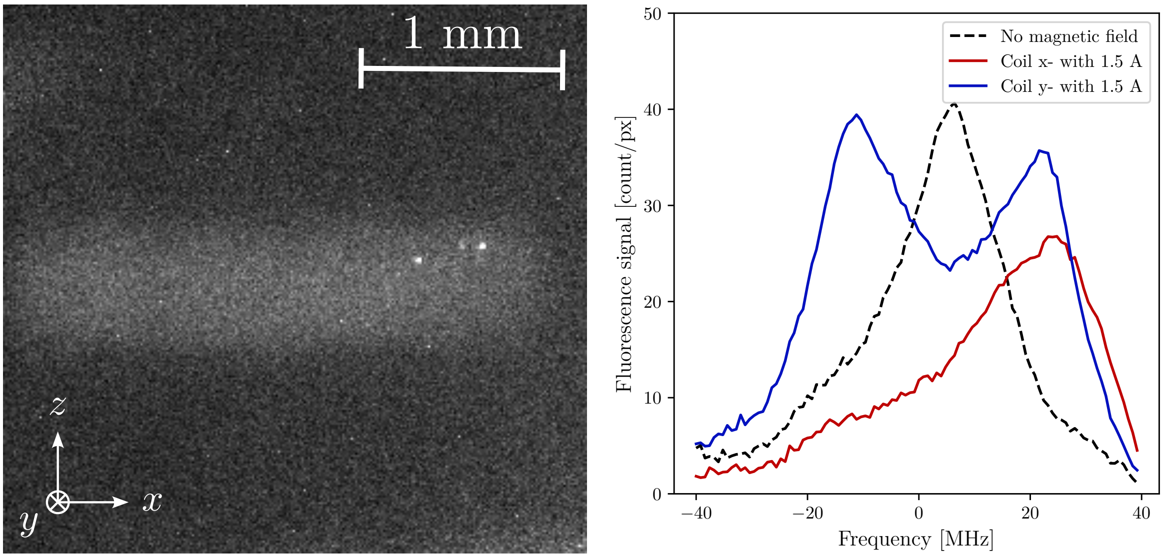

(a) Atoms fluorescence.

(b) Spectroscopy signals.

Figure 4.8. – **Atoms spectroscopy.** Typical fluorescence image 4.8a and associated spectroscopic signals 4.8b for different magnetic field directions, probed with circularly polarised light along x axis.

where $\mu_B g_{F=4}/h = 0.7\,\mathrm{MHz}\cdot\mathrm{G}^{-1}$ and $\mu_B g_{F=3}/h = 0.47\,\mathrm{MHz}\cdot\mathrm{G}^{-1}$ for rubidium 85. By measuring the atom fluorescence for different probe beam frequencies, it is possible to have information about the frequency shift, and so about the magnetic field. Examples of obtained spectroscopy signals are given in Figure 4.8b. For these signals, there are two different behaviours depending on whether the magnetic field is along the laser propagation axis x or along one of the orthogonal axis y and z.

In the first case, the quantisation axis set by the magnetic field is along the laser propagation axis, whose polarisation decomposes purely into σ_+ and σ_- for the atom. Here, the laser beam being right-handed circularly polarised and in the positive x direction, only one of the components appears and there is only one visible peak. For a positive magnetic field, the polarisation is σ_+ and the peak is due to the transitions for which $\Delta m_f = m_{f',F=4} - m_{f,F=3} = +1$. Due to optical pumping, one peak is obtained, corresponding to the transition $m_f = 3 \rightarrow m_{f'} = 4$ whose frequency is linearly shifted by the magnetic field with a slope $\pm\mu_B(m_{f'}\cdot g_{F=4} - m_f \cdot g_{F=3})/h = \pm\ 1.39\,\mathrm{MHz}\cdot\mathrm{G}^{-1}$.

For the second case, the magnetic field, and so the quantisation axis, is orthogonal to the laser beam propagation axis. In that case, the laser polarisation decomposes into a π component (linear part along the quantisation axis) and an equal amount of σ_+ and σ_- components. The π transitions have smaller dipole elements. They then weakly contribute to the fluorescence and are not observed. The $\sigma_\pm$ components lead to two symmetrically shifted peaks, corresponding to transitions where $\Delta m_f = \pm 1$. As

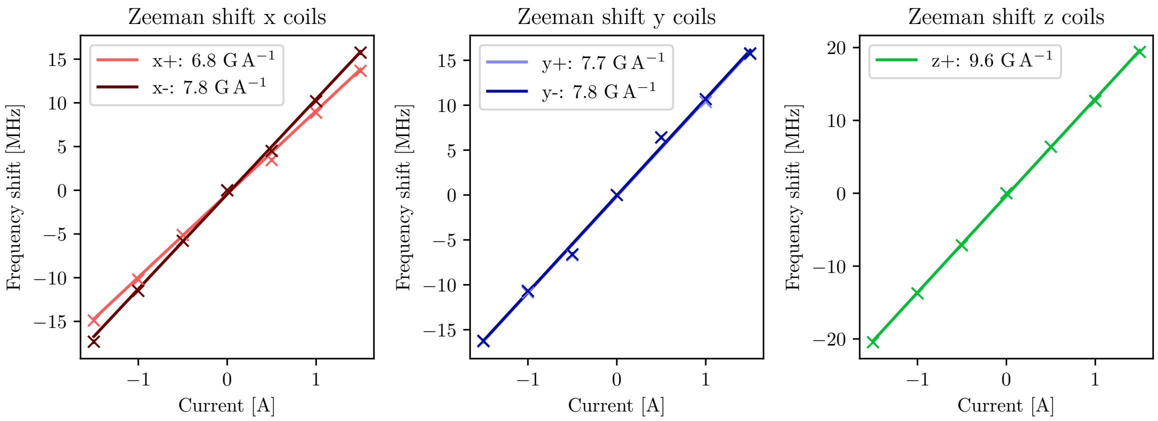

Figure 4.9. – **Magnetic field measurement.** Resonance frequency shift induced by the Zeeman effect, for different currents applied to the large coils. A linear fit (solid lines) allows one to measure the magnetic field produced by each coil for a given current. The z_{-} coil was only qualitatively checked.

Axis Direction	x	y	z
+	$6.8(1)\,\mathrm{G}\cdot\mathrm{A}^{-1}$	$7.7(1)\,\mathrm{G}\cdot\mathrm{A}^{-1}$	$9.6\,\mathrm{G}\cdot\mathrm{A}^{-1}$
−	$7.8(1)\,\mathrm{G}\cdot\mathrm{A}^{-1}$	$7.8(1)\,\mathrm{G}\cdot\mathrm{A}^{-1}$	//

Table 4.1. – **Summary of coils magnetic field** for the three axis, and two directions. No data were taken for the $-z$ coil.

for the previous situation, only states with extreme values ($m_f = \pm 3$) contribute, and their splitting linearly increases with the magnetic field with a slope $\pm 2\mu_B(m_{f'} \cdot g_{F=4} - m_f \cdot g_{F=3})/h = \pm 2.78\,\mathrm{MHz}\cdot\mathrm{G}^{-1}$. Carefully choosing the laser polarisation allows one to maximise the $\sigma_\pm$ components, which are sensible to magnetic field values.

Changing the current applied in the magnetic coils and fitting the spectroscopic signals obtained gives information about the magnetic field produced for a given current. Summary of the field generated for each coil is given in Table 4.1. For x coils, there is a difference of around 15 % between the two coils of the pair. It can be explained by a few millimetres shift in the coils position. Coil for the $z+$ direction creates a slightly larger field since it is closer. Estimated values from numerical simulations were around $6\,\mathrm{G}\cdot\mathrm{A}^{-1}$, and experimental values are thus consistent with the estimations.

Finally, the quadrupole field created by the x axis coils has also been characterised in a similar way. This time, the coils are set in an *anti-Helmholtz* configuration, and the magnetic field gradient is measured. To compensate for the imbalance mentioned

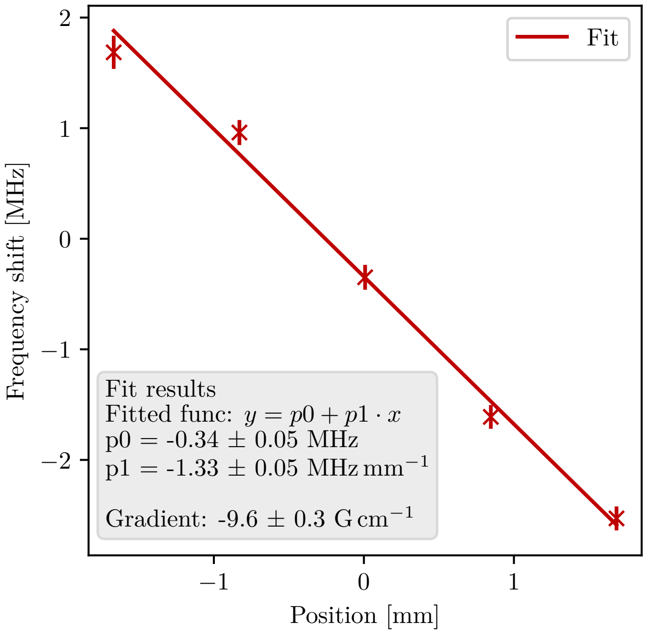

Figure 4.10. – Magnetic field gradient measurement. A Lorentzian fit of the spectroscopic signal for each slice allows one to extract the Zeeman shift for each position 4.10, which allows one to compute the magnetic field gradient.

earlier, the currents are different, with −1.5 A for the x_+ coil and 1.25 A for x_-. To measure the gradient, the same spectroscopy as earlier is performed but on different vertical slices of the image. The image is divided into 5 parts of around 0.8 mm. The size choice is a trade-off between spatial resolution and signal intensity.

Knowing the camera magnification, it is possible to get the central position of each slice and then plot the magnetic field measured for different positions, as depicted in Figure 4.10. This allows one to directly find the magnetic field gradient along x axis which is around $-9.6(3)\,\mathrm{G \cdot cm^{-1}}$. This gradient corresponds to the expected theoretical gradient.[3]

One important remark here concerns the coils operation. The use of superconducting wire required liquid helium to reach the superconducting regime. However, operating at liquid nitrogen temperature is enough to avoid coils excessive heating. At this temperature, resistance is low enough to operate the coils with a few amperes while keeping a constant temperature. The coils heating was monitored by measuring their resistance while operating them.

In addition, using sources with a voltage limitation provides another security. Experiment control was programmed such that coils are switched off between two runs, to

---

[3] This configuration creates a gradient in the wrong direction with respect to the laser beams polarisation set, and, for the 3D-MOT experiment later performed, opposite signs were taken.

avoid useless heating.

4.4.2. Optical setup

In addition to the magnetic field gradients, the realisation of a 3D-MOT requires a set of three pairs of counter-propagating beams. One pair along each of the three orthogonal axes is required to cool atoms in all directions. A circular polarisation in agreement with the gradient direction along each axis is also needed.

As for the 2D-MOT, laser beams are prepared on the preparation optical table, mixed inside a cluster before being sent to the cryostat optical table. A diagram of the geometrical configuration of the 3D-MOT beams can be found in Figure 4.12, and a simplified optical table scheme can be found in Figure 4.11. Due to the geometry imposed by the inhibition region, 3D-MOT beams are divided into two categories.

The first pair of counter-propagating beams is along the quadrupole main axis x, which goes in between the inhibition plates and is co-propagating with the dipole trap beams, as visible in Figure 4.12a. Consequently, the diameter of the beams needs to be smaller than the plates 2 mm spacing. In addition, the beams also go through the 10 cm lens that focuses the dipole trap. For the x cooling beams, a 20 cm lens is then placed outside the cryostat to get collimated beams at the 3D-MOT position. With all of these constraints in mind, the beam diameter before overlap with the dipole trap is 0.64 mm. This gives a waist of 0.32 mm at the 3D-MOT position.

The two other pairs of beams, named transverse beams pairs T_+ and T_-, have less geometrical constraints. The atomic beam is along the $+z$ direction. In order not to have optical elements near the atomic beam, the two transverse cooling directions are at 45° with respect to the z axis. In fact, the quadrupole main axis being the x axis, any pair of orthogonal directions in the Ozy plane could have been used.

For practical reasons, the beams were set to enter the cryostat horizontally, parallel to the optical table. The 45° deflection is realised *in-situ* with a frame with gilded mirrors depicted in Figure 4.12b.

Without the inhibition plates constraint, transverse beams can be larger. This allows one to increase the capture region, which facilitates the alignment. For the early stages of the experiment, beams with a waist of 3.75 mm were chosen. However, the sides of the beams were creating stray light inside the cryostat, considerably reducing the signal over noise ratio. Once the coarse alignment and first dipole trap experiments had been performed, smaller beam were taken. With a waist of 1.47 mm, the new beams led to less stray light and better imaging conditions.

The quadrupole field for the 3D-MOT is set with 1 A on coil x_+ and -0.8 A on coil x_-. This leads to a slightly smaller gradient than the one given in Figure 4.10. The

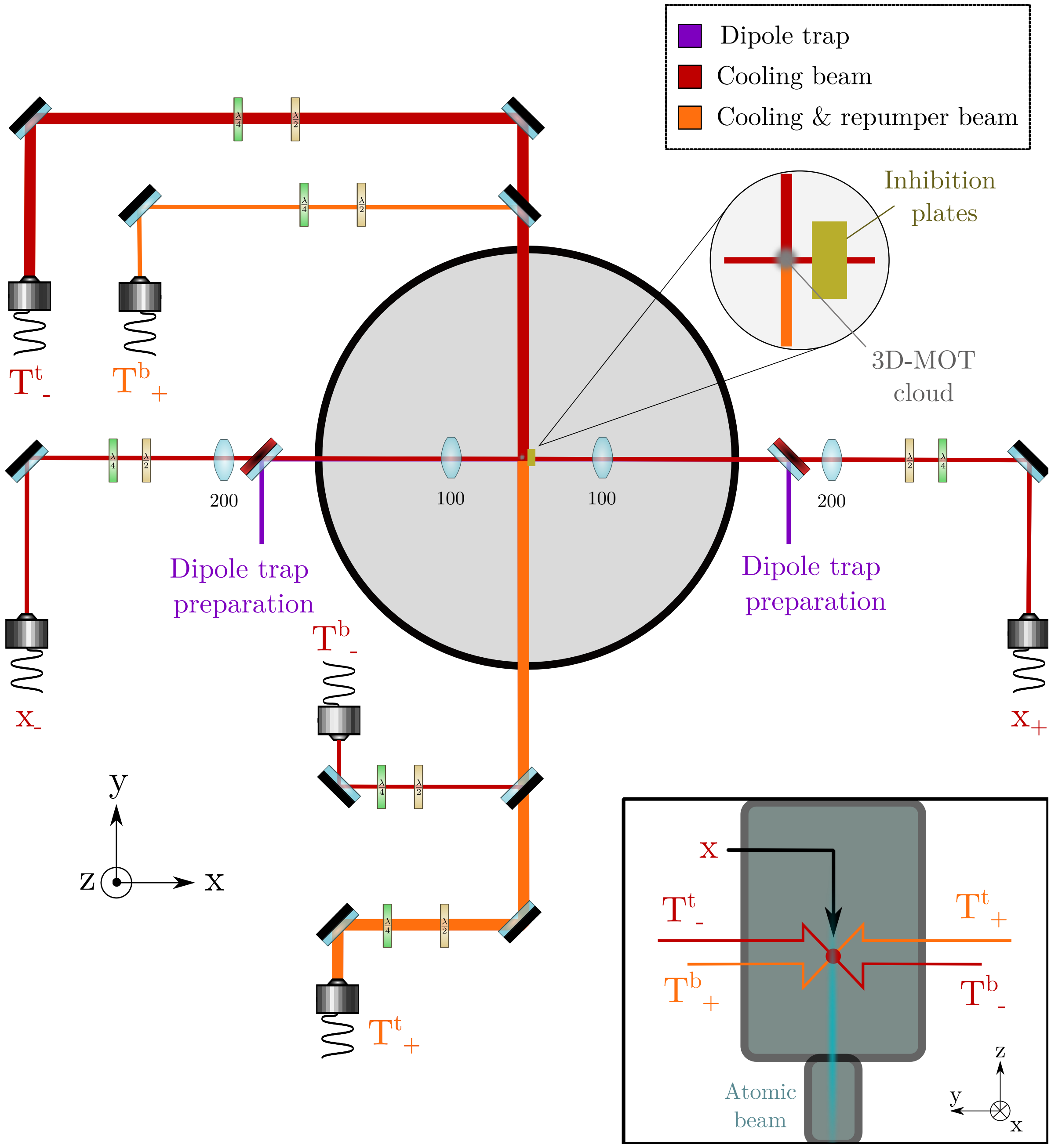

Figure 4.11. – **3D-MOT optical path** on the cryostat optical table. Transverse beams are entering the cryostat at different heights, as depicted on the side view inset. A more detailed plan is given in Appendix D.

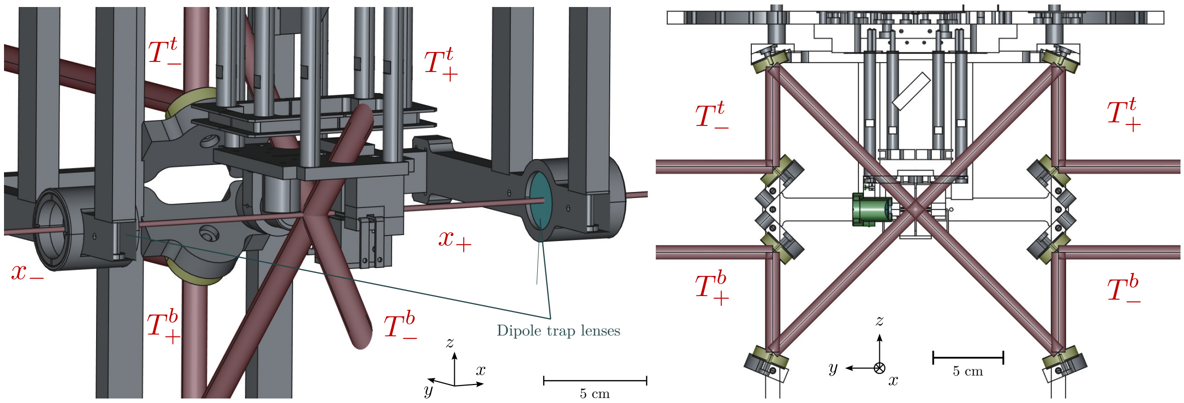

(a) Side view of the X beams.

(b) Side view of the transverse beams.

Figure 4.12. – 3D-MOT beams geometry. Technical drawing of the experiment core with the three pairs of 3D-MOT beams. x pair crosses the lenses used to focus the dipole trap. Crossing of transverse pairs $T_{\pm}$ is realised by a set of golden mirrors inside the cryostat.

current was here limited by the operation temperature, because no liquid helium was available. Despite this limitation, the obtained gradient was large enough to obtain atoms cooling.

The polarisation set for the different cooling beams is therefore a right-handed circular polarisation for x beams and left-handed polarisation for the transverse beams. This polarisation is set and adjusted a quarter-wave plate and a half-wave plate on each arm. This set of plates allows for the generation of any state of polarisation starting from a linear one, which makes it possible to compensate polarisation alteration of the beam.

The cooling beam intensity set for the transverse beams is around $13\,\mathrm{mW}\cdot\mathrm{cm}^{-2}$ per beam, which is around 8.1 times the saturation intensity of the cooling transition. Because of the size difference between the x and the transverse beams and limitations with the cluster power adjustments, the intensity inside the x beams was much higher, around 50 times the saturation intensity. The precise power set into each arm is carefully tuned using the fiber cluster in order to balance each pair and to maximise the number of atoms inside the cloud.

In addition to the cooling light, some repumper intensity was also added to one of the beams pair, in the T_+ pair, with a total intensity of around $17\,\mathrm{mW}\cdot\mathrm{cm}^{-2}$. Surprisingly, the power balance of the repumper light has shown to be determinant for the cloud stability with the largest beams.

Depending on the context, some other configurations have been implemented and will be detailed in the following. Finally, it is important to note that these values are typical operating values. Due to experiment misalignment with time, or other drifting effects, the exact optimal values can vary in time.

4.4.3. Realisation

With the experimental setup presented above, it has been possible to create a cloud of cold atoms used for dipole trap loading. Details about the experimental sequences as well as characterisation methods and results are presented below.

Experimental sequences

In order to have a high number of atoms with a temperature as low as possible, a sequence involving different cooling conditions has been implemented. Indeed, since there is a trade off between the number of atoms and the temperature for a given stage, one usual way is to first realise a 3D-MOT to cool a large amount of atoms and then go to a molasses stage to further lower the atom temperature. A typical cooling sequence is depicted in Figure 4.13. First, the 2D-MOT is switched on and the 3D-MOT cooling beams are switched on with a relatively small red-detuning of around $-1.7\,\Gamma$, and a large intensity of around $8.1\,\mathrm{I}_0$. These parameters have been optimised to maximise the number of atoms in the cloud. The current in the coils is set to get a gradient of around $46\,\mathrm{G}\cdot\mathrm{cm}^{-1}$. In addition, some bias field was found to be required to get a properly set zero magnetic field point. Required bias is around 0.17 G along the $+z$ direction (18 mA in the z coils pair). This step lasts for around 1 s to be sure to reach atom number saturation (see Figure 4.15c).

Once the cloud is saturated, the 2D-MOT is switched off and the 3D-MOT cooling beams detuning is lowered to around $-7.7\,\Gamma$ in order to further reduce the atom temperature. The intensity slightly increases due to the AOM configuration. The magnetic field gradient from the x coils is then switched off to prepare for the molasses stage. Beforehand, laser beams are switched off in order to prevent atom loss due to the unstable magnetic field during this step. After 2 ms, the gradient is turned off and the magnetic field is stable again. Note that the bias field is kept on, in order to compensate for parasitic field.

After that, the molasses stage is realised. Laser beams are then switched back on with a lower intensity of around $3.9\,\mathrm{I}_0$ and a detuning of $-14.9\,\Gamma$ to reach the lowest possible temperature. This step is usually performed for 5 ms before going on with the experiment.

The cloud can then be imaged by setting the beams in the same conditions as for the first step. Typical exposure time is between 0.2 and 20 ms depending on the property studied and the camera in use. Unless it is explicitly mentioned, the imaging system

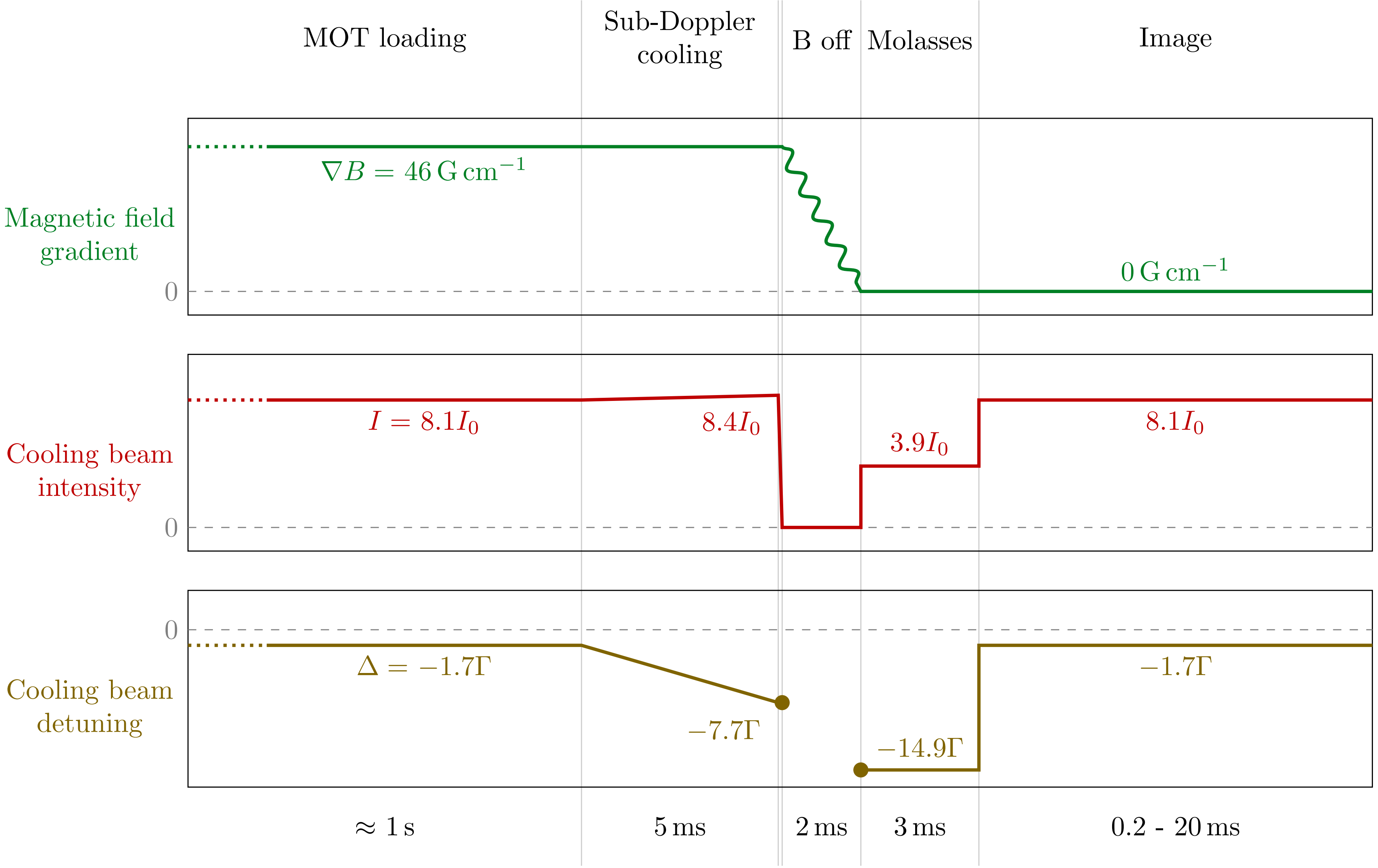

Figure 4.13. – **Typical cooling sequence.** Cooling lasers parameters and the magnetic field gradient are represented. Gray dashed lines indicate the zero value. Detuning is given with respect to the cooling transition, in linewidth unit $\Gamma = 2\pi \cdot 6.06\,\mathrm{MHz}$, and intensity is given in saturation intensity units $I_0 = 1.67\,\mathrm{mW \cdot cm^{-2}}$. Repumper light and magnetic field bias are also present during theses stages.

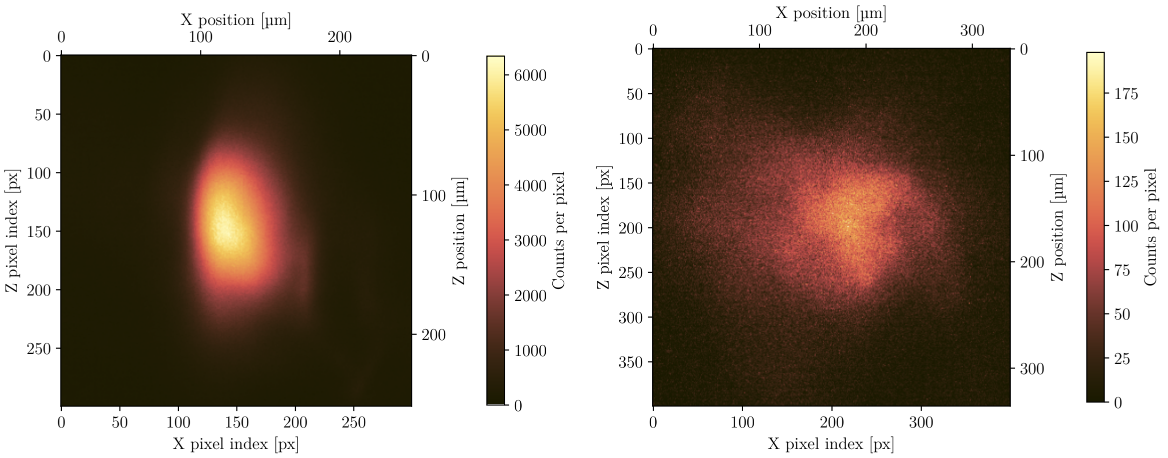

(a) 3D-MOT **(b)** Molasses

Figure 4.14. – **3D-MOT and molasses images.** Images of saturated 3D-MOT and molasses, taken with camera *ZL41 Wave*. Exposure time is 20 ms.

used is the side camera presented in section 3.3.1. An alternative is the *Zyla* sCMOS camera, also used for the dipole trap imaging. Typical fluorescence images of the cloud after each step are given in Figure 4.14, using the *Zyla* camera.

Note that for imaging, cooling beams can induce stray light. The associated amount of noise can depend on the conditions, for example if the beams intensity or frequency is scanned. Background images are hence taken and removed for the fluorescence measurement, leaving only the atoms light, if the noise fluctuations are low enough.

Atom number estimation

Measuring 3D-MOT fluorescence intensity gives information about the number of atoms in the cloud. In fact, the number of photons collected by the camera reads:

$$F_{col} = N_{atoms} \cdot R_{sc} \cdot \tau \cdot \frac{\Omega}{4\pi}, \tag{4.5}$$

where N_{atoms} is the number of atoms inside the cloud, τ the exposure time, Ω the solid angle with which photons are collected and R_{sc} the scattering rate. The cooling beams being off-resonance, the scattering rate reads:

$$R_{sc} = \frac{\Gamma}{2} \cdot \frac{I/I_{sat}}{1 + 4(\Delta/\Gamma)^2 + I/I_{sat}}, \tag{4.6}$$

where I is the laser intensity, I_0 and Γ the saturation intensity and linewidth of the cooling transition and Δ the detuning between the laser and the cooling transition. Corresponding values are given in Figure 4.13. All together, it gives an estimation of the number of atoms inside the cloud at around 9.8×10^5 atoms for the 3D-MOT. This value is far from the state of the art 3D-MOT, but here only few atoms are required to get enough Rydberg atoms. A more important parameter is the temperature, and the 3D-MOT was optimised towards low temperature rather that large atom number. The amount of atoms obtained is enough to efficiently load the dipole trap and no further optimisations were attempted.

The number of atoms in the molasses can be estimated in a similar way, by comparing the total fluorescence of the images depicted in Figure 4.14. Due to the large frequency detuning and smaller intensity, the atoms fluorescence is weaker. In addition, atoms are less localised without the help of a magnetic field. The signal over noise ratio is worse, and the estimation less precise. However, the use of the most sensitive camera allows one to collect enough light. Taking all this into account, atom number in the molasses is measured to be of the order of 1×10^5 atoms.

Loading and trapping time

One of the essential quantities to know about a 3D-MOT are the loading and trapping times. The first one gives information about the shortest duration needed to get a saturated cloud of atoms, which is necessary in order to get a stable loading into the dipole trap from shot to shot. The later corresponds to the timescale for which atoms are lost from the cloud once the 2D-MOT is off.

Since the atoms cooling relies on fluorescence emission, these quantities can be directly probed by looking at the cloud fluorescence over time. Typical sequences and corresponding fluorescence signals are depicted in Figure 4.15. To measure the loading time, the cooling beams, repumper and 2D-MOT are switched on, and the camera takes an image with 0.2 ms exposure at different times after the loading started (see Figure 4.15b). Fluorescence saturates when the maximum number of atoms is reached. Estimated loading time is 390 ms.

For the trapping time, the 3D-MOT is loaded until saturation is reached, and then the 2D-MOT is switched off for some time before an image is taken, again with 0.2 ms exposure time (see Figure 4.15d). The timescale associated to the 3D-MOT depletion is found to be of the order of 295 ms. This short trapping time is likely associated to the vacuum quality in the chamber. Gauges on the outer shell of the cryostat measured pressures of the order of 5×10^{-8} mbar, and the pressure can explain this trapping time [137] [138]. Another source of local vacuum deterioration can come from the leak on the helium reservoir mentioned in section 3.1.3.

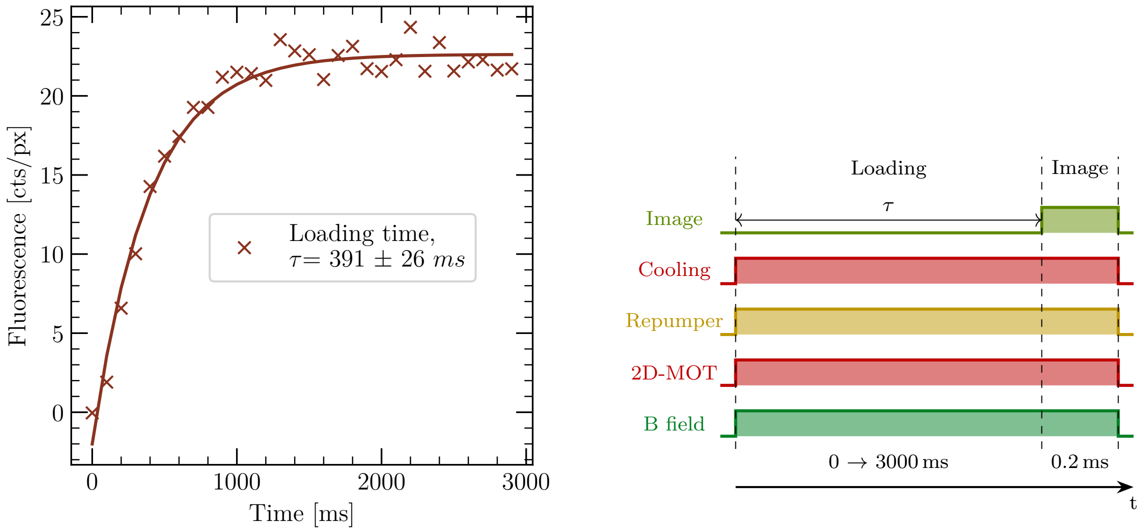

(a) Loading time measurement

(b) Loading time sequence

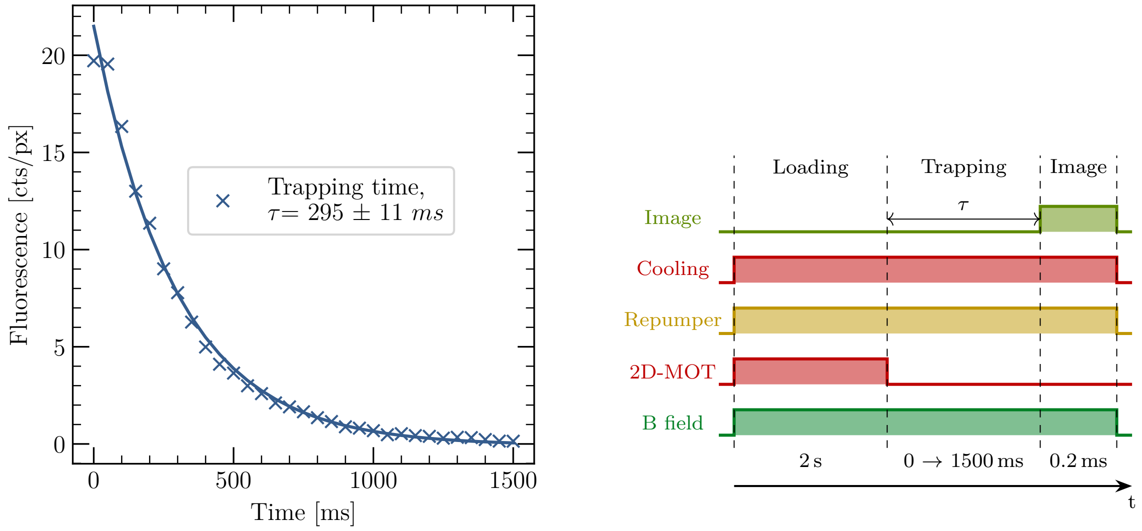

(c) Trapping time measurement

(d) Trapping time sequence

Figure 4.15. – Loading and trapping time measurement. Fluorescence signals are given in 4.15a and 4.15c. An exponential fit of allows one to measure the characteristic time associated. Sequences used to obtain these measurements are given in 4.15b and 4.15d.

Cloud temperature measurement

The last cloud property to estimate is the atoms temperature. Indeed, atoms are to be loaded in a dipole trap, with a typical depth of the order of 1 mK. Atoms need to have a temperature below this limit to remain trapped in the dipole trap. In addition, the colder the atoms, the closer they are to the bottom of the trap. This is a requirement to approximate the trap to an harmonic trap, which is useful for the trap characterisation.

A typical way to estimate the atom temperature is through a time of flight (ToF) measurement [139]. For this measurement, atoms are released for some time. The clouds then expands, with a velocity which depends on the atom temperature. The hotter the atoms, the faster the cloud expansion. Measuring the cloud size over time allows one to know its expansion speed, and, with it, the atom temperature.

A common assumption is that the atoms velocities within the cloud follows a Maxwell-Boltzmann distribution, with a standard deviation along a direction, for example x, which reads:

$$\Delta v_x^2 = \frac{k_b T}{m_{Rb}}, \tag{4.7}$$

where k_B is the Boltzmann constant, m_{Rb} the rubidium atomic mass and T the cloud temperature associated to this direction. Inside the cloud, the associated atoms density can be approximated by a Gaussian distribution.

For a time of flight measurement, the cloud is first loaded until saturation. The cooling beams are then switched off, and the cloud is left to expand for some time. It is then imaged to estimate the cloud size after expansion. Due to the velocity distribution, the cloud density after expansion remains Gaussian, with a position standard deviation, which reads:

$$\Delta x(t) = \sigma_x(t) = \sqrt{\sigma_0^x + \frac{k_B T}{m_{Rb}} t^2}, \tag{4.8}$$

where σ_0^x is the position standard deviation right before the expansion. A 2D Gaussian fit of several fluorescence images allows one to have an estimation of $\sigma_x(t)$, and fitting time evolution directly gives access to the atom temperature T. The two fit directions are labelled a and b, and are not necessarily x or z directions.

Sequences for the 3D-MOT and the molasses temperature measurements, as well as corresponding time of flight measurements are given in Figure 4.16. Note that a short exposure time is critical here to prevent the imaging beams from affecting the expanded cloud geometry. These measurements allowed us to extract typical temperatures after the 3D-MOT and molasses stages, found to be respectively around 50 μK and 10 μK. This measurement also gives a measurement of the initial cloud size, with a position standard deviation estimated to be around 0.2 mm.

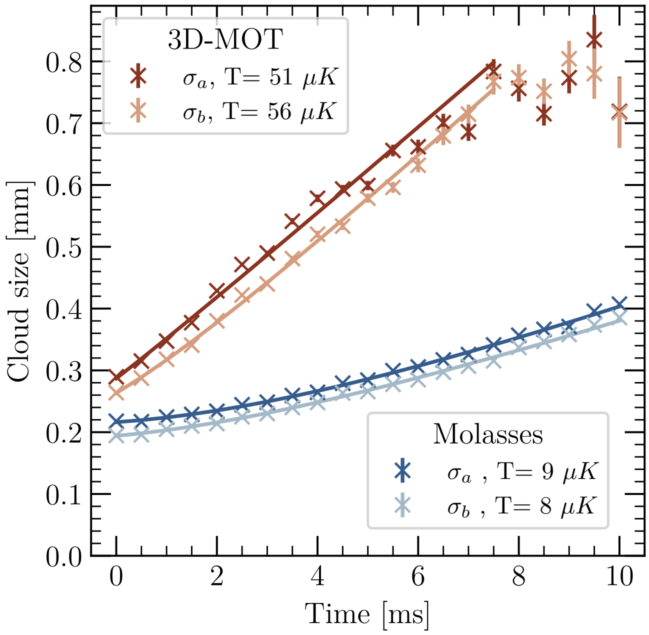

(a) Time of Flight (ToF) curves

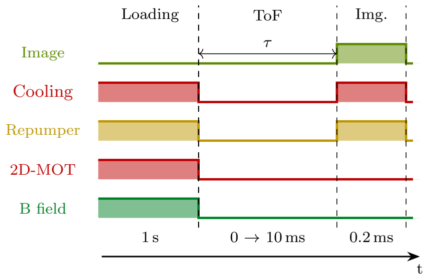

(b) 3D-MOT sequence

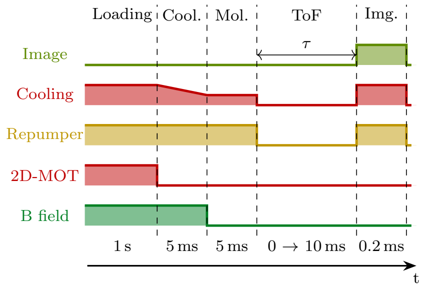

(c) Molasses sequence

Figure 4.16. – 3D-MOT and Molasses temperature measurements. Fit of the clouds size σ for different times of flight 4.16a with Equation 4.8 gives the clouds temperatures along the two main directions. Details about the sequences used are given for the 3D-MOT 4.16b and molasses 4.16c clouds.

The temperature after molasses stage is below the Doppler limit thanks to sub-Doppler cooling effects. The associated temperature is way below the 1 mK dipole trap depth expected.

Conclusion

The first step toward inhibition of the spontaneous emission relies on the efficient cooling of atoms in order to be able to trap them. This is performed using a 2D-MOT and a 3D-MOT, followed by a molasses stage. This requires a precise control of the magnetic field inside the experiment core. Numerical simulations have been used to design the experiment, and characterisations were performed to validate its experimental implementation.

Obtention of the cold atoms cloud has been shown to be especially challenging in the present configuration. The reduced optical access has been associated to a lot of stray light and many uncertainties about the behaviour of optical elements inside the cryostat. Additional difficulties related to the cryogenic environment were also faced, especially vacuum issues induced by leaks from the helium reservoir, leading to a vacuum above 1×10^{-6} mbar, a vacuum high enough to prevent first signal observation [138].

Overcoming these issues, and after a careful optimisation, a cloud of approximately 1×10^{5} atoms at $8\,\mu$K was obtained. This temperature is sufficient for an effective loading in the bottom of a 1 mK dipole trap.

To ensure atom number loading saturation the full step typically lasts for 1 s and is the longest step. The following steps consist of the efficient loading and transport of atoms between the capacitor plates with a dipole trap.

Atoms cooling summary

2D-MOT

- Velocity: $22\,\mathrm{m \cdot s^{-1}}$
- Atom flux: 3.4×10^{6} atoms $\cdot\,\mathrm{s}^{-1}$

3D-MOT

- Loading time (3τ): ≈ 1 s
- Temperature: $50\,\mu$K
- Atom number: $\approx 1 \times 10^{6}$ atoms
- Size (σ): 0.2 mm

Molasses

- Atom number: $\approx 1 \times 10^{5}$ atoms
- Temperature: $8\,\mu$K

Chapter 5

Atoms trapping and transport

Forward, in perpetual rebellion!
Which was, and is, and is to come
Glory and honour to that which liveth for ever and ever!
Out of the shadows and into the light
Once again!

— Trespasser, *Forward Into the Light!*

Once a cloud of cold atoms is obtained, it is necessary to move the atoms between the two conductive plates, where the inhibition will take place. This is realised by means of an optical dipole trap in a conveyor belt configuration. Like for the magneto-optical traps, its suffers from the low optical access due to the cryogenic environment.

To move the atoms, they are first transferred from the MOT cloud to a dipole trap. The atom trapping relies on the conservative dipole force. The trapping potential is realised with two counter-propagating beams, creating a standing wave. For red-detuned laser beams, ground state atoms are trapped in the anti-nodes.

By changing the relative detuning between the two laser beams, one can move the interference pattern, thus conveying the atoms between the two plates. To counterbalance the effect of the limited Rayleigh length, the waist position has to be displaced accordingly.

The first part of this chapter will provide a short introduction to the dipole trapping of Rubidium atoms. Details about the experimental implementation associated to the corresponding characterisations will be given. The second part is dedicated to the atoms transport and its optimisation.

5.1. Atoms trapping in a standing wave

In order to have a good control of their positions between the two plates, ground state atoms are trapped inside a dipole trap. A conveyor belt configuration is used for effective atoms transport. This section introduces the basics of dipole trapping as well as some theoretical estimations about the configuration used in this experiment. A more exhaustive discussion about dipole trapping can be found in the literature [132].

5.1.1. Neutral atom dipole trapping

The idea to use optical dipole force to trap particles emerged in the 60's [140], leading to the first trapping of micron-sized particles less than ten years later by Ashkin [141]. In the mean time, the possibility of trapping atoms as well has been considered by Letokhov [142] and neutral atoms have been optically trapped for the first time in the 80's [76].

Particle trapping – classical approach

The general idea can be formulated from a classical point of view which holds for particles as well as for atomic systems. When placed into laser light, a polarisable particle gets an induced dipole moment **p**. This dipole is proportional to the laser electric field **E** and to the particle polarisability α, which is complex and depends on the laser frequency ω_L.

The induced dipole then interacts with the electric field. This interaction is associated to a potential U^C_{dip} reading:

$$U^C_{dip}(\mathbf{r}) = -\frac{1}{2}\langle \mathbf{p}(\mathbf{r}) \cdot \mathbf{E}(\mathbf{r}) \rangle = -\frac{1}{2\epsilon_0 c}\operatorname{Re}(\alpha) I(\mathbf{r}), \tag{5.1}$$

where the brackets denotes the time average over rapid oscillating terms, $I(\mathbf{r}) = 2\epsilon_0 c|\mathbf{E}(\mathbf{r})|^2$ is the laser intensity and $\mathbf{r}$ is the particle position. The force $\mathbf{F}_{dip}$ associated to this potential reads:

$$\mathbf{F}_{dip}(\mathbf{r}) = -\nabla U_{dip}(\mathbf{r}). \tag{5.2}$$

For $\operatorname{Re}(\alpha) < 0$, this force attracts the particle to the field maximum. One application example are optical tweezers, widely used for trapping nano-particles or neutral atoms.

Since the dipole force is conservative, it doesn't cool the atoms. Atoms trapped in the bottom of the trap are those which have a temperature much lower than the trap depth. This motivates the use of magneto-optical traps to cool down the atoms beforehand.

Atom trapping - quantum approach

For the particular case of atom trapping, the above description can be used, provided that the atom polarisability is known. The latter can be computed using a classical approach, with Lorentz's classical oscillator description of an atom. Another possibility is a semi-classical approach, where the atom is described as a two-level quantum system interacting with a classical field. Both approaches give good approximations for many atoms in the very low saturation regime. They can however fail to describe some behaviours, especially those induced by the multi-level structure.

To better describe real atoms with more complex energy structure, one can use the "dressed state" approach to describe the light-matter interaction. Indeed, as previously discussed in subsection 1.3.3, an atom interacting with a far-detuned oscillating field experiences a light-shift of its energy states. More specifically, for a red-detuned laser of light intensity $I(\mathbf{r})$, an atom sees its electronic ground state energy reduced. This energy state lowering directly corresponds to a dipole trapping potential U^Q_{dip} which reads:

$$U^Q_{dip} = U_{dip} = \alpha_0 I(\mathbf{r}), \tag{5.3}$$

where α_0 depends on the laser light polarisation and wavelength.

In the context of this experiment, the trapping of ^{85}Rb atoms is performed with a 820 nm laser, far-detuned from the Rubidium D1 and D2 lines, respectively around

795 nm and 780 nm. Using *ARC-Alkali Rydberg Calculator*[68] it is possible to compute the associated ground state $^5S_{1/2}$ light-shift polarisability α_0 for a linearly polarised light, whose value is found to be:

$$\alpha_0/h = -18\,\mathrm{MHz}/(\mathrm{mW}/\mu\mathrm{m}^2)\,. \tag{5.4}$$

Note that there is in principle a dependence on the hyperfine state considered. The difference is especially large for a non-linear polarisation. However, for a linear polarisation, the difference is below 1% and is here neglected. Knowing the polarisability, atom trapping then only depend on the laser intensity profile.

Similarly, the excited state $^5P_{3/2}$ is lightshifted, with a polarisability

$$\alpha_1/h = +5\,\mathrm{MHz}/(\mathrm{mW}/\mu\mathrm{m}^2)\,. \tag{5.5}$$

Consequently, the $\left|^5S_{1/2}\right\rangle \rightarrow \left|^5P_{3/2}\right\rangle$ transitions are in average light-shifted by an amount:

$$(\alpha_1 - \alpha_0)/h = 23\,\mathrm{MHz}/(\mathrm{mW}/\mu\mathrm{m}^2)\,. \tag{5.6}$$

Note that for the excited state, different m_f states have different lightshift as well, this time with a non negligible difference. The value of α_1 given here is the average over all m_f, which is independent of F.

Trapping potential

The dipole trap is used to transport the atoms from the 3D-MOT region to the inhibition region, along the x axis. A tight confinement is thus required along the axial direction to precisely control the atoms position. To provide this confinement, a conveyor belt configuration has been chosen.

The static standing wave is obtained by means of two counter-propagating Gaussian beams, each one having a power $P/2$, a wave-vector $k_L = 2\pi/\lambda_L$ and a waist w_0. Interference of the two beams leads to the intensity profile, represented in Figure 5.1, which reads:

$$I(x,\rho) = I_{max}\,\frac{w_0^2}{w^2(x)}\,\exp\left\{-\frac{2\rho^2}{w^2(x)}\right\}\cos^2(k_L x - \Phi)\,, \tag{5.7}$$

with the maximum intensity $I_{max} = 4P/(\pi w_0^2)$, waist profile $w(x)^2 = w_0^2(1 + x^2/z_R^2)$ and Rayleigh length $z_R = \pi w_0^2/\lambda_L$, ρ and x being the radial and axial cylindrical coordinates.

The position of the interference fringes depends on the phase shift Φ between the counter propagating beams. For beams at the same frequency, this phase corresponds to a phase delay between the two beams, $\Phi = (\varphi_0 - \varphi_1)/2$. This shift is time-independent for a standing wave.

Following previous arguments, associated trapping depth corresponds to the intensity maximum and is given by $U_0 = \alpha_0 I_{max}$. In the experiment, the beam waist (2σ) was chosen to be around $w_0 = 12.3\,\mu$m with a total power of around $P = 250\,$mW (I=2.1 mW $\cdot\,\mu$m^{-2}). It leads to a maximum ground state lightshift:

$$\Delta f_{gs} = U_0/h = -38\,\text{MHz}\,, \tag{5.8}$$

where h is the Planck constant. Associated Rayleigh length is z_R =0.58 mm.

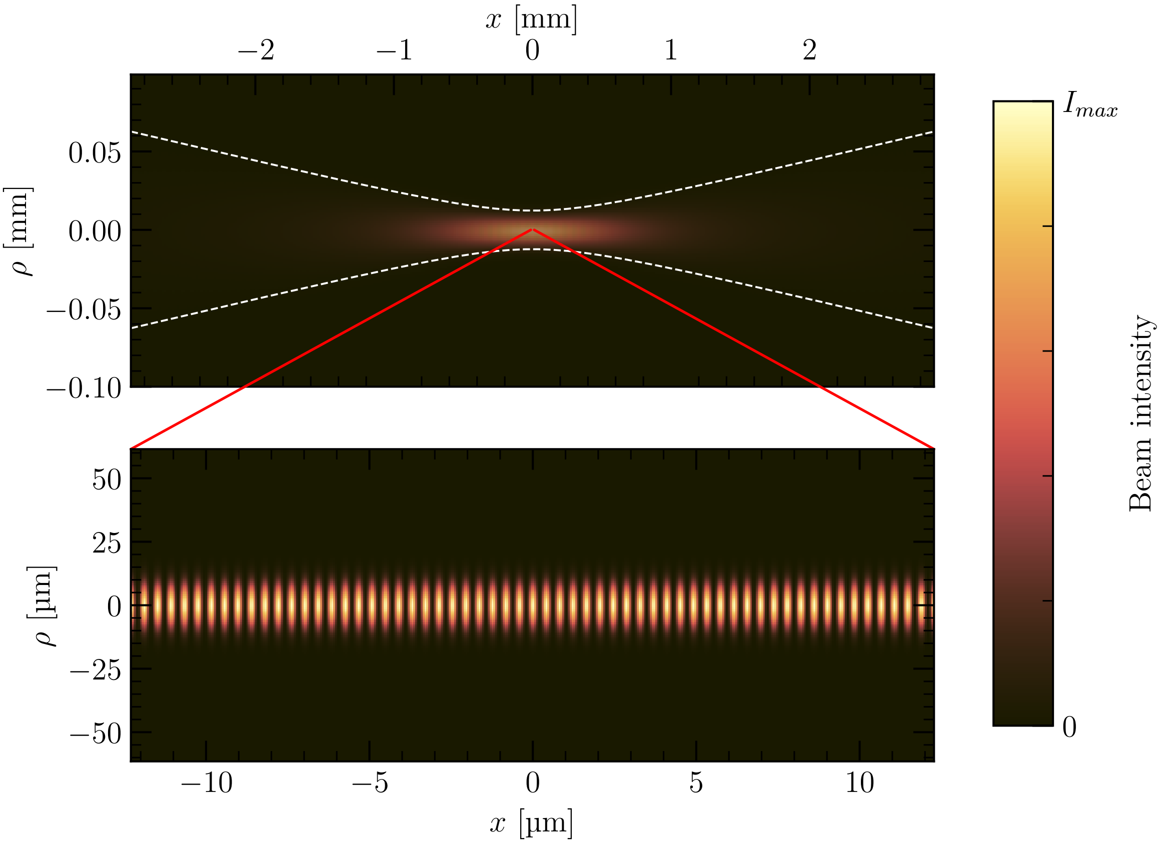

Figure 5.1. – Conveyor belt intensity profile. Intensity profile of the dipole trap in the conveyor belt configuration. Two counter propagating Gaussian beams create interference fringes. Ground state atoms are trapped in the intensity maxima. Dashed lines indicate the waist profile $w(x)$.

It is usually convenient to express the trapping depth in temperature units. It is found to be:

$$U_0/k_B = -1.82\,\text{mK}\,, \tag{5.9}$$

where k_B is the Boltzmann constant.

This value has to be compared with the 3D-MOT cooling value found in the previous chapter to be around $8\,\mu$K. The cooling temperature is way lower than the dipole trap temperature. It means that atoms will effectively be trapped in the bottom of the potential.

In general, the trap depth per intensity unit is given by:

$$-\alpha_0/k_B = 0.86\,\mathrm{mK}/(\mathrm{mW}/\mu\mathrm{m}^2)\,. \tag{5.10}$$

Scattering rate

If the lightshift effect shifts the energy of the eigenstates, it also changes the associated eigenvectors, as seen in Equation 1.61. The non-zero probability for dressed ground states to populate bare excited state is associated to photons scattering. In practice, essential contributions are due to $\left|5^2P_{3/2}\right\rangle$ and $\left|5^2P_{1/2}\right\rangle$ states, and the associated scattering rate can be reduced to:

$$\Gamma_{sc} = \frac{\pi c^2}{2\hbar}\left(\frac{2\Gamma_{3/2}^2}{\Delta_{3/2}^2\omega_{3/2}^3} + \frac{\Gamma_{1/2}^2}{\Delta_{1/2}^2\omega_{1/2}^3}\right) I\,, \tag{5.11}$$

where Γ_i, ω_i and $\Delta_i = \omega_L - \omega_i$ are respectively the decay rate, angular frequency and detuning associated to the transition $\left|5^2S_{1/2}\right\rangle \rightarrow \left|5^2P_i\right\rangle$. For the typical intensity mentioned above, scattering rate is found to be around $\Gamma_{sc} = 96\,\mathrm{photons}\cdot\mathrm{s}^{-1}$.

The diffusion of trap photons is associated to a heating rate:

$$\Gamma_{heat} = \frac{2\,E_{rec}\,\Gamma_{sc}}{k_B} = 32\,\mu\mathrm{K}\cdot\mathrm{s}^{-1}\,, \tag{5.12}$$

where $E_{rec} = k_B\,T_{rec} = \hbar^2 k_L^2/2m_{Rb}$ is the recoil energy associated to the diffusion of one trap photon, leading to a temperature increase of T_{rec}.

From this, one can estimated the trapping time limit associated to the diffusion of trap photons:

$$\tau_{sc} = \frac{U_0}{2E_{rec}\,\Gamma_{sc}} = 57\,\mathrm{s}\,. \tag{5.13}$$

Scattering rate and trap depth being both linear in laser beam intensity, this value is independent from the laser power.

This time equals the trapping time in the dipole trap if the atoms are loaded in the bottom of the trap, and if it is the only source of atoms loss. In practice, other loss mechanisms exist. For example, additional heating can come from laser intensity fluctuations or from frequency fluctuations inducing fringes shaking. Finally, atoms can get kicked out of the trap by collisions with residual gases.

Oscillation frequencies

One can approximate the bottom of the trap by a harmonic oscillator potential. When performing a Taylor expansion around the trap minimum within Rayleigh length, where $\rho \ll w_0$ and $x \ll \lambda_L$, the trapping potential becomes:

$$U(\rho, x) \approx U_0 \left(1 - \frac{2\rho^2}{w_0^2} - k_L^2 x^2\right), \tag{5.14}$$

which is a harmonic potential $V(q) = \kappa q^2/2$, with $q \in \{\rho, x\}$. A particle of mass m in such a potential oscillates with a frequency $\omega = \sqrt{\kappa}/m$. This allows one to identify radial and axial oscillation frequencies Ω_ρ and Ω_x for trapped atoms, which read:

$$\Omega_\rho = \sqrt{\frac{-4U_0}{m_{Rb} w_0^2}}, \qquad \Omega_x = \sqrt{\frac{-2U_0 k_L^2}{m_{Rb}}}. \tag{5.15}$$

For typical experimental values mentioned above, oscillation frequencies can be found to be around $\Omega_\rho/2\pi = 11\,\mathrm{kHz}$ in the radial direction and $\Omega_x/2\pi = 730\,\mathrm{kHz}$ in the axial direction.

The oscillation frequency in the axial direction is related to the maximal velocity acceptable for atom transport. In fact, the atom transport needs to be adiabatic with respect to the atoms oscillations along the transport axis x. Oscillations over a distance λ_L with a frequency Ω_x give a typical adiabatic velocity limit $v_{ad} = \Omega_x \lambda_L = 0.6\,\mathrm{m \cdot s^{-1}}$. This value is above the typical transport velocities used in the following, and the adiabaticity condition should hold.

These characteristic's can also be used for the trap characterisations. Their ratio reads

$$\frac{\Omega_\rho}{\Omega_x} = \frac{k_L \sqrt{2}}{w_0}. \tag{5.16}$$

The wave-vector k_L is well known for the single mode laser used. This ratio can be directly used to measure w_0.

5.1.2. Experimental setup

The optical dipole trap is realised with a laser at 820 nm, provided by a high power single mode tunable diode with a tapered amplifier *TA pro* from *Toptica*. It provides up to 3 W of laser power. The trapping being used in the far-detuned regime, there is no need for frequency lock of the laser.

Detailed illustration of the optical path is given in Figure 5.2, and the main elements are summarised here. Two blocks used for atoms transport are depicted here, and described in the second part of this chapter. The beam is brought to the optical table by an optical fiber directly connected to the laser head, to ensure a higher coupling stability. It is then split into two arms, named DT_0 and DT_1.

Each arm then goes through one AOM *MT110-B50A1,5-IR* from *AA Opto-electronic*, centered at 110 MHz and used to control the beam power. It is useful to adjust the trap depth during the different steps. After the AOM, two beam expanders are used to adjust the beam size before it enters the cryostat.

The AOM and beam expanders are also used to control the atoms transport. The associated setup is discussed in subsection 5.2.2. It especially involves tunable lenses used to control the waist positions of the beams. This feature was also used for the standing wave to make sure that both beams waist are at the same position, in front of of the imaging system.

Each beam is then overlapped onto the x axis MOT beams using short-pass dichroic mirrors *T785spxxr-UF2* from *Photon lines* just before entering the cryostat. These mirrors are reflecting at 820 nm and transmitting at 780 nm.

On the path, a pass band filter at 820 nm *FBH820-10* from *Thorlabs* is put to filter out parasitic 780 nm and 796 nm light coming from the trap laser. This parasitic light was responsible for atom loss and reduced trapping time. Transmission at 820 nm was measured to be around 97 %.

The beams then cross the different cryogenic shield windows. Each of the three windows crossed before the experiment core has a transmission of around 98 %. Beams are then focused inside the experiment core by means of 100 mm focal length plano-convex lenses (*48-764* from *TechSpec*). Expected waist size at the trap position is 12.3 μm. Taking into account losses before the cryostat, typical intensity obtained for a conveyor belt with maximal power on each beam was estimated to be up to 4.24 $\mathrm{mW} \cdot \mu\mathrm{m}^{-2}$, corresponding to a 3.7 mK trap depth.

It is to be noted that the relative alignment of the two beams was particularly critical. To obtain well-contrasted interference fringes, the micrometer sized beams have to be well overlapped, and in the focal plane of the imaging system.

5.1.3. Realisation

Using this setup, it has been possible to load cold atoms from the 3D-MOT cloud into the dipole trap. Several characterisations have then been performed in order to get a better understanding of the trap properties and use it more efficiently in the next steps.

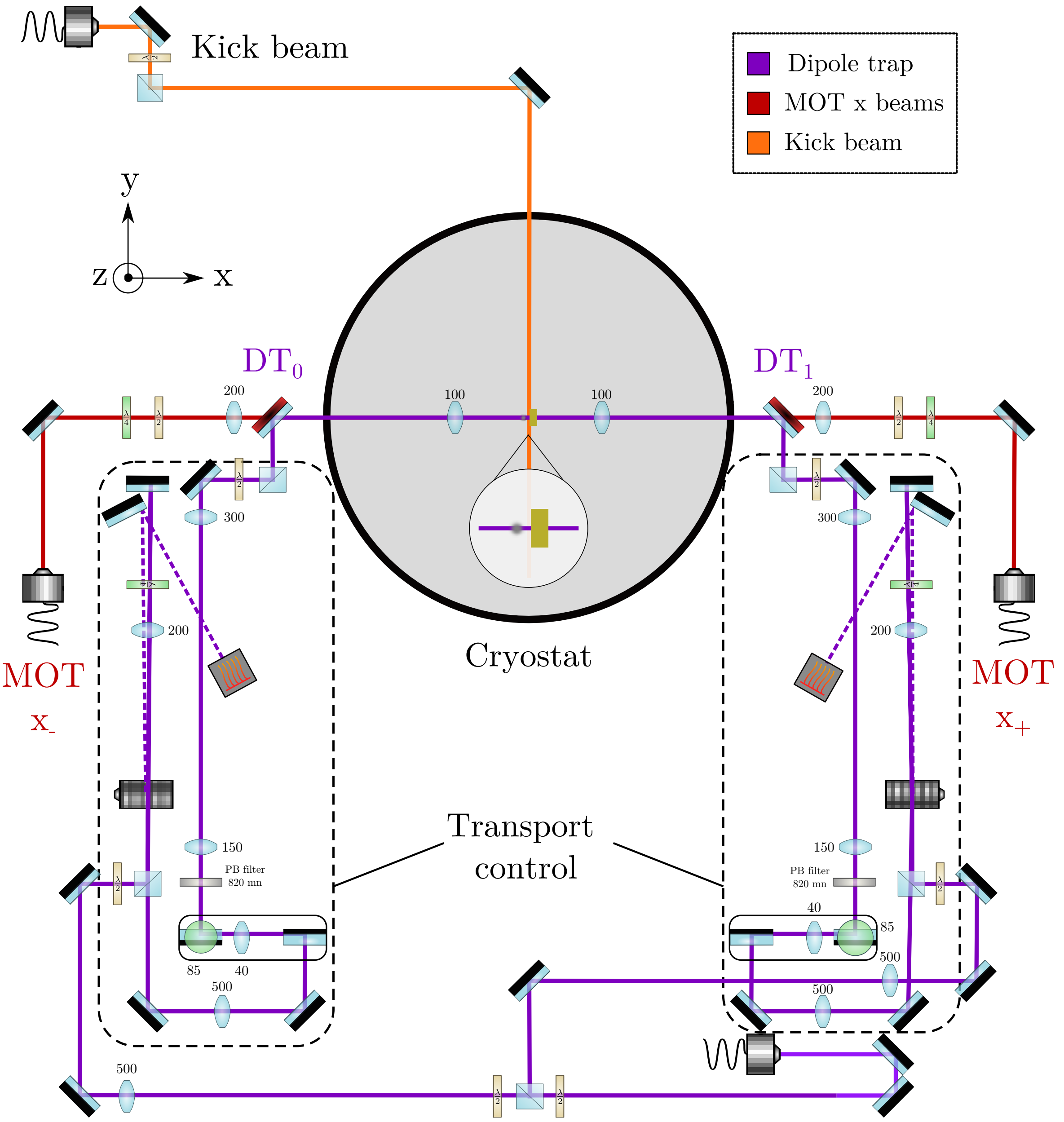

Figure 5.2. – **Dipole trap optical setup:** drawing of the optical table with elements involved in the dipole trap generation and characterisation. DT beam is split into two arms DT_0 and DT_1, each one going through a block used for transport control, before being focused inside the cryostat. Cooling beams in the x directions are overlapped with the DT by a dichroic mirror. A kick beam orthogonal to the trap propagation axis is used for characterisations.

Experimental sequences

The loading of the dipole trap is directly realised from the cold atom cloud. To do so, the cooling sequence is realised in the presence of the standing wave. Trapped atoms can then be imaged using fluorescence imaging. A typical sequence is depicted in Figure 5.3, and discussed in more details in the following. Note that the values are for information purpose, since the optimal values can change from one experiment to another.

The standing wave is switched on from the beginning with an intensity of $2.5\,\mathrm{mW}\cdot\mu\mathrm{m}^{-2}$. This corresponds to a trap depth of $2.2\,\mathrm{mK}$ and a lightshift of the cooling transition of around $50\,\mathrm{MHz}$. If a deeper trap would result in a better trapping, it would also result in a larger lightshift of the atomic transitions. Cooling from the molasses beams is expected inside the trap as well. A too large lightshift would reduce this additional cooling efficiency.

Once the dipole trap is loaded, all cooling beams are switched off for $30\,\mathrm{ms}$, in order to wait for the non-trapped atoms to fly away from the imaging region. The dipole trap power intensity is then reduced to around $0.74\,\mathrm{mW}\cdot\mu\mathrm{m}^{-2}$. This allows one to reduce the frequency shift of the cooling transition to $\Delta f_{cool} = 17\,\mathrm{MHz}$, which is the transition used for imaging.

The trapped atoms are imaged by switching on the cooling beams with an intensity of around $1.5\ I_0$ and a detuning of $-3.3\Gamma \approx -20\,\mathrm{MHz}$, with an exposure time of $20\,\mathrm{ms}$. A typical image obtained is shown in Figure 5.4. The fluorescence is proportional to the number of trapped atoms.

These imaging conditions highly depend on the dipole trap power used at the imaging stage. During the imaging step, atoms can be heated by the imaging light if it is too close to the lightshifted resonance or too powerful. In order to still get enough scattered photons, a trade-off between heating and scattering is to be found. The optimal values can change from one experiment to the other, depending on the measured property.

An alternative way to get a quantitative measurement of the number of atoms inside the dipole trap is to transfer the atoms inside a 3D-MOT. It is done by switching the cooling beams and magnetic field back on in a 3D-MOT configuration, while switching off the dipole trap. The main advantage of this method is that the imaging efficiency doesn't depend on the trap parameters.

The number of atoms is the main quantity measured for the trap characterisation. Most of the signals have been obtained by optimisation of the fluorescence intensity and shot-to-shot stability. No quantitative measurement of the loading efficiency have been performed, since only a few atoms are required for the Rydberg steps. Nevertheless, the relative evolution of the atom number has been measured, in order to perform several

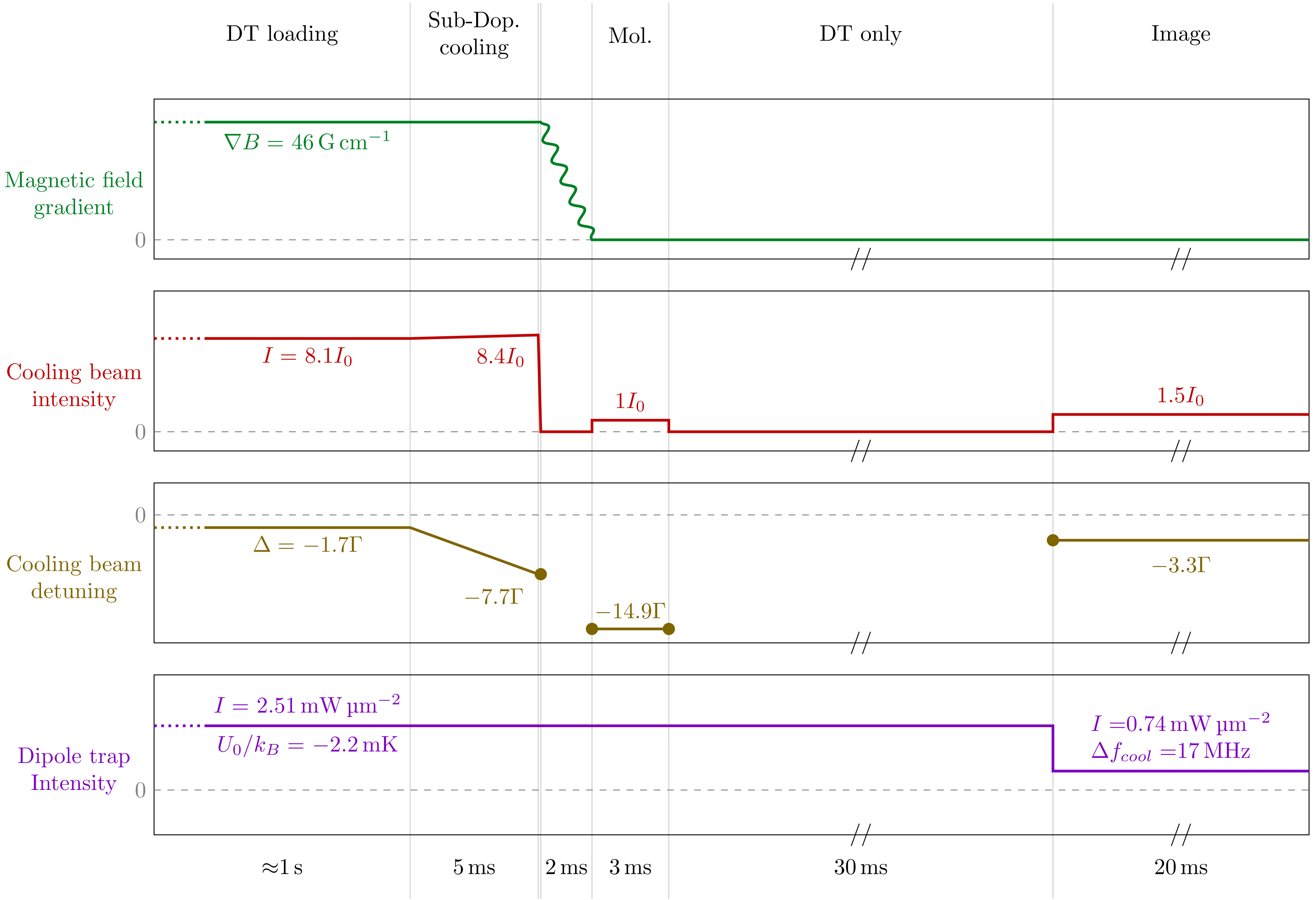

Figure 5.3. – Typical dipole trapping sequence. The dipole trap is switched on and loaded while the 3D-MOT cooling sequence is realised. Sub-Doppler cooling and molasses stages are then performed as usual. The DT is then left alone until non-trapped cold atoms fly away from the imaging region. Dipole trap can then be directly imaged by switching on cooling beams. Dipole trap intensity is reduced for imaging to reduce the lightshift. Dashed lines indicates the zero values.

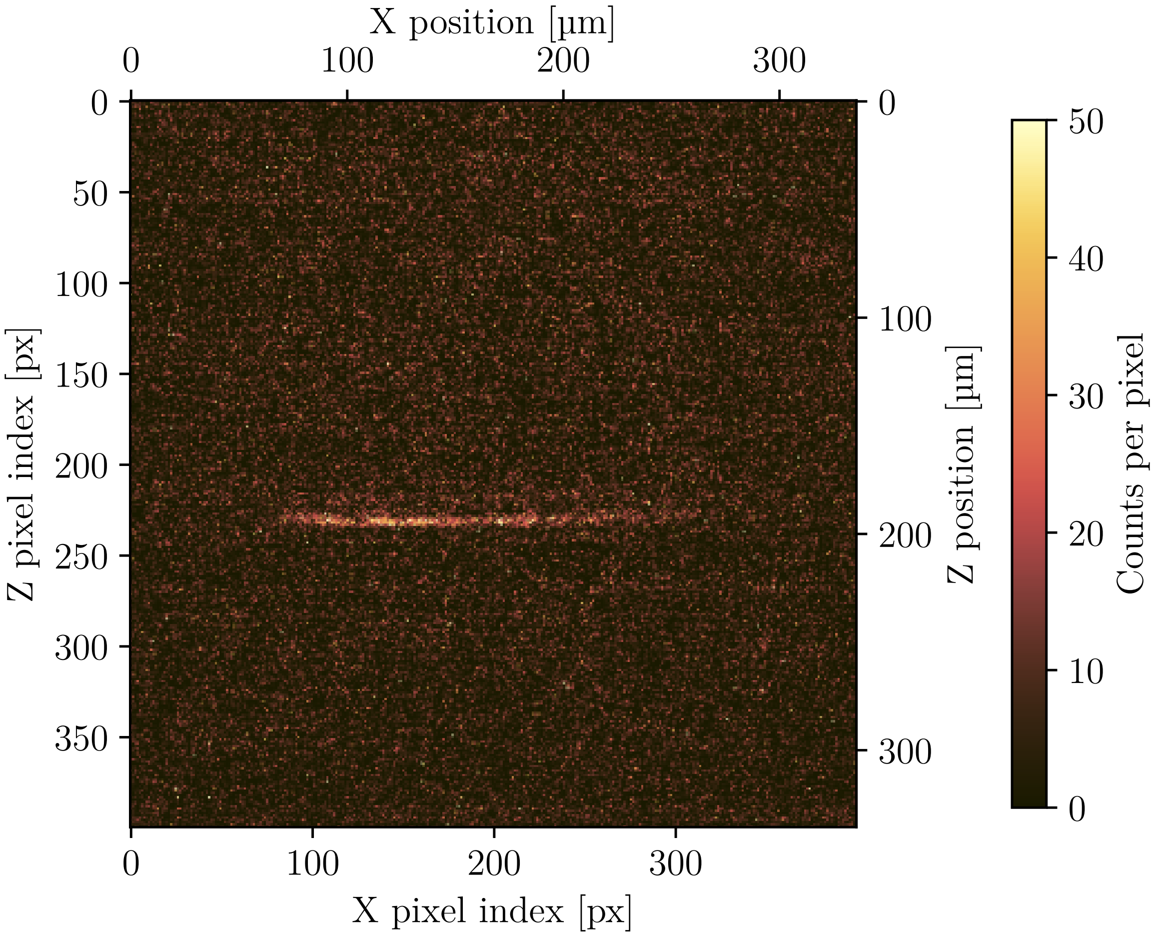

Figure 5.4. – Typical dipole trap image obtained by fluorescence imaging.

characterisations discussed in the following.

For data analysis, the fluorescence is obtained by taking the mean number of counts over a region of interest (ROI) around the trap region. Typical size of the ROI is 100 px × 5 px. Signal to noise ratio is increased by removing the background signal of an image taken in the same conditions without atoms.

Trapping time

The first property measured is the time during which atoms can remain trapped inside the dipole trap. It can be simply accessed by loading the trap and by measuring the remaining number of atoms after some time. The corresponding sequence and results for the trapping time in the standing wave are given in Figure 5.5. For this measurement, both dipole trap beams are on, with a depth around 2.17 mK (2.51 $\mathrm{mW} \cdot \mu\mathrm{m}^{-2}$). Trapping time is estimated to be around 193 ms.

The main factors limiting the trapping time have not yet been identified. It is likely due to the vacuum quality inside the chamber. Like for the 3D-MOT, these measurements have been realised with nitrogen cooling. This time is expected to increase thanks to cryopumping when helium cooling will be used. For now, it is good enough to study atoms transport and Rydberg excitation. Other possible limitations are fluctuations of the laser intensity or beam pointing instabilities.

It is interesting to note that the trapping time can fluctuate between different sequences, since it depends on the trapping power used for atoms loading and the vacuum inside the experiment chamber. Additional characterisations have been performed with a single beam dipole trap. This allowed for a better understanding of the trap properties without suffering from the beams overlap sensitivity. [1]

Spectral purity of the dipole trap — The first test was to see the effect of the remaining 780 nm (D2 line) and 796 nm (D1 line) resonant light. The highest contribution likely comes from the D1 line which is 55 dB below the 820 nm component, as shown on Figure 5.6. However, the trap is tightly focused to get a trap intensity of around 3 $\mathrm{mW} \cdot \mu\mathrm{m}^{-2}$. Associated spectral background intensity is then 950 $\mathrm{mW} \cdot \mathrm{cm}^{-2}$. This is way larger than the saturation intensity of the D1 lines: I_0^{D1} =4.5 $\mathrm{mW} \cdot \mathrm{cm}^{-2}$. This could be associated to important atom heating.

To reduce this effect, a pass band filter at 820 nm with an optical density of 6 is put on the optical path. Spectral background intensity goes down to 0.95 $\mu\mathrm{W} \cdot \mathrm{cm}^{-2} \approx$

---

[1] For two beams, the trap depth depends on the fringes contrast, which depends on the beams overlap, which can vary from one day to another. For a single beam, the trap depth doesn't depend on the alignment.

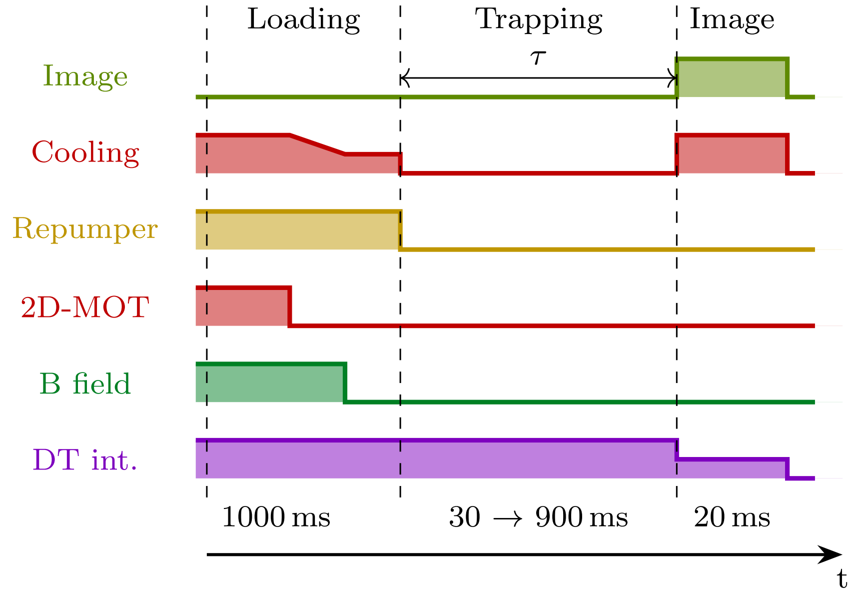

(a) Trapping time sequence

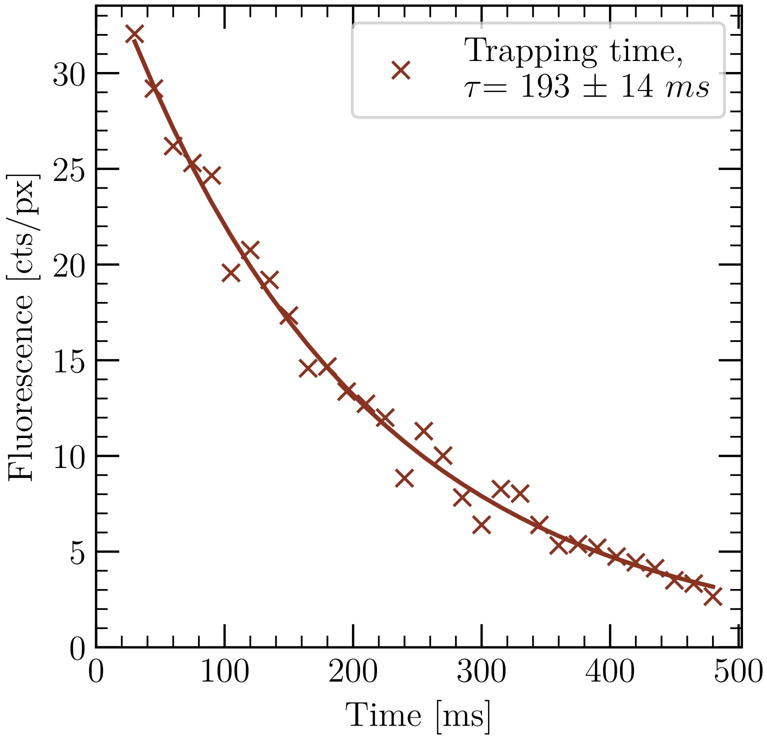

(b) Trapping time conveyor belt

Figure 5.5. – Conveyor belt trapping time measured for a standing wave configuration (2.17 mK). The two-beams dipole trap is loaded with cold atoms, and then all other beams are switched off to leave the trap alone. After some time, the trap is imaged after intensity reduction to estimate the amount of remaining atoms. Obtained fluorescence signals are fitted with an exponential decay to give the trapping time.

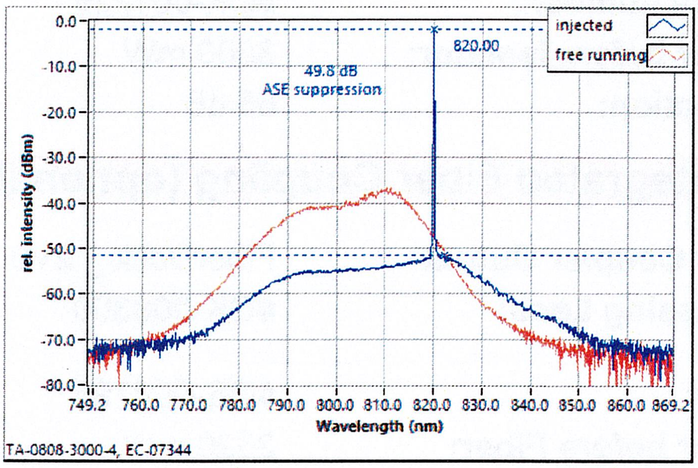

Figure 5.6. – Optical spectrum of the trapping laser. The relative intensity is given with respect to the 820 nm lasing mode. Background components are around −63 dB for 780 nm and −55 dB for 796 nm. Extracted from the *Toptica* laser datasheet.

$2.1 \times 10^{-4} I_0^{D1}$. The effect of this filter has been estimated by measuring the trapping time associated to a single beam DT_1 with a depth of around 1.6 mK ($1.85\,\mathrm{mW} \cdot \mu\mathrm{m}^{-2}$). The trapping time is measured to be 134 ms without the filter and 260 ms with the filter, *i.e.* nearly twice as long with the filter. In addition, the fluorescence difference at 0 ms indicates a different trapping efficiency. These two observations show that there was indeed a disturbance induced by the spectral impurity.

Intensity effect — The second step was to study the effect of the dipole trap intensity on the dipole trap. Indeed, if there is still heating associated to the resonant component in the trapping light, trapping time is expected to be reduced when intensity is increased. On the other side, if the limiting atom loss effect is due to atom heating then the trapping time is expected to be longer for a deeper trap. Finally, if the only heating effect is the scattering of trap photons, then trapping time should be independent from the trap intensity. However, this last option is less probable since the trapping times measured here are way shorter than τ_{sc} estimated in Equation 5.13.

The trapping time has been measured for different trap intensities, using the single beam DT_1. As previously mentioned, direct imaging of the dipole trap strongly depends on the trap power, and requires to go to lower intensity for imaging. In order to facilitate the comparison between different trap intensities, the remaining atoms are transferred from the dipole trap to the 3D-MOT before imaging. This is done by switching the cooling beams and magnetic field back on before switching off the dipole trap at the imaging stage.

The associated sequence and obtained results are depicted in Figure 5.8. The trapping

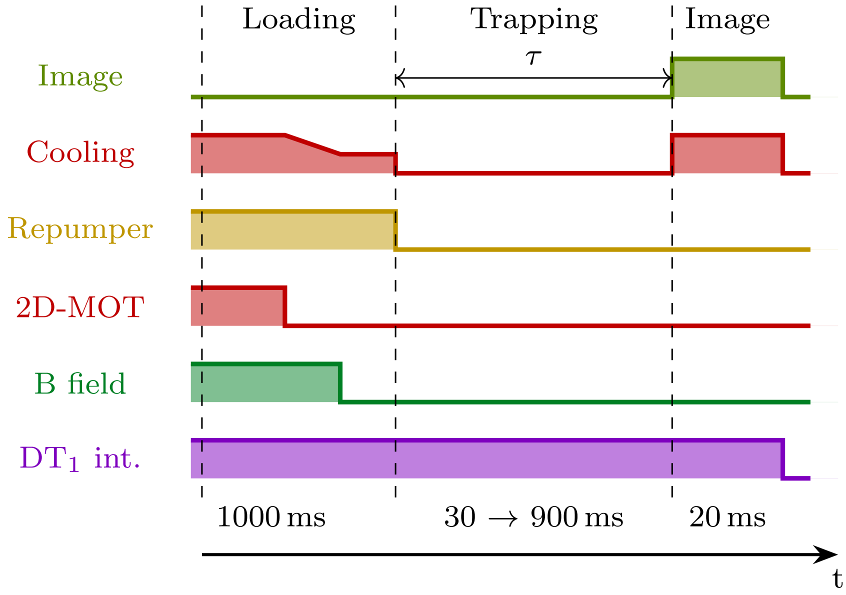

(a) Single trap trapping time sequence

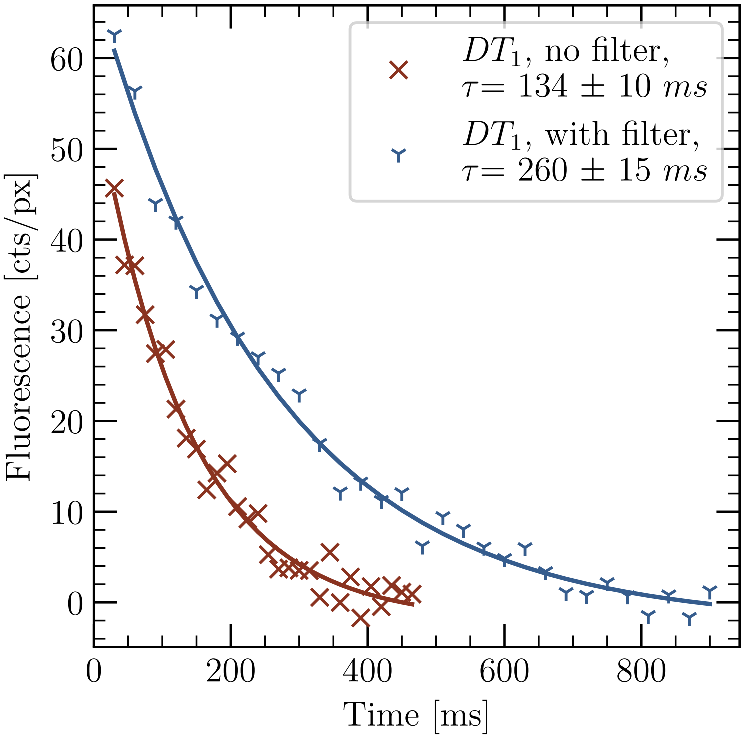

(b) Spectral impurity effect on DT_1

Figure 5.7. – Spectral purity effect: measurement of the effect of the laser spectral impurity on the trapping time of a single beam trap DT_1 (1.6 mK). The sequence is similar to the one for conveyor belt trapping time measurement, except that the intensity does not need to be reduced and cooling beams are readjusted for these imaging conditions. Fluorescence signals obtained are fitted with an exponential decay. Negative points are due to background compensation at low counts.

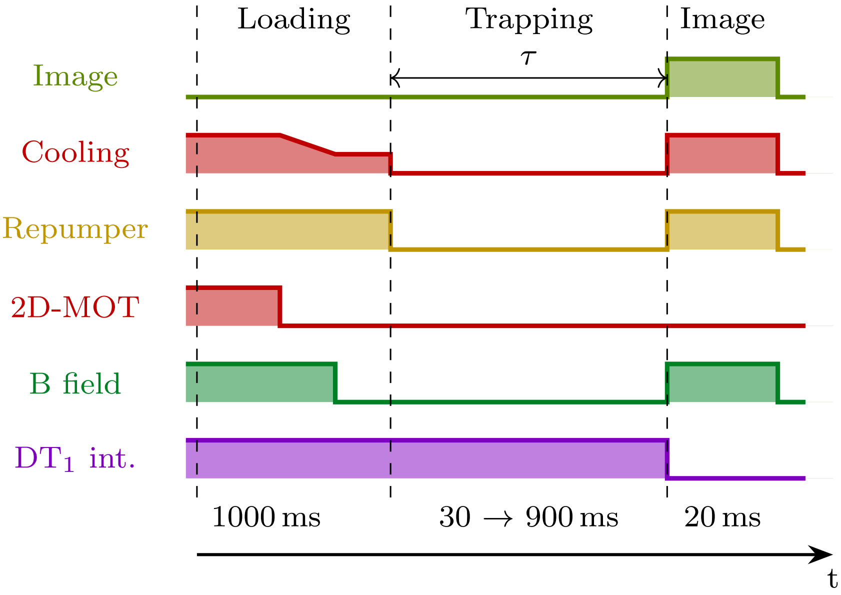

(a) Power effect sequence

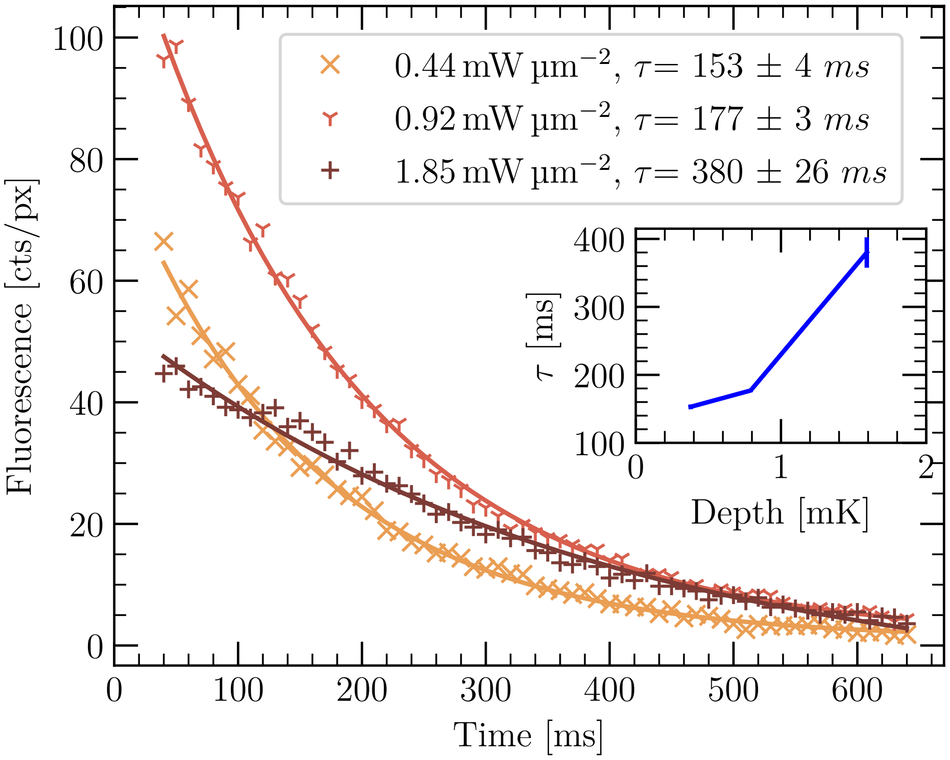

(b) Power effect DT_1

Figure 5.8. – **Intensity effect:** measurement of the effect of different single beam DT_1 dipole trap intensity on the loading efficiency and trapping time. Imaging is done by recapture into the 3D-MOT: cooling beams and magnetic field are switched on, and then the dipole trap is switched off to transfer atoms into the 3D-MOT. Obtained fluorescence signals are fitted with an exponential decay to give the trapping time. Inset of 5.8b gives evolution of the trapping time over trap depth.

time seems to increase with power. In addition, the amount of initially trapped atoms varies with power, in a non-monotonous way. If it is not surprising that more atoms are trapped in a deeper trap, the fact that the highest trap has less atoms indicates that loading is less efficient for a too deep trap. This is likely due to a too large lightshift in the bottom of the trap.

Attempts to mitigate this effect by a slow ramping up of the dipole trap power during the loading stage were not successful. Additional quantitative studies with a better knowledge of the real lightshift would allow one to optimise high power loading, for example by adding a repumper beam resonant with the lightshifted frequency.

Finally, the decay obtained for the highest intensity seems to be less perfectly described by an exponential decay, given the larger error. It is possibly a signature of different processes, with different timescales, involved in the atoms loss. Considered processes are usually collisions with background gases, leading to an exponential decay, and heating of atoms inside the trap, which is not exactly exponential. More details can be found in the literature [143].

These last observations suggest that heating processes might contribute to reduce the trapping time inside the dipole trap. These can be compensated by switching on cooling beams during the trapping time to keep a constant atom cooling. However, first attempts to do so led to shorter trapping times. This suggests that the molasses cooling inside the dipole trap was not efficient, likely due to a too large lightshift as well.

Light-shift and waist size

Previous observations on trapping time suggested that a better knowledge of the lightshift could be a way to improve atoms loading inside the dipole trap, both in number and temperature, as well as getting increased trapping times with cooling beams on. As shown in the previous section, the lightshift depends on the intensity experienced by the atoms, which depends on both the laser power and waist at the trap position. Due to losses on the different surfaces, as well as optical system imperfections, its value can vary from theoretical estimations.

To measure the real lightshift, one can perform the spectroscopy of a given transition in the presence of a single dipole trap beam DT_1. The chosen transition here was the repumping transition.[2] To do so, an experimental sequence adapted from previous experiments [61] has been implemented and is depicted in figure Figure 5.9.

Atoms are first trapped inside the dipole trap, with an intensity adjusted around

---

[2] The first spectroscopy attempted was to directly scan the imaging frequency $F = 3 \rightarrow F' = 4$. However, atoms heating was too high and a good photon collection with no atoms depletion hasn't been achieved.

$1.5\,\mathrm{mW}\cdot\mu\mathrm{m}^{-2}$ (1.3 mK), to ensure good enough loading. Associated expected light shift of the $\left|{}^5S_{1/2}\right\rangle \to \left|{}^5P_{3/2}\right\rangle$ transitions is around $\Delta f_0 = 35\,\mathrm{MHz}$. The cooling beams are then switched off and a delay of 20 ms is introduced to let the non-trapped atoms go.

Then, a depumper beam driving the $\left|{}^5S_{1/2}, F=3\right\rangle \to \left|{}^5P_{3/2}, F'=3\right\rangle$ transition is used to depump atoms from $F=3$ to $F=2$ in the ground state ${}^5S_{1/2}$. Bare splitting between the cooling and the depumping transitions is 120 MHz. The beam is set at 65 MHz below the bare cooling transition $F=3 \to F'=4$, partially taking into account the estimated lightshift while remaining in the AOM bandwidth (the later being shared with the cooling beams). This depumping stage lasts for 10 ms. Duration and detuning are optimised to get an efficient depumping with limited atom loss.

Once atoms are depumped, the dipole trap power is increased up to the target measurement value. This increases the lightshift to a value Δf_{meas}. Then, atoms are selectively repumped to the state $F=3$ with a probe repumper beam on the T_{-} MOT pair. Its frequency is scanned to perform the spectroscopy. This pulse lasts for $6\,\mu$s, to get a spectral resolution of around 0.17 MHz.

Then, the dipole trap is switched off, and a beam orthogonal to the trap, resonant with the bare transition $F=3 \to F'=4$ is used to kick the atoms in $F=3$ out of the trap region. This step lasts for $10\,\mu$s, to ensure that atoms in $F=2$ remain in the trap region while efficiently kicking atoms in $F=3$. This retrap delay is quantitatively visible in Figure 5.11b.

Finally, the dipole trap is switched back on at its initial intensity, in order to retrap the remaining atoms. These atoms are then imaged using the depumping beam set 70 MHz below the cooling transition, with the repumper switched on.

If the probe repumper is resonant with the lightshifted transition, all atoms are repumped in $F=3$ and get kicked out of the trap region. Otherwise, atoms are unaffected and trapped back. The imaging step being in the same conditions each time, it ensures that the depletion observed comes from the repumping / kick stages and that atoms lost during the imaging step don't affect the measurement precision.

The spectroscopic results for different dipole trap powers are given in Figure 5.10. The estimated power is obtained by taking the average between the power measured before and after the cryostat, to take into account losses. A linear fit of the obtained lightshift frequencies for different powers gives a slope $p_1 = 0.1\,\mathrm{MHz}\cdot\mathrm{mW}^{-1}$.

According to Equation 5.6, the expected lightshifted frequency is indeed linear in power and reads:

$$\Delta f = (\alpha_1 - \alpha_0)\cdot I = \frac{2(\alpha_1-\alpha_0)}{\pi w_0^2}\cdot P_L = p_1 \cdot P_L\,, \tag{5.17}$$

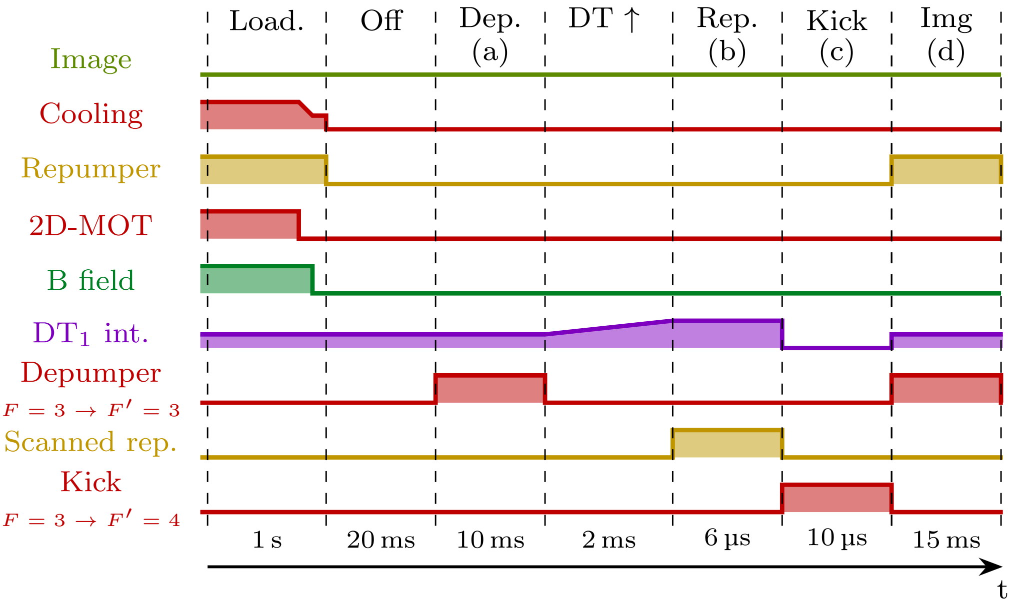

(a) Sequence

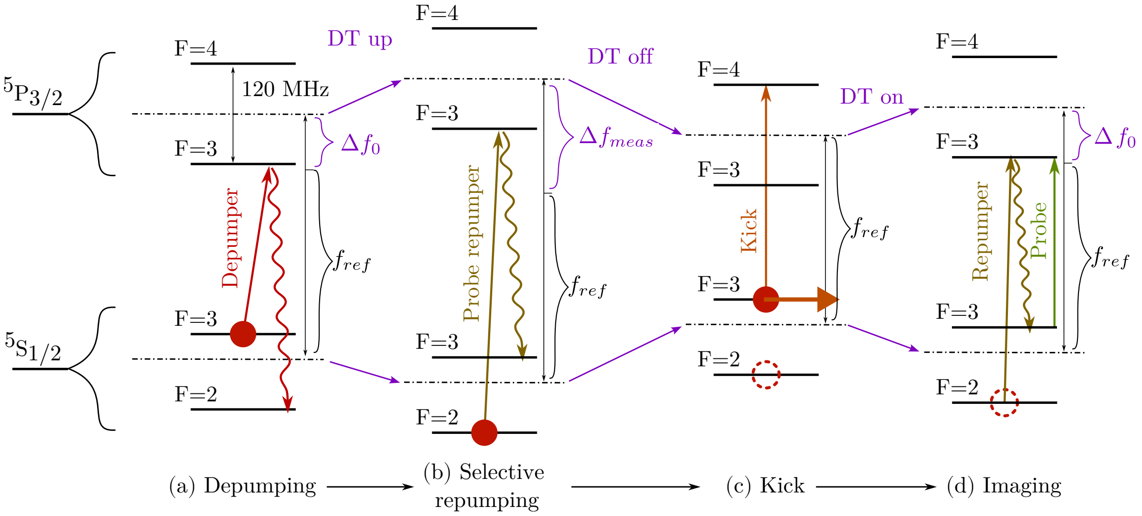

(b) Evolution illustration

Figure 5.9. – Lightshift measurement principle: experimental sequence and atoms evolution illustration. The first step is the same loading and off time as for the previous sequences. Then, a depumper beam tuned at resonance on the $F = 3 \rightarrow F' = 3$ lightshifted transition depumps atoms into the state $F = 2$ (a). The dipole trap intensity is then brought to the value to be measured, which changes the lightshift. Then, a probe repumper beam is switched on. If it is resonant with the lightshifted $F = 2 \rightarrow F' = 3$ repumping transition, atoms are repumped to the state $F = 3$. Otherwise they remain in $F = 2$ (b). After that, the dipole trap is switched off and a kick beam resonant with the transition $F = 3 \rightarrow F = 4$ expels atoms that were in $F = 3$ (c). Atoms are then imaged using the depumping beam (d). A dip in the atoms number is then observed when the probe repumper is resonant with the lightshifted transition, directly giving a measure of the lightshift.

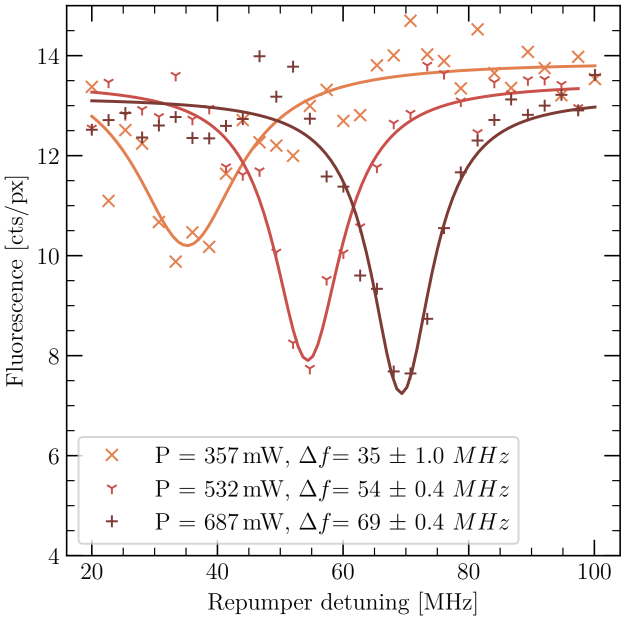

(a) Spectroscopy results

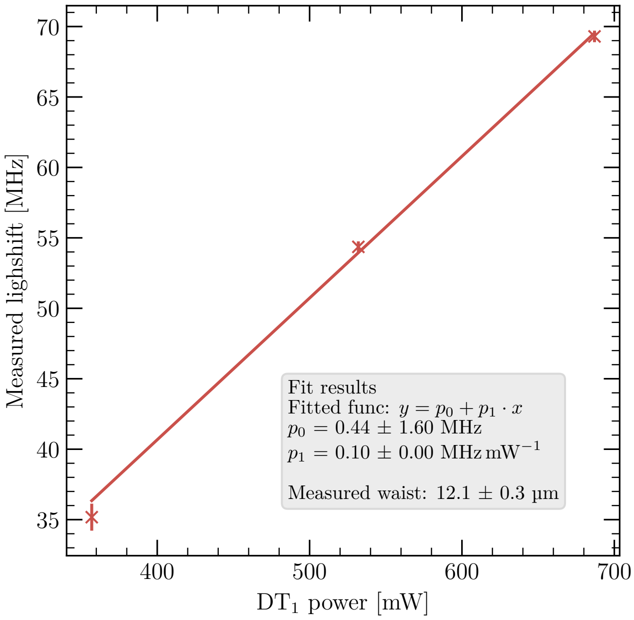

(b) Lightshift measurement

Figure 5.10. – Lightshift measurement results. Panel 5.10a gives the spectroscopy signals obtained for different estimated trap power. A Lorentzian fit of these signals allows one to extract the corresponding resonance frequency. Panel 5.10b shows the obtained frequency as a function of the estimated trap power. A linear fit to this curve gives access to the slope parameter p_1 defined in Equation 5.17, giving a dipole trap waist estimation w_0 =12.1(3) μm.

where P_L is the laser power. The polarisabilities being well known values, the slope coefficient gives the trap waist:

$$w_0 = 12.1(3)\mu\text{m}. \tag{5.18}$$

The obtained waist value matches the design values, within errorbars. However, it requires a good estimation of the laser power inside the cryostat. To complete this measurement, waist size could be measured through oscillations frequencies as well. In that case, the lightshift measurement would provide a precise estimation of the effective intensity inside the cryostat.

Finally, this measurement has only been realised for one beam. Since no major discrepancy compared to design values was observed for this beam, this measurement hasn't been repeated on the second one. Nevertheless, it could be useful to measure it in the future in case the losses aren't symmetric for all sides of the cryostat.

Oscillation frequencies

As previously discussed, oscillation frequencies can be used to have a better estimation of the trap parameters, while getting rid of the power estimation imprecision. Indeed, Equation 5.16 directly gives a measurement of the beam waist knowing the laser frequency. The critical point here is the assumption that atoms are effectively in the bottom of the trap. This would require an efficient cooling inside the trap. In addition, knowledge of the trap oscillation frequencies could allow to better understand spurious heating of the atoms.

This measurement has not yet been realised in the experiment, but could be implemented by using parametric heating. Indeed, by modulating the trap depth with a given frequency ω_{mod}, atoms are parametrically excited when the modulation frequency equals twice the trap frequency. It induces atoms depletion in the trap which can be directly used to probe the trap oscillation frequencies, as done in numerous other experiments [144] [145]. Alternative signals can be studied, such as cloud expansion geometry after a parametric excitation [146], or release-recapture experiments [61].

From a more practical point of view, the parametric excitation could be implemented on the experimental setup using the RF source driving the AOMs. It is already used to control the trap depth using an external analog voltage control provided by the computer controlling the experiment. Adding a periodic modulation of this control voltage would directly provide the required trap depth modulation.

Atom temperature

A last property to estimate is the atom temperature inside the trap. Indeed, the current trapping time is way shorter than the minute range required for the observation of long lifetime. A first possible explanation is the collisions with background gases, which can be reduced by improving the vacuum inside the chamber.

A second limitation for the trapping time could be spurious heating of the atoms inside the trap. It can be compensated by adding cooling beams adjusted for an efficient cooling inside the trap. A careful study of the possible heating mechanisms would then be required to increase the trapping time. Knowledge of the atom temperature inside the trap would provide a good criterion to identify and quantify the causes of atom heating.

In addition, this could be used as a criterion to optimise the sub-Doppler cooling inside the trap. So far the loading sequence has been optimised to have an efficient loading of the trap. This could be completed by an optimisation of the atom temperature.

To measure the temperature of trapped atoms, a common technique is to perform a release-recapture experiment, by switching off the dipole trap for some time and then on again to retrap the atoms. The recapture probability over different release time decays in a way that depends on the initial atom temperature. The comparison of the experimental data with Monte-Carlo simulations of the same experiment for different temperatures allows one to estimate the atom temperature inside the trap [147].

This measurement has been realised for a single trap beam DT_1. Measured recapture probability and experimental sequence are depicted in Figure 5.11, together with the Monte-Carlo simulation that fitted the best experimental data.

The release recapture sequence is the following. First the single beam dipole trap DT_1 is loaded from the cold atom clouds, with a depth of around 1.6 mK (1.88 $\mathrm{mW} \cdot \mu\mathrm{m}^{-2}$). Then an delay time of 40 ms is waited until atoms from the cloud fly away. Then, the dipole trap is switched off to release the atoms for a varying duration from 2 μs to 302 μs. The dipole trap is then switched back on to retrap the atoms for 30 ms until non-trapped atoms are gone. Finally, cooling beams and magnetic field are switched back on while the dipole trap is switched off, in order to retrap atoms inside a 3D-MOT for imaging. Using this imaging methods allows one to get a good enough signal even for a small number of atoms.

Monte-Carlo simulation — For simulating the release-recapture experiment in a single beam trap, the first step is to generate a set of atoms, whose position and velocity are sampled accordingly to the trap parameters for a given temperature T. Position and velocity are assumed to be following direction-independent Maxwell-Boltzmann

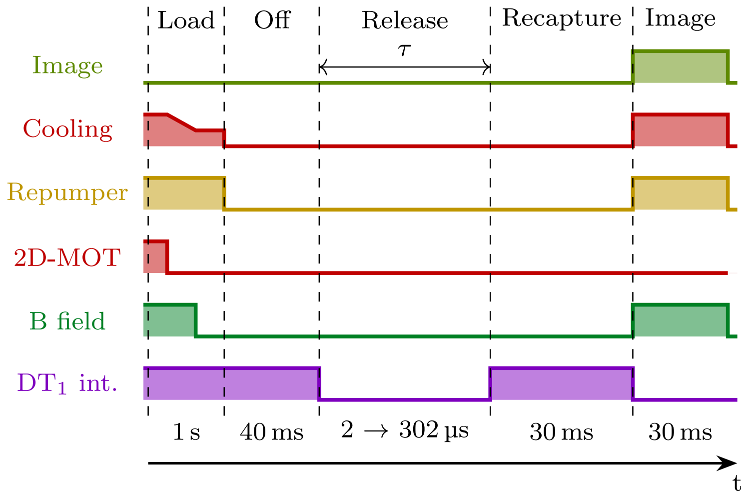

(a) Sequence

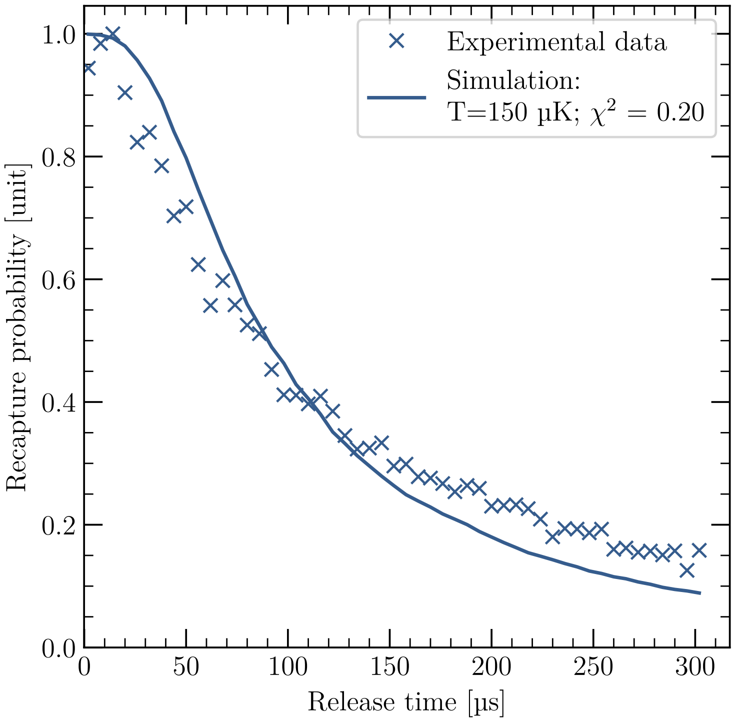

(b) Release - recapture probability curve

Figure 5.11. – **Temperature measurement:** estimation of the atom temperature inside the trap with a release-recapture experiment. Trap loading and off time are similar to previous experiments. The dipole trap is then switched off for some time. During this release step, atoms diffuse and eventually leave the trap region. The trap is then switched back on. The amount of recaptured atoms is related to the atomic temperature before release. The atoms are then imaged by recapture in the 3D-MOT. The recapture probability versus release time is compared to Monte-Carlo simulations to get a temperature estimation, found to be around $T = 150\,\mu$K.

thermal distributions:

$$\rho_r(x,y,z) \propto \exp\left(\frac{-U_{single}(x,y,z)}{k_B T}\right), \tag{5.19}$$

$$\rho_v(v_x,v_y,v_z) \propto \exp\left(\frac{-m(v_x^2+v_y^2+v_z^2)}{2k_B T}\right), \tag{5.20}$$

where U_{single} is the single beam trapping potential. In the harmonic approximation, they correspond to normal distributions, with standard deviations in position:

$$\Delta x = \sqrt{k_B T/m_{Rb}\Omega_{x,single}^2}, \tag{5.21}$$

$$\Delta z = \Delta y = \sqrt{k_B T/m_{Rb}\Omega_\rho^2}, \tag{5.22}$$

and standard deviation in velocity:

$$\Delta v = \sqrt{k_B T/m_{Rb}}. \tag{5.23}$$

Here, Ω_ρ is the radial oscillation frequency, and $\Omega_{x,single} = \sqrt{\frac{-2U_0}{m_{Rb}z_R}}$ is the single beam axial oscillation frequency. Using the waist value previously measured, the frequencies are Ω_ρ =10 kHz and $\Omega_{x,single}$ =159 Hz. In the simulations performed, samples of 5000 atoms were taken.

Once atoms are picked, their evolution after a release time Δt can be computed according to the following rule:

$$\begin{cases} x & \to x + v_x\Delta t\,, \\ y & \to y + v_y\Delta t\,, \\ z & \to z + v_z\Delta t - g\Delta t^2/2\,, \end{cases} \qquad \begin{cases} v_x & \to v_x\,, \\ v_y & \to v_y\,, \\ v_z & \to v_z - g\Delta t\,, \end{cases} \tag{5.24}$$

taking into account the gravity effect in the z direction.

After the evolution, the energy of each atom at the new position with the trap on is computed. Atoms are considered to be retraped if

$$\frac{m_{Rb}\mathbf{v}}{2} + m_{Rb}gz < |U_{single}(\mathbf{r})|\,. \tag{5.25}$$

Recapture probability is then computed by taking the ratio between the number of retraped atoms and the number of initial atoms.

Comparison with experimental data — In order to estimate the real temperature, the Monte-Carlo simulation is repeated for a range of temperatures, from 50 μK to

500 μK with 10 μK steps. The obtained recapture probability curves are given in Figure 5.12a.

In order to quantify which temperature fits the best, a non-weighted χ^2 parameter is computed for each simulation to estimate the distance between the simulated data and the experimental results, which reads:

$$\chi^2(T) = \sum_i \left[p_{exp}(\Delta t_i) - p_{sim}^T(\Delta t_i)\right]^2 , \tag{5.26}$$

where $p_{exp}(\Delta t_i)$ is the experiment recapture probability for a release time Δt_i, and $p_{sim}^T(\Delta t_i)$ the same for a simulation performed at a temperature T.

Results of the computed χ^2 are given in Figure 5.12b. The temperature for which the χ^2 is the smallest corresponds to the estimated temperature of the atomic sample, which is found to be around 150 μK.

The Monte-Carlo simulation for this temperature is plotted along with experimental data on Figure 5.11b. For experimental data, atoms are lost faster at short timescales, and less at long timescales. This could be explained by the fact that for the simulations, atoms are assumed to have the same temperature. If there are different classes of atom temperatures, different behaviour can appear. Hotter atoms will be lost at short times, where colder atoms will be lost at longer times.

If this analysis remains limited, it is a proof of principle that this method could be applied to this experimental setup. In addition, no experimental uncertainties were taken into account, but using these to compute a weighted χ^2 would allow one to have access to the error associated to the temperature estimation. A more complete study has been performed on another experiment of the group, and many details are to be found in Dr. Ravon's manuscript [61].

While one needs to remain circumspect on this result, it seems that the atom temperature inside the trap is much higher than the temperature obtained at the end of the molasses and even 3D-MOT stages. One explanation could be that the cooling of the atoms inside the trap leads to higher equilibrium temperature. Measurements of the temperature for different cooling beams configuration could be used to improve the cooling efficiency. However, this temperature being around 10% of the trap depth, it is still reasonable.

Another explanation could be that the temperature difference comes from the heating of the atoms between the loading and the measurement. If a perfect loading at 10 μK from the 3D-MOT is assumed, one can roughly estimate the heating to be of the order of 100 μK in 40 ms. The trap being 1.6 mK deep (1.88 mW $\cdot$ μm^{-2}), this linear heating of 2.5 μK $\cdot$ ms^{-1} would make a trapping time of the order of 640 ms, which

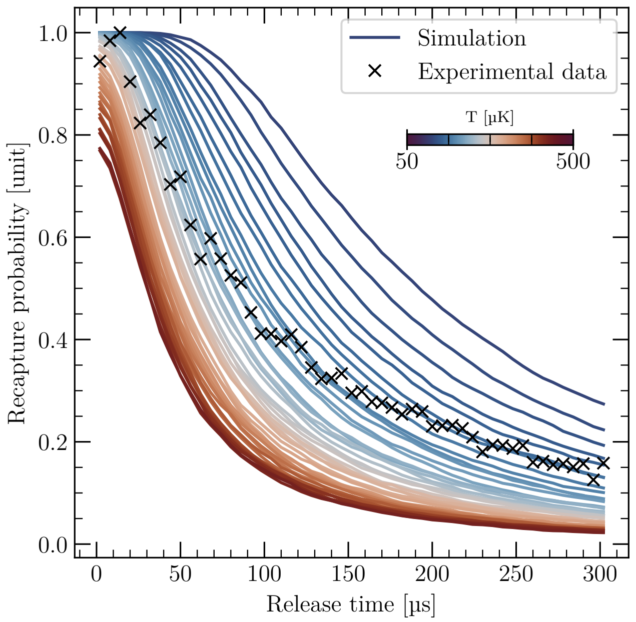

(a) Simulation results

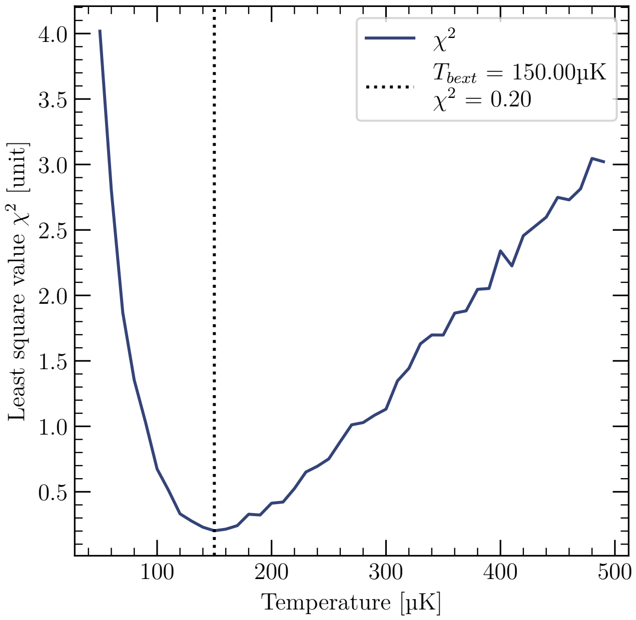

(b) χ^2 distance

Figure 5.12. – Monte-Carlo simulation results for the release-recapture experiment and comparison with experimental data. Monte-Carlo simulations have been performed for a wide temperature range. For each simulation, a non-weighted χ^2 is computed to estimate the distance to experimental data. This distance over the different temperatures T is plotted on panel 5.12b. The curve clearly shows a minimum at a temperature $T = 150\,\mu$K, chosen as the final temperature estimation.

could partially explain the trapping time given in Figure 5.8b (by a factor of 2). For a realistic estimation, it would be beneficial to measure the atom temperature with different delay times and try to see if there is indeed heating. If so, it would allow one to estimate its rate and possible origins. In any case, this heating rate is way larger than the one produced by trap photons scattering (see Equation 5.12). Other possible source of heating are for example intensity fluctuations and pointing instabilities.

5.2. Atom transport in a conveyor belt

After a demonstration of atom trapping inside the dipole trap, transport of the atoms between the two capacitor plates is the next step.

5.2.1. Atom transport

Transport of atomic ensemble in optical traps is a powerful tool used to precisely control the atoms position. For example, it can be used to move the sample to different regions of a setup, or to deterministically arrange an atomic sample [148, 149]. Many different approaches have been developed. For defect free arrays creation, atoms can be trapped in optical tweezers, that are then moved using an electro-optical deflector (EOD). Atoms can also be displaced along the trap propagation axis. One example is the use of a moving standing wave dipole trap, also called “conveyor belt” [130]. Another solution is to directly translate the waist of a focused Gaussian beam. This can be done with tunable lens [150] or a translation stage [151].

To avoid atoms heating, the transport needs to be adiabatic with respect to the axial oscillation frequency. A tight confinement in this directions increases this oscillation frequency, which allows for a faster transport. The use of a standing wave ensures a tight confinement, with oscillation frequencies of several hundred kilohertz. For comparison, the transport duration used in [150] are in the second range to comply with the axial oscillation frequency in the hertz range of their Gaussian beam.

A limitation for the conveyor transport is the maximal transport distance. It is in general limited by the beam divergence. At a distance larger than the Rayleigh length, the trap is shallower and atoms are no longer efficiently trapped. For transport over larger distances, the beam waist has to be synchronously moved with the fringes. Translation stages velocity is around tens of millimeters per second, and can suffer from hysteresis. Tunable lenses allow for faster transport in the meter per second range, and were therefore chosen for this experiment.

A combination of both an optical conveyor belt and waist position displacement has been used to deliver the atoms into the inhibition region. It allowed for a fast transport in the millisecond range over a relatively large distance of 14 mm.

Fringes position

The first element involved in the atoms transport is the fringes translation. The general idea is the following: atoms are trapped into stationary interference fringes created by the two counter-propagating beams, whose intensity profile is given in Equation 5.7. The position of the fringes is determined by the fringes phase Φ, which is time-independent for the standing wave.

If the phase delay becomes time-dependent, the wave is no longer standing. The fringes follow the time evolution of the phase delay, such that the fringes displacement d is

$$d(t) = \frac{\Phi(t) - \Phi(0)}{k_L}. \tag{5.27}$$

The initial phase $\Phi(0) = (\varphi_0 - \varphi_1)/2$ depends on the absolute definition of the position x. In the following, the convention $\Phi(0) = (\varphi_0 - \varphi_1)/2 = 0$ will be taken, meaning that there is an intensity maxima in $x = 0$.

This phase can be tuned by changing the beams frequencies, as shown in this simple example. If the beam DT_i is set to an angular frequency ω_i, such that the beams detuning $\Delta\omega = \omega_0 - \omega_1 \ll \omega_0, \omega_1$, then the phase delay time derivative reads

$$\frac{\mathrm{d}\Phi(t)}{\mathrm{d}t} = \frac{\Delta\omega}{2}, \tag{5.28}$$

taking the approximation that $k_0(t) + k_1(t) \approx 2k_L$.

From this expression, one can see that for a positive detuning ($\omega_1 < \omega_0$), the standing wave moves in the $+x$ direction[3] at a velocity

$$v = \frac{\Delta\omega}{2k_L} = \frac{\Delta\nu \cdot \lambda_L}{2}. \tag{5.29}$$

Control of the detuning over time thus allows one to move the atoms along the trap axis.

To give some quantitative insight, a detuning of the order of 1 MHz leads to velocities of around 0.41 $\mathrm{mm \cdot ms^{-1}}$ for a 820 nm laser. A transport over 14 mm would then take 34 ms.

In practice, the velocity is slowly increased to avoid large acceleration that would heat up the atoms. In that case, the fringes displacement due to the beams detuning is

---

[3] For a negative detuning, the standing wave moves in the opposite direction. A good thing to keep in mind is that the standing wave will move toward the laser arm that has the lower frequency.

given by

$$d_{AOM} = \int \frac{\Delta\omega(t)}{2k_L} \mathrm{d}t \ . \tag{5.30}$$

Finally, the control of the detuning is experimentally done using the two AOMs placed on each of the beam path.

Transport profiles

For optimisation of the transport efficiency, the profile with which atoms are transported plays a major role. In particular, a too large acceleration can kick the atoms out of the trap. In the moving reference frame, the accelerated trap potential corresponds to the sum of the standing wave and of a linear ramp in position [130]. This gives a fundamental limit to the maximal acceleration, which reads

$$a^{lim} = \frac{U_0 k_L}{m_{Rb}} . \tag{5.31}$$

For transport, the trap depth is set to 3.7 mK, and the associated maximal acceleration is estimated to be around $a^{lim} = 2.7 \times 10^3\,\mathrm{mm \cdot ms^{-2}}$.

To avoid too large accelerations, the velocity is linearly increased to its maximal value v_{max} in a time $\tau_{trans}/2$. The velocity is then decreased back to zero in the same way to stop the atoms. In the future, more complex shapes could be used to improve the retention efficiency [152], eventually using optimal control protocols.

A linear change of the velocity corresponds to a constant acceleration value $a_0 = \pm 2v_{max}/\tau_{trans}$. The final transport distance is $d_{trans} = v_{max}\tau_{trans}/2$. For a transport of 14 mm done in 50 ms, the corresponding acceleration and maximal velocities are respectively $a_0 = 0.022\,\mathrm{mm \cdot ms^{-2}}$ and $v_{max} = 0.56\,\mathrm{mm \cdot ms^{-1}}$.

The position is then quadratic in time. Taking into account the two halves of a one way transport, acceleration, velocity and position of reference fringes can be computed. Their analytic expressions and shape are given in Figure 5.13.

For most of the distance studies that were realised, duration was the parameter kept constant. The other possibilities are to keep the maximal velocity or the acceleration constant.

Waist position

As previously mentioned, a transport based only on fringes displacement is limited by the trap Rayleigh length. For a 820 nm wavelength trap with a waist of 12.3 μm the Rayleigh length is $Z_R = 0.58$ mm. This length is way smaller than the 14 mm distance between the 3D-MOT and the inhibition region center.

Acceleration

$$\begin{cases} a(t) = a_0\,, & t < \frac{\tau_{trans}}{2} \\ a(t) = -a_0\,, & t > \frac{\tau_{trans}}{2} \end{cases}$$

Velocity

$$\begin{cases} v(t) = a_0 t\,, & t < \frac{\tau_{trans}}{2} \\ v(t) = v_{max} - a_0 t\,, & t > \frac{\tau_{trans}}{2} \end{cases}$$

Displacement

$$\begin{cases} d(t) = \frac{a_0 t^2}{2}\,, & t < \frac{\tau_{trans}}{2} \\ d(t) = \frac{d_{max}}{2} + v_{max} t - \frac{a_0 t^2}{2}\,, & t > \frac{\tau_{trans}}{2} \end{cases}$$

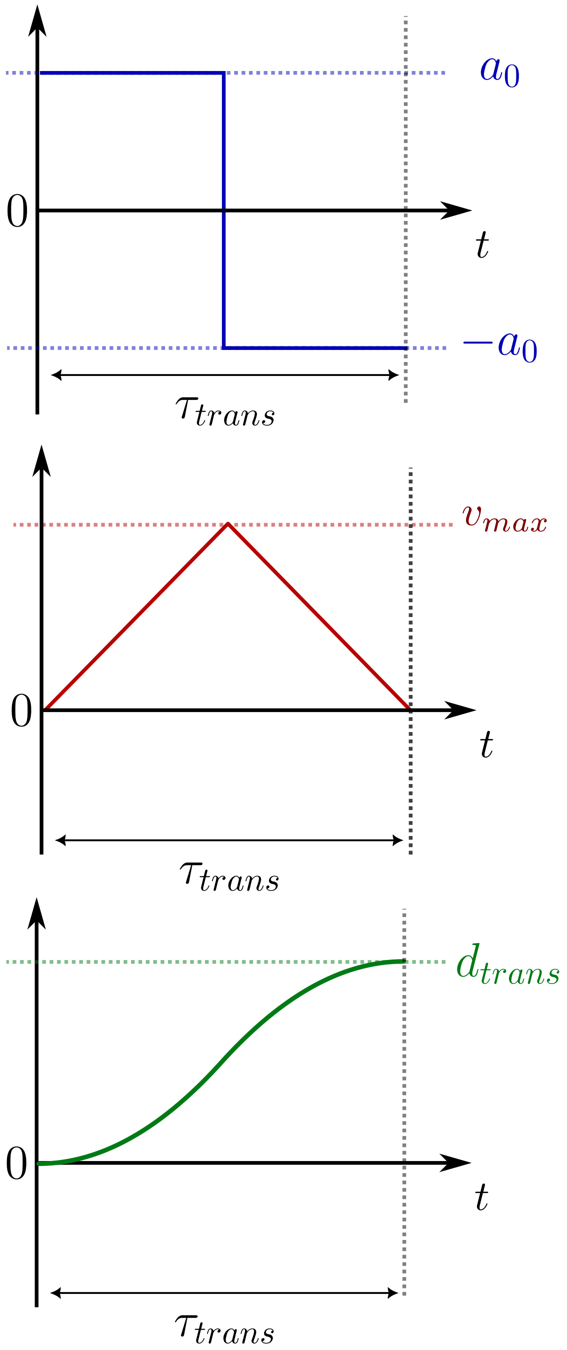

Figure 5.13. – Transport profiles with associated analytical expressions for a linear change of the detuning.

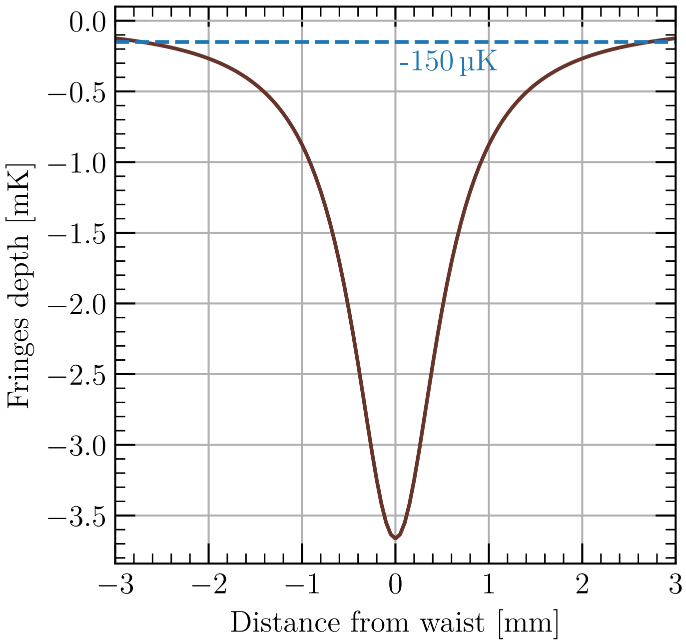

Figure 5.14. – Fringes depth along the trap as a function of their distance from the waist position. The blue dashed line indicates the atom temperature measured in the trap, found to be around 150 μK.

More quantitatively, Equation 5.7 shows that the fringes depth scales as $\propto (1 + x^2/z_R^2)^{-1}$, with x the distance from the trap waist placed at $x = 0$. The fringes depth for a −3.7 mK trap at focus is depicted in Figure 5.14. For instance, 2 mm away from the waist, fringes are already shallower than the atom temperature measured in the trap. In practice, adiabatic cooling processes could allow for transport above this limit [144]. Nevertheless, at 14 mm from the waist the fringes depth is 0.17 % of the trap depth and atoms are no longer trapped.

Experimentally, the waist position is moved with a tunable lens. This allows one to change the beam divergence before the focusing lens, hence changing the waist position. Details of the designed optical setup are discussed later in this chapter.

5.2.2. Experimental setup

Atoms transport is mainly realised by scrolling of the interference fringes of the conveyor belt toward the capacitor. In order to keep an efficient trapping all along the way, the waist position of the dipole trap has to be adjusted in consequence. In this section, details about the experimental implementation of the atoms transport are provided.

The associated setup can be divided in two parts, depicted in Figure 5.15. A first one is used to control the frequency of each arm, and so the fringes position. A second setup

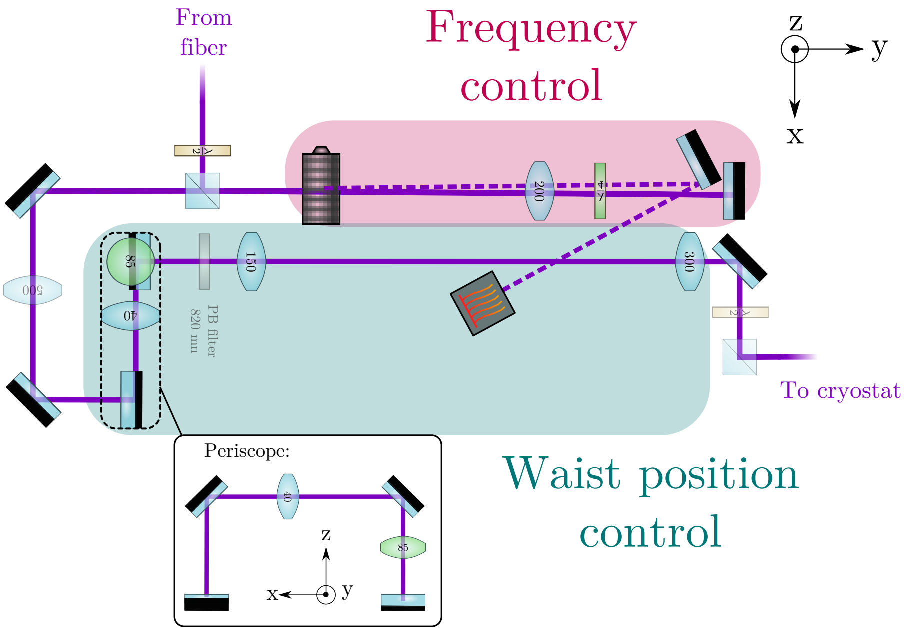

Figure 5.15. – **Transport setup** divided into two parts. The pink region is used to control the beam frequency. The teal region is used to control the waist position. The Optotune lens is indicated in green. This setup is repeated for each beam DT_0 and DT_1, as depicted in Figure 5.2.

is used to control the beam divergence before the trap lens, and so the waist position.

AOMs frequency control

The first ingredient for atoms transport is the control of the relative detuning between the two arms DT_0 and DT_1. Indeed, the fringes velocity, and thus the atoms velocity is directly proportional to the detuning between the two arms, as written in Equation 5.29. This can be experimentally tuned by changing the frequency of the RF signals used to drive the AOMs of each arm.

Each AOM is set in a double pass configuration, depicted in Figure 5.15. This allows one to change the beam frequency without changing its deflection.

In order to avoid additional phase accumulation or fluctuation, the two RF sources need to be locked in phase with one another. To ensure this, both RF signals are generated by a single Direct Digital synthesiser (DDS) *FlexDDS-NG dual*, providing two phase-coherent outputs.

On top of the phase coherence, the digital nature of this device allows for a programmable control of the RF signals, with the possibility to realise more complex detuning profiles with a 4 ns clock resolution. DDS update rate f_{DDS} can then go up to 250 MHz. This rate has to be much larger than the trap oscillations frequencies to avoid parametric heating [152].

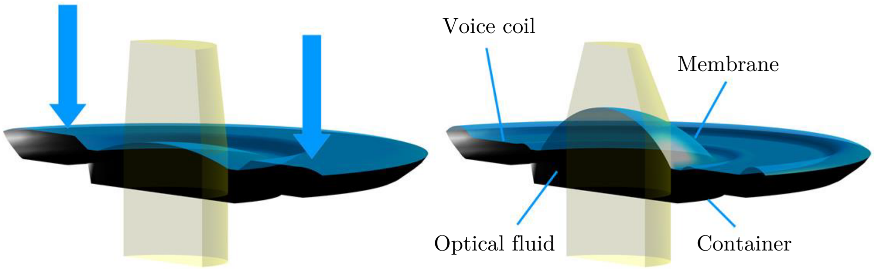

Figure 5.16. – Focus tunable lens working principle: the left picture shows the lens at rest, and the right one shows it when current is applied. In the latter, the coil presses the membrane, thus increasing the lens curvature. Figure from the *Optotune* lens datasheet.

Focus tunable lenses

The waist position of the dipole trap is controlled with a focus tunable lens *EL-10-30-TC* from *Optotune*, depicted in Figure 5.16. The lens is made up of a membrane filled with optical fluid of refractive index $n_{Opto} = 1.3$. Transmission of the lens at 820 nm is around 95%.

When a current is applied to the lens, the voice coil presses the membrane. It increases the lens curvature, which increases its optical power. Applying current to the lens allows one to tune its focal length from 50 mm to 120 mm. The associated range in optical power is from 20 dioptries (dpt) to 8.3 dpt. In terms of precision, the manufacturer's information claim a stability of ±6 mdpt over four days, and a repeatability of ±10 mdpt. It also shows no hysteresis.

In addition to the curvature change, the thickness of the lens changes with the current. As illustrated on Figure 5.16, a larger curvature leads to a thicker lens in the center. The constant part thickness is 2.35 mm.

In terms of temporal response, the lens exhibits a response time below 2.5 ms, and a settling time of around 15 ms when jumping from 4 to 8 dpt. For a smooth variation of the optical power as used for atoms transport, a more stable behaviour is expected. The associated tests are discussed in paragraph 5.2.2.

Because of the lens elastic nature, its shape can be distorted by gravity, making it a bit thicker in the bottom. To prevent additional Y-coma aberrations, the lens is mounted horizontally in a periscope-like setup, depicted in Figure 5.17. By doing so, the RMS wavefront error is kept below 0.2λ at 525 nm, removing the 0.4λ gravity induced error.

The lens is not compatible with a cryogenic environment, and cannot be directly used to focus the trap. In addition, the waist has to be kept constant during the transport. Changing the waist size would change the beams intensity, which can change the trap depth and the fringes contrast.

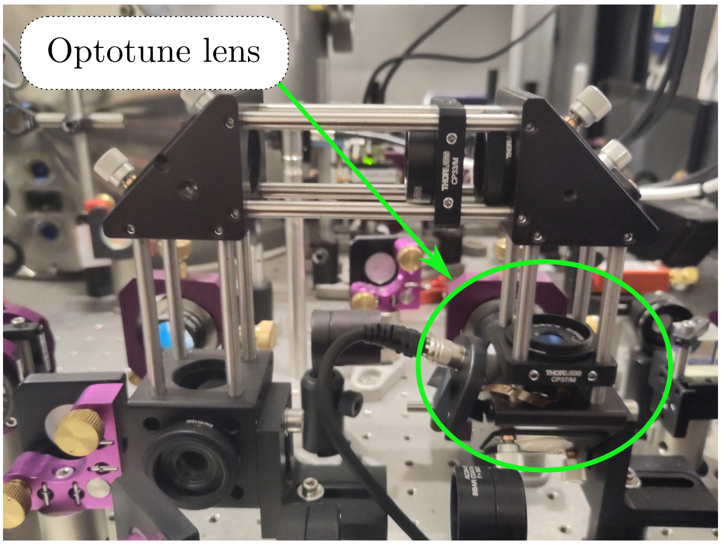

Figure 5.17. – **Periscope setup** used to horizontally mount the focus tunable lens to reduce wavefront distortion.

To comply with these constraints, the lens is used to control the beam divergence before the lens focusing the trap. This allows one to change the waist position while keeping its size constant, which is a method used in previous experiments [150].

To do so, the lens is put in one of the beam expander depicted in Figure 5.2 and Figure 5.15. In that configuration, changing the lens focal length slightly focus (resp. defocus) this tunable expander, giving the beam a small convergence (resp. divergence). The equivalent unfolded optical setup is depicted in Figure 5.18.

The beam first crosses a tunable beam expander consisting in the tunable lens, with a central focal length set to 85 mm, giving a M =2.125 magnification. A second beam expander with a magnification M' =2 is used to enlarge the beam. Finally, the beam enters the cryostat and is focused by a 10 cm lens. The waist position depends on the beam divergence before this last lens. For an input waist of 0.5 mm, the final trap waist is around 12.3 μm.

The central waist position is defined for an optical power F_c =11.7 dpt (f_c =85 mm). It corresponds to a trap centered between the 3D-MOT and the inhibition region, each of these being 7 mm apart from this point (in opposite directions). The required transport range is then ±7 mm, which corresponds to a theoretical optical power range from 9 to 15 dpt (see Equation 5.32).

Using Gaussian optics, it is possible to compute the waist size and position for the different optical powers F set to the tunable lens. The results are shown in Figure 5.19. The waist position is linear in optical power, with a slope of $\pm 2.5\,\mathrm{mm}\cdot\mathrm{dpt}^{-1}$. By construction, the displacements for each lenses are in opposite directions. The linear evolution facilitates the synchronisation of both lenses.

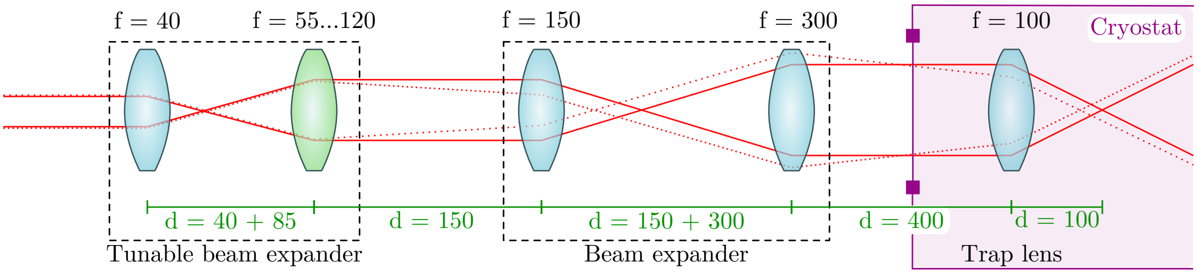

Figure 5.18. – Optical setup waist position. The lengths are given in millimeters. A first telescope with the tunable lens (green) is used to control the beam focus, which affects the trap waist position. Solid lines correspond to the default setting where the beam is collimated after the tunable lens. Dashed line is for a shorter focal length, which brings the trap waist closer to the lens.

The maximal waist displacement Δx is given by

$$\Delta x = \Delta F \frac{f_{trap}^2}{M'^2} = 25\,\mathrm{mm}\,, \tag{5.32}$$

where $\Delta F = 10\,\mathrm{dpt}$ is the optical power range of the lens, f_{trap} =10 cm the focal length of the trap lens and $M' = 2$ the magnification of the second beam expander.

In addition, this configuration has been designed such that the waist size remains constant during the transport. It is due to the fact that the second beam expander images the tunable lens plane into the trap lens object plane.

In practice, there is one tunable lens on each arm, and they are both controlled by a controller *ICC-4C-500* from *Optotune*. [4] The controller provides each lens current accordingly to an external analog input control, all of it being synchronised with other experiment part.

Preliminary characterisations — During the experiment design step, some characterisations have been performed to better understand the lens control and behaviour. More precisely, the temporal response and possible accumulated phase were studied. To do so, a small setup, depicted in Figure 5.20 has been realised. It aims at measuring the relative phase between a reference beam and one going through the focus tunable lens twice, creating a Michelson interferometer. The mirror is placed at a distance f_c =85 mm, such that the double-pass in the lens induces only a small divergence on the beam. This allows for a small variation of the beam size on the photodiode.

Indeed, when the optical power is increased, the lens thickness changes, which

---

[4] Previous current source used for the experiment was the *Lens driver 4* from *Optotune*, but a non-controllable regular temperature measurement around 20 Hz was disturbing the lens stability.

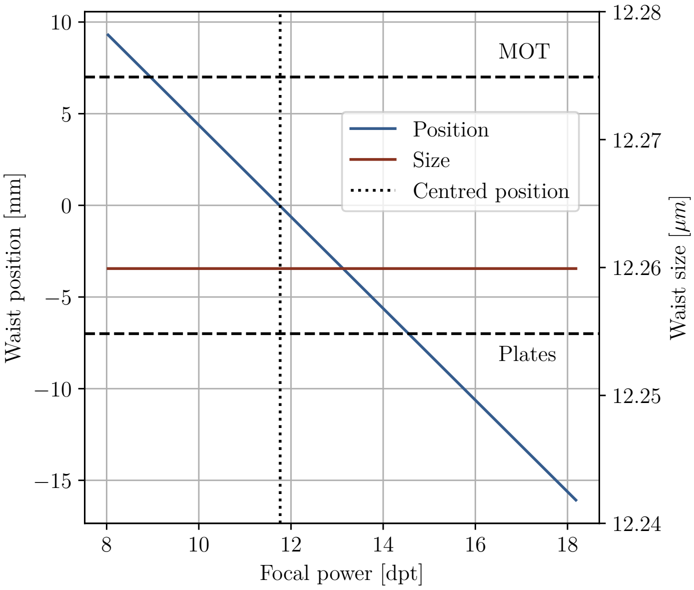

Figure 5.19. – Waist parameters during transport: numerical computation of the trap waist size and position for different optical power of the tunable lens. Input beam has a waist of 0.5 mm. Centered position corresponds to a collimated beam after the tunable lens whose focal length is then 85 mm. Slope is $-2.5\,\mathrm{mm}\cdot\mathrm{dpt}^{-1}$. 3D-MOT and inhibition plates positions are indicated for DT_1. For DT_0, positions are reversed.

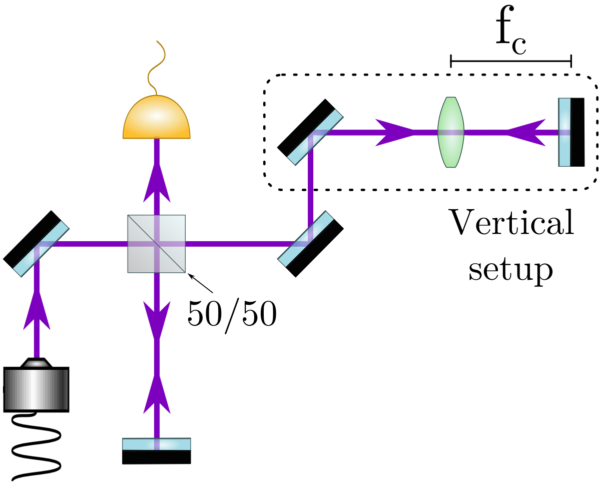

Figure 5.20. – Focus tunable lens characterisation setup: the laser beam is split in two arms by a 50:50 beam-splitter. One arm goes through the focus tunable lens (green) twice and is then overlapped with a reference beam. Interference between both beams are measured with a photodiode, giving phase information.

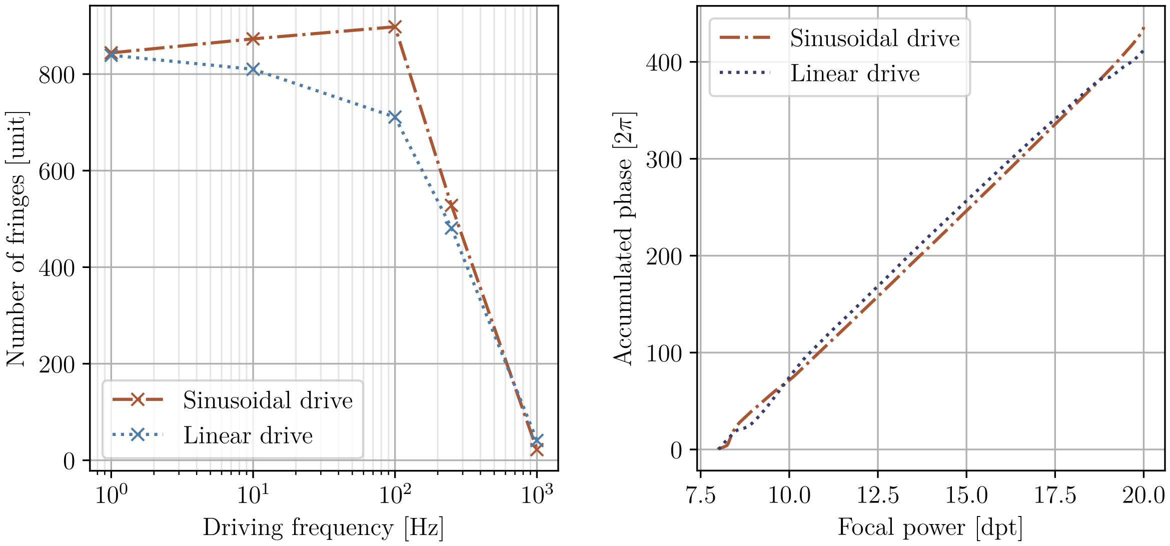

(a) Bandwidth

(b) Phase accumulation (10 Hz drive)

Figure 5.21. – **Focus tunable lens characterisation results.** The left panel 5.21a shows the number of interference fringes measured for an optical power scan back and forth between 8 and 20 dpt at different frequencies. The right panel 5.21b shows the accumulated phase as function of the optical power, relatively to 8 dpt setting.

induces a phase shift of the lens which reads

$$\varphi^{Opto}_{Double-pass} = 2\varphi^{Opto} = 2\,\frac{2\pi(n_{Opto} - n_{air})}{\lambda_L}\,\delta \tag{5.33}$$

where δ is the change of lens thickness, and with a factor 2 accounting for the double-pass in the lens. Counting the number of interference fringes covered in an optical power scan from 8.3 dpt to 20 dpt (the maximal range) then gives information about the lens behaviour. This has been tried for linear and sinusoidal variation of the optical power, with different frequencies. Associated results are depicted in Figure 5.21.

Figure 5.21a shows the number of counted fringes for different driving frequencies. It shows that whatever the driving shape, the number of counted fringes significantly drops above 100 Hz. the interpretation given here is that for too fast driving, the lens response is too slow. These estimations are consistent with the lens datasheet stating that the lens has a settling time of around 15 ms with a 4 dpt jump. In addition, the behaviour at 100 Hz suggests that the sinusoidal drive is more stable than the linear drive.

Figure 5.21b shows the accumulated phase for a double-pass through the lens as a function of the optical power, for a 10 Hz drive. It shows that the accumulated phase is linear with the optical power, meaning that the lens thickness follows a linear evolution as well. For a driving of 100 Hz and above, this behaviour is no longer observed, which is in agreement with the lens being driven too quickly. For the linear drive, the sudden change of direction induces small disturbances, visible at around 8 and 20 dpt. This is an additional signature that a sinusoidal drive is more stable for the lens.

Finally, the overall accumulated phase, for a double-pass through the lens, is estimated to be around $430 \times 2\pi$ rad. Using Equation 5.33, this corresponds to a change of 0.6 mm in the lens thickness.

Waist position error — For atom transport, two lenses are used. Each lens $j \in \{0, 1\}$ then gains an additional phase delay φ_j^{Opto}, depending on the optical power F_j. The fringes phase Φ has to be changed to take this shift into account

$$\Phi = \int \frac{\Delta\omega(t)}{2}\,\mathrm{d}t + \frac{\varphi_0^{Opto}(t) - \varphi_1^{Opto}(t)}{2}\,, \tag{5.34}$$

where the time-dependence depends on the time profile used for F_j.

In particular, since both lenses are driven in opposite direction, the phase effects add up and give the same phase shift as for the double-pass used in Figure 5.21b. The maximal accumulated phase measured (for a 8 to 20 dpt) is

$$d_{Opto}^{max} = \frac{\varphi_0^{Opto}(t) - \varphi_1^{Opto}(t)}{2k_L} = 430 \times \frac{\lambda_L}{2} = 0.18\,\mathrm{mm}\,. \tag{5.35}$$

Knowing $F_j(t)$, this could be compensated by changing the detuning profile $\Delta\omega(t)$. Finally, the real transport being from 9 to 15 dpt, the maximal associated shift is, in practice, around 0.9 mm, as depicted in Figure 5.22.

An additional error comes from the way lenses motion is programmed. Indeed, for programming simplicity, the chosen optical power shape $F(t)$ was an hyperbolic tangent shape, which reads:

$$F(t) = \frac{F_f - F_i}{2} \cdot \tanh\left(\frac{4(t - \tau_{trans}/2)}{\Delta t}\right) + \frac{F_f + F_i}{2}\,, \tag{5.36}$$

where F_i and F_f are respectively the initial and final optical power values, which depend on the lens. This profile slightly differs from the real fringes position displacement. The associated programming disagreement between waist and fringes can be computed and is depicted in Figure 5.22.

Currently, most of the error in the waist-fringes relative positioning comes from programming error. The phase shift induced by the lenses is here negligible. In any case, the sum of the two errors is below the Rayleigh length and should not significantly affect the atoms. This also could be easily fixed in the future with a more precise coding

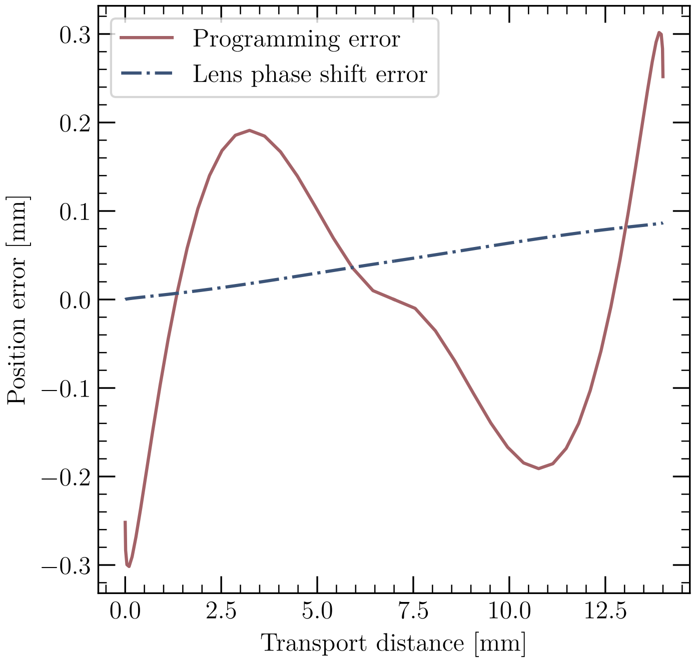

Figure 5.22. – **Waist position error** induced by the lens programming and phase shift. The figures gives the reference fringes and waist positions over time for a 14 mm transport, as well as the relative position error due to programmed shape.

of the lens profile.

5.2.3. Realisation

After the standing wave characterisations were performed, atoms transport has been implemented. For timing reasons, a practical approach has been chosen, and these characterisations are mostly preliminary. They could be completed with additional experiments to draw more reliable conclusions.

Experimental sequences

The transport of atoms is performed by a combination of a scrolling of the standing wave combined with a waist displacement. Atoms being in the ground state, their fluorescence is detected at the 3D-MOT position. Therefore, back and forth transport to the inhibition region has been used. A typical sequence used for transport characterisation is depicted in Figure 5.23.

First the dipole trap is switched on and loaded from the cold atom clouds, similarly to the last section. Trap intensity is reasonably small to avoid a too large lightshift, estimated to be around 40 MHz. Molasses conditions have been slightly readjusted, with a lower detuning and a reduced repumper power, to get a more stable loaded atoms count. However, this adjustment has been realised by eye, and quantitative measurements would probably further increase the stability.

Dipole trap intensity is then increased with a 3 ms ramp, to get a deeper trap. This increases the maximal acceleration allowed for atoms transport, as discussed in section 5.2.1. Note that this also increases the oscillations frequency inside the trap.

Transport in the forward direction is then triggered. A 4 ms delay is required to synchronise the AOMs with the tunable lenses. The detuning $\Delta\nu_{DDS}$ between the two arms is linearly increased to reach the maximal velocity in half of the transport duration[5], and then reduced back to obtain the velocity profile given in Figure 5.13.

In the same time, lenses optical power are changed such that the waist position follows the fringes. For the arm DT_0, the optical power is reduced, which increases the focal length and brings the waist closer to the capacitor, and the opposite happens for DT_1. This shape is not linear, and is discussed later.

Once the transport step is completed, a 5 ms waiting time is applied. Without it, atomic signal is lower, probably because the system needs time to stabilise. However, no quantitative study of this effect has been performed and precise explanation remains unknown.

In order to bring atoms back at the imaging position, a backward transport sequence is applied, with a negative detuning, and optical power of lenses being changed in the opposite direction.

When atoms are at the imaging position, the dipole trap intensity is reduced back to a lower value to reduce the lightshift, and cooling beams in the molasses configuration are switched on to cool down the atoms. The number of atoms is then directly measured by fluorescence imaging of the trap with a 10 ms exposure time. Imaging conditions found have a detuning of around $+\Gamma$ and a high intensity of around $1.5 I_0$. It is likely to be due to a mix of lightshift effect, with a trade-off between getting enough photons scattering and atoms heating.

The results presented in this section are normalised by the first point. An alternative would be to normalise by a witness sequence with no transport. However, some witnesses taken for the curves presented were not reliable. The same normalisation method for all curves has been chosen instead.

---

[5] Reminder that fringes moves toward the arm with the lowest frequency. Detuning is defined as $\nu_{DDS} = \nu_0 - \nu_1$, ν_i being the frequency associated to arm DT_i. With this definition, positive detuning is a move in the $+x$ direction.

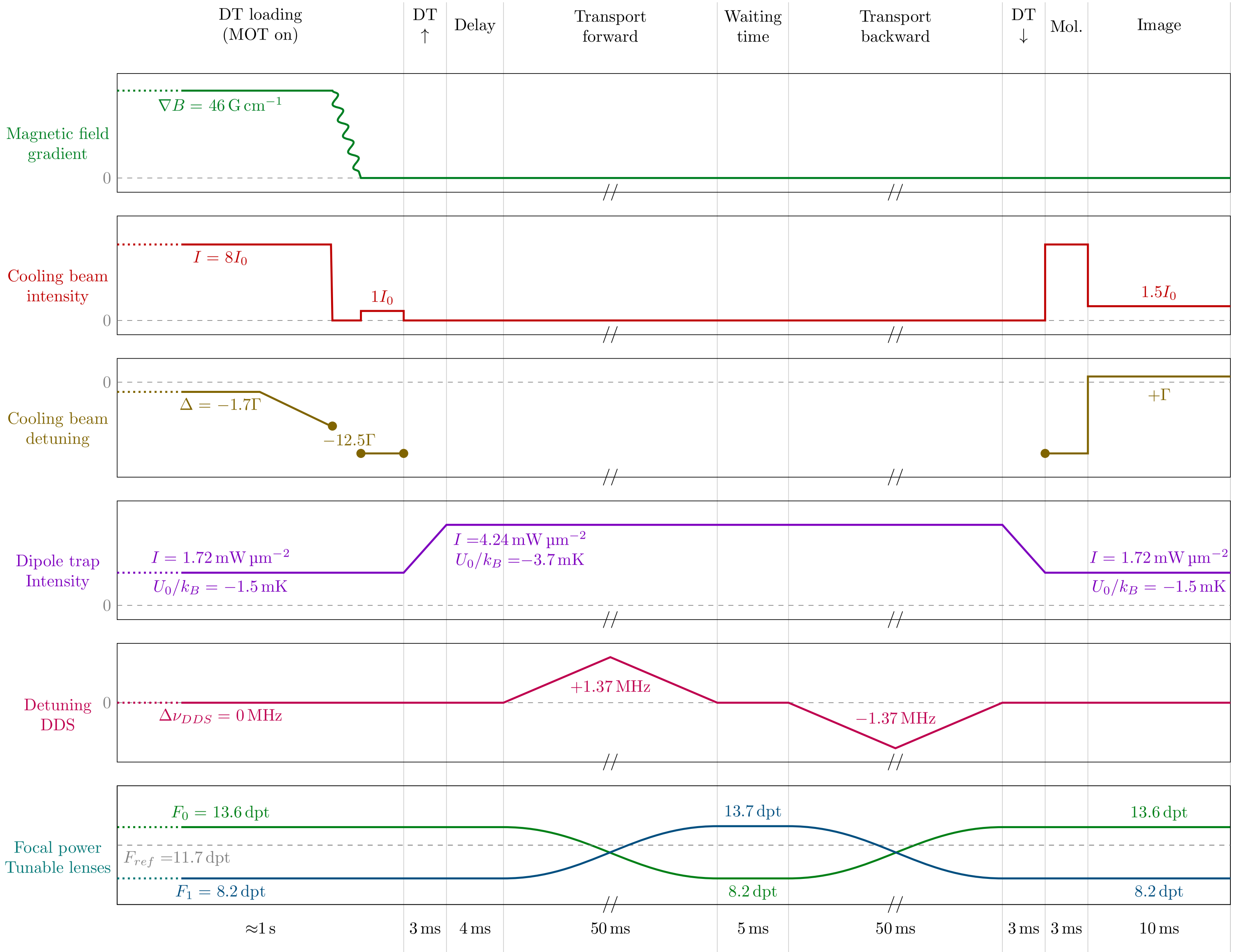

Figure 5.23. – Typical transport sequence: the dipole trap is switched on and loaded from the cold atoms clouds. Its intensity is then increased to deepen the trap. After some delay, a forward transport is started by both changing the DDS detuning and the lenses optical power. Once completed, some waiting time is required for atoms stabilisation. After that, transport backward is started. Dipole trap intensity is reduced back, a second molasse stage is used to cool the atoms before imaging is performed. Dashed lines correspond to zero values, except for the tunable lenses for which it corresponds to the default configuration.

Transport with no waist motion

The first transport sequence has been realised with without moving the waist position. It allowed for the quantification of the physical limits associated to the finite Rayleigh length z_R =0.58 mm. From a practical point of view, it allowed us to identify and fix issues without the uncertainties associated to the lenses control.

The corresponding sequence is depicted in Figure 5.24a. The main difference with the typical sequence is that the lenses optical powers are kept constant. The chosen transport duration was 40 ms. Different distances were obtained by scanning the maximal velocity, thus changing the acceleration. The obtained result is plotted on Figure 5.24b.

The interesting result here is that even if the transport efficiency drops with the distance, losses remain relatively small, below 50%, for distances up to five times the Rayleigh length. More quantitatively, at 3 mm from the waist position the trap depth drops by 96.5 %, leading to a depth of around 129 μK, which is of the order of the temperature earlier measured for a single beam configuration.

However, it is not that surprising since adiabatic cooling effect can occur when the trap depth is adiabatically reduced, as previously observed in other experiments [144]. This confirms that the position error estimated in figure Figure 5.22 should not be critical for the experiment, since transport is still efficient for a 0.6 mm distance.

Transport duration

The next step realised was to add the waist position motion to the transport sequence, by changing the lenses optical power along with the DDS detuning. In order to optimise this signal, a first characterisation has been done to estimate the effect of transport duration on its efficiency.

To study this effect, several transports with different durations were performed, changing the maximal fringes velocity reached in order to keep transport distance constant at 10 mm. This allows one to avoid possible loss of efficiency due to an imperfect overlap between the beams, leading to higher losses at higher distance. The associated sequence is depicted in Figure 5.25a.

The results of this measurement are depicted in Figure 5.25b. It shows that an optimal transport is obtained for a duration of 30 ms.

The efficiency drop for short durations suggests that the acceleration felt by the atoms is too strong. However, the maximal acceleration given by Equation 5.31 is around a^{lim} $=2.8 \times 10^3\,\mathrm{mm \cdot ms^{-2}}$. This is five to four orders of magnitudes above the accelerations applied here, as depicted in Figure 5.26a. Even if the finite temperature

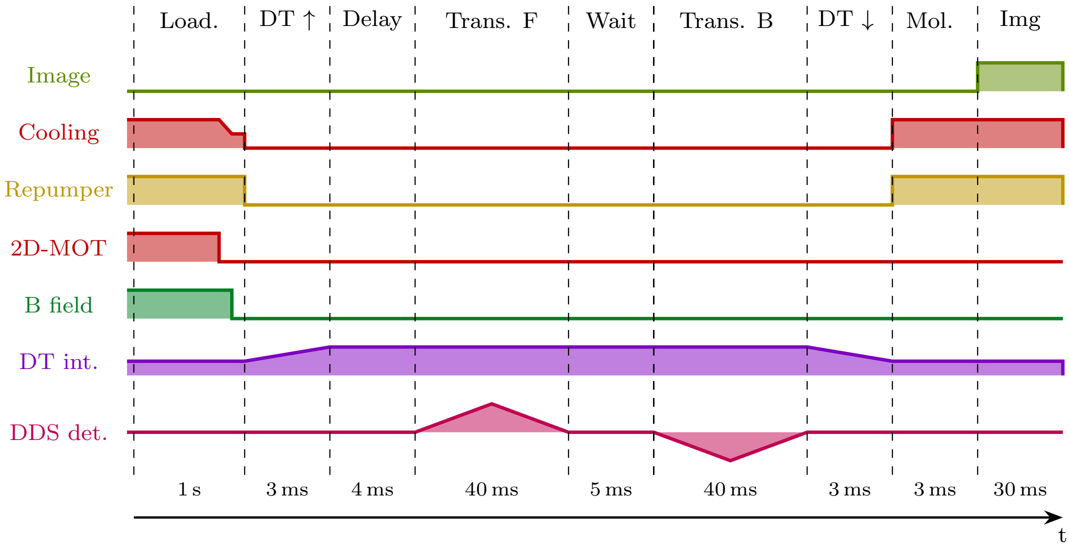

(a) Sequence

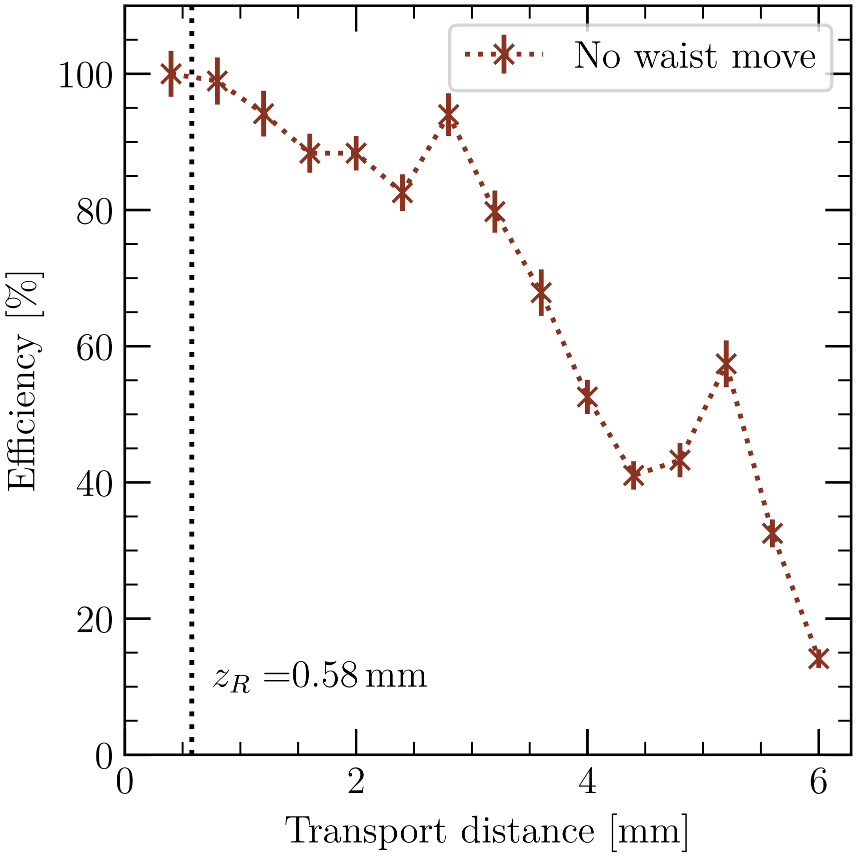

(b) Fringes only transport

Figure 5.24. – Transport with no waist motion: experimental sequence and results of a two ways transport. Signal normalised to the first point.

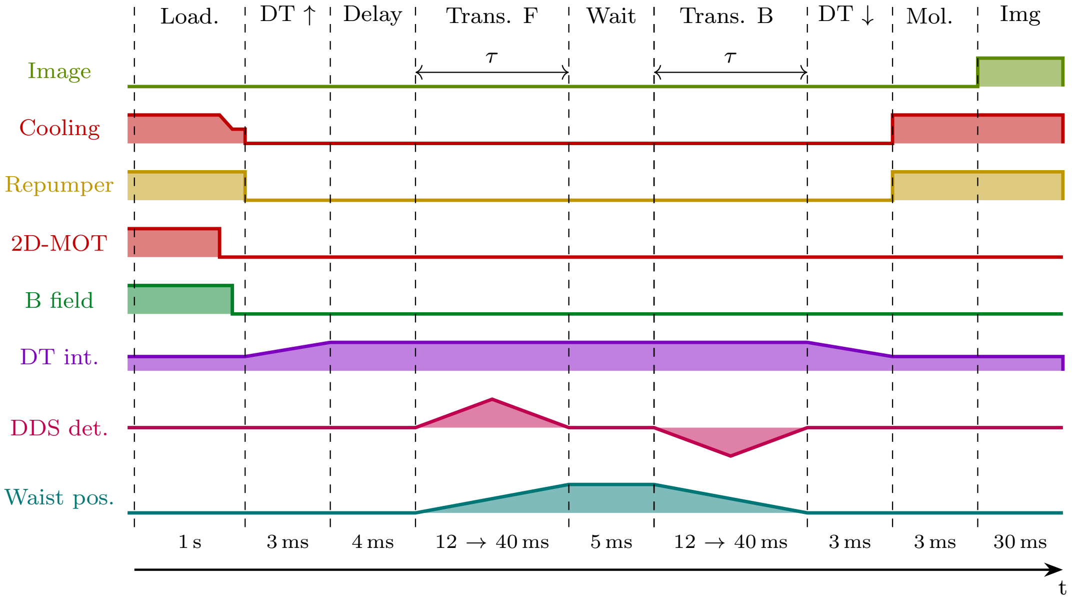

(a) Sequence

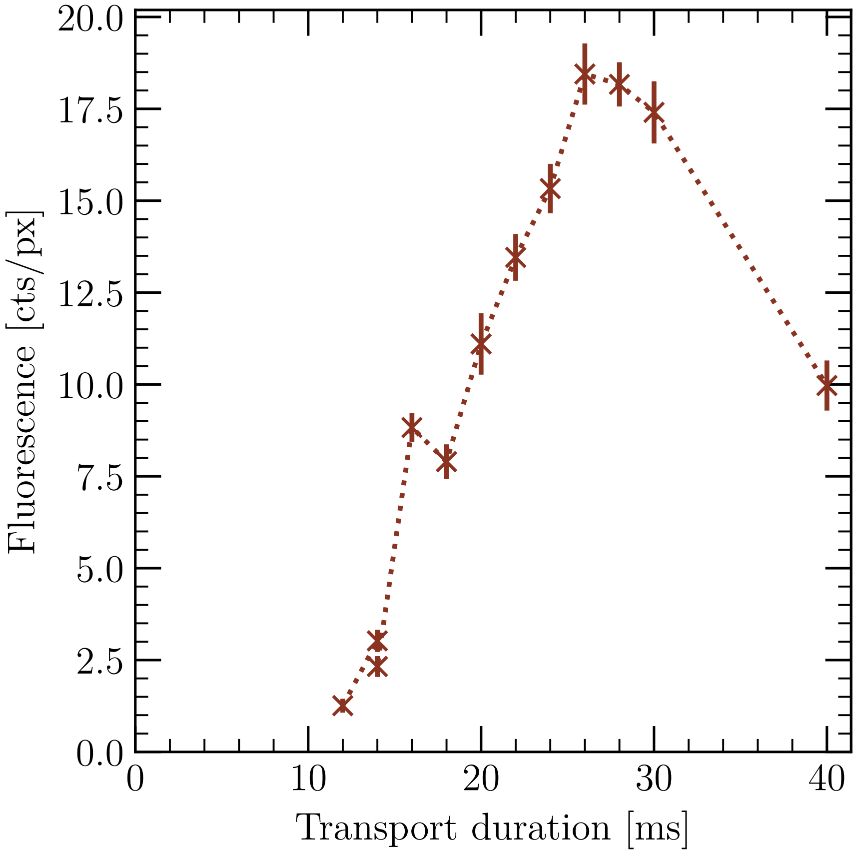

(b) Different durations effect

Figure 5.25. – **Duration effect:** study of the effect of different two ways transport durations, with a constant transport distance of 10 mm. Both forward and backward durations are changed together.

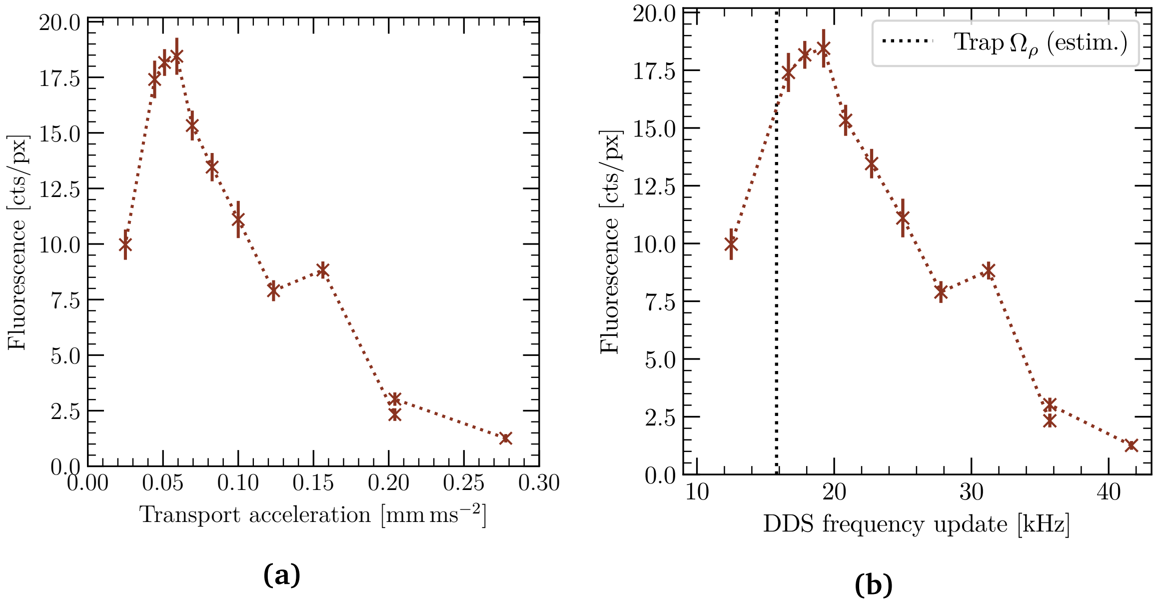

(a)

(b)

Figure 5.26. – Acceleration and DDS update frequency: same results as depicted in 5.25. Changing the duration in fact changed both the fringes acceleration and DDS update frequency f_{DDS}. Typical accelerations probed here are orders of magnitude below the fundamental maximal acceleration allowed: a_{max} =2.8 × 10^3 mm · ms^{-2}. However, DDS update frequency is comparable with the estimated trap radial oscillation frequency $\Omega_\rho/2\pi = 15.8$ kHz, which could lead to important losses.

of the atoms is taken into account, this effect alone cannot explain this depletion.

Another source of atom loss, associated to the time discretisation of the frequency ramp, has been found in the literature [152]. In practice, the DDS doesn't apply a perfect linear ramp, but updates their frequency output step by step with an update frequency f_{DDS}, that can go up to 250 MHz.

If this frequency comes close to the trap oscillation frequency, atoms can be parametrically heated and leave the trap. More precisely, this effect has been studied in the vicinity of the axial oscillation frequency for which the effect is expected to be strong. For the radial oscillations, the effect should be much smaller but could play a role.

In the present configuration, the trap depth leads to axial and radial oscillations frequencies of around $\Omega_x/2\pi = 1040$ kHz and $\Omega_\rho/2\pi = 15.8$ kHz respectively.

For the results of Figure 5.25, the frequency ramps were programmed with a fixed ramp discretisation of 500 points, leading to different update rate f_{DDS} for different durations, of the order of a few tens of kilohertz. This is illustrated in Figure 5.26b.

The axial oscillation frequencies are two orders of magnitude above the update frequencies and no parametric heating should be associated. [6] The radial oscillation

---

[6] In the cited article [152], atom loss has been observed when f_{DDS} is one order of magnitude below Ω_ρ. In this range, parametric heating should be small but other effects might come into play.

frequency however is in the range of the spanned update frequencies. To better understand if this could explain the atom depletion, measurements of the oscillation frequency should be done. If this is indeed the source of atom loss, increasing the number of points for the ramp digitalisation will increase the update frequency and should fix the issue.

Long range transport optimisation

With these first characterisations in mind, the optimisation of the transport efficiency for the full transport range has been performed. During this stage, one critical criteria found was the beam alignment onto the tunable lenses. If the beam is not centered enough onto the lens, the tuning of the optical power induces a pointing error.

A precise alignment was indeed critical to obtain a long range transport. The trap waist being around 12 μm, obtaining a proper beam overlap over the 14 mm transport range was challenging. In practice, coarse alignment is done on the beams outside the cryostat. Fine tuning is done using atomic signal. On top of it, synchronisation between the tunable lenses and the DDS had to be optimised as well.

After optimisation, the transport efficiency could be kept, with reasonable atoms losses, for the target distance of 14 mm in 50 ms. The applied sequence and obtained results are depicted in Figure 5.27, along with the curve of Figure 5.24 for comparison. Different distances are obtained by changing the maximal velocity, while keeping transport duration constant (see section 5.2.1).

Normalisation is given relatively to the first point with a transport distance of 1 mm. This normalisation leading in principle to an underestimation of the real efficiency, real transport efficiency for a two ways transport is estimated to be above 65% at 14 mm. With no surprise, this efficiency overcomes the transport efficiency with no waist motion, confirming the need for waist position adjustment.

So far, the limitations of the transport efficiency have not been clearly identified. One aspect is probably the beams alignment, which is not stable in time and has to be optimised daily. To get a more quantitative and reproducible insight, mirror mounts with piezo-electric control are to be installed. In the long-term, this could allow for a stabilisation feedback loop for the beams alignment. Other limitations could be associated to the tunable lens stabilisation or the DDS control of the frequency.

Transport verification — In order to ensure that atoms did reach the capacitor, a verification experiment has been implemented. The corresponding sequence is depicted in Figure 5.28a. To confirm the atoms presence between the inhibition plates, a kick beam resonant with the $\left|5^2S_{1/2}, F=3\right\rangle \rightarrow \left|5^2P_{3/2}, F=4\right\rangle$ transition is sent

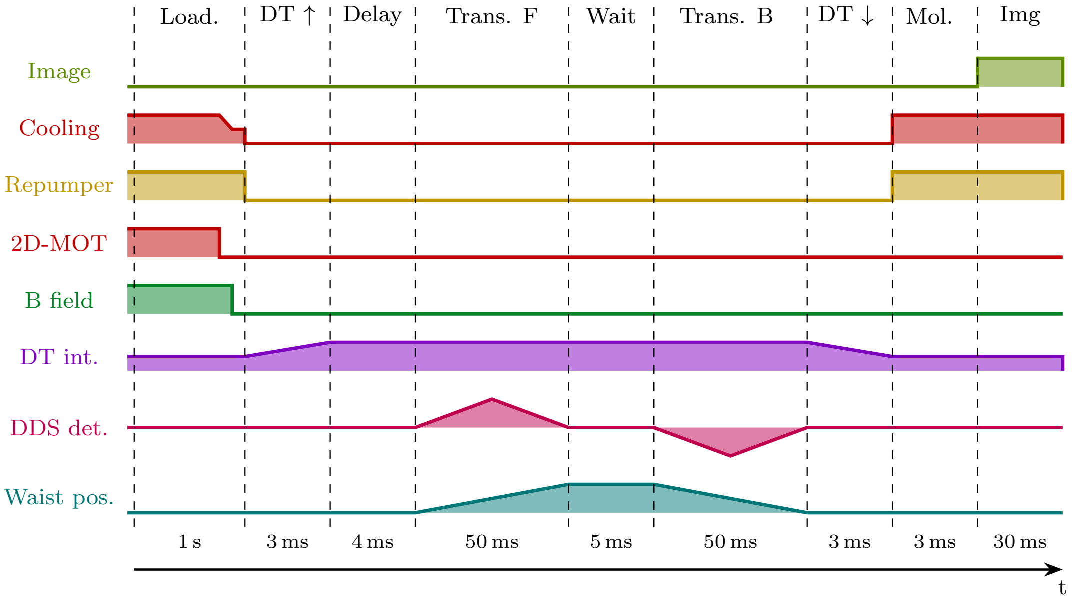

(a) Sequence

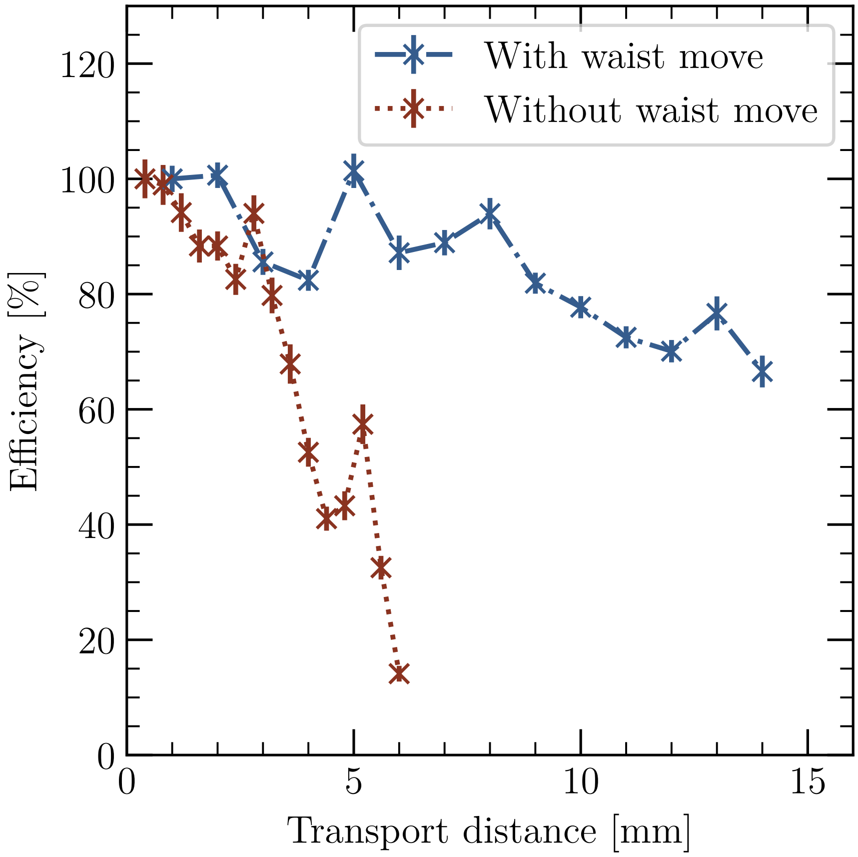

(b) Atoms transport after optimisation

Figure 5.27. – **Atoms transport** efficiency for different transport distances. Duration is kept constant, maximal velocity being changed to reach different distances. The curve with no waist motion is plotted for comparison. At 14 mm the relative efficiency is above 65%. The signals are normalised to the first point.

perpendicularly to the trap, in the center of the inhibition region. Once atoms are transported, the conveyor belt is switched of, and the kick beam is switched on for 8 μs. To improve the kick efficiency, repumper light is required as well and is switched on before the trap is switched off.

The conveyor belt is then switched back on and atoms are transported back to their initial position for imaging. The results of this experiment are shown in Figure 5.28b. Each point is normalised by a sequence for which the kick beam was not applied, and taken right after the run with a kick. A clear dip is seen at 14 mm, with a survival probability below 5%, confirming atoms presence between the inhibition plates. The kick beam waist is 0.4 mm, which is comparable with the observed dip width.

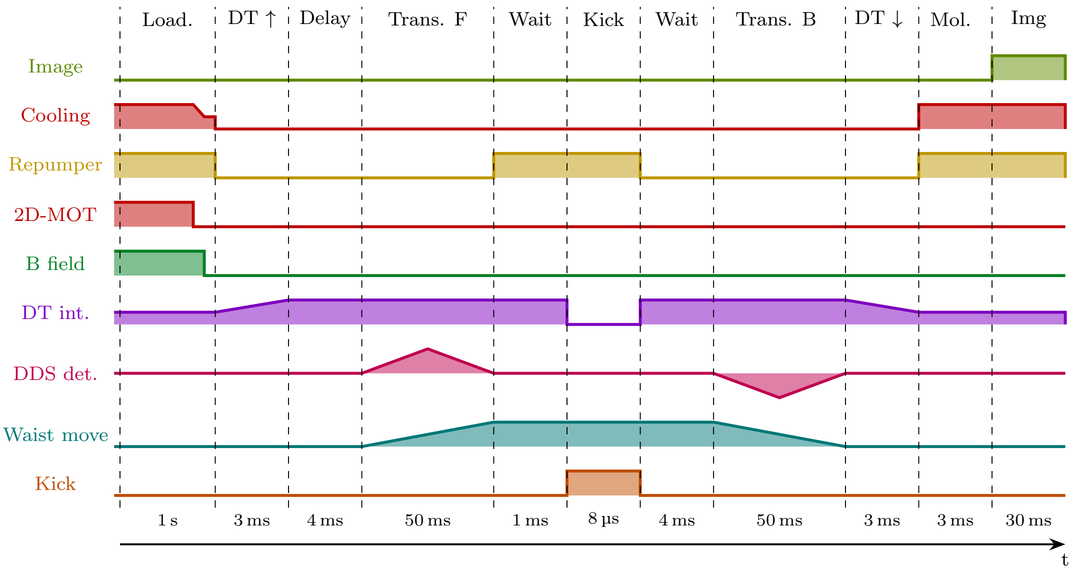

(a) Sequence

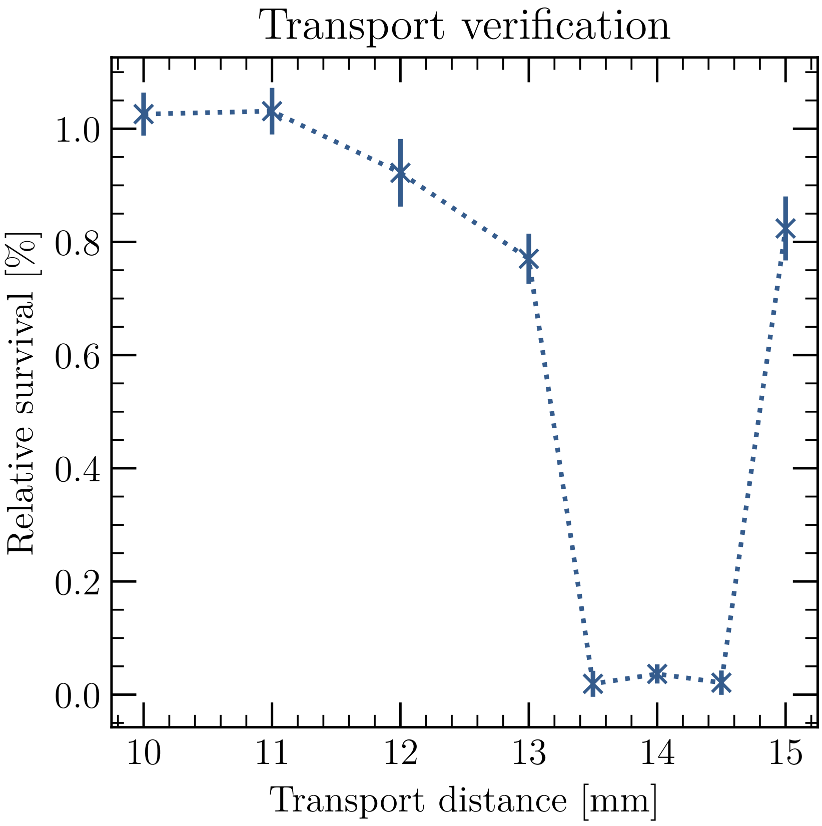

(b) Transport verification

Figure 5.28. – **Transport verification** experiment performed to confirm atoms transport between the two inhibition plates. A kick beam resonant with the cooling transition, together with a repumper beam, is applied between the two inhibition plates, while the conveyor trap is switched off. Each point is normalised by a sequence for which no kick is applied. A clear dip with a survival probability below 5% is centered at 14 mm, certifying that atoms were indeed brought at this position.

Conclusion

Deterministic delivery of atoms between the inhibition plates is a key feature toward the observation of circular Rydberg states with extended lifetimes. This is realised by the dipole trapping of ground state atoms. The trap is made of two counter-propagating Gaussian beams, creating a conveyor belt configuration which is used to precisely transport the atoms between the two inhibition plates.

Preliminary studies on one of the single Gaussian beam showed the trapping of ground state atoms. The associated trapping time is found to be in the hundred of millisecond range, depending on the laser trapping intensity. This duration cannot be solely explained by atoms heating due to trap photons scattering, and additional studies are to be performed to identify if this limited trapping time is due another heating source or to collisions with background gases. In addition, a $5^2S_{1/2} \rightarrow 5^2P_{3/2}$ transition lightshift measurement allowed for the estimation of an effective lightshift over a single beam trap power of $0.1\,\text{MHz}\cdot\text{mW}^{-1}$. This would corresponds to a trap waist of $12.1(3)\,\mu$m, which is in agreement with theoretical estimations. Finally, the atom temperature after 40 ms spent in the trap was estimated to be around $150\,\mu$K. This higher temperature could be explained by an imperfect cooling inside the trap during its loading and/or additional heating mechanisms inside the trap, on top of trap photons scattering.

Afterwards, transport in the conveyor belt configuration has been studied. It is done by scrolling of the standing wave fringes, together with a translation of the waist position. The trap intensity during transport was set to $4.2\,\text{mW}\cdot\mu\text{m}^{-2}$ ($U_0/kB = -3.7\,\text{mK}$). To move the interference fringes, a frequency detuning is applied between the two beams with the DDS controlling the trap AOMs. Velocity is linearly increased to v_{max} and decreased during transport to avoid atom heating. In the mean time, the waist of the trap is moved accordingly by changing the optical power of two tunable lenses set on each arm path. The atoms are first transported to a distance d_{trans} and then brought back at the 3D-MOT position to be imaged. After some characterisations, transport has been optimised to get a relative transport efficiency above 65% for a transport distance of $d_{trans} = 14\,\text{mm}$. This has been obtained for a duration $\Delta t = 50\,\text{ms}$ and a maximal velocity $v_{max} = 0.56\,\text{mm}\cdot\text{ms}^{-1}$. The atoms presence inside the inhibition region has been confirmed using a kick beam experiment.

This efficiency is high enough to deliver atoms inside the inhibition region, ready to be prepared into the circular Rydberg state. In the mean time, possible optimisation criteria have been identified, and could be used in the future if a higher efficiency is needed. For example, improvement of the vacuum quality should increase the trapping time. Measurement of the lightshift of the second beam and in the standing wave could help optimise the cooling inside the trap. Increasing the frequency ramp discretisation should get rid of the possible parametric heating effects associated. Finally, a more systematic measurement of the atom temperature can be used to identify possible atom heating sources, in particular ones associated to the transport.

Atoms trapping and transport summary

Single trap beam

(for I_{max} =1.85 mW $\cdot\,\mu$m^{-2} $\Rightarrow U_0/k_B = -1.64$ mK)

- Trap waist: 12.1 μm
- Trapping time: $\tau \sim 380$ ms
- Light-shift (D_2): Δf =43.6 MHz
- Atom temperature[1]: T ~150 μK

[1]: after 40 ms in the trap.

Conveyor belt transport

(back and forth transport with d_{max} =14 mm and U_0/kB =3.7 mK)

- Duration: $\Delta t = 50$ ms
- Max. vel.: $v_{max} = 0.56\,\text{mm}\cdot\text{ms}^{-1}$
- Acceleration: $a_0 = 2.2 \times 10^2\,\text{mm}\cdot\text{ms}^{-2}$
- Efficiency[3]: >65%

[3]: relative to a 1 mm transport.

Conclusion and outlook

Vienne la nuit sonne l'heure
Les jours s'en vont je demeure

— Guillaume Apollinaire, *Alcools*

In this manuscript, a new experimental setup to protect circular Rydberg atoms from spontaneous emission is presented. It combines different techniques previously developed in the Rydberg atom group at LKB. The main goal is to push forward the inhibition of circular Rydberg atom decay to a cryogenic environment in order to get rid of BBR. In addition, the ability to trap circular Rydberg atoms should allow one to fully take advantage of the extended lifetime.

The experimental part of the manuscript starts with the last results of the previous experimental setup used in this cryostat. In this experiment, entropy production of decorrelation processes has been studied using circular Rydberg atoms flying through superconducting cavities. Different decorrelating environments have been simulated with this quantum system, taking advantage of the ultimate control over it. Entropy production is shown to be quantified by the Kullback-Liebler divergence. The most challenging aspect of this work was the estimation of this non-linear function of the density matrix from experimentally reconstructed density matrices. An original method has been developed to overcome non-physical results. Final results show a relatively good agreement between simulated and experimentally measured data.

The second part of the manuscript presents the spontaneous emission inhibition setup. Designing this experiment has been especially challenging. The experiment core needs to be well isolated from BBR, with good vacuum and electromagnetic field control. In addition, the inhibition setup requires a specific geometry, involving two parallel plane conductive plates, spaced by 2 mm.

All of these requirements have to comply with the need for atom control as well. Excitation to the circular Rydberg states requires the generation of a radio-frequency field inside the inhibition region, together with a laser excitation pulse. Furthermore,

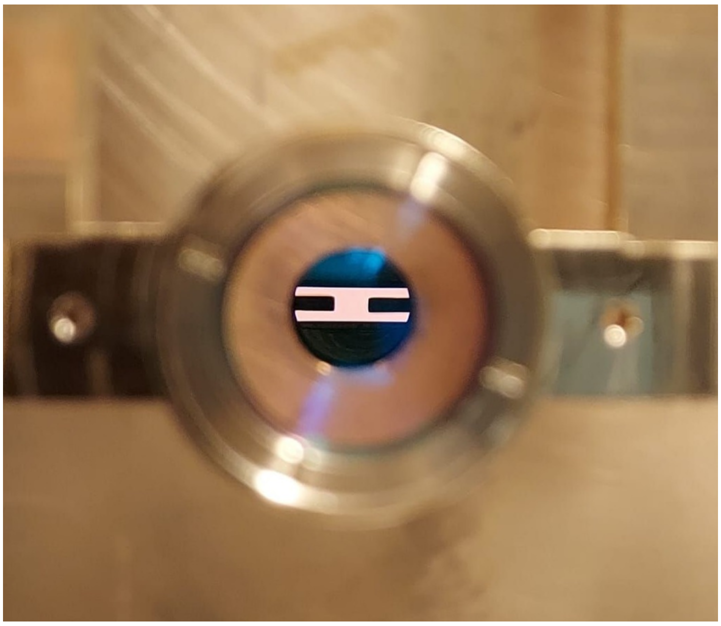

Figure 5.29. – View of the inhibition plates through the dipole trap lenses in the x direction, with the shades of the RF electrodes visible on both sides of the inhibition region.

the trapping of atoms in ground and Rydberg states is done using laser beams and thus requires optical access. This access also was a key point of the detection, since most of the characterisations of ground state atoms are realised through fluorescence detection.

The trade-off between good isolation and good control has been at the heart of the experiment design. In the proposed solution, the atom preparation can be divided into a few steps. First, atoms are cooled down using a 3D-MOT fed by a 2D-MOT. Once cold, ground state atoms are loaded into a dipole trap in a conveyor belt configuration. This allows one to move them between the two inhibition plates. There, atoms can be excited to the circular Rydberg state and trapped in a ponderomotive trap. Then their lifetime can be measured using ionisation detection.

Once the design was finalised and the manufacturing of the different parts was done, the experiment was finally assembled and started up in February 2024. [7] So far, the cooling, trapping and transport stages have been successfully realised.

For the atom cooling, challenges came from the constrained geometry. The need for screening external BBR highly restricted the optical access. In addition, one of the cooling axes goes through the inhibition region, and its size is then limited by the inhibition plates, visible in Figure 5.29. This geometry induced stray light, which made atom imaging difficult in the early stage of the experiment. Nevertheless, a cloud of cold atoms around $8\,\mu$K has been obtained.

---

[7] In between, the experimental setup has been moved from Paris to Toulouse, where the adventure will continue.

Cold atoms can then be loaded inside a dipole trap in a conveyor belt configuration, realised by means of two counter-propagating Gaussian beams. One of the main challenges of this step was to properly overlap the beams on top of the cold atom clouds and in the focal plane of the imaging lens.

Characterisations allowed for the demonstration of a trapping consistent with the design expectations. One concern is the trapping time, currently limited to a few hundred milliseconds. Possible explanations are a low vacuum quality inside the experiment core, cooled down to only 77 K with liquid nitrogen, or unidentified heating mechanisms. However, the current trapping time being long enough to study atom transport, its optimisation has been postponed.

For atom transport, a combination of two techniques is used. First, changing the relative frequency detuning of the two trap beams allows for the scrolling of the interference fringes inside which the atoms are trapped. Second, the beams waists are moved to follow the atoms. Indeed, the required transport distance is 14 mm, which is larger than the Rayleigh length of the focused transport beams. The beams waists position consequently have to be moved as well. This is done with tunable lenses.

The combination of these two techniques presented some challenges as well. The motion of the interference fringes requires an overlap of the two beams over the whole transport distance, with a precision much better than the 12 μm beams waist. Meanwhile, the beams tend to move when tuning the lenses. A careful alignment on the lenses was thus critical to ensure an efficient transport. In the end, transport with an efficiency above 65% has been demonstrated.

Now that atoms have been efficiently transported inside the inhibition region, excitation to the circular Rydberg state can be realised. This is the work currently realised by two PhD students, Ankul Prajapati and Gauthier Rey. As I write these lines, the first Rydberg states have been detected in the experiment, and the first circularisation attempts are ongoing.

Once the circular Rydberg excitation is realised, the remaining step is the trapping of the circular Rydberg atoms. Afterwards, lifetime measurement should be straightforward. The challenge then will lie in the optimisation of different points of the experiment to increase the lifetime as much as possible. Examples of the challenges to overcome are vacuum issues, the limited trapping time, and possible electric and magnetic fields inhomogeneity. The theoretical lifetime expected for this setup is in the tens of seconds range for a single atom.

The long-term perspective of this experimental setup is to perform quantum simulation. The designed trap is meant to trap a chain of circular Rydberg atoms. Using this configuration, the dynamic of a chain of a few tens of spins could be emulated. This

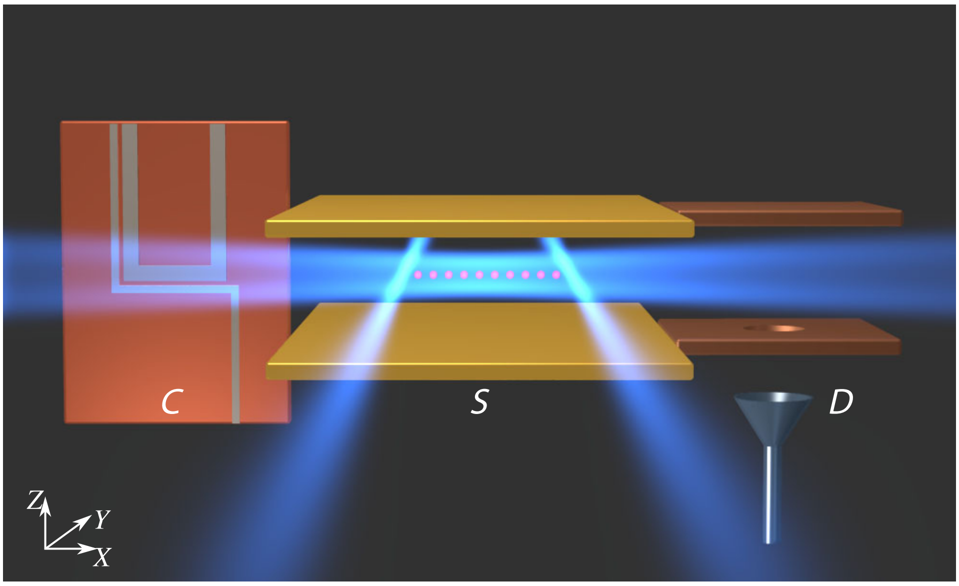

(a) Initial proposal

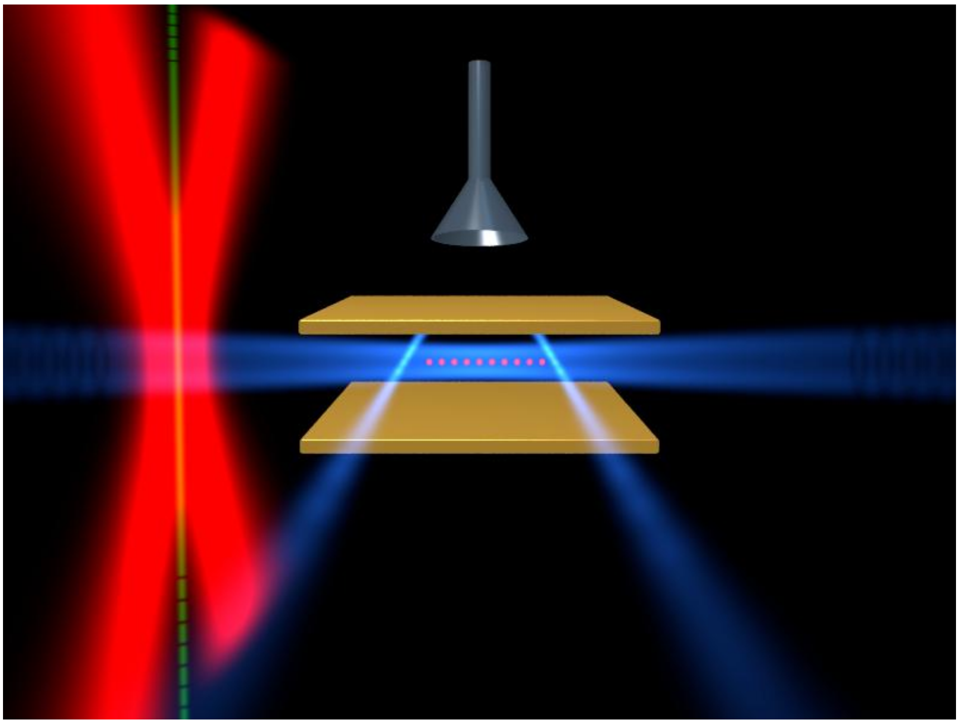

(b) Actualised proposal

Figure 5.30. – Simulator initial and actualised proposals with the trap beam (along x) and the plug beams on both sides (along y). In the initial proposal [47], atom cooling was performed with an atom chip C and detection region D was supposed to be outside of the inhibition region S. Image taken from [47]. In the actualised setup, atom cooling is performed by a 3D-MOT, and the detection is done *in-situ*.

corresponds to the proposal done by the group [47], depicted in Figure 5.30a. Since then, the initial proposal has evolved. The atom cooling is no longer realised by an atom chip but by a 3D-MOT, and the detection is now directly done *in-situ*. An updated version of the proposal is given in Figure 5.30b. The missing element in the current design is a way to prepare a defect-free chain. This could in principle be implemented by means of so-called plug beams on both sides of the chain.

Bibliography

[1] M. Planck. *Annalen der Physik*, **1901**, *309*, 553–563. (cited on page 17)

[2] N. Bohr. *The London, Edinburgh, and Dublin Philosophical Magazine and Journal of Science*, **1913**, *26*, 1–25. (cited on page 17)

[3] K. A. Peacock. *The Quantum Revolution: A Historical Perspective*. Bloomsbury Publishing USA, **2007**. ISBN 978-0-313-33448-1. (cited on page 17)

[4] J. P. Gordon, H. J. Zeiger, and C. H. Townes. *Physical Review*, **1955**, *99*, 1264–1274. (cited on page 17)

[5] S. Haroche and J.-M. Raimond. *Exploring the Quantum: Atoms, Cavities and Photons*. Oxford University Press, **2006**. ISBN 978-0-19-850914-1. (cited on page 17, 44, 56, 111, 116, 132)

[6] A. Aspect, P. Grangier, and G. Roger. *Physical Review Letters*, **1981**, *47*, 460–463. (cited on page 18)

[7] T. S. Kuhn and I. Hacking. *The Structure of Scientific Revolutions*. University of Chicago Press, **2012**. ISBN 978-0-226-45811-3. (cited on page 18)

[8] M. Arndt, O. Nairz, J. Vos-Andreae, C. Keller, G. Van Der Zouw, and A. Zeilinger. *Nature*, **1999**, *401*, 680–682. (cited on page 18)

[9] M. Brune, E. Hagley, J. Dreyer, X. Maître, A. Maali, C. Wunderlich, J. M. Raimond, and S. Haroche. *Physical Review Letters*, **1996**, *77*, 4887–4890. (cited on page 18)

[10] I. M. Georgescu, S. Ashhab, and F. Nori. *Reviews of Modern Physics*, **2014**, *86*, 153–185. (cited on page 18, 19)

[11] S. Lloyd. *Science*, **1996**, *273*, 1073–1078. (cited on page 19)

[12] P. W. Shor. *SIAM Journal on Computing*, **1997**, *26*, 1484–1509. (cited on page 19)

[13] D. Hangleiter, J. Carolan, and K. P. Y. Thébault. *Analogue Quantum Simulation: A New Instrument for Scientific Understanding*. Springer International Publishing, **2022**. ISBN 978-3-030-87215-1. (cited on page 19)

[14] O. Morsch, G. M. Palma, and D. Rossini. *La Rivista del Nuovo Cimento*, **2025**, *48*, 275–313. (cited on page 19)

[15] B. Cheng, X.-H. Deng, X. Gu, Y. He, G. Hu, P. Huang, J. Li, B.-C. Lin, D. Lu, Y. Lu, C. Qiu, H. Wang, T. Xin, S. Yu, M.-H. Yung, J. Zeng, S. Zhang, Y. Zhong, X. Peng, F. Nori, and D. Yu. *Frontiers of Physics*, **2023**, *18*, 21308. (cited on page 19)

[16] M. J. Hartmann. *Journal of Optics*, **2016**, *18*, 104005. (cited on page 19)

[17] C. Noh and D. G. Angelakis. *Reports on Progress in Physics*, **2016**, *80*, 016401. (cited on page 19)

[18] S. Slussarenko and G. J. Pryde. *Applied Physics Reviews*, **2019**, *6*, 041303. (cited on page 19)

[19] J. Wang, F. Sciarrino, A. Laing, and M. G. Thompson. *Nature Photonics*, **2020**, *14*, 273–284. (cited on page 19)

[20] F. Flamini, N. Spagnolo, and F. Sciarrino. *Reports on Progress in Physics*, **2018**, *82*, 016001. (cited on page 19)

[21] M. Hartmann, F. Brandão, and M. Plenio. *Laser & Photonics Reviews*, **2008**, *2*, 527–556. (cited on page 19)

[22] X.-s. Ma, B. Dakic, W. Naylor, A. Zeilinger, and P. Walther. *Nature Physics*, **2011**, *7*, 399–405. (cited on page 19)

[23] M. Foss-Feig, G. Pagano, A. C. Potter, and N. Y. Yao. *Annual Review of Condensed Matter Physics*, **2025**, *16*, 145–172. (cited on page 19)

[24] K. Kim, M.-S. Chang, S. Korenblit, R. Islam, E. E. Edwards, J. K. Freericks, G.-D. Lin, L.-M. Duan, and C. Monroe. *Nature*, **2010**, *465*, 590–593. (cited on page 19)

[25] S.-A. Guo, Y.-K. Wu, J. Ye, L. Zhang, W.-Q. Lian, R. Yao, Y. Wang, R.-Y. Yan, Y.-J. Yi, Y.-L. Xu, B.-W. Li, Y.-H. Hou, Y.-Z. Xu, W.-X. Guo, C. Zhang, B.-X. Qi, Z.-C. Zhou, L. He, and L.-M. Duan. *Nature*, **2024**, *630*, 613–618. (cited on page 19)

[26] X.-h. Peng and D. Suter. *Frontiers of Physics in China*, **2010**, *5*, 1–25. (cited on page 19)

[27] Z. Li, M.-H. Yung, H. Chen, D. Lu, J. D. Whitfield, X. Peng, A. Aspuru-Guzik, and J. Du. *Scientific Reports*, **2011**, *1*, 88. (cited on page 19)

[28] X. Peng, J. Zhang, J. Du, and D. Suter. *Physical Review Letters*, **2009**, *103*, 140501. (cited on page 19)

[29] J. Cai, A. Retzker, F. Jelezko, and M. B. Plenio. *Nature Physics*, **2013**, *9*, 168–173. (cited on page 19)

[30] P. J. Vetter, C. Findler, A. Verdú, M. Kost, R. Blinder, J. Fuhrmann, C. Osterkamp, J. Lang, M. B. Plenio, J. Prior, and F. Jelezko. *Room-Temperature Quantum Simulation with Atomically Thin Nuclear Spin Layers in Diamond*, **2025**. doi: 10.48550/arXiv.2510.27374. (cited on page 19)

[31] M. Chen, C. Li, G. Palumbo, Y.-Q. Zhu, N. Goldman, and P. Cappellaro. *Science*, **2022**, *375*, 1017–1020. (cited on page 19)

[32] W. Ji, Z. Chai, M. Wang, Y. Guo, X. Rong, F. Shi, C. Ren, Y. Wang, and J. Du. *Physical Review Letters*, **2022**, *128*, 090602. (cited on page 19)

[33] Y. Yao and L. Xiang. *Entropy*, **2024**, *26*, 592. (cited on page 20)

[34] D. A. Abanin, E. Altman, I. Bloch, and M. Serbyn. *Reviews of Modern Physics*, **2019**, *91*, 021001. (cited on page 20)

[35] K. Xu, J.-J. Chen, Y. Zeng, Y.-R. Zhang, C. Song, W. Liu, Q. Guo, P. Zhang, D. Xu, H. Deng, K. Huang, H. Wang, X. Zhu, D. Zheng, and H. Fan. *Physical Review Letters*, **2018**, *120*, 050507. (cited on page 20)

[36] I. Bloch, J. Dalibard, and S. Nascimbène. *Nature Physics*, **2012**, *8*, 267–276. (cited on page 20)

[37] M. Schreiber, S. S. Hodgman, P. Bordia, H. P. Lüschen, M. H. Fischer, R. Vosk, E. Altman, U. Schneider, and I. Bloch. *Science*, **2015**, *349*, 842–845. (cited on page 20)

[38] A. Browaeys and T. Lahaye. *Nature Physics*, **2020**, *16*, 132–142. (cited on page 20, 21)

[39] M. Morgado and S. Whitlock. *AVS Quantum Science*, **2021**, *3*, 023501. (cited on page 20)

[40] P. Scholl, M. Schuler, H. J. Williams, A. A. Eberharter, D. Barredo, K.-N. Schymik, V. Lienhard, L.-P. Henry, T. C. Lang, T. Lahaye, A. M. Läuchli, and A. Browaeys. *Nature*, **2021**, *595*, 233–238. (cited on page 20, 21)

[41] G. Semeghini, H. Levine, A. Keesling, S. Ebadi, T. T. Wang, D. Bluvstein, R. Verresen, H. Pichler, M. Kalinowski, R. Samajdar, A. Omran, S. Sachdev, A. Vishwanath, M. Greiner, V. Vuletić, and M. D. Lukin. *Science*, **2021**, *374*, 1242–1247. (cited on page 20, 21)

[42] F. Nogrette, H. Labuhn, S. Ravets, D. Barredo, L. Béguin, A. Vernier, T. Lahaye, and A. Browaeys. *Physical Review X*, **2014**, *4*, 021034. (cited on page 20)

[43] J. M. Raimond, M. Brune, and S. Haroche. *Reviews of Modern Physics*, **2001**, *73*, 565–582. (cited on page 20)

[44] H. Bernien, S. Schwartz, A. Keesling, H. Levine, A. Omran, H. Pichler, S. Choi, A. S. Zibrov, M. Endres, M. Greiner, V. Vuletić, and M. D. Lukin. *Nature*, **2017**, *551*, 579–584. (cited on page 20, 21)

[45] A. Reinhard, T. C. Liebisch, B. Knuffman, and G. Raithel. *Physical Review A*, **2007**, *75*, 032712. (cited on page 21)

[46] D. Comparat and P. Pillet. *JOSA B*, **2010**, *27*, A208–A232. (cited on page 21)

[47] T. L. Nguyen, J. M. Raimond, C. Sayrin, R. Cortiñas, T. Cantat-Moltrecht, F. Assemat, I. Dotsenko, S. Gleyzes, S. Haroche, G. Roux, Th. Jolicoeur, and M. Brune. *Physical Review X*, **2018**, *8*, 011032. (cited on page 21, 22, 23, 63, 94, 96, 97, 220, 221)

[48] L. Henriet, L. Beguin, A. Signoles, T. Lahaye, A. Browaeys, G.-O. Reymond, and C. Jurczak. *Quantum*, **2020**, *4*, 327. (cited on page 21)

[49] B. Ravon, P. Méhaignerie, Y. Machu, A. D. Hernández, M. Favier, J. M. Raimond, M. Brune, and C. Sayrin. *Physical Review Letters*, **2023**, *131*, 093401. (cited on page 22, 23, 52, 94)

[50] P. Méhaignerie, Y. Machu, A. Durán Hernández, G. Creutzer, D. Papoular, J. Raimond, C. Sayrin, and M. Brune. *PRX Quantum*, **2025**, *6*, 010353. (cited on page 22)

[51] Y. Machu. *Mesure non destructive et manipulation locales d'atomes de Rydberg circulaires en pinces optiques*. Ph.D. thesis, Sorbonne Université, **2024**. (cited on page 22, 29, 39, 106, 132)

[52] D. Kleppner. *Physical Review Letters*, **1981**, *47*, 233–236. (cited on page 22, 58)

[53] R. G. Hulet, E. S. Hilfer, and D. Kleppner. *Physical Review Letters*, **1985**, *55*, 2137–2140. (cited on page 22)

[54] H. Wu, R. Richaud, J.-M. Raimond, M. Brune, and S. Gleyzes. *Physical Review Letters*, **2023**, *130*, 023202. (cited on page 22, 23, 62, 94)

[55] M. Brune and D. J. Papoular. *Physical Review Research*, **2020**, *2*, 023014. (cited on page 22)

[56] R. G. Cortiñas, M. Favier, B. Ravon, P. Méhaignerie, Y. Machu, J. M. Raimond, C. Sayrin, and M. Brune. *Physical Review Letters*, **2020**, *124*, 123201. (cited on page 23)

[57] C. Cohen-Tannoudji, B. Diu, and F. Laloë. *Mécanique quantique - Tome 1*. EDP Sciences, **2018**. ISBN 978-2-7598-2287-4. (cited on page 26)

[58] E. Schrödinger. *Physical Review*, **1926**, *28*, 1049–1070. (cited on page 27)

[59] M. L. Bellac. *Physique quantique*. EDP Sciences, **2007**. ISBN 978-2-86883-998-5. (cited on page 27, 42, 43, 53, 54)

[60] J. R. Rydberg. *The London, Edinburgh, and Dublin Philosophical Magazine and Journal of Science*, **1890**, *29*, 331–337. (cited on page 28)

[61] B. Ravon. *Préparation et Piégeage d'atomes de Rydberg Circulaires Individuels Pour La Simulation Quantique*. Ph.D. thesis, Université Paris sciences et lettres, **2022**. (cited on page 29, 51, 94, 106, 132, 133, 182, 186, 190)

[62] A. Facon. *Chats de Schrödinger d'un Atome de Rydberg Pour La Métrologie Quantique*. Ph.D. thesis, Université Pierre et Marie Curie - Paris VI, **2015**. (cited on page 30, 33, 116, 249)

[63] L. D. Landau and E. M. Lifshitz. *Quantum Mechanics*. 978-0-08-020940-1, pergamon edn., **1977**. ISBN 0-08-020940-8. (cited on page 31)

[64] B. H. Bransden and C. J. Joachain. *Physics of Atoms and Molecules*. Prentice Hall, **2003**. ISBN 978-0-582-35692-4. (cited on page 34)

[65] S. Pasternack. *Physical Review*, **1938**, *54*, 1113–1113. (cited on page 35)

[66] W. E. Lamb and R. C. Retherford. *Physical Review*, **1947**, *72*, 241–243. (cited on page 35)

[67] T. F. Gallagher. *Rydberg atoms*. Cambridge University Press, **1994**. ISBN 978-0-521-38531-2. (cited on page 35)

[68] N. Šibalić, J. D. Pritchard, C. S. Adams, and K. J. Weatherill. *Computer Physics Communications*, **2017**, *220*, 319–331. (cited on page 36, 50, 168)

[69] D. A. Steck. *Rubidium 85 D Line Data*. (cited on page 37, 38, 140)

[70] H. Wu. *Millisecond-Lived Circular Rydberg Atoms in a Room-Temperature Experiment*. Ph.D. thesis, Sorbonne Université, **2022**. (cited on page 41, 55, 61, 62, 94, 97, 114, 119)

[71] C. Cohen-Tannoudji, B. Diu, and F. Laloë. *Mécanique quantique - Tome 2*. EDP Sciences, **2018**. ISBN 978-2-7598-2286-7. (cited on page 42, 49)

[72] R. G. Cortiñas. *Laser Trapping of Cold Circular Rydberg Atoms for Quantum Simulation*. Ph.D. thesis, Université Paris sciences et lettres, **2020**. (cited on page 48, 146)

[73] R. G. Hulet and D. Kleppner. *Physical Review Letters*, **1983**, *51*, 1430–1433. (cited on page 47)

[74] A. Signoles, E. K. Dietsche, A. Facon, D. Grosso, S. Haroche, J. M. Raimond, M. Brune, and S. Gleyzes. *Physical Review Letters*, **2017**, *118*, 253603. (cited on page 48)

[75] A. Larrouy, S. Patsch, R. Richaud, J.-M. Raimond, M. Brune, C. P. Koch, and S. Gleyzes. *Physical Review X*, **2020**, *10*, 021058. (cited on page 48)

[76] S. Chu, J. E. Bjorkholm, A. Ashkin, and A. Cable. *Physical Review Letters*, **1986**, *57*, 314–317. (cited on page 48, 166)

[77] V. S. Letokhov. *Laser Control of Atoms and Molecules*. Oxford University Press, **2007**. ISBN 978-0-19-852816-6. (cited on page 52)

[78] A. Einstein. *Physikalische Gesellschaft Zürich*, **1916**, *18*. (cited on page 52)

[79] C. Cohen-Tannoudji, B. Diu, and F. Laloë. *Mécanique quantique - Tome 3*. EDP Sciences, **2017**. ISBN 978-2-7598-2107-5. (cited on page 53, 54)

[80] R. G. Cortiñas, M. Favier, B. Ravon, P. Méhaignerie, Y. Machu, J. M. Raimond, C. Sayrin, and M. Brune. *Physical Review Letters*, **2020**, *124*, 123201. (cited on page 56, 63, 106)

[81] E. M. Purcell, H. C. Torrey, and R. V. Pound. *Physical Review*, **1946**, *69*, 37–38. (cited on page 58)

[82] D. Bates and B. Bederson. *Advances in Atomic, Molecular, and Optical Physics*. Academic Press, **1991**. ISBN 978-0-12-003828-2. (cited on page 59)

[83] J. D. Jackson. *Classical Electrodynamics*. Wiley, **1999**. ISBN 978-0-471-30932-1. (cited on page 60)

[84] S. Haroche, J.-M. Raimond, J. Dalibard, and J. Zinn-Justin. *Systèmes Fondamentaux En Optique Quantique*. Elsevier Science Ltd, **1992**. ISBN 978-0-444-89736-7. (cited on page 61)

[85] M. W. Zemansky and R. H. Dittman. *Heat and Thermodynamics*. McGraw Hill Higher Education, **1997**. ISBN 978-0-07-114816-0. (cited on page 66)

[86] M. Esposito, K. Lindenberg, and C. Van den Broeck. *New Journal of Physics*, **2010**, *12*, 013013. (cited on page 66)

[87] T. Sagawa and M. Ueda. *New Journal of Physics*, **2013**, *15*, 125012. (cited on page 66)

[88] H. Parrondo, Juan M. R. *Nature Physics*, **2015**, *11*, 131–139. (cited on page 66)

[89] G. T. Landi and M. Paternostro. *Reviews of Modern Physics*, **2021**, *93*, 035008. (cited on page 66, 68, 70)

[90] J. Goold, M. Huber, A. Riera, L. del Rio, and P. Skrzypczyk. *Journal of Physics A: Mathematical and Theoretical*, **2016**, *49*, 143001. (cited on page 66)

[91] R. Kosloff. *Entropy. An International and Interdisciplinary Journal of Entropy and Information Studies*, **2013**, *15*, 2100–2128. (cited on page 66)

[92] H. Tasaki. **2000**. (cited on page 67)

[93] S. Suomela, P. Solinas, J. P. Pekola, J. Ankerhold, and T. Ala-Nissila. *Physical Review B*, **2014**, *90*, 094304. (cited on page 67)

[94] S. Kullback and R. A. Leibler. *The Annals of Mathematical Statistics*, **1951**, *22*, 79–86. (cited on page 67)

[95] H. Umegaki. *Tohoku Mathematical Journal*, **1954**, *6*, 177–181. (cited on page 67)

[96] T. B. Batalhão, A. M. Souza, R. S. Sarthour, I. S. Oliveira, M. Paternostro, E. Lutz, and R. M. Serra. *Physical Review Letters*, **2015**, *115*, 190601. (cited on page 67)

[97] P. A. Camati, J. P. S. Peterson, T. B. Batalhão, K. Micadei, A. M. Souza, R. S. Sarthour, I. S. Oliveira, and R. M. Serra. *Physical Review Letters*, **2016**, *117*, 240502. (cited on page 67)

[98] B.-L. Najera-Santos, P. A. Camati, V. Métillon, M. Brune, J.-M. Raimond, A. Auffèves, and I. Dotsenko. *Physical Review Research*, **2020**, *2*, 032025. (cited on page 67, 73)

[99] L. Mancino, M. Sbroscia, E. Roccia, I. Gianani, F. Somma, P. Mataloni, M. Paternostro, and M. Barbieri. *npj Quantum Information*, **2018**, *4*, 20. (cited on page 67)

[100] P. M. Harrington, D. Tan, M. Naghiloo, and K. W. Murch. *Physical Review Letters*, **2019**, *123*, 020502. (cited on page 67)

[101] M. Rossi, L. Mancino, G. T. Landi, M. Paternostro, A. Schliesser, and A. Belenchia. *Physical Review Letters*, **2020**, *125*, 080601. (cited on page 67)

[102] A. Galindo and M. A. Martín-Delgado. *Reviews of Modern Physics*, **2002**, *74*, 347–423. (cited on page 67, 68)

[103] N. Gisin, G. Ribordy, W. Tittel, and H. Zbinden. *Reviews of Modern Physics*, **2002**, *74*, 145–195. (cited on page 67, 68)

[104] S. Haroche. *Reviews of Modern Physics*, **2013**, *85*, 1083–1102. (cited on page 68, 73)

[105] G. Manzano, J. M. Horowitz, and J. M. R. Parrondo. *Physical Review X*, **2018**, *8*, 031037. (cited on page 68)

[106] Y. Morikuni and H. Tasaki. *Journal of Statistical Physics*, **2011**, *143*, 1–10. (cited on page 68)

[107] M. Campisi, P. Hänggi, and P. Talkner. *Reviews of Modern Physics*, **2011**, *83*, 771–791. (cited on page 68)

[108] Y. Murashita, Z. Gong, Y. Ashida, and M. Ueda. *Physical Review A: Atomic, Molecular, and Optical Physics*, **2017**, *96*, 043840. (cited on page 68)

[109] P. A. Camati and R. M. Serra. *Physical Review A: Atomic, Molecular, and Optical Physics*, **2018**, *97*, 042127. (cited on page 69)

[110] V. Vedral. *Reviews of Modern Physics*, **2002**, *74*, 197–234. (cited on page 69)

[111] G. Bellomo, A. Majtey, A. Plastino, and A. Plastino. *Physica A: Statistical Mechanics and its Applications*, **2014**, *405*, 260–266. (cited on page 70, 71)

[112] S. Luo. *Physical Review A: Atomic, Molecular, and Optical Physics*, **2008**, *77*, 022301. (cited on page 71)

[113] D. R. Terno. *Physical Review A: Atomic, Molecular, and Optical Physics*, **1999**, *59*, 3320–3324. (cited on page 72)

[114] E. Hagley, X. Maître, G. Nogues, C. Wunderlich, M. Brune, J. M. Raimond, and S. Haroche. *Physical Review Letters*, **1997**, *79*, 1–5. (cited on page 72)

[115] V. Métillon. *Trajectory Tomography of Delocalized States of Two Microwave Cavities*. Ph.D. thesis, Université Paris sciences et lettres, **2019**. (cited on page 73, 82, 85, 101)

[116] V. Métillon, S. Gerlich, M. Brune, J. M. Raimond, P. Rouchon, and I. Dotsenko. *Physical Review Letters*, **2019**, *123*, 060404. (cited on page 74)

[117] C. Guerlin, J. Bernu, S. Deléglise, C. Sayrin, S. Gleyzes, S. Kuhr, M. Brune, J.-M. Raimond, and S. Haroche. *Nature*, **2007**, *448*, 889–893. (cited on page 74)

[118] S. Deléglise, I. Dotsenko, C. Sayrin, J. Bernu, M. Brune, J.-M. Raimond, and S. Haroche. *Nature*, **2008**, *455*, 510–514. (cited on page 75, 77)

[119] V. Métillon, S. Gerlich, M. Brune, J. M. Raimond, P. Rouchon, and I. Dotsenko. *Physical Review Letters*, **2019**, *123*, 060404. (cited on page 75)

[120] M. Penasa, S. Gerlich, T. Rybarczyk, V. Métillon, M. Brune, J. M. Raimond, S. Haroche, L. Davidovich, and I. Dotsenko. *Physical Review A: Atomic, Molecular, and Optical Physics*, **2016**, *94*, 022313. (cited on page 77)

[121] R. Blume-Kohout. *New Journal of Physics*, **2010**, *12*, 043034. (cited on page 86)

[122] M. H. Kalos and P. A. Whitlock. *Monte Carlo Methods*. Wiley, **2008**. ISBN 978-3-527-40760-6. (cited on page 87)

[123] N. Metropolis, A. W. Rosenbluth, M. N. Rosenbluth, A. H. Teller, and E. Teller. *The Journal of Chemical Physics*, **1953**, *21*, 1087–1092. (cited on page 87)

[124] S. Gleyzes. *Vers la préparation de cohérences quantiques mésoscopiques : réalisation d'un montage à deux cavités supraconductrices*. Ph.D. thesis, Université Pierre et Marie Curie - Paris VI, **2007**. (cited on page 101)

[125] P. Méhaignerie. *Interactions Entre Atomes de Rydberg Circulaires Piégés Pour La Simulation Quantique*. Ph.D. thesis, Sorbonne université, **2023**. (cited on page 106, 107)

[126] K. Jousten. *Handbook of Vacuum Technology*. Wiley-VCH, **2016**. ISBN 978-3-527-68826-5. (cited on page 108, 109)

[127] M. D. Lukin. *Physical Review Letters*, **2001**, *87*, 037901. (cited on page 113)

[128] D. Grosso. *Des atomes froids pour sonder et manipuler des photons piégés*. Ph.D. thesis, Université Pierre et Marie Curie - Paris VI, **2017**. (cited on page 113, 114, 143, 249)

[129] A. Signoles. *Manipulations Cohérentes d'états de Rydberg Elliptiques Par Dynamique Zénon Quantique*. Ph.D. thesis, Université Pierre et Marie Curie - Paris VI, **2014**. (cited on page 114)

[130] D. Schrader, S. Kuhr, W. Alt, M. Mueller, V. Gomer, and D. Meschede. *Applied Physics B*, **2001**, *73*, 819–824. (cited on page 125, 192, 194)

[131] C. J. Picken, R. Legaie, and J. D. Pritchard. *Applied Physics Letters*, **2017**, *111*, 164102. (cited on page 130)

[132] R. Grimm, M. Weidemüller, and Y. B. Ovchinnikov. *Advances In Atomic, Molecular, and Optical Physics*, **2000**, *42*, 95–170. (cited on page 138, 166)

[133] T. W. Hänsch and A. L. Schawlow. *Optics Communications*, **1975**, *13*, 68–69. (cited on page 139)

[134] S. Chu, L. Hollberg, J. E. Bjorkholm, A. Cable, and A. Ashkin. *Physical Review Letters*, **1985**, *55*, 48–51. (cited on page 139)

[135] P. D. Lett, R. N. Watts, C. I. Westbrook, W. D. Phillips, P. L. Gould, and H. J. Metcalf. *Physical Review Letters*, **1988**, *61*, 169–172. (cited on page 140)

[136] E. L. Raab, M. Prentiss, A. Cable, S. Chu, and D. E. Pritchard. *Physical Review Letters*, **1987**, *59*, 2631–2634. (cited on page 140)

[137] T. Arpornthip, C. A. Sackett, and K. J. Hughes. *Physical Review A*, **2012**, *85*, 033420. (cited on page 160)

[138] R. Boudot, J. P. McGilligan, K. R. Moore, V. Maurice, G. D. Martinez, A. Hansen, E. de Clercq, and J. Kitching. *Scientific Reports*, **2020**, *10*, 16590. (cited on page 160, 164)

[139] R. C. Teixeira. *Effets mécaniques de l'interaction dipolaire des atomes de Rydberg sondés par spectroscopie microonde*. Ph.D. thesis, Université Pierre et Marie Curie - Paris VI, **2014**. (cited on page 162)

[140] G. A. Askaryan. *Zhur. Eksptl'. i Teoret. Fiz.*, **1962**, *Vol: 42*. (cited on page 166)

[141] A. Ashkin. *Physical Review Letters*, **1970**, *24*, 156–159. (cited on page 166)

[142] V. S. Letokhov. *Soviet Journal of Experimental and Theoretical Physics Letters*, **1968**, *7*, 272. (cited on page 166)

[143] B. Darquié. *Manipulation d'atomes dans des pièges dipolaires microscopiques et émission contrôlée de photons par une atome unique*. Ph.D. thesis, Université Paris Sud - Paris XI, **2005**. (cited on page 182)

[144] W. Alt, D. Schrader, S. Kuhr, M. Müller, V. Gomer, and D. Meschede. *Physical Review A*, **2003**, *67*, 033403. (cited on page 186, 196, 207)

[145] S. Friebel, C. D'Andrea, J. Walz, M. Weitz, and T. W. Hänsch. *Physical Review A*, **1998**, *57*, R20–R23. (cited on page 186)

[146] S. Balik, A. L. Win, and M. D. Havey. *Physical Review A*, **2009**, *80*, 023404. (cited on page 186)

[147] C. Tuchendler, A. M. Lance, A. Browaeys, Y. R. P. Sortais, and P. Grangier. *Physical Review A*, **2008**, *78*, 033425. (cited on page 187)

[148] M. Endres, H. Bernien, A. Keesling, H. Levine, E. R. Anschuetz, A. Krajenbrink, C. Senko, V. Vuletic, M. Greiner, and M. D. Lukin. *Science*, **2016**, *354*, 1024–1027. (cited on page 192)

[149] G. Pichard, D. Lim, É. Bloch, J. Vaneecloo, L. Bourachot, G.-J. Both, G. Mériaux, S. Dutartre, R. Hostein, J. Paris, B. Ximenez, A. Signoles, A. Browaeys, T. Lahaye, and D. Dreon. *Physical Review Applied*, **2024**, *22*, 024073. (cited on page 192)

[150] J. Léonard, M. Lee, A. Morales, T. M. Karg, T. Esslinger, and T. Donner. *New Journal of Physics*, **2014**, *16*, 093028. (cited on page 192, 199)

[151] A. Couvert, T. Kawalec, G. Reinaudi, and D. Guéry-Odelin. *Europhysics Letters*, **2008**, *83*, 13001. (cited on page 192)

[152] G. T. Hickman and M. Saffman. *Physical Review A*, **2020**, *101*, 063411. (cited on page 194, 197, 210)

[153] R. W. P. Drever, J. L. Hall, F. V. Kowalski, J. Hough, G. M. Ford, A. J. Munley, and H. Ward. *Applied Physics B*, **1983**, *31*, 97–105. (cited on page 251)

Appendix A

Protocols for inhibition plates and golden mirrors preparation

Some elements of the experiment core required additional attention to be prepared and assembled. This appendix provides some protocols followed for these elements.

A.1. Inhibition plates

Inhibition plates are the heart of the experiment. Their surface being the closest one to the atom, special attention has been given to its surface preparation and glueing.

A.1.1. Polishing

The first step for the inhibition plate preparation was their polishing. This has been realised at the ENS mechanical workshop. Rugosity after polishing has been measured using an atomic-force microscope (AFM).

Measurements of the surface were performed over $20\,\mu\text{m} \times 20\,\mu\text{m}$ and $100\,\mu\text{m} \times 100\,\mu\text{m}$ large areas. Several parameters can be computed over the scanned region, with associ-

Parameter	Value
R_q [nm]	40.7
R_a [nm]	31.1
R_{max} [nm]	474

Parameter	Value
R_q [nm]	32.3
R_a [nm]	19.9
R_{max} [nm]	434

Parameter	Value
R_q [nm]	24.1
R_a [nm]	15.9
R_{max} [nm]	519

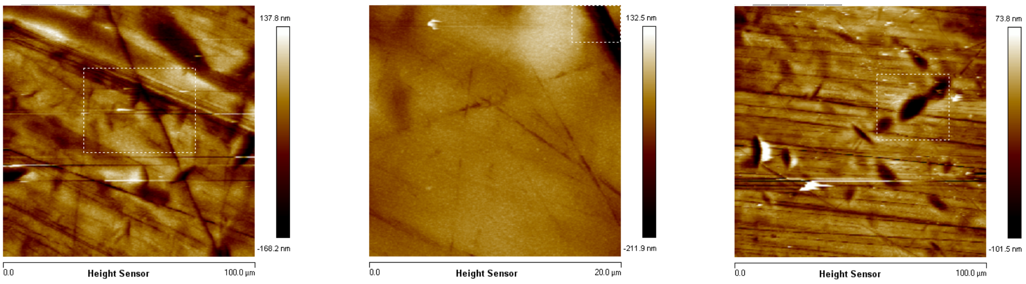

(a) 100 μm × 100 μm scan, lower plate **(b)** 20 μm × 20 μm scan, lower plate **(c)** 100 μm × 100 μm scan, upper plate

Figure A.1. – AFM pictures and results.

ated definitions:

$$R_a = \frac{1}{L}\int_0^L |z(x)|dx\,, \tag{A.1}$$

$$R_q = \sqrt{\frac{1}{L}\int_0^L z(x)^2 dx}\,, \tag{A.2}$$

$$R_{max} = max(|z|)\,, \tag{A.3}$$

A.1.2. Surface preparation

Before gold coating the surface, it is first cleaned to get rid of remaining impurities or oxidation. The protocol followed was the following:

- Clean for 60 s in acetone;
- Clean for 60 s in propan-2-ol (IPA);
- Dry with N_2;
- Clean for 3 min in a sulfamic acid solution ($5\,\mathrm{g}\cdot\mathrm{L}^{-1}$);
- Clean for 30 s in osmosis-purified water;
- Dry with N_2.

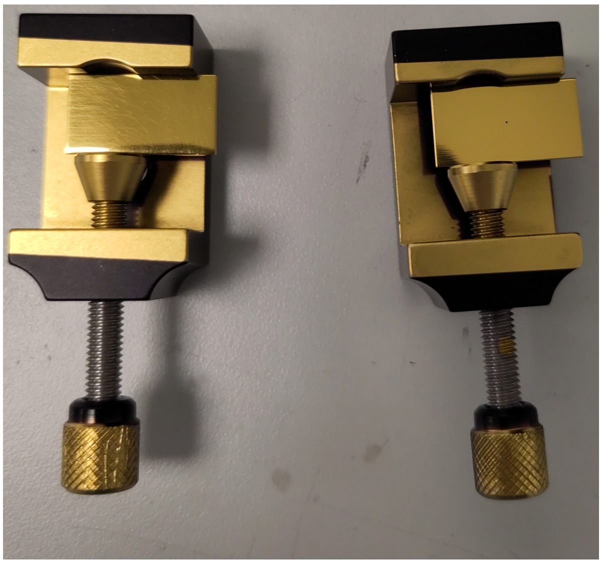

Figure A.2. – Holder used for plates gold coating.

After cleaning, the surface colour changes, probably because some oxidation is removed. The surface also looks much cleaner (by eye), but major defects, such as scratches, remain.

A.1.3. Gold coating

Once the surface is cleaned and polished, it is gilded using evaporation. To avoid shadows on the plates, they were held using two supports with screws.

For the evaporation, the chamber is pumped at a pressure around 3×10^{-6} mbar. Deposition rate was set around $2\,\text{Å}\cdot\text{s}^{-1}$. The final gold coating thickness was around 150 nm.

A.1.4. Plates gluing

Plates are glued to the capacitor block. Due to their small thickness, use of screws is not possible. In addition, the gap between the plates and the block needs to be sealed to avoid microwave leakage.

The chosen solution is an epoxy glue *330-Glue3* from *Allectra*. This glue possesses both good thermal and electric conductivities. The first is required for a good thermalisation of the plate. The second is required to seal the gap from microwave propagation, as well as a good control of the plate potential.

To avoid uneven spreading of the glue, which could lead to plate misplacement, a groove is dug in the piece on which the plate is glued, as depicted in Figure A.3. Glue is applied with a brush to get a thin layer, and thus a more even spreading of the glue.

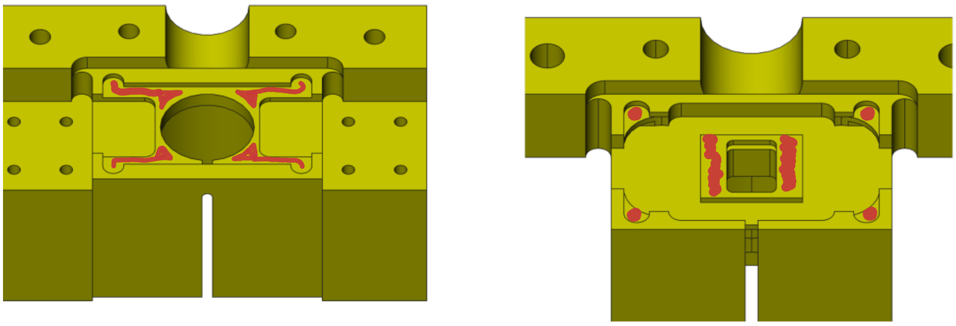

Upper plate block

Lower plate block

Figure A.3. – **Drawing of the plates block:** to which they are glued. Places where the glue was applied is indicated in red.

Glue is then cured. Note that the curing step is essential to get electric conductivity. It is thus useless to test the conductivity before curing the glue.

The glueing protocol was the following:

- Glue compounds are mixed, 10 mass equivalents of part A for 1 mass equivalent of part B;
- Glue is heated to 60 °C to increase its fluidity;
- It is applied using a brush to get a thin layer on the regions depicted in Figure A.3;
- First curing stage:
  - Heat up to 80 °C in 10 min;
  - Cure for 1 h at 80 °C;
- Second curing
  - Heat up to 130 °C in 10 min;
  - Cure for 2 h at 130 °C;
- Let the pieces cool down.

Pictures of the plates once glued are given in Figure A.4. Once glueing was completed, electric conductivity and mechanical resistance at room and liquid nitrogen temperatures were tested.

Other solutions have been considered. Melted indium was an effective solution to ensure sealing and plate glueing. However, indium is superconducting at 4 K, which is not compatible with an efficient control of the magnetic field. *Stycast* with metallic dust has also been considered but not tested.

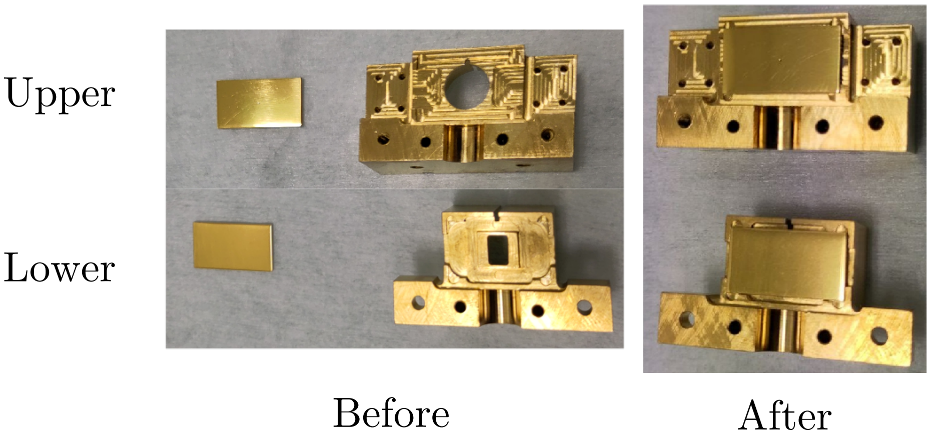

Figure A.4. – Plates and holding block: before and after gluing.

A.2. 3D-MOT gold mirrors

The mirrors used for the 3D-MOT inside the cryostat have been prepared in a similar way. To have a better surface quality, metallic mirrors have been bought with optical polishing already done.

A.2.1. Surface preparation

Before gold coating the surface, it is first cleaned to get rid of remaining impurities or oxidation. The protocol followed was the following:

- Clean for 60 s in acetone;
- Clean for 60 s in propan-2-ol (IPA);
- Dry with N_2;
- Clean for 3 min in a sulfamic acid solution ($5\,\mathrm{g} \cdot \mathrm{L}^{-1}$);
- Clean for 30 s in osmosis-purified water;
- Dry with N_2.

A.2.2. Gold coating

Once the surface is cleaned and polished, it is gilded using evaporation. To gild the mirror side, the mirrors are screwed to bars that are put on the evaporator. For coating the backside, shadows are less critical and mirrors are put on the bars as depicted in Figure A.5.

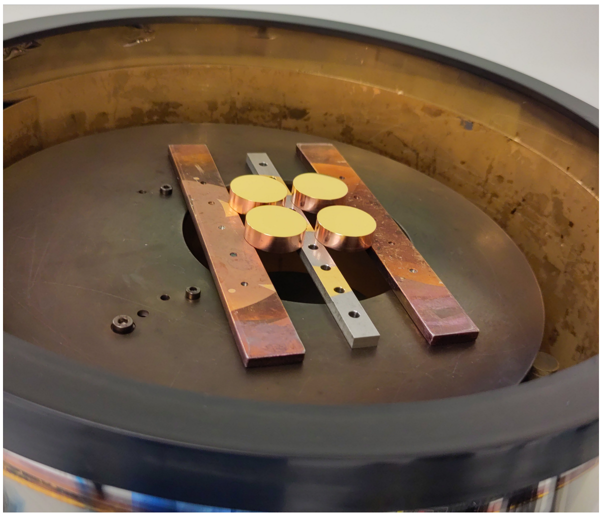

Figure A.5. – Holder used for mirrors gold coating: here for the back side. The mirror side is already coated. For coating the mirror side, mirrors are directly screwed to the holder.

For the evaporation, the chamber is pumped at a pressure around 3×10^{-6} mbar. Deposition rate was set around $2\,\text{Å} \cdot \text{s}^{-1}$. The gold layer on the mirror side is 150 nm, and the layer on the backside is 250 nm.

Appendix B

Cooling procedure

This appendix describes a typical cooling procedure, in order to give a better understanding of the timescales involved in the procedure. Data presented here comes from the 4th He cooling, realised between the 10/04/2025 and the 12/04/2025. Timestamps are given to allow future students to find the corresponding raw data.

B.1. Pumping

Once the cryostat is closed, the first step is to pump the main chamber to get a good vacuum inside. This first step is required to get rid of most of the residual gases before cooling the cryostat. In fact, even if cryo-pumping helps get a low pressure, this is essentially done by turbo-pumping the main chamber. Typical pumping curves for short and long times are depicted in Figure B.1.

First, the primary pump is first started alone (*10/04/2025, 20:30:00*). Once the pressure is below 1 mbar, typically after 15 min, the turbo pump can be started. The pressure then quickly drops, within a few minutes, to values below 1×10^{-2} mbar. After a dozen hours, it goes below 1×10^{-4} mbar.

In principle, it is better to let this pumping stage last for as long as possible, for a full weekend, for example. It is, however, sufficient to have a vacuum in the 1×10^{-5} mbar range to start the cooling stage.

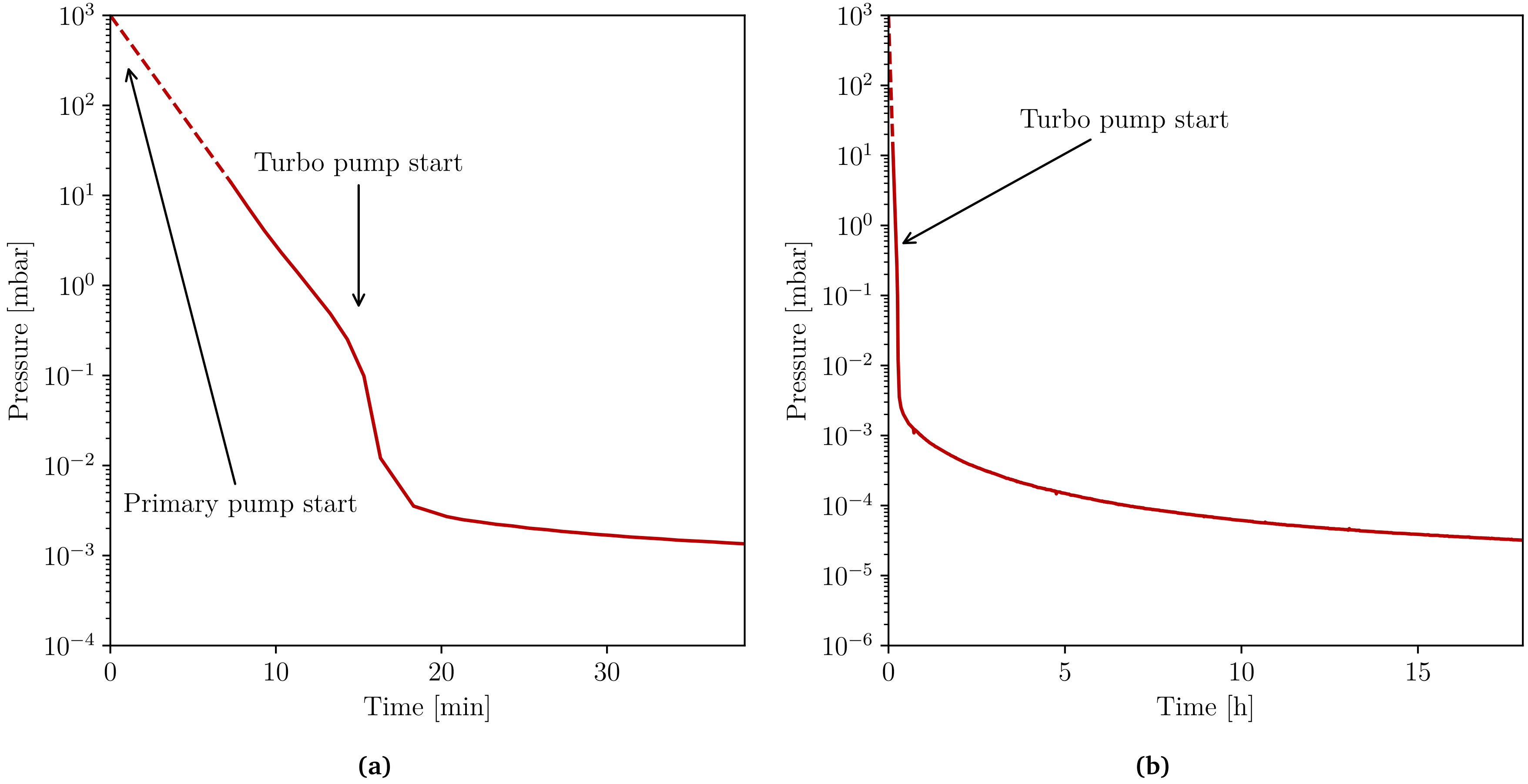

(a) **(b)**

Figure B.1. – Typical pumping curves: on a short (B.1a) and long (B.1b) time range. Data from the 10/04/2025. Time zero is 10/04/2025, 20:30:00.

B.2. Nitrogen cooling

Once the vacuum is of the order of 1×10^{-5} mbar, the first cooling stage can be performed. It consists in filling the nitrogen reservoir with liquid nitrogen (*11/04/2024, 15:00:00*). This brings the nitrogen shield down to the liquid nitrogen temperature of around 77 K. Typical temperature curves for the nitrogen shield and nitrogen reservoir (bottom) are depicted in Figure B.2a.

As soon as the reservoir is filled with nitrogen (typically a few minutes), its bottom is thermalised to the liquid nitrogen temperature. Thermalisation of the top of the reservoir (not depicted here) is slower and doesn't go this low, because it is in contact with room temperature elements.

In the meantime, the nitrogen shield goes down in temperature as well. While the reservoir is in direct contact with liquid nitrogen, the shield is only in thermal contact over a much smaller surface with the reservoir. Its thermalisation is then much slower. The reference point here is on the bottom of the shield, the furthest away from the contact with the reservoir, and therefore the last point to thermalise.

After a few hours, typically 5 h it reaches its final temperature. Note that the thermalisation speed highly depends on the contact quality between the shield and the reservoir. For example, during one of the first coolings, the screws connecting the two were not tight enough, and the thermalisation took more than 10 h. In the meantime, the experiment core (and other helium parts), which has some thermal contacts through the very top of the cryostat, starts to go down in temperature as well.

Last but not least, the vacuum quality increases thanks to the cryo-pumping effect. When the nitrogen shield goes down in temperature, some of the residual gases stick to its surface and don't contribute to the residual pressure anymore. This allows one to bring the pressure down to values around 1×10^{-7} mbar.

This effect is one of the main reasons to first cool down the nitrogen parts. In fact, if the helium parts, including the experiment core, were first cooled down, residual gases would stick to these surfaces instead of the nitrogen shield. This could deteriorate the experiment's core surfaces, such as the lenses, mirrors or inhibition plates. Another reason is simply economical. Liquid nitrogen being way cheaper than helium, it is better to use it for prior cooling rather than liquid helium.

Last but not least, some other chambers of the cryostat, such as the nitrogen exchanger or the helium reservoir, have to be pumped prior to the nitrogen cooling. In fact, if these parts stay at atmospheric pressure, humidity contained in the air can condense and then freeze when the cooling occurs, which can damage the cryostat.

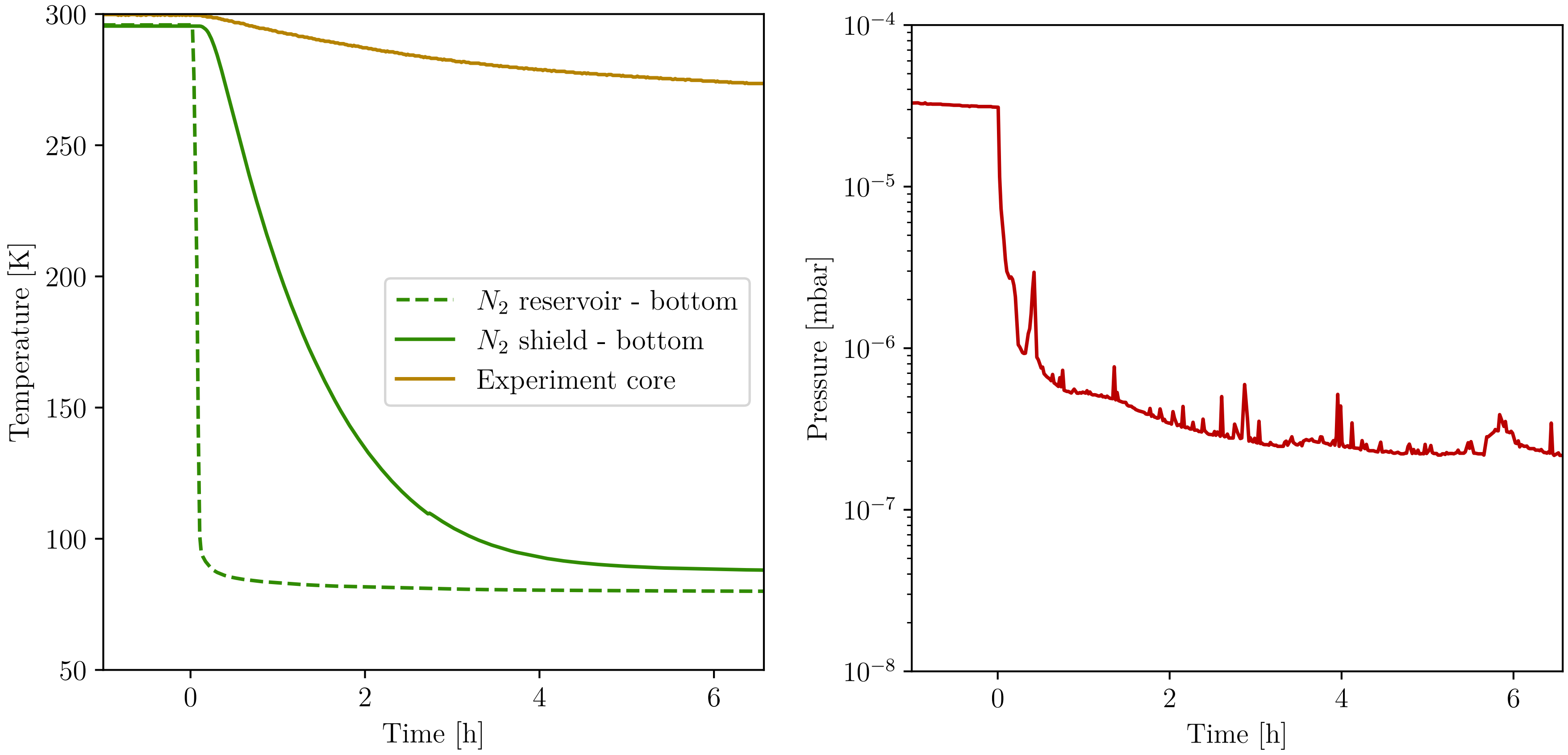

(a)

(b)

Figure B.2. – **Nitrogen cooling curves:** for temperatures (B.2a) and vacuum (B.2b). Data from the 11/04/2025. Time zero is 11/04/2024, 15:00:00.

B.3. Helium cooling

The last step of the cooling procedure is helium cooling. This step is similar to the nitrogen cooling one, instead filling the helium reservoir with liquid ^{4}He (*12/04/2024, 08:30:00*). However, filling the reservoir is more critical.

The bottom of the reservoir is where some helium is taken for ^{3}He cooling. Therefore, the presence of impurities in the helium reservoir is more detrimental. It is thus important to avoid leaks that can be induced by mis-manipulation of the transfer line. In addition, the pressure in the helium tank [1] used to fill the cryostat is built with helium gas, whereas it is done with air pressure in the nitrogen tank.

In addition, the helium enthalpy of vaporisation is lower, meaning that it instantaneously vaporises on the bottom of the reservoir, where vaporisation of the nitrogen is slower. A too-high flow of liquid helium into the reservoir can then quickly build high pressure in the reservoir, which can have disastrous effects. To avoid this, the helium flow is maintained around $2\,\mathrm{L}\cdot\mathrm{s}^{-1}$ during this procedure.

During this step, the helium shield goes down in temperature, as well as the experiment core and other parts which are directly connected to the helium reservoir. Typical cooling curves for temperature are given in Figure B.3. Note that two kinds of different temperature probes are used, each kind having a different working temperature range.

First are resistance thermometers based on platinum, so-called “platines”, which are efficient around room temperature but can give wrong estimations around liquid helium temperature. Others are bolometers, which are precise at helium temperature but can give wrong values at higher temperatures (as visible on the curves).

For these curves, the temperature of the reservoir goes down until it stabilises, which is symptomatic of the first helium drop that doesn’t vaporise, since thermalisation of the reservoir bottom is done. It occurs a few hours after the helium transfer starts. Starting from there, thermalisation of the other parts of the experiment is faster, and the reservoir is filled with liquid helium in the meantime.

Note that this step can be quickened by means of the so-called nitrogen exchanger. This is a small reservoir directly connected to the ^{4}He plate that can be filled with liquid nitrogen. It allows small amounts of liquid nitrogen to vaporise to speed up the temperature decrease. However, this has to be stopped, and the exchanger needs to be emptied before the liquid nitrogen temperature is reached. Otherwise, the nitrogen stays liquid and can even become solid below 63 K. This can clog the nitrogen exchanger, build pressure and damage the cryostat.

---

[1] Terminology precision: “reservoir” refers to the cryostat part where the corresponding cryogenic liquid is put, and “tank” refers to the container from which cryogenic liquid is taken from to be transferred into the cryostat.

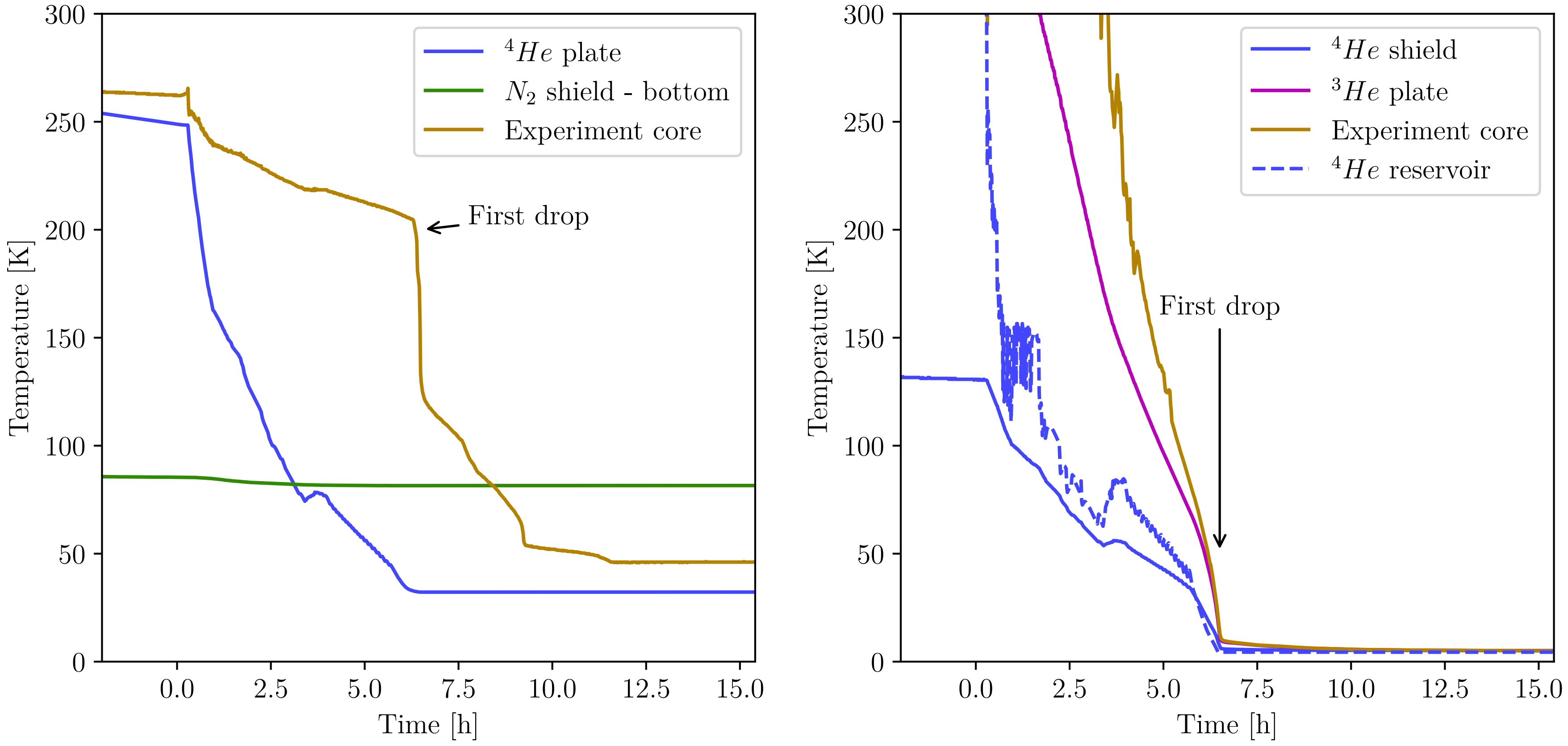

(a) Platines

(b) Bolomoters

Figure B.3. – **Helium cooling curves:** for temperatures using platine probes (B.3a) and bolometers (B.3b). Data from the 12/04/2025. Time zero is 12/04/2024, 08:30:00.

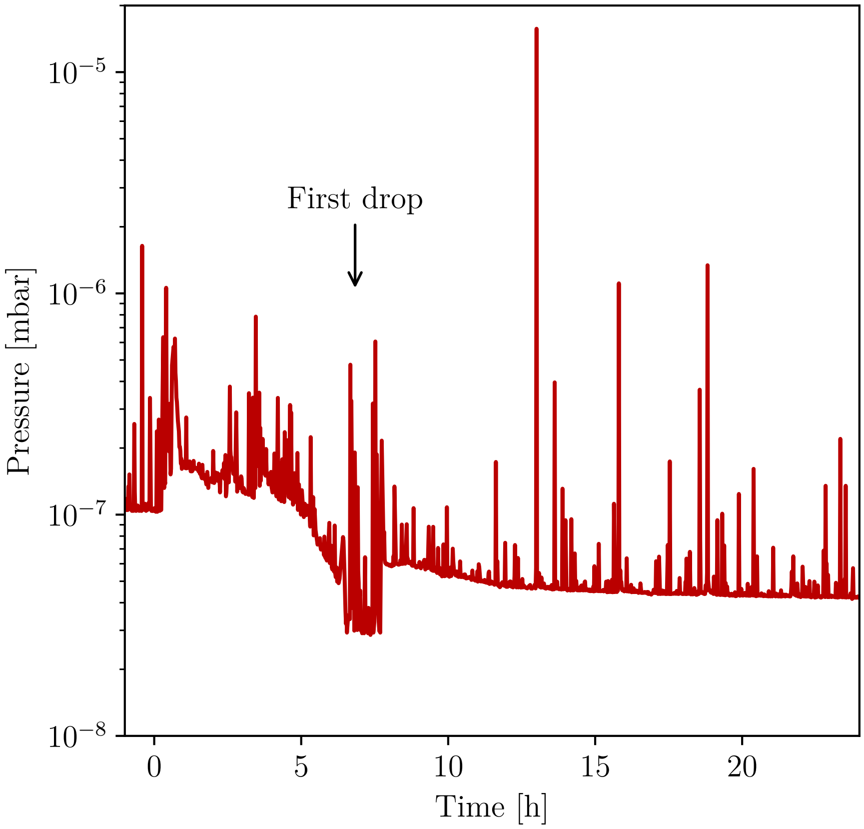

Figure B.4. – Helium cooling vacuum: measured on one of the outer chamber gauges. Data from the 12/04/2025. Time zero is 12/04/2024, 08:30:00. Arrow indicates the first helium drop .

Last but not least, the vacuum also changes during this step, as depicted in Figure B.4. However, even if the liquid helium cryo-pumping is more efficient, it occurs inside the helium shield region. This is far from the vacuum gauges, and only a small effect is measured on them. Nevertheless, measured pressure slowly decreases and usually stabilises around 3.8×10^{-8} mbar within a few days.

Vacuum inside the experiment core is expected to be lower thanks to helium cryo-pumping. However, the presence of a leak between the helium reservoir and the experiment core deteriorated the vacuum while experimenting. This region can't be directly probed by a vacuum gauge, and it is therefore hard to estimate is the real vacuum inside is and how it evolves with time, especially in the presence of potential leaks.

In addition, some details can be given about the procedure to heat up the cryostat. It usually takes a few days for the reservoirs to evaporate (*cf.* below). A way to speed up the process is to remove the cryogenic liquid from the different reservoirs. This is done by applying a slight overpressure inside the reservoir, with a transfer line installed, to push the liquid outside. This procedure is quite critical since a too high a pressure inside the reservoir can damage the cryo. Another (complementary) way is to blow hot gas to blow out cold gases from inside.

B.4. Cryostat general properties

In its steady state, some typical parameters of the cryostat are important to know, such as its cryogenic liquid consumption, its autonomy or typical pressures. These values can vary from one experiment core structure to another, but might also depend on other factors (leaks, spurious thermal contacts). Values given here are typical values observed for the current configuration.

The nitrogen reservoir has to be refilled on a regular basis. This is automatically done by electronic devices. Depending on the devices settings, the refills can be more or less frequent, but always before the reservoir is completely empty. The tank (100 L) used for these automatic refills usually has to be refilled twice a week.

In terms of helium consumption, cooling the cryostat usually requires around 100 L of liquid helium until the first drop appears, and then 30 L to fill the reservoir. Once filled, typical heat dissipation measured in the helium bath for this setup is around 290 mW, which corresponds to an evaporation rate around $0.4\,\mathrm{L \cdot h^{-1}}$. In practice, associated autonomy was found to be around 58 h.[2]

Atoms cooling summary

Nitrogen reservoir

- Volume: 31 L
- Autonomy: ≈0 h
- Evaporation rate: $\approx 0\,\mathrm{L \cdot h^{-1}}$

Helium reservoir

- Volume: 24 L
- Evaporation rate: $0.4\,\mathrm{L \cdot h^{-1}}$
- Power dissipation: 290 mW
- Autonomy: 58 h

Misc.

- Pressure: 3.8×10^{-8} mbar
- Exp. core temp.: 4.7 K

---

[2] Reference data: cryostat refilled on the 29/03/2024 at 18:40:00. The last drop evaporated on the 01/04/2025 around 04:50:00.

Appendix C

Laser lock system

Atom manipulation requires precisely addressing optical transitions. In this experiment, it is required for the atoms' cooling and Rydberg excitation. The frequency of the used laser beams needs to be precisely controlled, with a required precision given by the associated transition linewidth. Stabilisation of the laser frequency is also called frequency lock.

This appendix will provide general elements about the lasers' frequency lock, as well as details about the experimental methods used to do it. A summary of the lasers locked, with their use frequency and linewidth, is given in Table C.1. Note that most of the lasers are not exactly locked on the associated transition but usually tens of megahertz below. This is because AOMs are used later on the path, lifting the frequency usually by around 100 MHz.

One key aspect of the laser frequency lock is their relative stability. If each laser needs

Name	Transition	Wavelength	Use
780 MOPA	$\left|5^2S_{1/2}, F=3\right\rangle \rightarrow \left|5^2P_{3/2}, F=4\right\rangle$	780 nm	Cool. / 1st Ryd. / Probe
Repumper	$\left|5^2S_{1/2}, F=2\right\rangle \rightarrow \left|5^2P_{3/2}, F=3\right\rangle$	780 nm	Cool. / Ryd. / Probe
776	$\left|5^2P_{3/2}, F=4\right\rangle \rightarrow \left|5^2D_{5/2}, F=5\right\rangle$	776 nm	2nd Ryd.
1258	$\left|5^2D_{5/2}, F=5\right\rangle \rightarrow \left|52f, \lvert m\rvert=2\right\rangle$	1258 nm	3rd Ryd.

Table C.1. – Summary of laser beams that are frequency locked.

to have an individually stabilised frequency, the relative phase between all lasers is required to obtain an efficient excitation for processes that involve successive excitation. In practice, this is ensured by locking all lasers successively on a signal coming from a reference laser. The reference laser here is the 780 MOPA.

The general procedure will be explained here. To maintain a laser at the right frequency, it is necessary to have a frequency reference. Different possibilities exist for this reference, and a few examples will be covered in the following. Note that this setup was used for previous experiments, and more details can be found in other thesis [128][62].

Through the different frequency lock methods, lasers are usually not locked exactly on the transition frequency, but rather around 100 MHz below. This allows to place an acousto-optical modulator later in the optical path to fine-tune the frequency. Once all lasers are frequency locked, they are sent to the cryostat optical table where they are overlapped and sent in the cryostat, after polarisation adjustment. Details about the optical path can be found in Appendix D.

C.1. 780 MOPA

The first excitation step corresponds to the $\left|{}^5S_{1/2}, F=3\right\rangle \rightarrow \left|{}^5P_{3/2}, F=4\right\rangle$ transition at 780 nm. It is the one used for atom cooling and the first Rydberg excitation step. This corresponds to the ^{85}Rb D_2 line, directly visible on the rubidium spectral lines. The setup used to frequency lock the corresponding laser is given in Figure C.1. A fragment of the associated laser is sent to a heated rubidium cell to obtain a saturated absorption spectrum, depicted in Figure C.2. Knowing the spectroscopic structure, it is possible to set a feedback loop to stabilise the laser frequency at a target absorption peak position.

The saturated absorption allows one to get rid of the Doppler broadening of the transition. In fact, for a simple absorption spectrum, the velocity distribution of the atoms inside the cell allows atoms that are not exactly at resonance with respect to the atomic transition to absorb light, thanks to the Doppler effect. An example of non-saturated absorption is given in Figure C.2, for which the half-peak broadening is around 1 GHz.

To get rid of this broadening, a counter-propagating beam, often called "pump" is sent to the cell with an intensity high enough to saturate the atoms. Let's assume that the lasers propagation vector is $\pm\vec{k}$. If the laser is non-resonant with the atomic transition, with a detuning Δf, the two beams will be absorbed by two classes of atoms: one beam with atoms for which $\vec{k}\cdot\vec{v} = 2\pi\Delta f$, the other with atoms for which $-\vec{k}\cdot\vec{v} = 2\pi\Delta f$. If the laser is resonant with the transition, then $\Delta f = 0$ and both lasers are resonant with

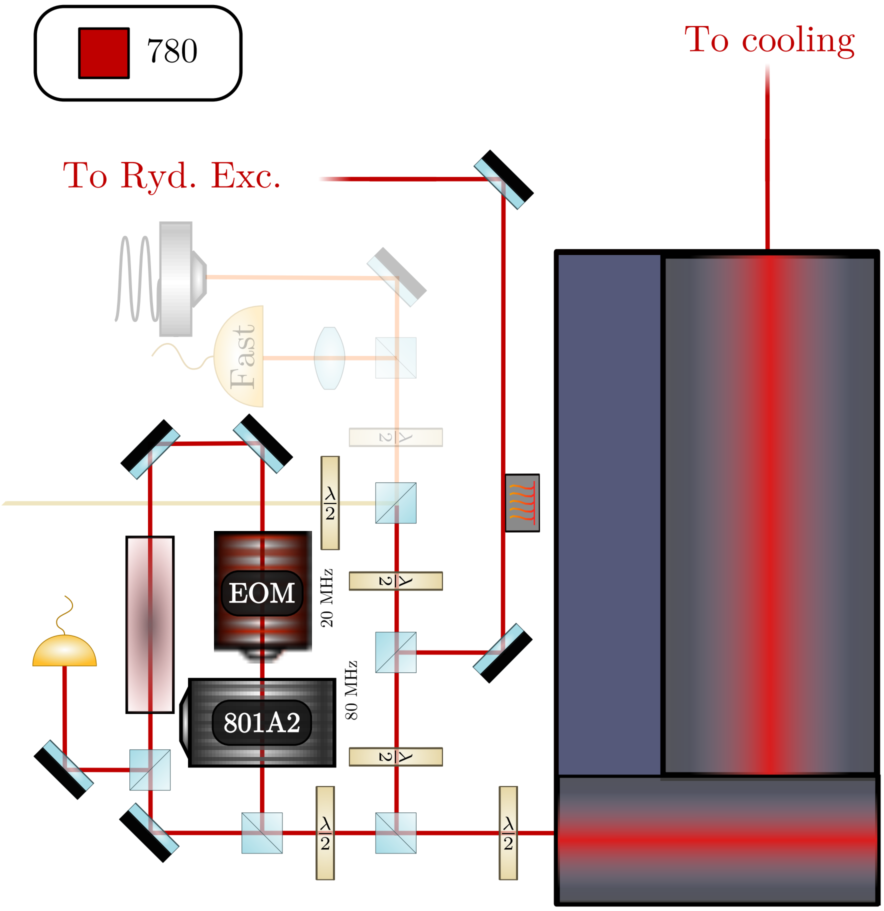

Figure C.1. – 780 MOPA lock setup.

the same class of atoms. Since the pump laser saturates the atom, the second "probe" laser is not fully absorbed and a peak appears in the absorption signal.

This configuration also shows peaks for which the pump and the probe beams are absorbed by the same class of atoms, but through different transitions. These peaks are called cross-overs. The peak on which the laser is locked is the peak $C(3,4)$, for which the atoms with a velocity $\vec{v}$ are resonant with the transition $F=3 \rightarrow F'=4$ at frequency $f_{3,4}$ for one beam and $F=3 \rightarrow F'=3$ at frequency $f_{3,3}$ for the other beam. The Doppler resonance condition therefore gives that

$$\begin{cases} 2\pi f_{3,3} & = -\vec{k} \cdot \vec{v} \\ 2\pi f_{3,4} & = +\vec{k} \cdot \vec{v}\,. \end{cases} \tag{C.1}$$

The cross-over frequency is then $f = (f_{3,3} + f_{3,4})/2$, which is 60 MHz below the $\left|{}^5S_{1/2}, F=3\right\rangle \rightarrow \left|{}^5P_{3/2}, F=4\right\rangle$ transition. Last but not least, in this setup an AOM at f_{AOM} =80 MHz is put on the probe beam path. The corrected cross-over frequency is thus

$$\begin{cases} 2\pi f_{3,3} & = 2\pi f_{AOM} - \vec{k} \cdot \vec{v} \\ 2\pi f_{3,4} & = +\vec{k} \cdot \vec{v}\,. \end{cases} \tag{C.2}$$

The lock frequency is then $f = (f_{3,3} + f_{3,4} + f_{AOM})/2$, which is 100 MHz below the $\left|{}^5S_{1/2}, F=3\right\rangle \rightarrow \left|{}^5P_{3/2}, F=4\right\rangle$ transition. The EOM on the path is put to modulate the phase of the probe beam, in order to stabilise the laser frequency using a Pound-Drever-Hall scheme [153].

C.2. Repumper

Frequency lock of the repumper laser is done using the previously locked 780 MOPA laser as reference at a frequency f_{MOPA}. The difference in frequency between the cooling and repumping transitions is known to be 2.914 GHz. The setup used to lock the repumper is given in Figure C.3. A fragment of the cooling beam is taken and overlapped with a fragment of the repumper beam at a frequency f_{rep} on a fast photodiode. The latter needs to be able to detect sinusoidal signals of a few gigahertz. The obtained beating signal is mixed with a reference signal to give a second beating signal depicted in Figure C.4. The beating signal frequency equals $f_b = f_{MOPA} - f_{rep}$, the high frequencies being filtered out by the photodiode.

This signal is mixed with a reference signal at f_{ref} =2.981 MHz produced by a frequency synthesiser *SG4400L*. The obtained signal is then amplified, and interferes

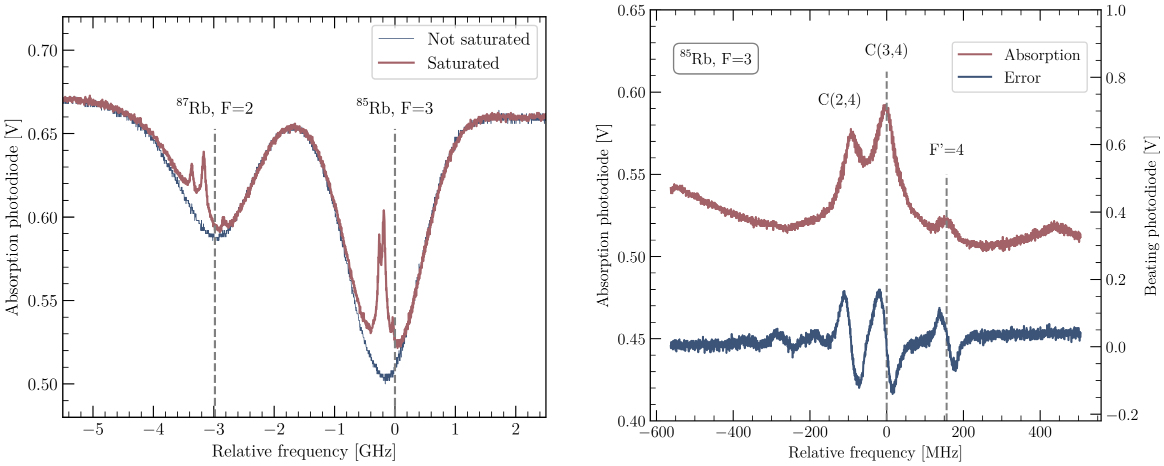

Figure C.2. – ^{85}Rb saturated absorption: used for laser locking. The left panel shows a wide scan, where the dip corresponding to the transitions from $\left|^5S_{1/2}, F=3\right\rangle$ for ^{85}Rb and from $\left|^5S_{1/2}, F=2\right\rangle$ for ^{87}Rb can be seen. Saturated absorption (red) allows one to resolve the hyperfine structure by getting rid of the Doppler broadening. The right panel shows a scan restricted to the transitions from $\left|^5S_{1/2}, F=3\right\rangle$. On the absorption signal, the small peak corresponds to the $\left|^5S_{1/2}, F=3\right\rangle \rightarrow \left|^5P_{3/2}, F=4\right\rangle$ transition to be locked on. In practice, the feedback loop is adjusted to the crossover C(3,4). The blue signal gives the error signal used for locking.

with itself in a Mach-Zender configuration of length ΔL. The associated phase difference is $\varphi_l = n(f_b - f_{ref})\Delta L/c$, where c/n is the signal velocity in the cables. The signal is then filtered by a low-pass filter. The obtained signal is the error signal used to lock on, which is null for different values of f_{rep} labelled by $m \in \mathbb{Z}$

$$f_{rep,m} - f_{MOPA} = f_{ref} + \frac{c[1+2m]}{4n\Delta L}. \tag{C.3}$$

The cable length gives $c/4n\Delta L$ =66.3 MHz. The value of m taken for locking is $m = -1$, stabilising the lock frequency

$$f_{rep} = f_{MOPA} + 2.9147\,\mathrm{GHz}, \tag{C.4}$$

as required. Note that since the 780 MOPA is locked 100 MHz from its target transition, it is the same for the repumper.

C.3. 776 nm laser

The 776 nm laser is also locked using part of the 780 nm MOPA beam, directly using the absorption signal. The associated setup is given in Figure C.5. Part of the

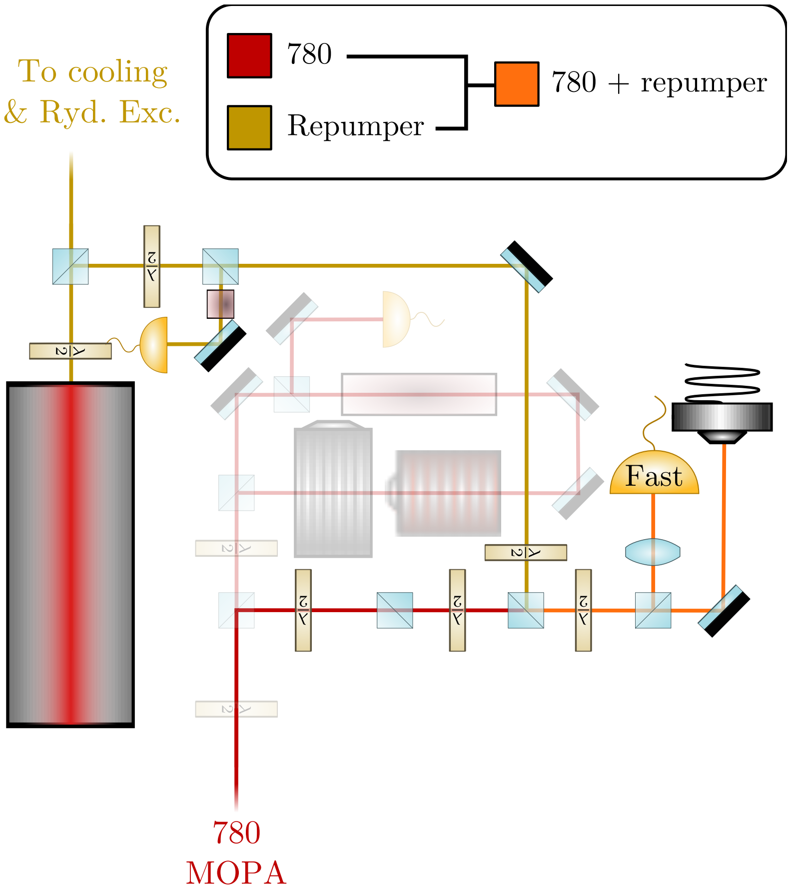

Figure C.3. – **Repumper lock setup.**

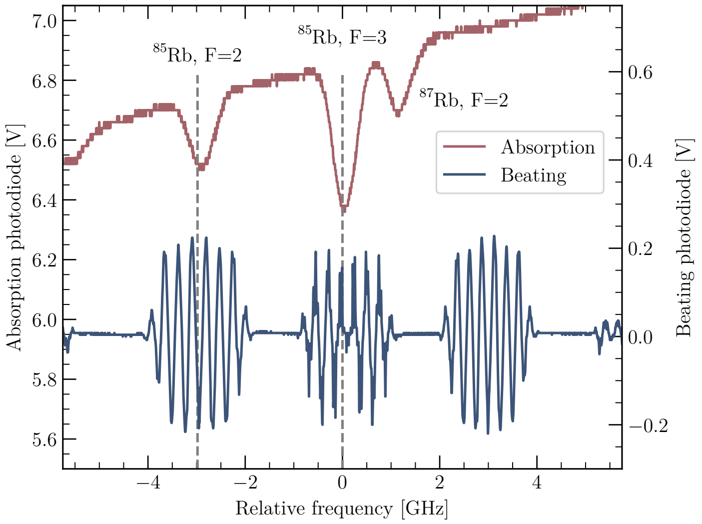

Figure C.4. – **Repumper lock signal:** where the absorption signal (red) is given for reference. In blue, the beating signal is obtained by mixing the beating signal of the repumper and cooling laser fragments with a reference signal at 2.981 GHz. This creates two groups of fringes at ±2.981 GHz.

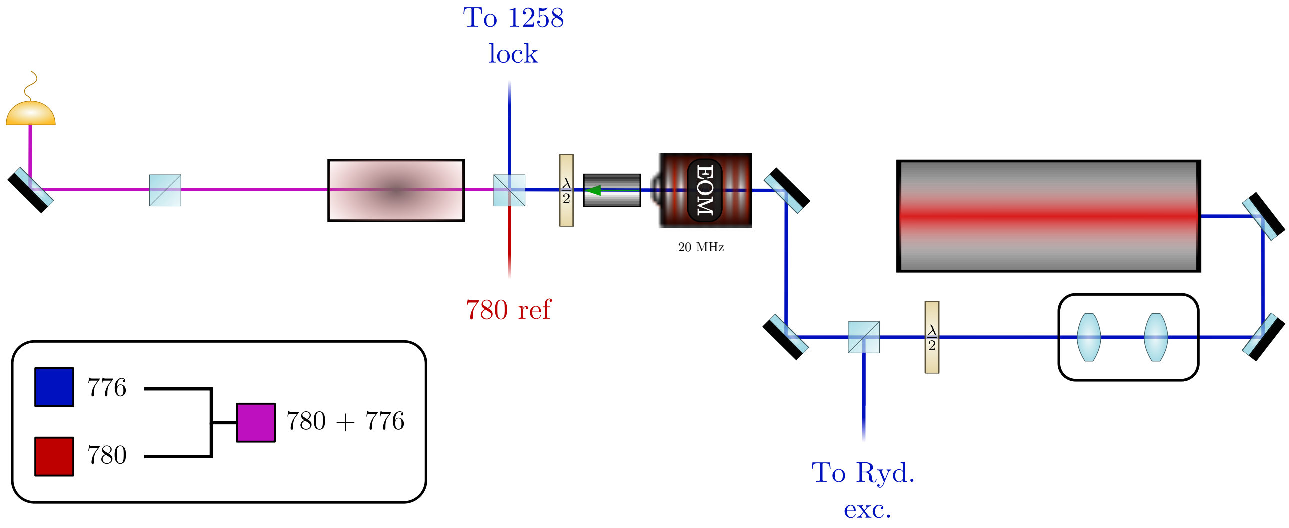

Figure C.5. – **776 nm lock setup.**

776 nm laser beam is overlapped with MOPA laser light, and sent through a heated rubidium cell. Atoms are first excited by the cooling laser, and then scanning the frequency of the 776 nm laser gives the absorption signal depicted in Figure C.6. The $\left|{}^5P_{3/2}, F=4\right\rangle \rightarrow \left|{}^5D_{5/2}, F=5\right\rangle$ transition corresponds to the absorption dip. Note that for this method, the Doppler broadening is already cancelled, the cooling laser only exciting one velocity class.

C.4. 1258 nm

At last, the 1258 nm laser is locked on the 776 laser using a Fabry-Perot cavity whose length L can be scanned. The associated setup is given in Figure C.7. For a laser of wavelength λ_L entering the cavity, the resonance condition is fulfilled if:

$$L = 2m\lambda_L\,, \tag{C.5}$$

where m is an integer associated with the resonance multiplicity. When it is the case, a peak in the transmission can be measured. Both lasers are sent inside the cavity, and their transmission signal is measured. An example of a transmission signal when scanning the cavity length, with constant laser frequencies is given in Figure C.8a.

In this spectrum, several are observed for each laser, corresponding to different multiplicities. A peak for the 776 nm laser is chosen, and the associated error signal is used to lock the cavity length. The 1258 nm laser can then be scanned, leading to the transmission spectrum depicted in Figure C.8b. The laser frequency is then locked on

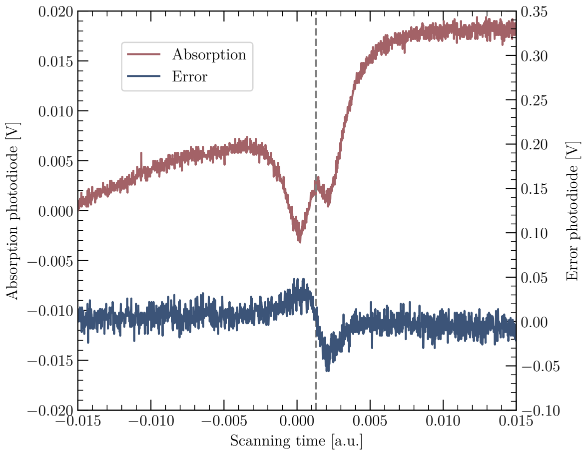

Figure C.6. – 776 nm laser absorption signal: from a cell firstly excited by cooling laser light. The dip corresponds to the $\left|{}^5P_{3/2}, F = 4\right\rangle \rightarrow \left|{}^5D_{5/2}, F = 5\right\rangle$ transition. The associated error signal is given in blue.

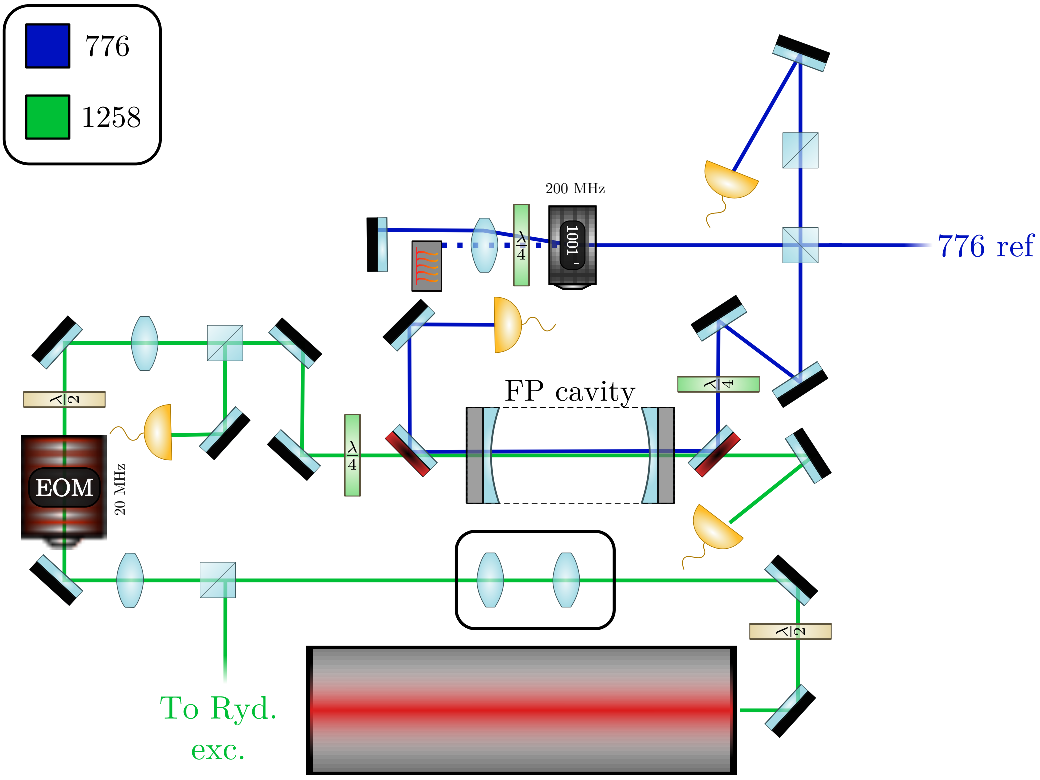

Figure C.7. – 1258 nm lock setup.

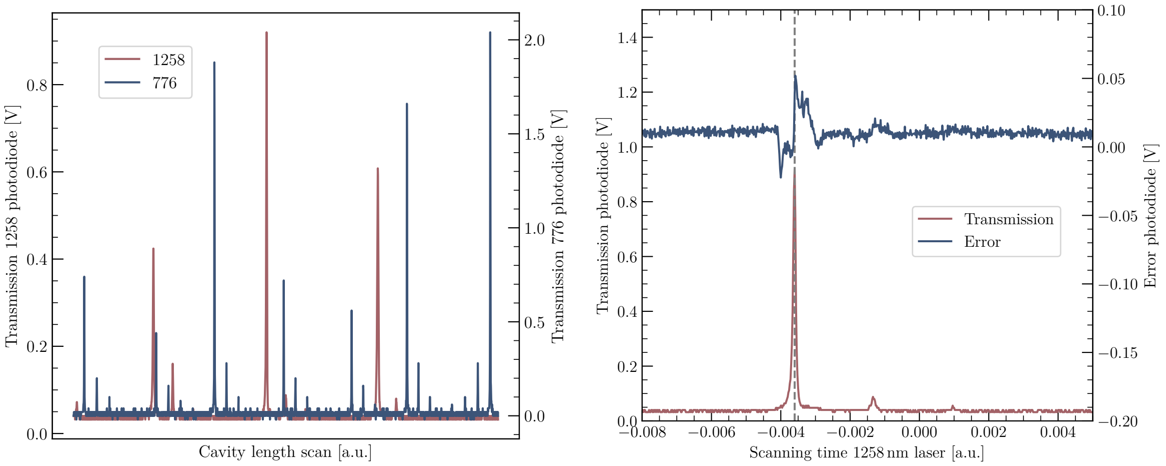

(a) Scanned cavity

(b) Scanned laser

Figure C.8. – Fabry-Perot cavity for 1258 nm laser lock: the left panel corresponds to the transmission signals of both lasers while scanning the cavity length, both laser frequencies being constant. Each peak corresponds to a cavity length for which the resonance condition is fulfilled. The right panel gives the transmission signal while scanning the 1258 nm laser frequency, when the cavity length is locked.

the transmission peak.

Some subtleties exist for this locking method. The existence of many resonance multiplicities for each laser leaves some freedom in the final locking frequency, with some constraints as well. Firstly, the 1258 nm frequency has to be *a priori* tuned such that it is within tuning range[1] of the target Rydberg transition $\left|{}^5D_{5/2}\right\rangle \rightarrow |52f, |m| = 2\rangle$. Then, the 776 nm laser peak chosen to lock the cavity length needs to be close to a 1258 nm laser peak in order to have a peak to lock on.

---

[1] Acousto-optic modulators are used in the setup to fine-tune the laser frequency after lock. This condition is then fulfilled if the lock frequency is within the AOM range from the target transition frequency.

Appendix D

Optical tables

One of the main elements of the experiment is the laser system. Two optical tables are used in this experiment. The first one, named “preparation table” in this manuscript, is the one where frequencies and power of the cooling and Rydberg excitation beams are adjusted. Once this preparation is done, beams are sent to the cryostat table where their geometrical properties, like propagation axis and size, are adjusted.

The second table, also called the “cryostat table”, is the one put around the cryostat and attached to the cryostat structure. It is in fact made of two parts that can be connected and disconnected for opening the cryostat. On this table are set up the six 3D-MOT beams, the two standing wave beams, the Laguerre-Gauss beam and the Rydberg excitation beams.

Last but not least, in between the preparation and cryostat tables, the cooling and repumper light used for the 2D-MOT and the 3D-MOT are redistributed using two optical clusters. These devices allow the distribution of power between the different cooling directions, especially providing a handy adjustment of the cooling power balance for each pair of counter-propagating beams.

Parts of these tables appear in the main text. This appendix will provide the table diagram with all the optical elements used for the experiment.

D.1. Preparation table

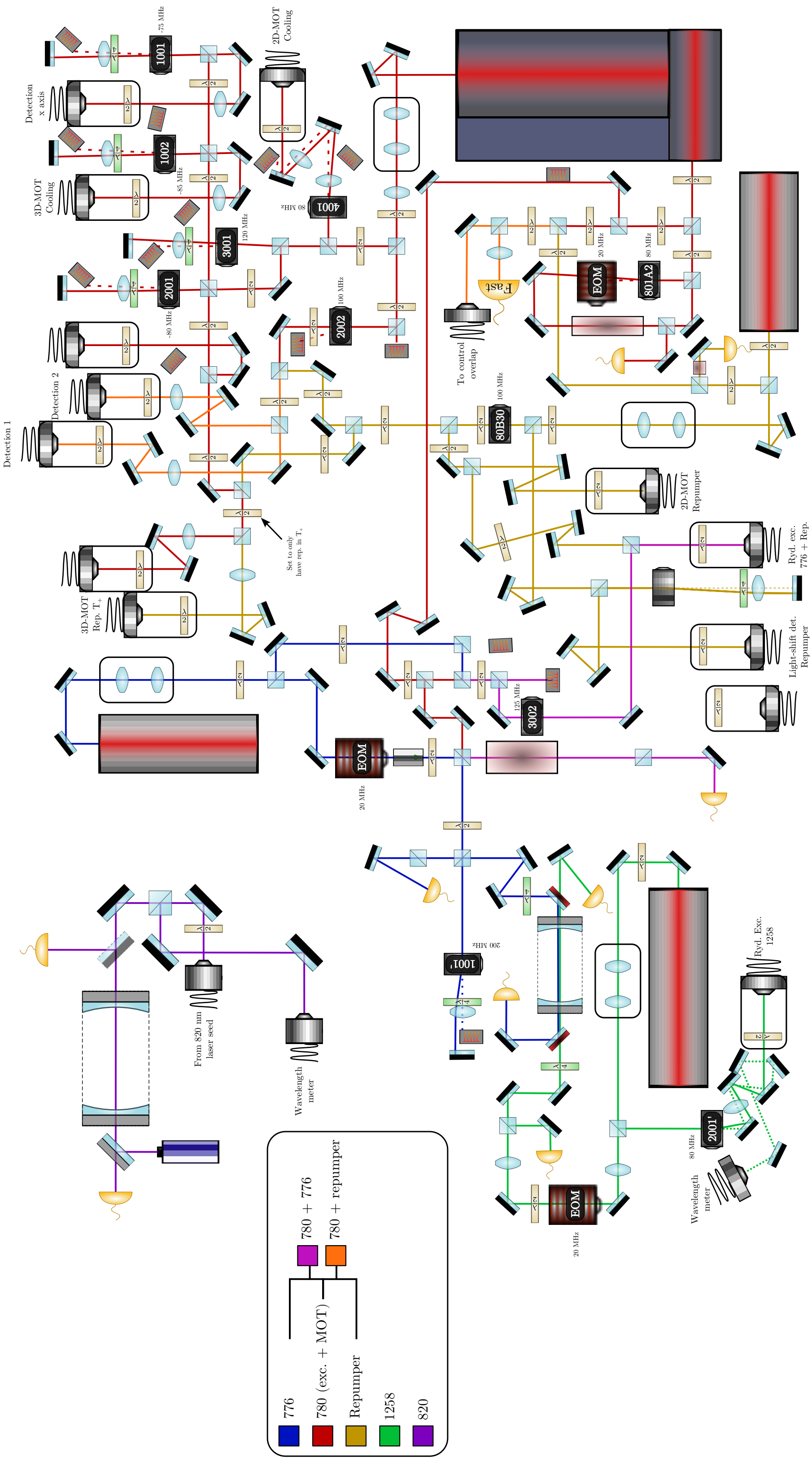

Figure D.1. – Preparation table diagram.

D.2. Fiber clusters

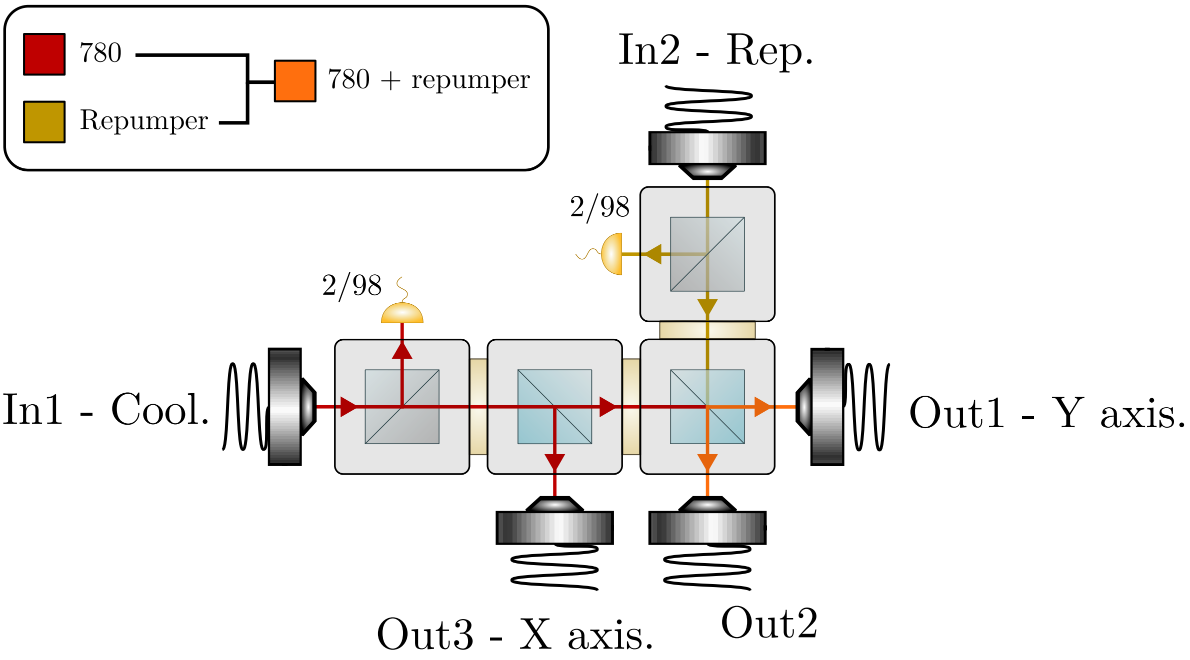

(a) 2D-MOT fiber cluster.

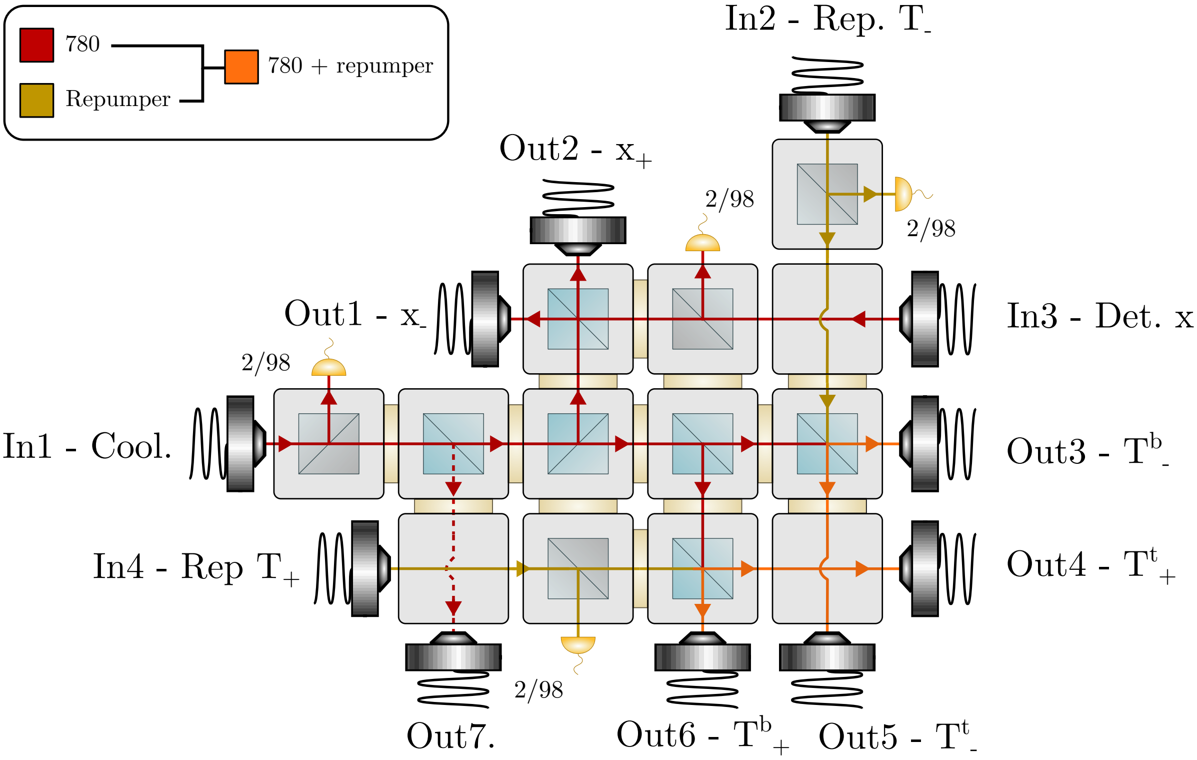

(b) 3D-MOT fiber cluster.

Figure D.2. – Fiber clusters.

D.3. Cryostat table

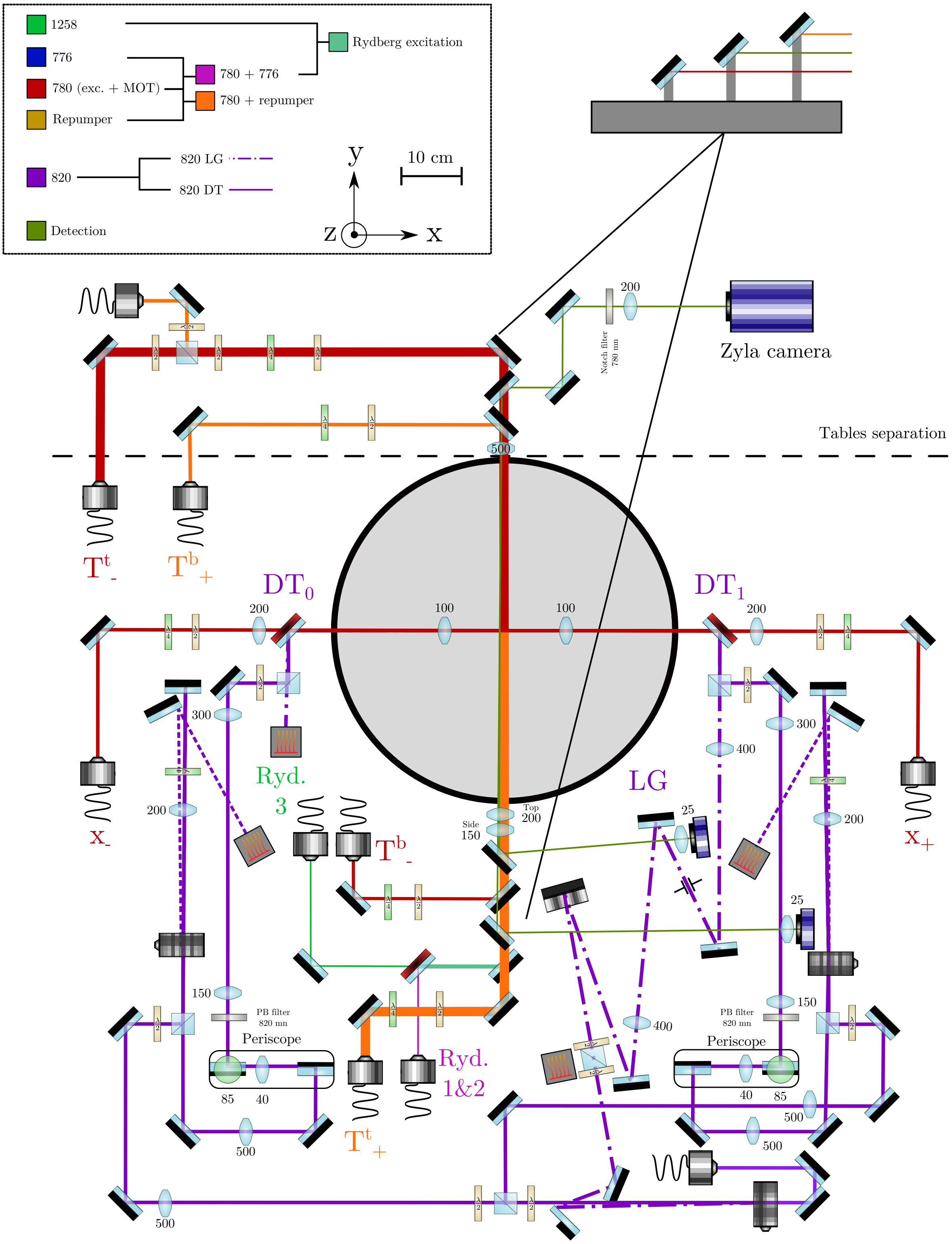

Figure D.3. – Cryostat table diagram.

Appendix E

Qats: popularising quantum physics with cards and dice

During my PhD, I worked on additional side projects on top of my research work. I especially got involved in a popularisation project as part of a doctoral school training. The goal was to create a board game that will be used to popularise quantum physics. This project has been realised in collaboration with other PhD students, Kim Vallée, Thiziri Aissaoui and Gautier Creutzer, with the support of the Quantum Information Center of Sorbonne Université and the constant help of Khamsa Habouchi.

E.1. General idea

Our main goal was to create a board game that can be used as a support to ease the popularisation of quantum physics. One of our first observations was that popularisation was often complicated by the popular idea that quantum mechanics is mysterious, almost magical, making it impossible to grasp. To overcome this issue, our idea was to take some of the basic rules of quantum mechanics, turn them into game rules and make people use these rules by playing a board game. By doing so, our hope was that people would be passively familiarised with some concepts of quantum physics, hence easing the popularisation.

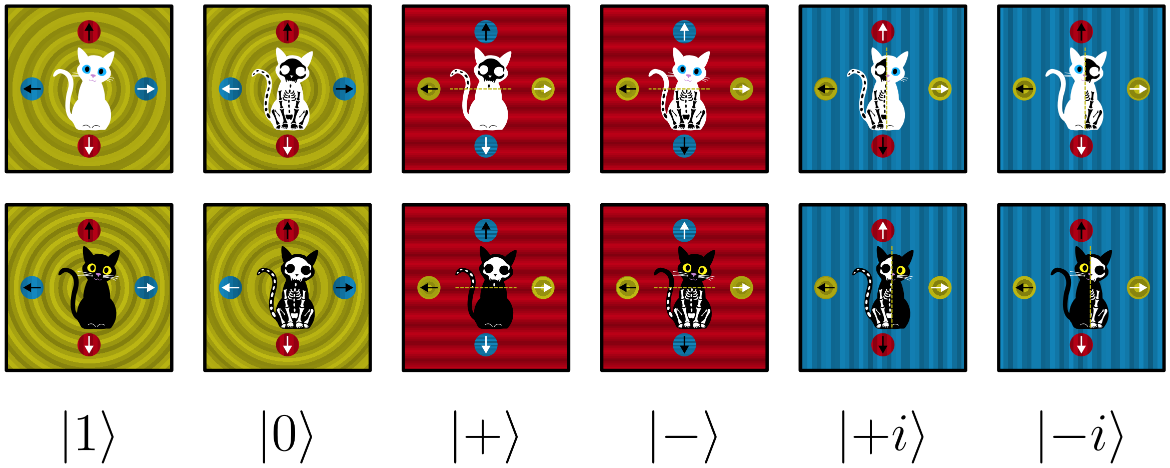

Figure E.1. – **Possible states for the cats.** Yellow states correspond to classical states "dead" and "alive". Red and blue states correspond to two pairs of superposition states. Each state corresponds to a state of the Bloch sphere, indicated below each column.

E.2. Game elements

In practice, we decided to map some key concepts of quantum mechanics into elements that are widely used in board games. To create a story around the game, we decided to use a representation including manipulation of cats' states, with the overall goal to create specific state combinations.

E.2.1. Quantum state

The first concept introduced is the quantum state. In the game, this corresponds to the states of two cats, one white and one black. Each can corresponds to a two-level system. They can be either dead or alive, or in two different pairs of superposition states. Corresponding states are illustrated in Figure E.1.

In the game, these states are represented on dice with six faces. It is used to recreate a kind of simplified Bloch sphere, only keeping the eigenstates of the Pauli matrices. This mapping is illustrated in Figure E.2. Eigenstates of σ_z are the alive/dead states in yellow, eigenstates of σ_x are the superposed states top/bottom in red, and the eigenstates of σ_y are the superposed states left/right in blue.

During a game, there are two dice on the board, each one symbolising the state of a cat. The goal of the players will be to manipulate the cats' states (*i.e.* rotate the dice) to obtain specific states.

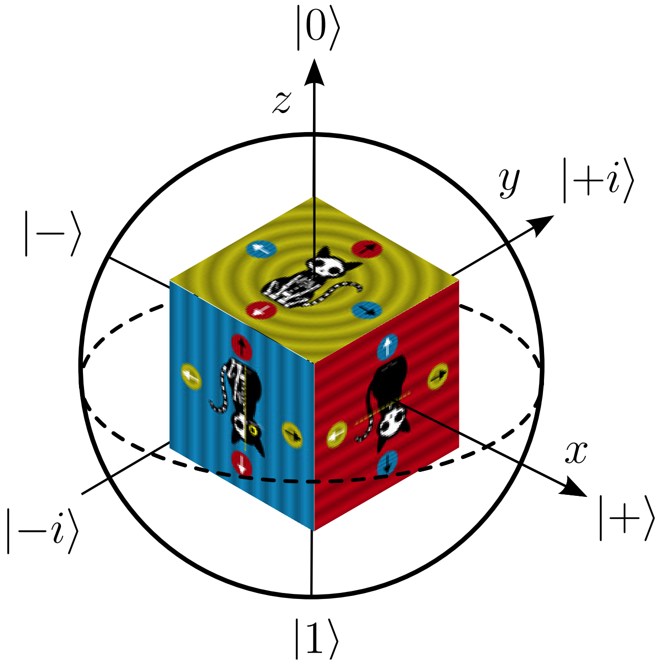

Figure E.2. – **Bloch sphere mapping on a dice.** Each face of the dice corresponds to a state of the Bloch sphere.

E.2.2. Quantum operation

The second concept introduced is the quantum operation. More precisely, we want to illustrate that the quantum states can be changed by manipulating the system. Mathematically, an operation on a two-level system corresponds to a rotation in the Bloch sphere. Thanks to the mapping between a dice and the Bloch sphere, an operation thus corresponds to a rotation of the dice. It is illustrated in Figure E.3a.

Each rotation axis has a colour which corresponds to the associated eigenstates. For example, rotations around the x axis are in red. For each rotation, there are two possible directions, differentiated by two arrow colours: a black arrow or a white arrow.

In the game, these operations are associated with cards, which are depicted in Figure E.3b. When the players want to rotate the dice, they have to play the associated operation card. If there is a single arrow on the card, the dice moves by one face ($\pi/2$ rotation). If there are two arrows, it's a two-face movement (π rotation).

During the game, each player has cards in their hand that they can play to change the cats' states (*i.e.* rotate the dice).

E.2.3. Quantum measurements

The third concept introduced is the quantum measurement. More precisely, the idea we wanted to convey is that a system can be measured in different ways depending

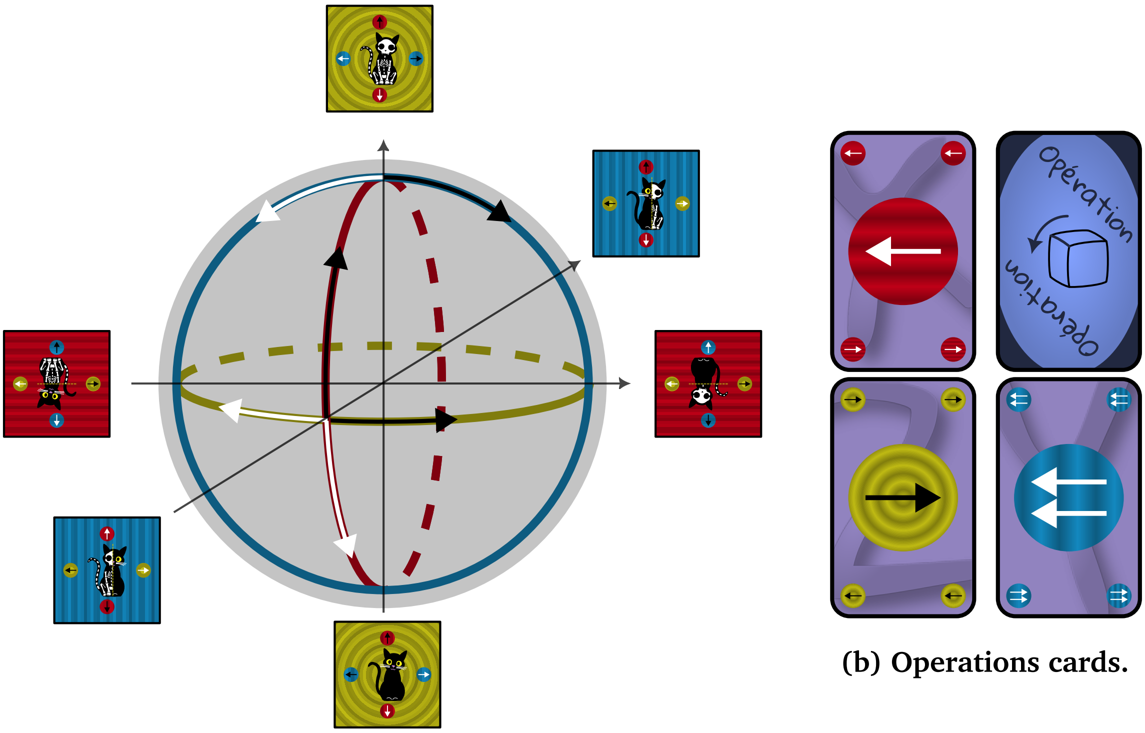

(b) Operations cards.

(a) Operations representation in the Bloch sphere.

Figure E.3. – Operations in the game. Operations, which correspond to rotations in the Bloch spheres, can be mapped onto rotations of the dice. They correspond to arrows on the different faces, with a background colour associated to the rotation axis and an arrow colour associated to the direction. In game, operations correspond to cards, which are depicted on the right.

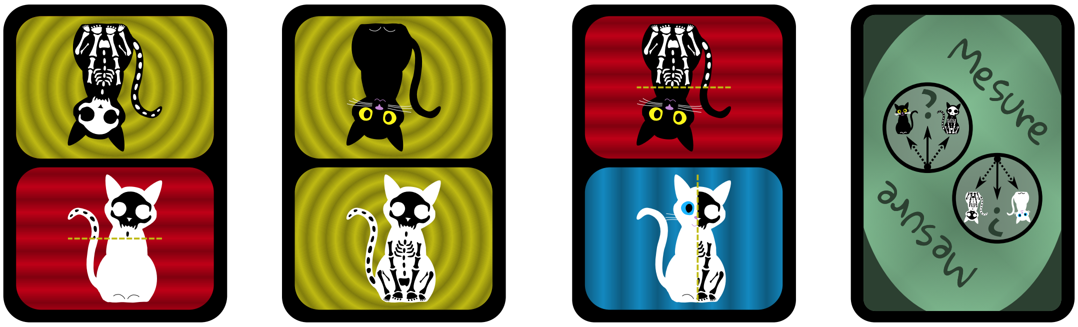

Figure E.4. – **Measurements cards.** They corresponds to states that have to be prepared to be able to perform a successful measurement and win points.

on the kind of state we want to measure. So far, the probabilistic outcome of a measurement doesn't appear in the game.

In the game, measurements are objectives that the players need to validate to win points. They correspond to cards that each player has in hand, which are represented in Figure E.4. In order to win a point, a player has to perform a successful measurement. To do so, they need to use operations to obtain the right states for both cats (*i.e.* have the right dice face pointing up). At the end of the turn, they can perform the corresponding measurement by playing the measurement card that fits the dice faces.

E.2.4. Entanglement

The last concept introduced is the entanglement. In the game, we decided to only use maximally entangled states and use Bell pairs. More precisely, players can use an entanglement card during their turn to create a Bell pair out of the cats states that are on the board. In practice, it means that a second copy of the dice will be put on the board, with the opposite face for each cat. The card and a use example are given in Figure E.5.

Once the entangled state is created, the players can measure either one part or the other part of the pair, depending on the cards they have in hand. This freedom of choice would correspond to a kind of post-selection (we only keep the measurements that worked), with the idea that it should be felt as an advantage, since it increases the possibility of performing a successful measurement.

A second idea we want to convey is that entanglement is a resource. In practice, it means that each player starts with three entanglement cards that they can play but can't draw more.

When a player performs a measurement on one of the pairs, the other pair (which doesn't correspond to the measurement done) is removed, meaning that the non-measured dice are removed from the game. With this, the idea is to have a kind of

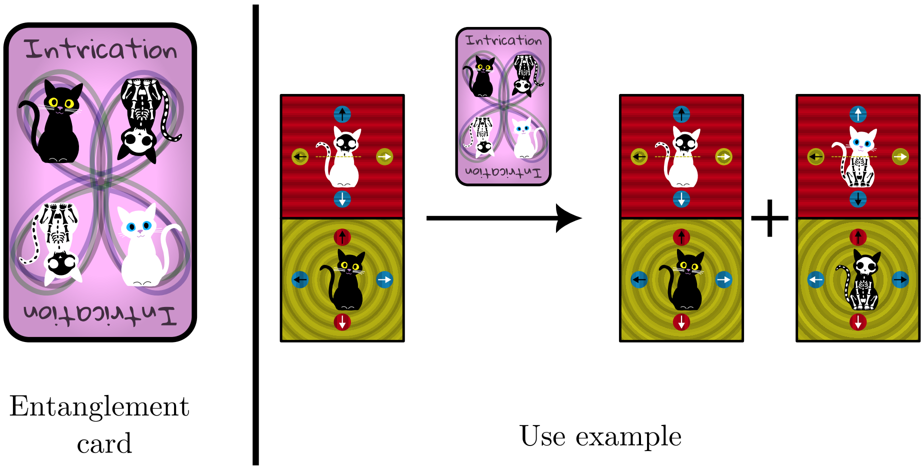

Entanglement card

Use example

Figure E.5. – Entanglement in the game. The left side of the figure shows the entanglement card. The right side shows an example of the use of the entanglement card.

projective measurement.

E.2.5. The board

The game is played on a board, shown in Figure E.6. Different slots are used to put the different card decks, and slots are used in the centre to put the dice.

E.3. Current status and perspectives

Using the game elements introduced above, we created a board game with a set of rules that are not detailed here. It has been used several times for popularisation activities, with a diverse audience. Overall, the game has been well received. We are currently working on improved versions to correct for some game mechanics issues and increase the scientific representation in the graphical elements.

In addition, new game elements will possibly be added to add more content about quantum physics. For example, one aspect which is absent in the game is the probabilistic measurement outcome and the projective measurement. A possible solution would be to allow for measurements on states that don't correspond to the states on the measurement card, with success determined by a coin flip. If the measurement succeeds, the dice would be put on the measured state, and if not, on the opposite.

Overall, the game seemed to ease the popularisation sessions we took part in. We will continue to work on improved versions and try to multiply the interventions, especially in schools, to try to reach a broader audience.

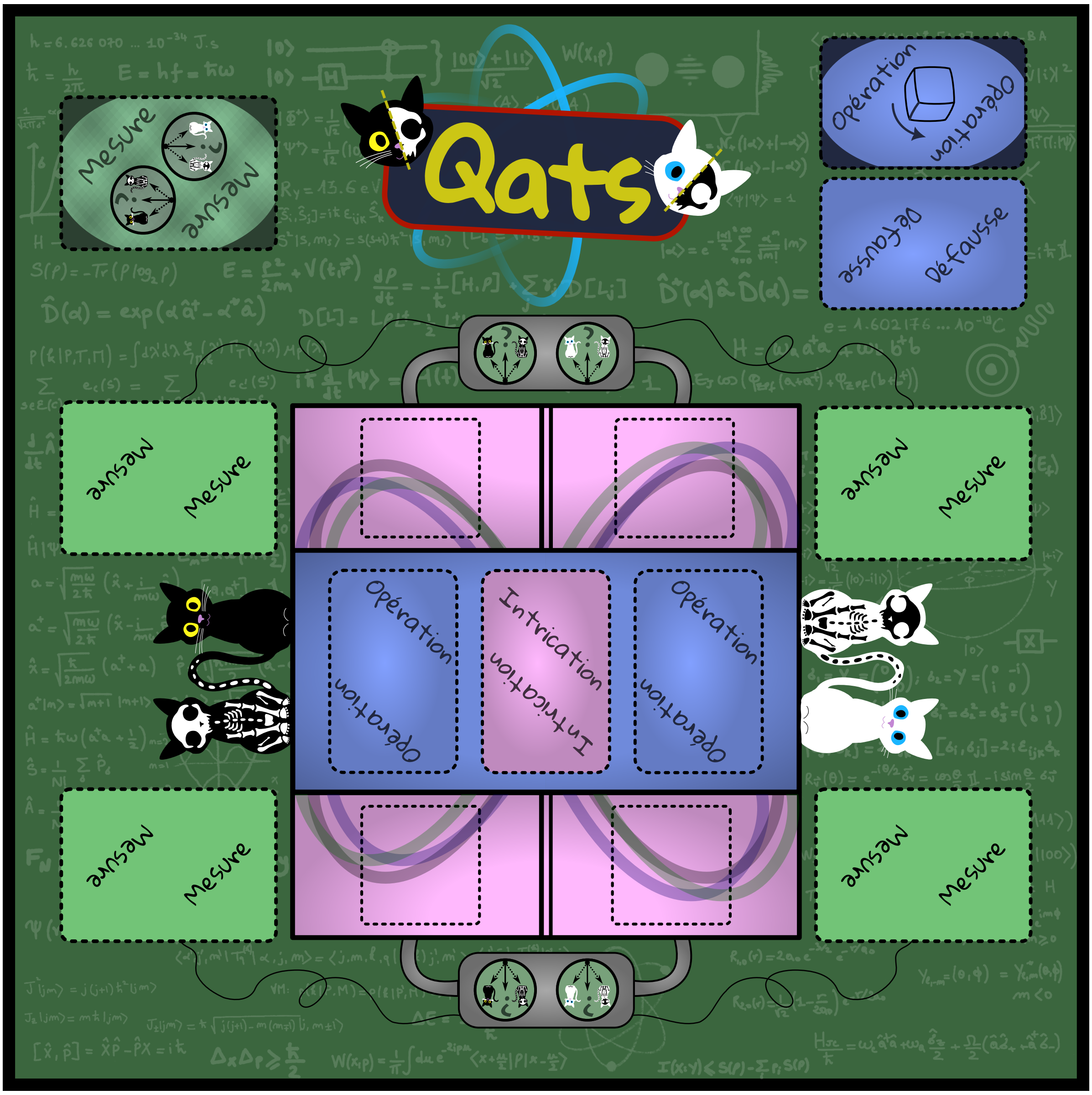

Figure E.6. – Board used in the game.

Résumé en français

Chapitre 1

Le premier chapitre introduit les éléments théoriques utilisés pour la description des expériences présentées dans ce manuscrit. La première partie introduit la description de systèmes atomiques isolés, nécessaires à la description des atomes de Rydberg.

Pour cela, le modèle de l'atome d'hydrogène est tout d'abord rappelé, avec notamment l'expression des fonctions d'onde de l'électron de valence en coordonnées sphériques ainsi que les nombres quantiques associés. Sont ensuite introduits les états de Rydberg, qui sont des états fortement excités avec un grand nombre quantique principal $n \gg 1$. Les états qui nous intéressent particulièrement ici sont les états de Rydberg possédant un moment angulaire maximal, aussi appelés états de Rydberg circulaires. Nous introduisons au passage la base parabolique et les nombres quantiques associés. Cette base est particulièrement pratique pour la description des états circulaires, en particulier pour leur couplage avec des champs électriques statiques. Enfin, quelques limites du modèle de l'atome d'hydrogène sont introduites, avec la prise en compte de l'effet du cœur atomique. Dans un premier temps, on présente le couplage du moment orbitalaire de l'électron avec les autres moments angulaires atomiques qui mène aux structures fines et hyperfines. Dans un second temps, le modèle du défaut quantique est introduit, permettant de décrire la déviation du comportement des atomes alcalins vis-à-vis de l'atome d'hydrogène.

La seconde partie présente le couplage des atomes avec des champs externes. Est d'abord abordé le couplage avec un champ magnétique statique, ce qui correspond à l'effet Zeeman. Le couplage avec un champ électrique statique est ensuite décrit, ce qui correspond à l'effet Stark. Enfin, le couplage avec un champ oscillant est discuté. Pour cela, l'Hamiltonien de couplage est d'abord dérivé dans le cadre de l'approximation dipolaire. Dans le cas d'un champ quantifié, cela permet l'introduction du formalisme des états habillés.

La troisième partie présente quelques exemples d'application du couplage atome-champ utilisés plus tard dans l'expérience. La première application est le passage adiabatique, qui permet de transférer efficacement une population atomique d'un état à un autre. Cette même technique est ensuite discutée dans le cadre plus précis de la préparation des états de Rydberg circulaires, aussi appelée circularisation. Une seconde situation correspond au cas où les transitions atomiques et le champ sont fortement désaccordés. Cela mène au phénomène de déplacement lumineux, utilisé pour le piégeage dipolaire des atomes dans l'état fondamental. Dans le cas des atomes de Rdyberg circulaires, le cas du piégeage pondéromoteur est brièvement discuté.

La dernière partie aborde la description du temps de vie des états atomiques. La première étape est le calcul des taux de transition, ce qui correspond à la dérivation de la règle d'or de Fermi. Le cas particulier du temps de vie dans un état de Rydberg circulaire est ensuite discuté. On montre en particulier qu'en espace libre, le temps de vie est principalement limité par les transitions d'un état circulaire $|nC\rangle$ aux états circulaires les plus proches $|(n\pm1)C\rangle$. La gamme de fréquences associée à ces transitions est autour de 50 GHz. À 0 K, seule l'émission spontanée vers l'état circulaire inférieur subsiste et limite le temps de vie à environ 30 ms pour $n \approx 50$. L'on montre ensuite que cette transition peut être inhibée en plaçant l'atome entre deux plaques parallèles conductrices. Cela permettrait d'obtenir des temps de vie de l'ordre de la minute pour un atome isolé, dans des conditions d'expérience réalistes.

Chapitre 2

Le second chapitre décrit une expérience de thermodynamique quantique réalisée sur le précédent montage d'électrodynamique quantique en cavité, et finalisée lors des premiers mois de ma thèse. Dans cette expérience, l'interaction entre un atome et une cavité supraconductrice est utilisée pour simuler différents environnements de décorrélation et mesurer l'entropie produite associée.

La première partie introduit quelques notions de thermodynamique quantique. On y introduit notamment la divergence de Kullback-Leibler, qui quantifie l'entropie produite. On présente aussi le cycle thermodynamique étudié, qui se découpe en trois étapes : une étape unitaire "aller" permettant la création de corrélations entre l'atome et le champ, suivie d'un processus non-unitaire correspondant à la décorrélation par l'environnement, pour finir par une étape "retour" où l'on applique l'inverse de l'opération unitaire aller, afin de fermer le cycle.

La seconde partie présente la théorie nécessaire à la description des différents environnements étudiés. Dans un premier temps, on présente le cas où il n'y a pas de perte de corrélation, ce qui ne crée pas d'entropie. Un second cas est le déphasage, pour lequel les corrélations quantiques sont détruites. Le dernier cas correspond à une décorrélation complète qui détruit toute corrélation entre les deux systèmes. Pour tous les environnements étudiés, on montre que l'entropie produite par le cycle complet correspond à la quantité de corrélations effacées par l'environnement. La quantité d'information effacée est donnée par la diminution d'information mutuelle après la décorrélation.

La troisième partie discute de la simulation expérimentale des différents environnements de décorrélation. Le système utilisé est une plateforme d'électrodynamique quantique en cavité, permettant un contrôle précis de l'interaction entre un atome et une cavité supraconductrice. Une méthode de reconstruction basée sur l'estimation du maximum de vraisemblance permet de reconstruire la matrice densité du système joint atome-cavité. L'opération unitaire de corrélation correspond à une interaction résonnante $\pi/2$ entre l'atome et la cavité, générant un état maximalement intriqué. L'environnement de déphasage est obtenu en appliquant un grand désaccord entre l'atome et la cavité. La décorrélation complète est obtenue à l'aide d'un atome et d'une cavité auxiliaires.

La dernière partie discute le traitement des données et les résultats obtenus. Le calcul direct de l'entropie produite par la divergence de Kullback-Leibler mène à des divergences anormales. Cela s'explique par le processus de reconstruction, qui tend à créer des matrices de rang non maximal. Couplé au bruit expérimental, cela conduit à des valeurs mesurées d'entropie produites anormalement hautes. Ce problème est contourné en définissant le maximum de vraisemblance d'une fonction. Cette méthode a permis de calculer l'entropie produite à partir des résultats expérimentaux, et de la comparer à la quantité de corrélation effacée, et ce pour chaque environnement simulé. En comparant avec des simulations prenant en compte les imperfections expérimentales, ces différentes valeurs semblent concorder, même si certaines différences restent encore inexpliquées.

Chapitre 3

Le troisième chapitre discute la conception et la fabrication du montage expérimental réalisé pour l'étude de l'inhibition de l'émission spontanée des atomes de Rydberg. À terme, ce dispositif expérimental devrait permettre la simulation d'une chaine de spin-1/2, dont le long temps de vie permettrait l'étude de processus lents.

La première partie se concentre sur les éléments nécessaires à une bonne isolation de l'atome. On présente dans un premier temps les plaques d'inhibition, espacées de 2 mm, permettant de découpler l'atome des fluctuations quantiques du vide. La question du contrôle du champ magnétique et du champ électrique dans cette région est aussi discutée, ce contrôle étant essentiel pour obtenir une inhibition efficace. La structure du cryostat est aussi discutée, celui-ci permettant d'obtenir une réduction du rayonnement de corps noir dans la zone d'inhibition. Enfin, le système de piégeage des atomes de Rydberg circulaires dans un piège pondéromoteur est introduit. Ce piégeage nécessite un bon contrôle du vide au cœur du montage expérimental, ainsi qu'une bonne stabilité relative entre le cryostat et le système optique, et les détails associés à ces deux points sont aussi présentés.

La seconde partie présente le dispositif conçu pour la préparation des atomes dans l'état de Rydberg circulaire $n = 51$. La première étape est une excitation laser jusqu'à l'état de Rydberg $|52f, m = 2\rangle$, effectuée via trois échelons d'excitation. La seconde étape est la circularisation, qui débute par un branchement Stark du niveau $|52f, m = 2\rangle$ au niveau $|n = 52, m = 2, k = -47\rangle$. S'ensuit un passage adiabatique à plusieurs photons, à l'aide d'un champ radiofréquence produit par quatre électrodes placées entre les plaques d'inhibition. Enfin, un transfert microonde permet de transférer la population dans l'état $|51C\rangle$, ce qui permet d'ioniser la multiplicité $n = 52$ et ainsi de purifier l'ensemble de toute possible contamination dans des états elliptiques. La préparation d'atomes dans l'état de Rydberg circulaire nécessite au préalable d'avoir un ensemble d'atomes froids dans l'état fondamental piégés entre les plaques d'inhibition. Pour cela, une fontaine atomique alimente un piège magnéto-optique à trois dimensions (3D-MOT) où les atomes sont refroidis à une température d'environ $10\,\mu$K. Les atomes sont ensuite piégés dans un piège dipolaire en configuration d'onde stationnaire, qui peut être utilisée pour transporter les atomes entre les plaques. À noter que ces deux dernières étapes nécessitent un bon accès optique, et certains éléments du montage optique sont placés directement à l'intérieur du cryostat.

La dernière partie décrit les moyens mis en place pour la détection des atomes, permettant de s'assurer de la bonne réalisation de chaque étape de l'expérience. La détection des atomes dans l'état fondamental est réalisée optiquement. Deux chemins de détection avec un large angle de vue ont été utilisés pour certaines caractérisations du 3D-MOT. La fluorescence des atomes y est mesurée à l'aide de caméras CCD. Pour imager les atomes piégés dans le piège dipolaire, un chemin de détection avec une lentille de grande ouverture numérique est utilisé. Combiné à une caméra sCMOS plus performante que les caméras CCD standard, cela permet une mesure du faible signal de fluorescence des atomes dans le piège dipolaire. Enfin, la détection des états de

Rydberg est discutée. Celle-ci est réalisée en détectant les ions issus de l'ionisation des atomes entre les deux plaques. Pour cela, un chemin de détection avec plusieurs électrodes a été conçu et simulé numériquement.

Chapitre 4

Le quatrième chapitre discute de la réalisation des deux pièges magnéto-optiques: un 2D-MOT permettant la réalisation de la fontaine atomique et un 3D-MOT utilisé pour le refroidissement des atomes.

La première partie rappelle le fonctionnement du piégeage magnéto-optique. Celui-ci repose sur le refroidissement Doppler, pour lequel des paires de faisceaux contrapropageants permettent de générer une force de friction effective sur les atomes. Combiné à un gradient de champ magnétique, et une polarisation circulaire des faisceaux laser, cela permet l'obtention d'un nuage d'atomes froids localisé.

La seconde partie présente la préparation des faisceaux laser utilisés pour les deux pièges magnéto-optiques. Les faisceaux de refroidissement sont préparés sur une table annexe, et ajustés en fréquence à quelques dizaines de mégahertz en dessous de la fréquence de résonance de la transition $\left|5^2S_{1/2}, F=3\right\rangle \rightarrow \left|5^2P_{3/2}, F=4\right\rangle$. Afin de compenser le pompage des atomes dans l'état $\left|5^2S_{1/2}, F=2\right\rangle$, un faisceau de repompage est aussi ajouté, accordé sur la transition $\left|5^2S_{1/2}, F=2\right\rangle \rightarrow \left|5^2P_{3/2}, F=3\right\rangle$.

La troisième partie présente la réalisation de la fontaine atomique. Pour cela, un dispositif fourni par le SYRTE est utilisé. Le refroidissement des atomes dans deux directions permet l'obtention d'un jet atomique dans la direction verticale. On mesure une vitesse des atomes aux alentours de $22\,\mathrm{m}\cdot\mathrm{s}^{-1}$ et un flux atomique d'environ 3.4×10^6 atomes par seconde.

La quatrième partie détaille la réalisation du 3D-MOT. Un premier ingrédient nécessaire est un bon contrôle du champ magnétique afin d'obtenir un gradient dans les trois directions de refroidissement, correspondant aux trois axes de paires de faisceaux. Pour cela, deux configurations de bobines ont été conçues, dont une compacte qui devrait pouvoir être utilisée à long terme. La mesure *in situ* des champs magnétiques obtenus est aussi présentée. Le second ingrédient nécessaire à l'obtention d'un 3D-MOT est le montage optique. Pour obtenir les trois paires de faisceaux contrapropageants, la déflection de deux paires de faisceaux est réalisée directement à l'intérieur du cryostat. La dernière paire passe entre les plaques d'inhibition, ce qui contraint sa géométrie. Enfin, les résultats associés sont présentés. L'étape de 3D-MOT permet l'obtention d'environ un million d'atomes à $50\,\mu\mathrm{K}$. Un refroidissement supplémentaire, appelé mélasse optique, permet d'obtenir un nuage d'une centaine de milliers d'atomes à $8\,\mu\mathrm{K}$.

Chapitre 5

Le cinquième chapitre présente les résultats liés au piégeage et au transport des atomes. Il se compose de deux parties, une première dédiée au piégeage dans l'onde stationnaire, et une seconde partie dédiée au transport des atomes.

La première partie débute par une introduction au piégeage dipolaire, avec un rapide historique. On y présente les valeurs clés du piégeage d'atomes de rubidium ainsi que le potentiel de piégeage associé à une onde stationnaire. On présente ensuite le montage optique associé. Enfin, les différentes caractérisations opérées sur le piège dipolaire. Tout d'abord, on présente une mesure du temps de piégeage ainsi que l'effet de différents paramètres sur celui-ci, comme la pureté spectrale du faisceau et l'influence de la puissance laser. On discute ensuite de la mesure du déplacement lumineux, permettant une mesure de la taille du faisceau focalisé. Enfin, l'on détaille des résultats préliminaires sur la mesure de la température des atomes dans le piège.

La seconde partie se concentre sur le transport des atomes. Pour ce faire, deux techniques sont combinées. La première consiste à changer le désaccord entre les faisceaux contrapropageants à l'origine de l'onde stationnaire, ce qui a pour effet de faire défiler les franges d'interférence, ce qui déplace les atomes. La distance de transport associée est limitée par la longueur de Rayleigh des deux faisceaux focalisés, estimée autour de 0.58 mm. Pour dépasser cette limite, une seconde technique est utilisée pour que le point de focalisation des deux faisceaux suive les atomes. Pour cela, deux lentilles de longueur focale variable sont placées sur le chemin optique, permettant ainsi de changer la convergence des faisceaux avant focalisation et avec cela la position de focalisation. La réalisation du transport est ensuite présentée. On y discute quelques études préliminaires, telles que la distance limite de transport en l'absence de déplacement du waist, ainsi que l'effet de la durée de transport. Enfin, on présente le résultat final de transport obtenu, avec une efficacité supérieure à 65% pour une distance de 14 mm, ce qui correspond à la distance entre le 3D-MOT et le centre de la zone d'inhibition.

RÉSUMÉ

La description de l'évolution des systèmes quantiques à grands nombres de particules est une tâche difficile. Leur complexité computationnelle empêche les calculs *ab-initio* sur des ordinateurs classiques au-delà d'une centaine de particules. Une possible alternative est la simulation quantique analogique. Dans ce contexte, notre équipe a proposé un nouveau simulateur basé sur des atomes de Rydberg circulaires piégés et protégés de l'émission spontanée. Refroidi en dessous d'un kelvin, ce dispositif atteindrait des temps de simulation plus longs, permettant ainsi l'étude de processus jusque là hors de portée d'autres plateformes expérimentales.

La première partie du manuscrit présente une expérience de thermodynamique quantique, réalisée sur un ancien montage d'électrodynamique quantique en cavité. En exploitant l'interaction entre un atome et une cavité supraconductrice, nous avons simulé des environnements associés à différents processus de décorrélation et mesuré leur production d'entropie, à l'échelle microscopique des particules quantiques uniques. La discussion met en avant les difficultés de mesure de l'entropie relative et les solutions de traitement de données utilisées.

La seconde partie présente la conception et la mise en service d'un nouveau montage expérimental visant à terme la simulation d'une chaîne de spins $1/2$. Pour cela, le dispositif et les procédures du précédent montage ont dû être modifiés et adaptés. L'inhibition de l'émission spontanée est réalisée par deux plaques conductrices parallèles réduisant la densité de modes dans lesquels les atomes peuvent se désexciter. Afin de maximiser le temps de vie des états atomiques, l'ensemble du montage a été conçu pour isoler les atomes tout en maintenant les moyens de contrôles nécessaires. À ce jour, le résultat le plus important obtenu est la réalisation d'une source déterministe d'atomes froids piégés dans la zone d'inhibition. Les éléments nécessaires à la préparation et la détection des atomes de Rydberg circulaires ont été assemblés et sont actuellement testés sur les atomes.

MOTS CLÉS

Atomes de Rydberg circulaires, simulation quantique, piégeage dipolaire, inhibition de l'émission spontanée, thermodynamique quantique, production d'entropie

ABSTRACT

The description of the evolution of many-body quantum systems is a difficult task. However, the associated computational complexity prevents *ab-initio* calculation on classical computers. A possible alternative is analogue quantum simulation. In that context, our group proposed a new quantum simulator based on trapped circular Rydberg atoms protected from the spontaneous emission. Cooled down below one Kelvin, this setup is expected to reach longer simulation times, allowing for the study of processes out of reach of other experimental platforms.

The first part of this manuscript presents a quantum thermodynamics experiment, carried out on a previous cavity quantum electrodynamics setup. Using the interaction between an atom and a superconducting cavity, we simulated different decorrelating environments and measured their entropy production, at the microscopic scale of the single quantum particle. The discussion emphasises the difficult measurement of the relative entropy and solutions used for data-processing .

The second part presents the design and implementation of a new experimental setup intended for the future simulation of a spin-$1/2$ chain. For this purpose, the previous experimental setup and procedures had to be modified and adapted. Inhibition of the spontaneous emission is realised by two conductive parallel plates reducing the density of modes into which atoms can decay. To maximise the atomic states lifetime, the setup has been designed to isolate the atoms while preserving the necessary control capabilities. So far, the main result obtained is the realisation of a deterministic source of trapped cold atoms inside the inhibition region. All elements required for the circular Rydberg atoms preparation and detection have been assembled and are currently being tested on the atoms.

KEYWORDS

Circular Rydberg atoms, quantum simulation, dipole trapping, inhibition of the spontaneous emission, quantum thermodynamics, entropy production